An experimental study on the behaviour of copper and other trace elements in magmatic systems

Dissertatation
zur Erlangung des Grades eines Doktors der Naturwissenschaften

der Geowissenschaftlichen Fakultät
der Eberhard-Karls-Universität Tübingen

vorgelegt von
Patrick Were
aus Jinja (Uganda)

2007

Thesis jury

Tag der mündlichen Prüfung: 14. Mai 2007

Dekan: Prof. Dr. Peter Grathwohl

1. **Berichterstatter:** Prof. Dr. Hans Keppler
2. **Berichterstatter:** Prof. Dr. Dr.h.c. Muharrem Satir

Acknowledgements

I would like to thank my in-laws, Mr. and Mrs. Higwira for keeping my family during the period I have been abroad. I am indeed grateful for their support, patience and understanding.
Funding of this research was provided by DFG grant Gottfried Wilhelm Leibniz-Preis 2001 to Professor Dr. Hans Keppler. I am very grateful to him for having given me the chance to do my Ph.D research work, benefiting from his grant. As my supervisor, he carefully read through the entire dissertation and made many suggestions for its improvement, in matters of substance as well as style. I am grateful for his generous effort on his part, but any remaining errors are of course mine.
Professor Dr. Muharrem Satir opened my eyes as regards to the use of stable and radioactive isotopes in geochemistry. I would also like to thank him for the moral support and advice he often offered me whenever I had difficulties of any kind.
I should like to extend my thanks to the entire academic staff of the Institute of Mineralogy at the University of Tübingen for their endeavours in teaching me the theory and practical aspects necessary for safe use of experimental and analytical equipment. Dr. Thomas Wenzel, the chief of the Microprobe laboratory, helped me a great deal with the chemical analysis of samples using the Electron microprobe.
Andreas Audetat, then a post-graduate and head of our research team, helped me a great deal with the calculations necessary for the preparation of the starting glasses and mixtures for my experiments.
The technical team at the Bayerisches Geoinstitut, particularly Mr. Detlef and Anke, also deserve many thanks. They helped me to get some analytical results of my problematic samples using Electron microprobe.
I would also like to thank the workshop staff, particularly the Meister, Mr. Walker, and Barbara, for the care and maintenance of the experimental and analytical equipment, and Mrs. Gill-Kopp, for fine polishing of my samples.
Finally I would like to thank my family for all their love and prayers.

Table of Contents

LIST OF FIGURES

LIST OF TABLES

Abstract

1. Distribution of trace elements between biotite and hydrous granitic melt.

The synthetic system haplogranite-anorthite-biotite-H_2O, doped with a suite of trace elements (V, Cr, Co, Ni, Cu, Zn, Rb, Cs, Sr, Ba, Mo, W, Nb, Ta, REE, Pb and Zr) was experimentally investigated over the temperature interval of 700–800°C at 200 MPa (H_2O) to study the distribution of trace elements between biotite and coexisting hydrous melt. The starting materials were a series of volatile-free synthetic glasses obtained by heating a mixture of appropriate reagent grade chemicals (oxides, carbonates or hydroxides) corresponding to ~76 wt% haplogranite (35 wt% SiO_2, 40 wt% $NaAlSi_3O_8$ and 25 wt% $KAlSi_3O_8$), ~8 wt% anorthite, ~15 wt% biotite (with a 1:1 molar ratio of Mg/Fe) and ~1 wt% total trace elements, so selected as to avoid peak interference during microprobe analysis. Experiments were carried out under water-saturated conditions in cold-seal autoclaves with run durations of between 35 and 45 days. The oxygen fugacity was close to the Ni-NiO buffer. Run products were analysed by electron microprobe.

Besides biotite, run products contained other phases including amphibole (hornblende), clino-pyroxene, plagioclase, magnetite, allanite and glass.

Measured partition coefficients indicate that most alkalis, alkaline earth metals and transition metal elements favoured biotite over the melt (e.g. D_{Rb} ~ 2.6, D_{Cs} ~0.6, D_{Ba} ~1.8, D_{Sr} ~0.6, D_{Co} ~34, D_{Ni} ~84, D_{Zn} ~8.1, D_V ~26, D_{Cr} ~15, and D_{Ti} ~10). The converse is, however, true for the REEs, with D-values decreasing from D_{La} ~0.6 to D_{Gd} ~0.04 and again rising to D_{Lu} ~0.4. The variation of trace element partition coefficients with ionic radius was described by an elastic strain model. The alkalis (Cs^+, Rb^+, and Na^+) and alkaline earths (Ba^{2+}, Sr^{2+}, and Ca^{2+}), including Pb^{2+}, follow K^+ into the largest interlayer site of the biotite crystal, each group fitting onto separate parabolic curves to yield fit parameters $D^{+}_{o(K)}$~3.37, $E^{+}_{(K)}$~370 kbar, $r^{+}_{o(K)}$~1.41 Å and $D^{2+}_{o(K)}$~1.79, $E^{2+}_{(K)}$~650 kbar, $r^{2+}_{o(K)}$~1.36 Å, respectively. Most of the other trace elements, including 2+ (Ni, Co, Zn, Cu, and Fe), 3+ (V and Cr), 4+ (Ti and Zr), 5+ (Nb and Ta), and 6+ cations (W and Mo) follow Mg^{2+} into the M2 site, in 6-fold co-ordination, with each group following its own parabolic curve. However, only the divalent group, with more than two trace elements, has been treated onto the elastic strain model with fit parameters $D^{2+}_{o(M2)}$~90, $E^{2+}_{(M2)}$~6850 kbar and $r^{2+}_{o(M2)}$~0.67 Å.

The REEs show a partitioning pattern, which cannot be explained by substitution onto a single lattice site. They apparently partition into two crystallographic sites of the biotite (i.e. K and M1). The LREEs predominantly partition into the K-site, the MREEs show mixed partitioning character in both the K and M1 sites and the HREEs predominantly partition into the M1 site. The measured partition coefficients, therefore, fit onto two parabolic curves with fit parameters $D^{3+}_{o(M1)}$~0.46, $E^{3+}_{(M1)}$~13630 kbar and $r^{3+}_{o(M1)}$~0.84 Å and $D^{3+}_{o(K)}$~3.37, $E^{3+}_{(K)}$~3230 kbar, $r^{3+}_{o(K)}$~1.14 Å.

The accessory mineral allanite was found in run products belonging to some samples doped with REEs in the starting mixtures. The REEs are highly compatible in allanite with their partitioning behaviour possibly being influenced by temperature (e.g. D_{Ce} ~390, D_{Pr} ~340, D_{Nd} ~290, D_{Er} ~40, at 800°C and D_{Pr} ~650, D_{Nd} ~630, D_{Er} ~60, at 775°C).

Brice model fit-curves show that all REEs partition into the octahedral Ca-site of the allanite crystal, with fit-parameters ($D^{3+}_{o(Ca)}$ ~420, $E^{3+}_{(Ca)}$ ~2600 kbar and $r^{3+}_{o(Ca)}$ ~1.04 Å) at 800°C and ($D^{3+}_{o(Ca)}$ ~670, $E^{3+}_{(Ca)}$ ~4600 kbar, $r^{3+}_{o(Ca)}$ ~1.00 Å) at 775°C.

Biotite is an early crystallising mineral in magmatic systems and tends to fractionate a greater proportion of the compatible trace elements from the melt, rendering them unable to form viable ore deposits. On the other hand, incompatible trace elements are progressively enriched in the melt with increasing crystallisation and fractionation of biotite, with the result that at fluid saturation, a good proportion of these elements will be extracted from melt by exsolved and migrating hydrothermal fluids, to be later concentrated and deposited to form ore deposits. Allanite-melt partition coefficients for REEs are so high that a very small fraction of crystallisation and fractionation of allanite may drastically deplete the melt of its REE content close to zero.

2. Speciation and oxidation state of copper in silicate melts

The oxidation state of copper in silicate melts of variable composition was studied at 1 bar at temperatures of between 1250 and 1400°C under controlled oxygen fugacity. Synthetic silicate glasses (each doped with 1 wt% Cu, as CuO) of haplogranites, tholeiite, alkali-basalt and andesite were prepared from appropriate amounts of reagent-grade oxides, carbonates and hydroxides. With regard to the haplogranites, a series of 4 separate glasses were prepared with varying molar ratios of $[Na_2O+K_2O]/Al_2O_3$ (i.e. 0.6, 0.93, 1.42 and 1.75) but keeping the SiO_2 content and the molar ratio Na_2O/K_2O relatively constant, to represent a range of naturally occurring melts, including peraluminous, subaluminous, and peralkaline varieties.

Experiments were conducted using a gas-mixing technique to investigate the effect of oxygen fugacity on the redox ratio of copper (Cu^{2+}/Cu^{+}) in silicate melts, at various equilibrium temperatures (1250-1400°C). Oxygen fugacity inside the furnace (1 bar total pressure) was imposed by pure CO_2 and CO_2/H_2 gas mixtures with varying ratios. A Y- doped ZrO_2 oxygen sensor assembly was installed in the furnace as a means of monitoring the imposed oxygen fugacity inside the furnace.

A Bruker IFS 125 HR Fourier-Transform-Spectrometer (FTIR) was used to measure absorbance due to crystal field bands of Cu^{2+} in the run product glasses. The Cu^{+} content in the glasses was determined as the difference between the total Cu determined by electron microprobe and the Cu^{2+} measured by optical spectroscopy.

Glass standards containing only Cu^{2+} were also prepared under high oxygen partial pressure generated by the decomposition of PtO_2 in sealed Pt/Rh capsule at 1250°C.

The extinction coefficients ε (l/mol/cm) in glass standards were calculated to be 12.8 for alkalibasalt, 16.8 for tholeiite, 11.6 for andesite, 7.26 for haplogranite with the molar ratio (Na + K)/Al = 0.6, 33.2 for haplogranite with (Na + K)/Al = 0.93, 15.6 for haplogranite with (Na + K)/Al = 1.42 and 15.4 for haplogranite with (Na + K)/Al = 1.75.

Peraluminous haplogranite glass with molar ratio (Na+K)/Al = 0.60 entirely contained Cu^{+} ions, which could not be converted into Cu^{2+} ions even under the most oxidising conditions using PtO_2.

For a given glass composition under the same gas atmosphere, absorbance (A), colour intensity and ratio Cu^{2+}/Cu^{+}, increase with decreasing run temperatures. On the other hand, if temperature is kept constant and gas atmosphere varied, absorbance (A), glass colour intensity and the ratio Cu^{2+}/Cu^{+}, increase with increasing oxygen fugacity.

Generally the maximum absorption band due to Cu^{2+} ions at any run temperature appeared at ~ 13000 cm^{-1} (wavenumber) for andesite, alkalibasalte, and tholeiite glass and ~ 12500 cm^{-1} for haplogranite glasses.
For a silicate melt of a given composition, plots of log (Cu^{2+}/Cu^{+}) against log fo_2 at any run temperature exhibit a linear relationship, with graphs for different temperatures trending almost parallel to each other with slopes in the range of 0.239 to 0.256. The lowest and highest temperature curves lie uppermost and lowermost, respectively. At a fixed run temperature T, plots of log (Cu^{2+}/Cu^{+}) against log fo_2 for a silicate melt of any given composition exhibit a similar linear relationship, with curves for the granitic , dioritic and basaltic melts lying upper-most , intermediate and lowest, respectively.
ΔH for the oxidation of Cu^{+} to Cu^{2+} was estimated to be -531.3, -392.8, -386.9, -394.3, -473.9 and -521.9 kJ/mol, for tholeiite, alkali-basalt, andesite, haplogranite with (Na + K)/Al = 0.93, haplogranite with (Na + K)/Al = 1.42 and haplogranite with (Na + K)/Al = 1.75, respectively.
The redox ratios Cu^{2+}/Cu^{+} for granitic and dioritic magmatic systems that often crystallise at temperatures in the range 700 – 800°C, under oxygen fugacities between those of QFM (quartz-fayalite-magnetite), Ni-NiO, and H-M (hematite-magnetite) was estimated. The results show a predominance of Cu^{2+} in granitic and dioritic plutons, i.e. the ratio Cu^{2+}/Cu^{+} is always greater than one. Basaltic melts, however, seem to behave differently. They crystallise in the temperature range (1100 – 1200°C), under oxygen fugacities between those of QFM and Ni-NiO buffer systems, with a predominance of Cu^{+} over Cu^{2+} ions in their melts, i.e. with very low ratios of Cu^{2+}/Cu^{+} (usually less than one).

3. Solubility of copper in common rock-forming minerals

A range of synthetic systems was experimentally investigated (in two options) at isobaric and isothermal conditions (2 kbar and 600-700°C) to determine the solubility of copper in some common rock-forming minerals (muscovite, phlogopite, orthoclase, and albite) which crystallized from hydrothermal solutions in equilibrium with excess metallic Cu and Cu_2O. Samples for option one experiments were prepared simply by mixing reagent grade chemicals corresponding to ~65 wt% mineral and ~ 35 wt% Cu_2O, whereas samples for option two experiments consisted of mixtures corresponding to ~90 wt% mineral and ~ 10 wt% hypothetical Cu-bearing mineral (e.g. for the mineral muscovite 90 wt% KAl_2 $[AlSi_3O_{10}]$ $[OH]_2$ + 10 wt% $Cu^{+}Al_2(AlSi_3O_{10})(OH)_2$).
Experiments were carried out in cold seal bombs at 600 – 700°C with run durations of 15 – 20 days using capsules made of pure copper.
Depending on the composition of the starting mixtures, different copper solubilities were observed as different mixtures stabilised different mineral assemblages. For instance, the solubility of Cu (as wt% Cu_2O) in orthoclase (Cu_{Or}) is in the range 0.863-0.049 and 0.089-0.049 in run products of option 1 (Or1) and 2 (Or2) mixtures, respectively. In albite, Cu_{Ab} ranges from 1.175-0.630 in Ab1 and 0.041 in Ab2. In muscovite, Cu_{Mu} ranges from 0.965-0.634 in Mu1 and 0.08 in Mu2. In phlogopite, Cu_{Phl} ranges from 1.142-0.555 in Phl1. In quartz, Cu_{Qtz} ranges from 1.336-1.173 in Qtz1 and 0.054-0.049 in Qtz2. The upper and lower values of the solubility ranges correspond to 600 and 700°C, respectively. Many other phases crystallised in the run products of both experimental options remain to be identified whilst others simply exist in very low proportions. So there is seemingly still more work left to be done. In principle, once the experimental samples are fully characterised, the results obtained

in these experiments can be combined with those of copper solubility studies in hydrothermal fluids, available from thermodynamic data bases, to calculate partition-coefficients of copper between fluid and minerals existing in equilibrium.

Zusammenfassung

1. Die Verteilung von Spurenelementen zwischen Biotit und wasserhaltiger granitischer Schmelze

Das synthetische System Haplogranit-Anorthit-Biotit-H_2O dotiert mit einer Reihe von Spurenelementen (V, Cr, Co, Ni, Cu, Zn, Rb, Cs, Sr, Ba, Mo, W, Nb, Ta, REE, Pb und Zr) wurde experimentell untersucht im Temperaturbereich von 700-800°C und bei einem Druck von 200 MPa (H_2O) um das Verteilungsverhalten von Spurenelementen zwischen Biotit und der koexistierenden Schmelze zu erforschen. Die Ausgangsmaterialien waren eine Reihe von synthetischen Gläsern mit der Zusammensetzung von ungefähr 76 wt% Haplogranit (35 wt% SiO_2, 40 wt% $NaAlSi_3O_8$ und 25 wt% $KAlSi_3O_8$), 8 wt% Anorthit, 15 wt% Biotit (mit 1:1 Molarverhältnis von Mg/Fe) und insgesamt 1 wt% Spurenelementen. Die Spurenelementen wurden so gewählt, dass während der Analysen mit der Mikrosonde ihre Peaks einander nicht überlagern. Die Experimente wurden zwischen 35 und 45 Tage lang in cold-seal Autoklaven unter wassergesättigten Bedingungen durchgeführt. Die Sauerstoff-Fugazität entsprach in etwa dem Ni-NiO Puffer. Die Produkte der Experimente wurden mit der Elektronenmikrosonde analysiert.
Außer Biotit enthielten die Produkte der Experimente andere Phasen, darunter Amphibol (Hornblende), Klinopyroxen, Plagioklas, Magnetit, Allanit und Glas.
Die gemessenen Verteilungskoeffizienten zeigen, dass die meisten Alkalien, Erdalkalien und Übergangsmetalle im Biotit eingereichert wurden (z. B. D_{Rb} ~ 2.6, D_{Cs} ~0.6, D_{Ba} ~1.8, D_{Sr} ~0.6, D_{Co} ~34, D_{Ni} ~84, D_{Zn} ~8.1, D_V ~26, D_{Cr} ~15, and D_{Ti} ~10). Das Umgekehrte gilt jedoch für die REEs, mit D-Werten, die von 0,04 bis 0,6 variieren (z. B. D_{La} ~ 0.6, D_{Gd} ~0.04 und D_{Lu} ~0.4). Die Variation des Verteilungskoeffizienten der Spurenelemente in Abhängigkeit ihrer Ionenradien wurde beschrieben durch ein elastisches Verformungsmodell. Die Alkalien (Cs^+, Rb^+ und Na^+) und Erdalkalien (Ba^{2+}, Sr^{2+} und Ca^{2+}) einschließlich Pb^{2+} folgen K^+ in die Zwischenschichtgitterposition des biotite-Kristalls. Jede Gruppe hat eine eigene parabolische Kurve, die folgenden Fit-Parameter ergibt: $D^{+}_{o(K)}$~3.37, $E^{+}_{(K)}$~370 kbar, $r^{+}_{o(K)}$~1.41 Å für die Alkalien und $D^{2+}_{o(K)}$~1.79, $E^{2+}_{(K)}$~650 kbar, $r^{2+}_{o(K)}$~1.36 Å für die Erdalkalien. Die meisten anderen Spurenelemente einschließlich den zweiwertigen (Ni, Co, Zn, Cu und Fe), dreiwertigen (V und Cr), vierwertigen (Ti und Zr), fünfwertigen (Nb und Ta) und sechswertigen Kationen (W und Mo) folgen Mg^{2+} in die M2-Position, in 6-facher Koordination, wobei jede Gruppe ihre eigene parabolische Kurve bildet. Für die zweiwertigen Kationen ergeben sich als Fit-Parameter $D^{2+}_{o(M2)}$~90, $E^{2+}_{(M2)}$~6850 kbar, $r^{2+}_{o(M2)}$~0.67 Å.
Die Seltenen Erden (REE) zeigen ein Verteilungsmuster, das nicht durch Die Substitution auf einer einzigen kristallographischen Position erklärt werden kann. Sie verteilen sich auf zwei kristallographischen Positionen des Biotites (d. h. K und M 1). Die LREEs und HREEs besetzen überwiegend die K- beziehungsweise M 1-Positionen. Die MREEs werden auf beiden Gitterpositionen eingebaut. Die gemessenen Verteilungskoeffizienten folgen daher zwei parabolischen Kurven mit Fit-Parametern von $D^{3+}_{o(M1)}$~0.46, $E^{3+}_{(M1)}$~13630 kbar und $r^{3+}_{o(M1)}$~0.84 Å beziehungsweise $D^{3+}_{o(K)}$~3.37, $E^{3+}_{(K)}$~3230 kbar, $r^{3+}_{o(K)}$~1.14 Å.
Das akzessorische Mineral Allanit wurde in den Produkten der Experimente gefunden, deren Ausgangsmischungen mit REEs dotiert waren. Die REEs sind sehr kompatibel mit Allanit mit ihrem Verteilungsverhalten, das möglicherweise durch die

Temperatur beeinflusst wird (D_{Ce} ~390, D_{Pr} ~340, D_{Nd} ~290, D_{Er} ~40, bei 800°C und D_{Pr} ~650, D_{Nd} ~630, D_{Er} ~60, bei 775°C).
Die Fit-Kurven auf der basis eines Brice-Modells fit-Kurven zeigen, dass alle REEs auf der Ca-Position des Allanit-Kristalls eingebaut werden, mit Fit-Parameters von $D_{o(Ca)}^{3+}$ ~420, $E_{(Ca)}^{3+}$ ~2600 kbar und $r_{o(Ca)}^{3+}$ ~1.04 Å bei 800°C und $D_{o(Ca)}^{3+}$ ~670, $E_{(Ca)}^{3+}$ ~4600 kbar, $r_{o(Ca)}^{3+}$ ~1.00 Å bei 775°C. Biotit ist ein früh kristallisierendes Mineral in magmatischen Systemen, es tendiert dazu, einen größeren Anteil der kompatiblen seltenen Elemente aus der Schmelze zu fraktionieren und verhindert daher, dass diese Elemente zu Erzlagerstätten eingereichert werden. Andererseits werden inkompatible seltene Elemente allmählich in der Schmelze angereichert mit zunehmender Kristallisation und Fraktionierung des Biotits. Das Ergebnis ist, dass bei Wasser-Sättigung der Schmelze ein großer Teil dieser Elemente durch hydrothermale Fluide aus der Schmelze extrahiert wird, um später konzentriert und in Erzlagerstätten abgelagert zu werden. Der Verteilungskoeffizient der REEs zwischen Allanit und der Schmelze ist so hoch, dass eine sehr kleine Kristallisation und Fraktionierung von Allanit den REE-Gehalt der Schmelze schnell bis auf fast null verringern kann.

2. Speziation und Oxidationsstufe des Kupfers in Silikatschmelzen

Der Oxydationszustand des Kupfers in Silikatschmelzen mit variabler Zusammensetzung wurde bei 1 bar und Temperaturen zwischen 1250 und 1400°C unter kontrollierter Sauerstoff-Fugazität untersucht. Aus Haplograniten, Tholeiit, Alkalibasalt und Andesit bestehend synthetische Silikatgläser (jedes dotiert mit 1 wt% Cu, in Form von CuO) wurden hergestellt aus entsprechenden Oxid-, Hydroxid- und Carbonat-Mischungen. Von den haplogranitischen Zusammensetzungen wurde eine Reihe von vier verschiedenen Gläsern hergestellt, in denen sich das Mol-Verhältnis von $[Na_2O+K_2O]/Al_2O_3$ (d. h. 0.6, 0.93, 1.42 und 1.75) veränderte, aber der SiO_2-Inhalt und das Mol-Verhältnis Na_2O/K_2O ungefähr gleich blieb, um eine Reihe von peraluminischen, subaluminischen und peralkalischen Zusammensetzungen zu untersuchen.
Die Experimente wurden mit einer Gasmisch-Technik durchgeführt, um den Effekt der Sauerstofffugazitäten auf den Redox-Zustand von Kupfer (Cu^{2+}/Cu^{+}) in Silikatschmelzen im Temperaturbereich von 1250 - 1400°C zu untersuchen. Die Sauerstoff-Fugazität in dem Ofen (1 bar Gesamtdruck) wurde eingestellt durch reines CO_2 und eine Mischung verschiedener Anteilen von CO_2 und H_2. Ein Y-dotierter ZrO_2 Sauerstoffsensor wurde im Ofen installiert, um die Sauerstofffugazität zu messen.
Ein Bruker IFS 125 HR Fourier-Transform-Spektrometer (FTIR) wurde benutzt, um die Absorption durch die Kristallfeldbanden von Cu^{2+} in den abgeschreckten Gläsern zu messen. Der Cu^{+}-Gehalt in den Gläsern wurde ermittelt als Differenz zwischen dem gesamten Cu, das gemessen wurde durch Elektronen-Mikrosonde, und dem Cu^{2+}, das durch optische Spektroskopie bestimmt wurde.
Standardgläser (die nur Cu^{2+} enthielten) wurden unter hohem Sauerstoffpartialdruck hergestellt, der durch den Zerfall von PtO_2 in einer versiegelten Pt/Rh-Kapsel bei 1250°C erzeugt wurde. Die Extinktionskoeffizienten ε (l/mol/cm) von den Standardgläsern wurden ermittelt als 12.8 für Alkalibasalt, 16.8 für Tholeiit, 11.6 für Andesit, 7.26 für Haplogranit mit (Na + K)/Al = 0.6, 33.2 für Haplogranit mit (Na + K)/Al = 0.93, 15.6 für Haplogranit mit (Na + K)/Al = 1.42 und 15.4 für Haplogranit mit (Na + K)/Al = 1.75.

Das Glas von peraluminischem Haplogranit mit Mol-Verhältnis (Na+K)/Al = 0.60 enthielt nur Cu^{+}-Ionen, die selbst unter den höchst oxidierenden Bedingungen mit PtO_2 nicht in Cu^{2+}-Ionen verwandelt werden konnten.
Für eine gegebene Glaszusammensetzung unter unveränderter Gasatmosphäre steigen die Absorption (A), die Farbintensität und das Cu^{2+}/Cu^{+}-Verhältnis mit sinkenden Temperaturen im Experiment. Andererseits wachsen die Absorption, die Intensität der Glasfarbe und das Cu^{2+}/Cu^{+}-Verhältnis mit zunehmender Sauerstoff-Fugazität, wenn die Temperatur gleich bleibt und die Gasatmosphäre verändert wird.
Im Allgemeinen lag das Maximum der von Cu^{2+}-Ionen verursachten Absorptionsbande bei ~ 13000 cm^{-1} für Andesit-, Alkalibasalt- und Tholeiit-Gläser sowie bei ~ 12500 cm^{-1} für Haplogranit-Gläser.
Für eine Silikatschmelze mit einer gegebenen Zusammensetzung zeigen die Diagramme von log (Cu^{2+}/Cu^{+}) im gegen log fo_2 bei jeder Temperatur im Experiment eine Gerade, wobei die Geraden für verschiedene Temperaturen fast parallel zueinander sind mit Steigungen zwischen 0.239 und 0.256. Die Kurven für die niedrigsten und höchsten Temperaturen liegen am höchsten beziehungsweise am niedrigsten. Bei einer gegebenen Temperatur T zeigen die Diagramme von log (Cu^{2+}/Cu^{+}) gegen log fo_2 für verschiedene Silikatschmelzen eine ähnliche Abfolge, wobei die Kurven für die granitischen-, dioritischen und basaltischen Schmelzen am höchsten, in der Mitte beziehungsweise unten liegen.
ΔH für die Oxidation von Cu^{+} zu Cu^{2+} wurde für Tholeiit auf -531.3, für Alkali-Basalt auf -392,8, für Andesit auf -386.9, für Haplogranit mit (Na + K)/Al = 0.93 auf -394.3, für Haplogranit mit (Na + K)/Al = 1.42 auf -473.9 und für Haplogranit mit (Na + K)/Al = 1.75 auf -521.9 kJ/mol geschätzt.
Die Redox-Verhältnis von Cu^{2+}/Cu^{+} für granitische und dioritische Magmen, die oft bei Temperaturen von 700 bis 800°C kristallisieren und unter Sauerstoff-Fugazitäten zwischen denen von QFM (Quartz-Fayalit-Magnetit), Ni-NiO und H-M (Hämatit-Magnetit) kristallisieren, wurden abgeschätzt. Die Ergebnisse zeigen ein Überwiegen von Cu^{2+}-Ionen in granitischen und dioritischen Plutons, das heißt, das Verhältnis Cu^{2+}/Cu^{+} ist immer größer als eins. Basaltische Schmelzen scheinen sich jedoch anders zu verhalten. Sie kristallisieren im Temperaturbereich zwischen 1100 und 1200°C unter Sauerstoff-Fugazitäten zwischen denen von QFM und Ni-NiO Puffern. Bei ihnen überwiegen Cu^{+}- über Cu^{2+}-Ionen in der Schmelze.

3. Löslichkeit von Kupfer in gesteinsbildenden Mineralien

Eine Reihe von synthetischen Systemen wurde experimentell (in je zwei Reihen von Experimenten) bei gleich bleibenden Druck- und Temperaturbedingungen (2 kbar und 600-700°C) erforscht, um die Löslichkeit von Kupfer in einigen gewöhnlichen gesteinsbildenden Mineralien (Muskovit, Phlogopit, Orthoklas und Albit) zu untersuchen, die aus hydrothermalen Lösungen im Gleichgewicht mit überschüssigem metallischem Kupfer und Kupferoxid kristallisierten. Proben für die erste Reihe der Experimente wurden vorbereitet, indem Chemikalien entsprechend ~65 wt% Mineralien und ~ 35wt% Cu_2O gemischt wurden, während die Proben für die zweite Reihen der Experimente aus Mischungen mit der Zusammensetzung von ~90 wt% Mineralien und ~ 10 wt% hypothetischem Cu-haltigem Mineral bestanden (z. B. für Muskovit: 90 wt% $KAl_2\,[AlSi_3O_{10}]\,[OH]_2$ + 10 wt% $Cu^{+}Al_2(AlSi_3O_{10})(OH)_2$).
Die Experimente wurden in cold-seal-Autoklaven bei 600 – 700°C über einen Zeitraum von 15 bis 20 Tagen in Kapseln aus reinem Kupfer durchgeführt.
Abhängig von der Zusammensetzung der Ausgangsmischungen wurden verschiedene Kupferlöslichkeiten beobachtet, weil verschiedene Mischungen

verschiedene Mineralansammlungen produzierten. Die Löslichkeit von Kupfer (als Gewicht % Cu_2O) in Orthoklas zum Beispiel liegt zwischen 0.863 und 0.049 für die Produkte der ersten Reihe von Experimenten (Or1) beziehungsweise zwischen 0.089 und 0.049 für die Produkte der zweiten Reihe von Experimenten (Or2). In Albit, liegt Cu_{Ab} zwischen 1.175 und 0.630 für Ab1 beziehungsweise bei 0.041 für Ab2. In Muskovit liegt Cu_{Mu} zwischen 0.965 und 0.634 für Mu1 und bei 0.08 für Mu2. In Phlogopit liegt Cu_{Phl} zwischen 1.142 und 0.555 für Phl1. In Quartz liegt Cu_{Qtz} zwischen 1.336 und 1.173 für Qtz1 beziehungsweise zwischen 0.054 und 0.049 für Qtz2. Die höchsten und niedrigsten Werte der Löslichkeit werden bei 600 beziehungsweise 700°C erreicht. Viele Phasen in den Produkten der beiden Reihen von Experimenten, sind noch nicht identifiziert, zum Teil sie nur in sehr geringern Mengen auftraten. Die Untersuchungen zu diesem Teilprojekt sind daher noch nicht abgeschlossen. Wenn die Proben vollständig charakterisiert sind, können im Prinzip die in diesen Experimenten erhaltenen Ergebnisse mit thermodynamisch berechneten Kupferlöslichkeiten in hydrothermalen Fluiden kombiniert werden, um die Verteilungskoeffizienten von Kupfer zwischen Fluiden und Mineralien, zu berechnen.

1. Introduction to magmatic-hydrothermal systems

1.1. Basic concepts

Hydrothermal systems powered by magmatic intrusions dominate fluid movement in the upper crust, and are responsible for the convection of a large proportion of Earth's heat to the surface. At the same time, the fluids transport metals, forming the single most important class of ore deposits, those of the hydrothermal category (Hedenquist and Lowenstern, 1994). For example, large low-grade deposits of copper (plus molybdenum or gold) within shallow igneous intrusions, known as porphyries, provide more than half of the world supply of copper and molybdenum. It is generally agreed that many hydrothermal ore systems derive their thermal energy from magmas (Cathles, 1981 and Norton, 1982), with multiple intrusions necessary to maintain activity for hundreds of thousands of years, the life time of some hydrothermal systems. A confluence of structural, fluid inclusion, isotopic and experimental evidence suggests that most porphyry-type deposits were formed when an ore-bearing magmatic volatile phase exsolved from a magma and precipitated ore upon physical or chemical modification of the ore fluid (Holland, 1972, Candela and Holland, 1984).

Evidence from active hydrothermal systems, coupled with results from a variety of field and experimental studies, clearly indicates that magmas contribute components such as water, metals and ligands to hydrothermal fluids (Hedenquist and Lowenstern, 1994). Not surprisingly, this evidence wanes as the distance from the intrusion increases, meteoric water becomes dominant, and the fluid salinity and acidity decreases. Even in such distal environments though, there are indications that discrete, episodic addition of magmatic components in the form of high-pressure vapour may be critical to the ore-forming process (Henley and Ellis, 1983).

The interaction between magmatic and hydrothermal processes is extremely important for the formation of a wide variety of ore deposit types, especially in near surface environments, where magmas and fluids are spatially and genetically linked (Sillitoe, 1989 & Titley, et al., 1981). The majority of ore deposits around the world are either a direct product of concentration processes arising from the circulation of hot, aqueous solutions through the Earth's crust, or have been significantly modified by such fluids. Many different types of fluids are involved in hydrothermal ore-forming processes. The most primitive or juvenile of these are the magmatic-hydrothermal fluids that originate from magmas as they cool and crystallize at various levels in the Earth's crust, and a number of important ore deposit types are related to the concentration of metals that arise from circulation of such solutions. Magmatic fluids have an important role in carrying metals from a source region to their ultimate deposition and preservation in an ore deposit. They are typically dominated by H_2O, and are generally supercritical; that is, they exist at conditions greater than the critical point (374°C and ~220 bars for pure H_2O). Magmatic fluids may also contain other volatile components such as Cl and other halides, H_2S, SO_2, CO_2, CH_4, N-compounds, and B (King and White 2004). The volatile constituents, especially H_2O, CO_2, S, and Cl, play an important role in the generation, evolution, and eruption of magma. Knowledge of the abundance and flux of these volatiles is important for understanding the hazardous implications of volcanic activity, the explosive-eruptive behaviour of volcanoes, recycling of volatiles in subduction zones, formation of magmatic-hydrothermal ore deposits, additions of volcanic gases to the Earth's

atmosphere, and the potential climatic impacts of large volcanic eruptions (Wallace, et al., 2003). Examples of such ore deposits include the large family of porphyry Cu and Mo deposits, as well as the high-sulfidation epithermal Au-Ag deposits that often represent the surface or volcanic manifestations of porphyry deposits. Also included are the greisen-related Sn-W ores, polymetallic skarn mineralization, and pegmatite-related deposits. Important characteristics of these deposits are an intimate fracturing of the host rock and pervasive wall-rock alteration and fluid inclusions found in and around these deposits. Several features of many hydrothermal ore deposits, particularly the porphyry-type copper and molybdenum, recur with such frequency on a worldwide basis as to suggest that the ores, the fluids that transported them, and the shallow-seated bodies of intrusive igneous rocks with which they are intimately associated, descended from a common ancestor/source (Burnham, 1979).
In addition to magmatic fluids, there are four other major types of hydrothermal fluids. They include sea-water, meteoric water, connate water (water entrapped in the interstices of a sedimentary rock at the time when the rock was deposited) and metamorphic water. There is, in addition, a fluid reservoir that results from the mixing of two or more of the above mentioned water types.

1.2. Sources of metals in magmas

Metals can enter magmas through a variety of pathways, including mantle melting, mass transfer from the subducting slab and melting of the crust (Hedenquist and Lowenstern, 1994). Some siderophile elements such as Sn, Mo, Au, and the Pt-group of elements may be present in the Fe-Ni sulfides in the upper mantle, although most of these elements may be locked away in the Fe-Ni core (Lorand, 1990). During partial melting of the mantle, these sulphides are partially consumed, and contribute metals to the basaltic liquids which then ascend into the crust, both along mid-ocean ridges and at the subduction zones (**Fig. 1.1**). The erupted basalts are commonly altered, and together with their associated oceanic sediments, are eventually subducted below the continental crust, inducing melting in the mantle wedge beneath the volcanic arc. Many arc magmas show evidence for the addition of components such as oxidised sulphur, alkali-group elements, water and Cl from the subducted slab (Albarede and Michard, 1989), transferred as a fluid or a silicate melt. Subduction also contributes additional metals, such as Cu and Zn, to arc magmas, derived from hydrothermal mineralization of the subducted sea floor (Sillitoe, 1972).

Ore components may also be acquired during magma transit through the crust, e.g. the isotopic signature of most porphyry copper deposits is strongly correlated with that of their local basements, implying that the intrusions contain significant amounts of assimilated crust (Titley, et al., 1990), whereas in the case of Sn and W deposits the ore-bearing magmas may be produced entirely by melting of the crust (Ishihara, 1981). Fusion of previously melted crustal rocks can also result in high magmatic concentrations of F, due the breakdown of refractory, F-rich hydrous silicates. These minerals may also contain significant amounts of Sn and Mo, which are concentrated with F in some ore deposits.
The source of metals, however, may be of less importance, in terms of metal concentration, than the magmatic processes that operate during the final ascent and differentiation of the magma (Lowenstern, et al., 1994).
Crystallization is one of the main controls on the concentration of ore components in the magmas. The dominant minerals that crystallize in most igneous systems are silicates and oxides. Elements that partition into these minerals will have their

concentrations lowered, whereas incompatible elements may become more concentrated in the residual melt. The degree of compatibility is a function of crystal structure, melt composition, magma oxidation state, and the temperature and pressure of crystallization. For example, Mo and Zn concentrations are commonly high in magmas that contain low abundances of Fe-Ti oxides and titanite, minerals that tend to be rich in these elements (Lowenstern, et al., 1993). Furthermore lack of Cu mineralization associated with high-silica granites may be attributed to the early crystallization of pyrrhotite which acts as a sink for Cu and therefore lowering its concentration in the residual melt (Candela, 1989). Conversely, because Mo starts at a lower concentration and is more incompatible than Cu, crystal fractionation is necessary to produce the higher Mo/Cu ratio observed in the high-silica granites (Candela, 1989).

Metal concentrations, however, are still lower than the grades of economic ore in associated porphyry-style mineralization, even after extensive crystallization. Other processes are therefore necessary to concentrate metals from the magma into an ore deposit.

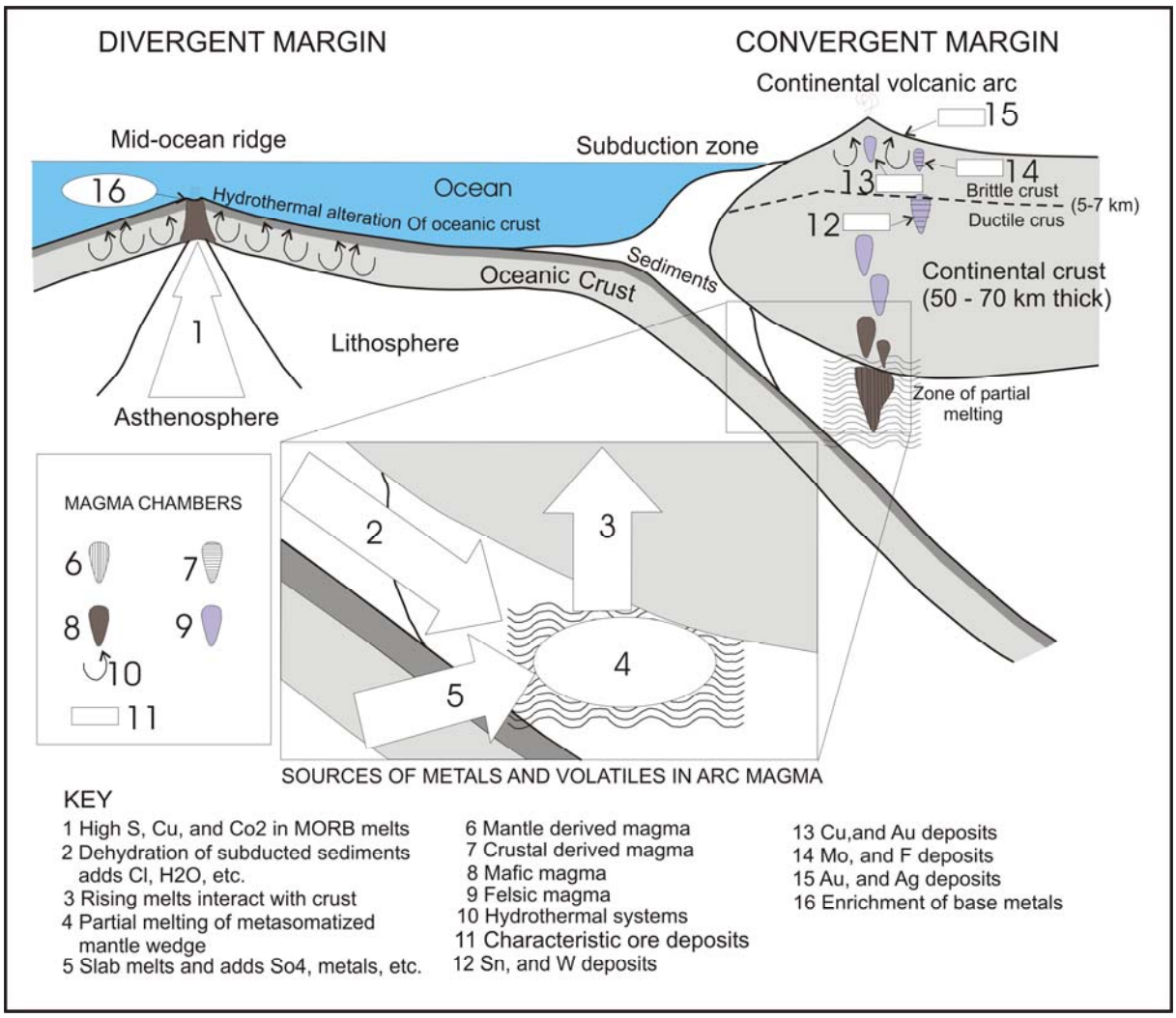

Fig. 1.1. Schematic section showing the principal components of magma genesis, fluid flow and metallogenesis in divergent- and convergent-margin settings (redrawn after MacLean, 1969).

Exsolved fluids in magma at an appropriate composition will, however, partition most of the metals as chloride, bisulfide and hydroxyacid complexes (Hemley, et al., 1992).

1.3. Sources of a magmatic aqueous phase

Water is the most abundant volatile component in silicate rocks and is highly soluble in granitic melts. For example, at 700 MPa (7 kbar) a granitic melt may dissolve up to 14 wt% H_2O (Tuttle & Bowen, 1958). Water solubility is primarily dependent on pressure (Tuttle & Bowen, 1958; Robb, 2005) and therefore the granitic melt can dissolve increasingly less H_2O as it moves to lower pressure regions in the upper crust. The solubility of water in silicate magmas is determined mainly by pressure and to a lesser extent temperature. Results of experimental determination of H_2O in melts of basaltic, andesitic, and granitic, or pegmatitic compositions suggest that H_2O content is strongly dependent on pressure, with magma at the base of the crust (~10 kbar) being able to dissolve between 10 and 15 wt% H_2O (Burnham, 1979). **Figure 1.2** shows that for any given pressure, felsic melts are able to dissolve more H_2O than mafic ones.

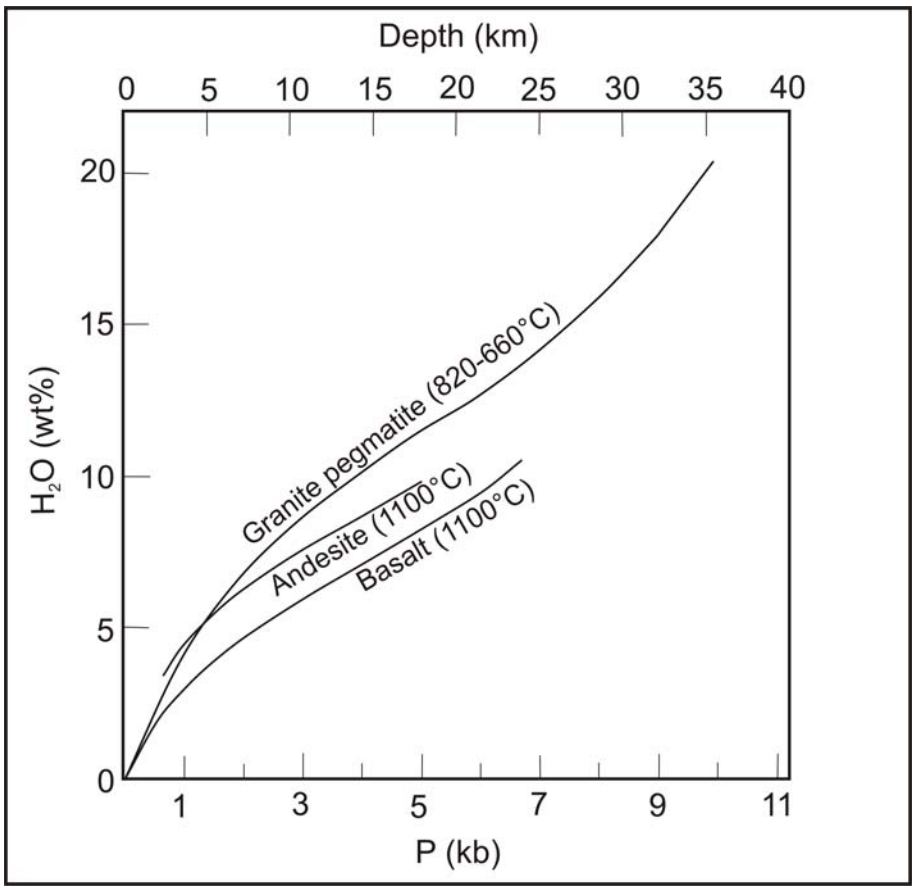

Fig.1.2. Experimentally determined solubilities of water in silicate melts as a function of pressure. The lowermost curve is for a basaltic melt at 1100°C, the middle curve is andesite melt at 1100°C, and the uppermost curve is for a granitic pegmatite melt between 660-820°C.(The figure is redrawn after Burnham, 1979).

Dissolved water in a magma exists essentially as OH groups, although at higher water contents discrete molecular water (H_2O) may also exist (Stolper, 1982).

The solubility of water in silicate magmas is thought to be primarily governed by the following equilibrium reaction:

$$H_2O(molecular) + O \Leftrightarrow 2OH \quad (1.1)$$

where O is a non-protonated oxygen atom in the silicate structure of the magma.

At low water contents, however, the mole fraction squared of water dissolved in any magma is proportional to the water fugacity (f_{H_2O}) of the magma which is strongly dependent on pressure.

Subduction of oceanic crust that has been highly altered and hydrated by percolating sea-water is a scenario that can be used to explain the water content of most arc-related andesitic and basaltic magmas. Therefore arc-related magmas probably contain dissolved water derived from mixing primitive, mantle-derived fluids and sea water plus a minor component of meteoric fluids. Hydrous basaltic magmas that pond at the base of the crust, and whose heat is responsible for initiating anatexis of the lower crust to form granitic melts, may contribute their waters to these melts (Whitney, 1989). He suggested that there would be a diffusive transfer of elements and volatile species across the boundary layer between the more dense mafic magma and a felsic magma chamber.

Most of the water present in granitic magmas is, however, derived from the dehydration of minerals in the crust that were themselves melted to form the magma (Burnham, 1979). The process can best be explained by considering the phase equilibria of three minerals, namely muscovite, biotite, and hornblende. The approximate conditions for dehydration melting of these minerals in relation to an average geothermal gradient are shown in **Figure 1.3** (redrawn after Burnham, 1997). The amount of water contained within these three minerals decreases from around 8-10% in muscovite, to 3-5% in biotite and 2-3% in hornblende. Accordingly, the water activity in melts formed at breakdown of these hydrous minerals will vary considerably and a magma derived from anatexis of a muscovite-bearing precursor is likely to contain more dissolved water than one derived by the melting of an amphibolite. It is apparent (see **Figure 1.3**) that granites of variable composition derived from different levels in the crust will initially contain very different water contents.

Melting of a muscovite or a muscovite + biotite-bearing source rock, represented in nature by rocks such as metasediments, is likely to yield peraluminous, S-type granite compositions. The types of granites with which most Sn-W-U ore assemblages are typically associated will, therefore, be relatively wet, and contain high initial water contents. S-type granites generally correlate with the relatively reduced ilmenite-series granites of Ishihara (1977), which inherit their low f_{O2} character by melting of graphite-bearing metasedimentary material.

By contrast, melting of biotite- or biotite + hornblende-bearing source material, represented in nature by meta-igneous rocks, will yield metaluminous, I-type granite compositions. The porphyry Cu-Mo suite of ore deposits are associated globally with the I-type granites and are relatively dry compared to S-type granites. Ishihara's magnetite-series granites are often correlatable with I-type granites and these are characterised by higher f_{O2} magmas (Ishihara, 1981).

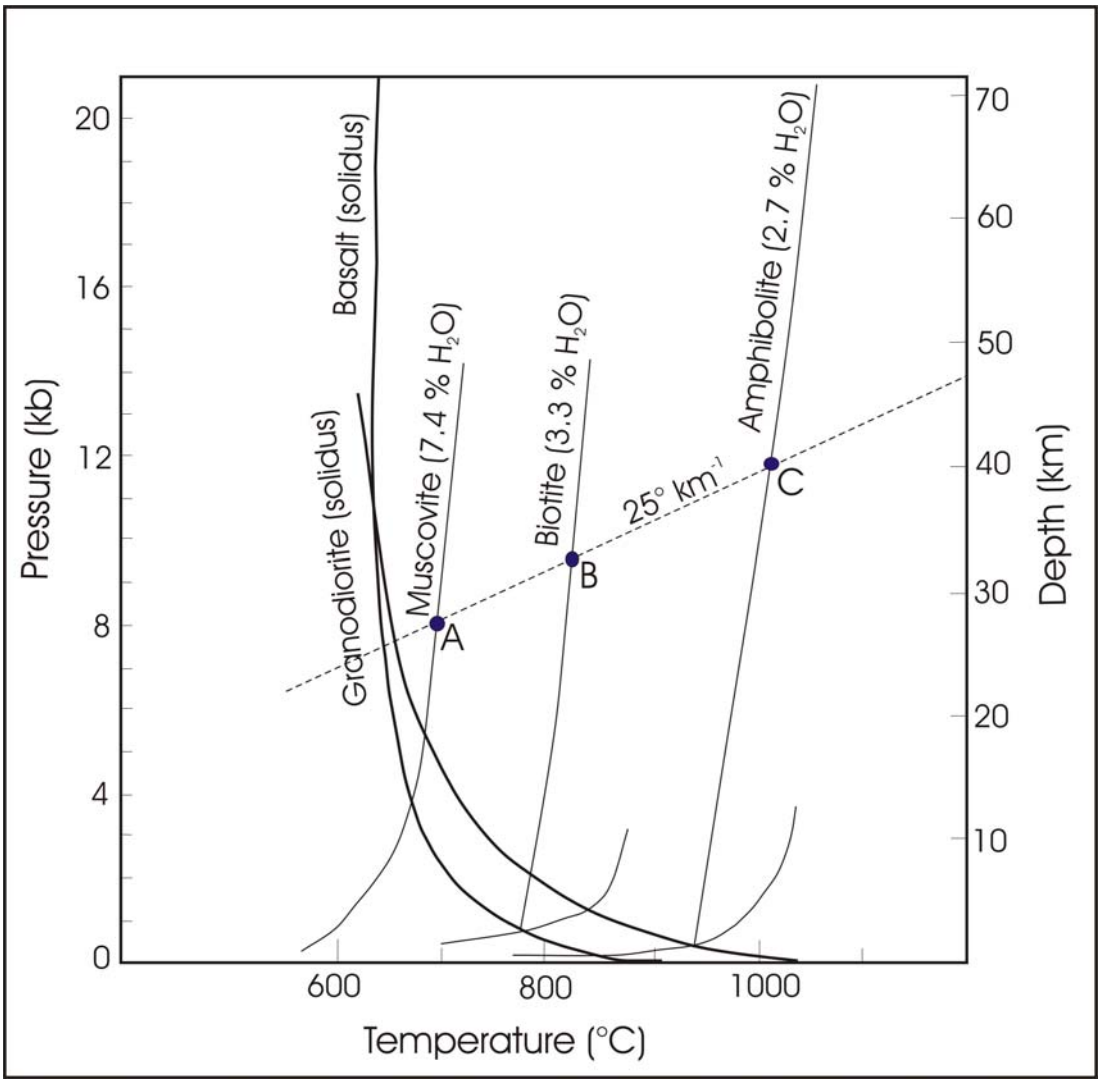

Fig.1.3. Pressure-temperature plot showing the approximate conditions under which dehydration melting of muscovite, biotite-, and hornblende-bearing assemblages would take place in relation to a 25°C/km geothermal gradient. Melts formed at A, B, and C respectively are likely to contain different initial water contents. The solidus curves for granite and basalt are for water-saturated conditions. (redrawn after Burnham, 1997).

Burnham, 1967, 1979, and 1997, emphasized the importance of processes whereby zones of water-saturated magma are formed and localized toward the roof of a granite intrusion, and their significance with respect to granitoid related ore deposits.

When a granitic magma crystallizes the liquidus assemblage is dominated by anhydrous minerals and the concentration of dissolved incompatible constituents, including water and other volatile species, increases by processes akin to Rayleigh fractionation (Lowenstern, et al., 1994). At some stage, either early or late in the crystallization sequence, granitic magma will become water-saturated, resulting in the exsolution of an aqueous fluid to form a chemically distinct phase in the silicate melt. This process is called water-saturation, but often also referred to as either boiling or vapour-saturation. This aqueous fluid has a density that is considerably lower than that of the granitic magma and will therefore rise to concentrate in the roof, or carapace, of the magma chamber. The amount of magmatic-hydrothermal water formed in this way is quite high, although some of the original OH^- in the magma may

be utilised to form hydrous rock forming minerals, such as biotite and hornblende (Stolper, 1982).

Vapor-saturation or boiling occurs when the equilibrium vapour pressure of the magma equals that of the load pressure on the system and bubbles of gas nucleate in the magma. These bubbles of gas may be steam or water vapour, CO_2, N_2, SO_2, H_2S, etc. Vapour-saturation of low solubility volatiles such as CO_2 may be unrelated to, and can precede, H_2O-saturation. The process of water-saturation can be achieved in two ways, either by progressive crystallization of magma, or by decreasing the pressure of the system (Evans, 1993).

The concept of the formation of a zone of H_2O-saturated magma in a high-level granite intrusion which initiatially contained some 2.7 wt% H_2O is schematically illustrated in **Figure 1.4** (after Burnham, 1979).

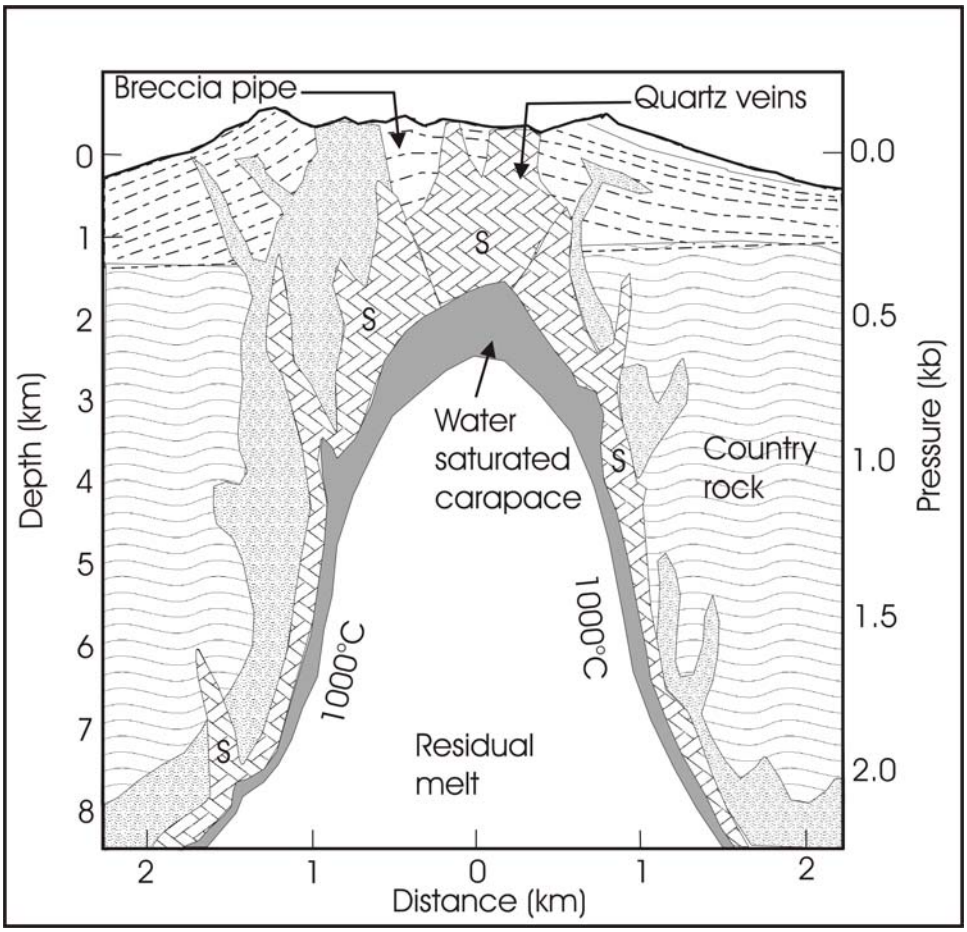

Fig.1.4. Section through a high-level granodioritic intrusion undergoing progressive crystallisation and shows the hypothetical position in space of the water-saturated granite solidus, S, as well as the zone (in grey) where aqueous fluid saturation occurs in the residual magma(redrawn.after.Burnham,1979).

At these shallow depths H_2O-saturation is achieved after only about 10% crystallization, when the water content of the residual magma reaches 3.3 wt%. At these low pressures the fluid will boil, since the equilibrium vapour pressure equals the load pressure on the magmatic system and bubbles of gas (i.e. water vapour plus other volatiles such as CO_2) will vesiculate. The process whereby vapour saturation is achieved by virtue of decreasing pressure (i.e. because of upward emplacement of

magma or mechanical failure of the chamber) is called “first boiling” and is particularly applicable to high level granite systems (Evans, 1993). However, it is also possible to achieve saturation of an aqueous fluid by progressive crystallization of dominantly anhydrous minerals under isobaric conditions. This process is specifically referred to as “second boiling” and is particularly applicable to more deep-seated magmatic systems and occurs only after a relatively advanced stage of crystallization (Evans, A., 1993). The difference between the first and second boiling, and more specifically the timing of H_2O fluid saturation relative to the progress of solidification of the magma, is very important in understanding how different granite related ore deposits form (Guilbert and Park, 1986).

In addition to the strong dependence of boiling on pressure, fluid saturation is also a function of the original water content of the initial melt. Melts that are more enriched in water and volatiles will achieve saturation earlier, relative to the progression of crystallization, than those that are poorer in these components. **Figure 1.5** (redrawn after Whitney, 1989) compares the attainment of H_2O-saturation in a typical granite melt at high and low pressures, in terms of crystallization sequences and initial water content. In a situation deep in the earth’s crust (i.e. 8 kbar), where the original granite melt contained 2 wt% H_2O, crystallization would have commenced with nucleation of plagioclase at temperatures around 1100°C, followed by the appearance of K-feldspar and Quartz on the liquidus at lower temperatures, path A-A’-A’’. H_2O-saturation is achieved at temperatures that are just a few degrees above the solidus, at A’, and only after over 80% of the melt had crystallized (see **Figure 1.5a**). The solidus is intersected at 650°C, at which point the granite has totally solidified. If however this granite was initially water saturated at 8 kbar, it would have contained at least 12 wt% H_2O and would not have started to crystallize plagioclase until the melt temperature had cooled to around 750°C. In this case solidification would have progressed quite rapidly between 750 and 650°C entirely in the presence of H_2O fluid.

At shallower levels in the crust (2 kbar) the situation is quite different. The same granite magma composition would be saturated in water if it originally contained only 6-7 wt% H_2O and in this situation crystallization in the presence of H_2O fluid would take place at a wider temperature interval (920-720°C) than at greater depth, path D-D’ (see **Figure 1.5b**).

A melt with a low initial water content would crystallize over a significant temperature interval in the undersaturated field, as happens deeper in the crust, but in this case H_2O-saturation would be achieved at a higher temperature, around 700°C, at C and only after some 60-70% crystallization, path C-C’-C’’.

These experimental data reinforce the concept that aqueous fluids will exsolve from a granitic melt as a normal consequence of its crystallization. This model has great relevance to the formation of a wide range of ore deposit types including the porphyry Cu-Mo suite of deposits, epithermal precious metal ores, and polymetallic skarn type deposits.

The appearance of an exsolved H_2O fluid within magma is also accompanied by the release of mechanical energy, since the volume per unit mass of silicate melt plus low density H_2O fluid is greater than the equivalent mass of H_2O saturated magma (Burnham, 1979). At shallow levels in the crust the volume change accompanying H_2O fluid production may be as much as 30%. This results in overpressuring of the chamber interior and can cause brittle failure of the surrounding rocks. This is called hydrofracturing. Hydrofractures tend to emanate from zones of H_2O fluid production in the apical portions of the granite body and may propagate into the country rock and even reach the surface (see **Figure 1.6**).

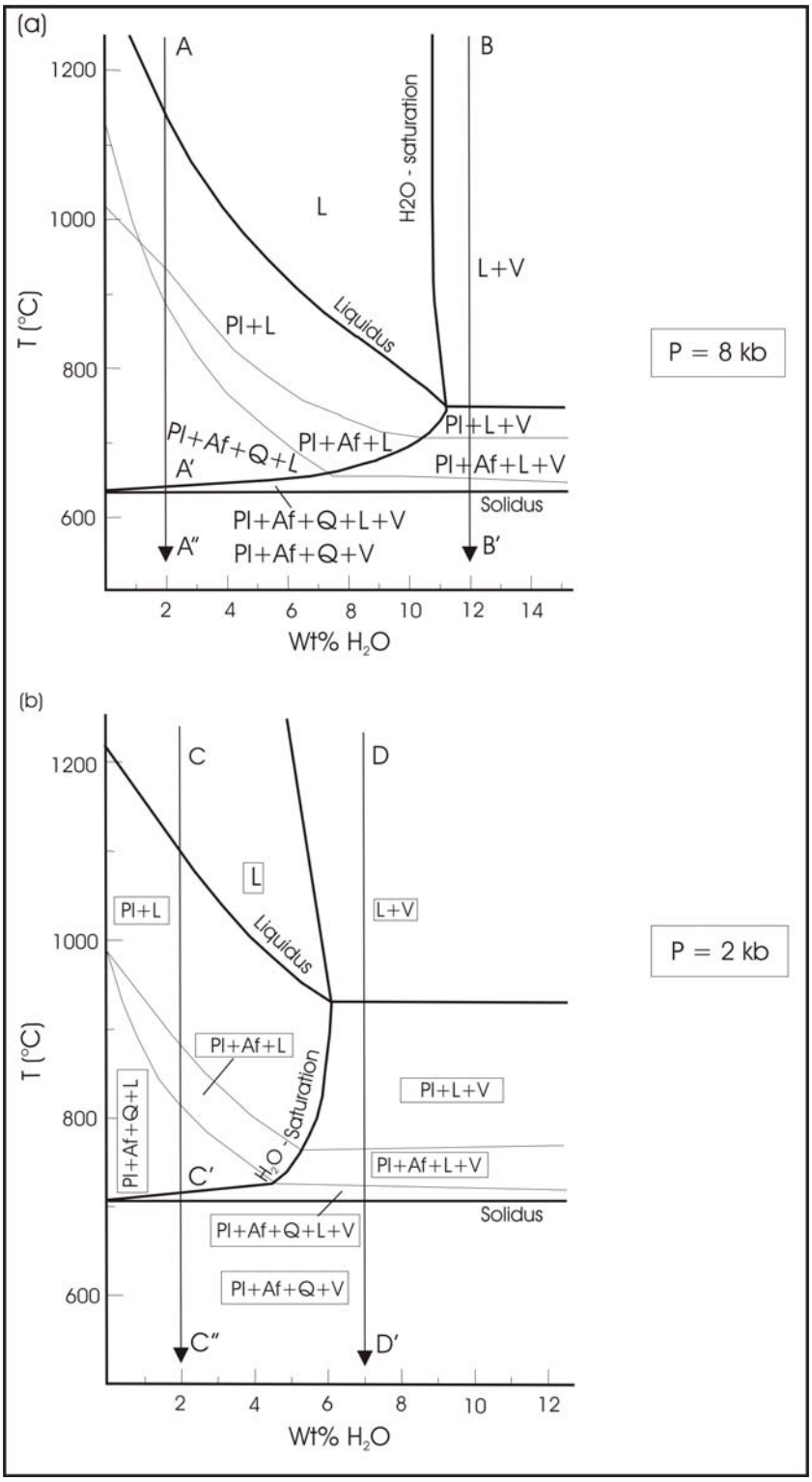

Fig.1.5. Plots of temperature versus H_2O content showing the crystallisation sequences for granitic melts cooling and solidifying at (a) deeper crustal levels (8 kbar) and (b) shallower crustal levels (2 kbar). The bold lines in both cases refer to the water-saturation curve, and also the liquidus and solidus. The diagrams are redrawn after Whitney, 1989. Pl, stands for plagioclase; Q, quartz; Af, alkali feldspar; L, melt; V, H_2O fluid. Crystallisation paths refer to hypothetical situations where the granite was either initially oversaturated in water (B-B' and D-D') or markedly under saturated in water (A-A'-A" and C-C'-C").

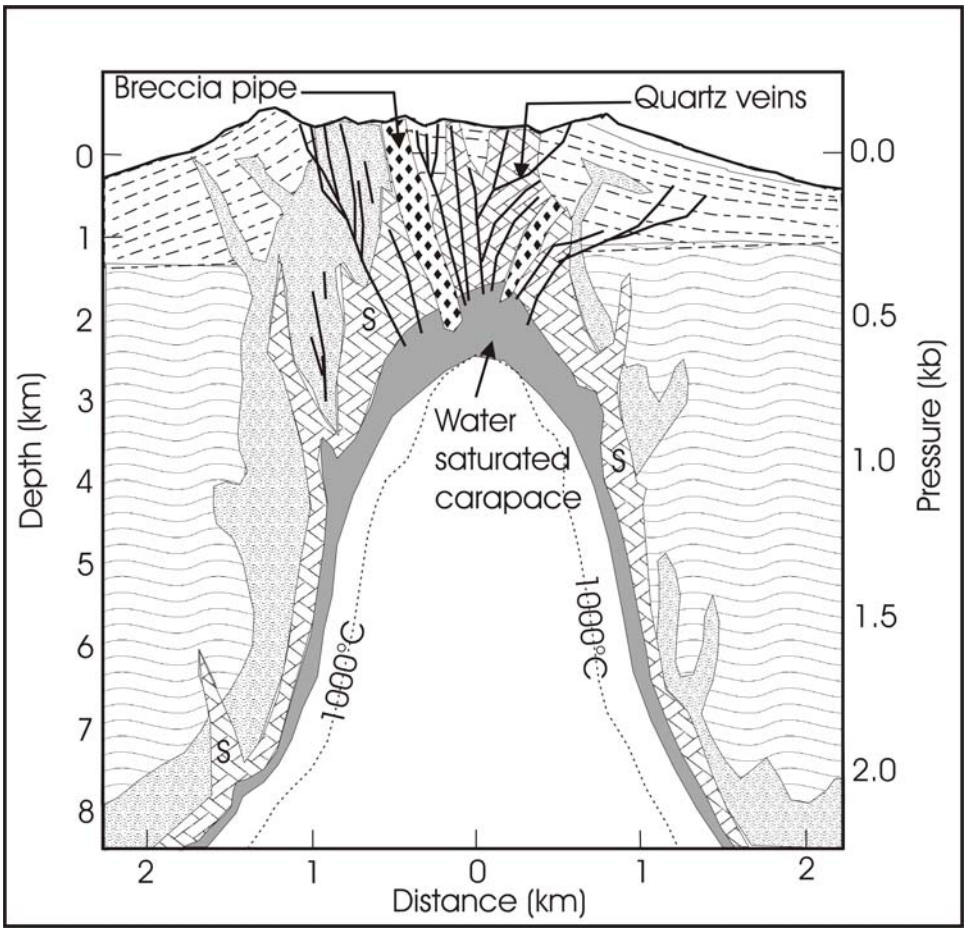

Fig.1.6. Section through a high-level granodioritic intrusion showing the nature of hydrofracturing and breccia pipe formation around the apical portion of a granite body (redrawn after Burnham, 1979).

Experimental work has confirmed that high level granite emplacement enhances the possibility of brittle failure, both in the intrusion itself and in the surrounding country rocks, thereby providing excellent ground preparation for the efficient circulation of ore-bearing fluids (Dingwell, et al., 1997). The factors that help to promote brittle failure in high level granite-related ore-forming systems include volatile saturation, which increases magma viscosity because of dehydration, bubble vesculation, and rapid cooling.

1.4. Composition and characteristics of magmatic-hydrothermal Solutions

Silica in the form H_4SiO_4 is a typical constituent of hydrothermal solutions, hence the common occurrence of quartz in veins. In addition to silica, water can dissolve significant amounts of other major elements, such as alkali metals**.** Burnham, (1967), reacted granite with pure water under a variety of conditions and showed that at high pressures and temperatures the total solute content of the solution was about 9 wt% and comprised Si, Na, and K in proportions that are approximately the same as the granite eutectic (or minimum melt) composition. This indicates that materials precipitating from an aqueous solution at high P-T could have the same composition and mineralogy as granite that crystallized from a silicate melt (i.e. quartz + plagioclase + K-feldspar in approximately equal proportions).

At progressively lower pressures and temperatures, however, the total solute content of the solution decreases (to about 0.7 wt% at 2 kbar), with the alkali metals (i.e. Na +K) also decreasing relative to silica. Close to the surface, therefore, the products of precipitation from the aqueous hydrothermal solutions comprise mainly silica (see **Figure 1.7**, redrawn after Burnham, 1967).

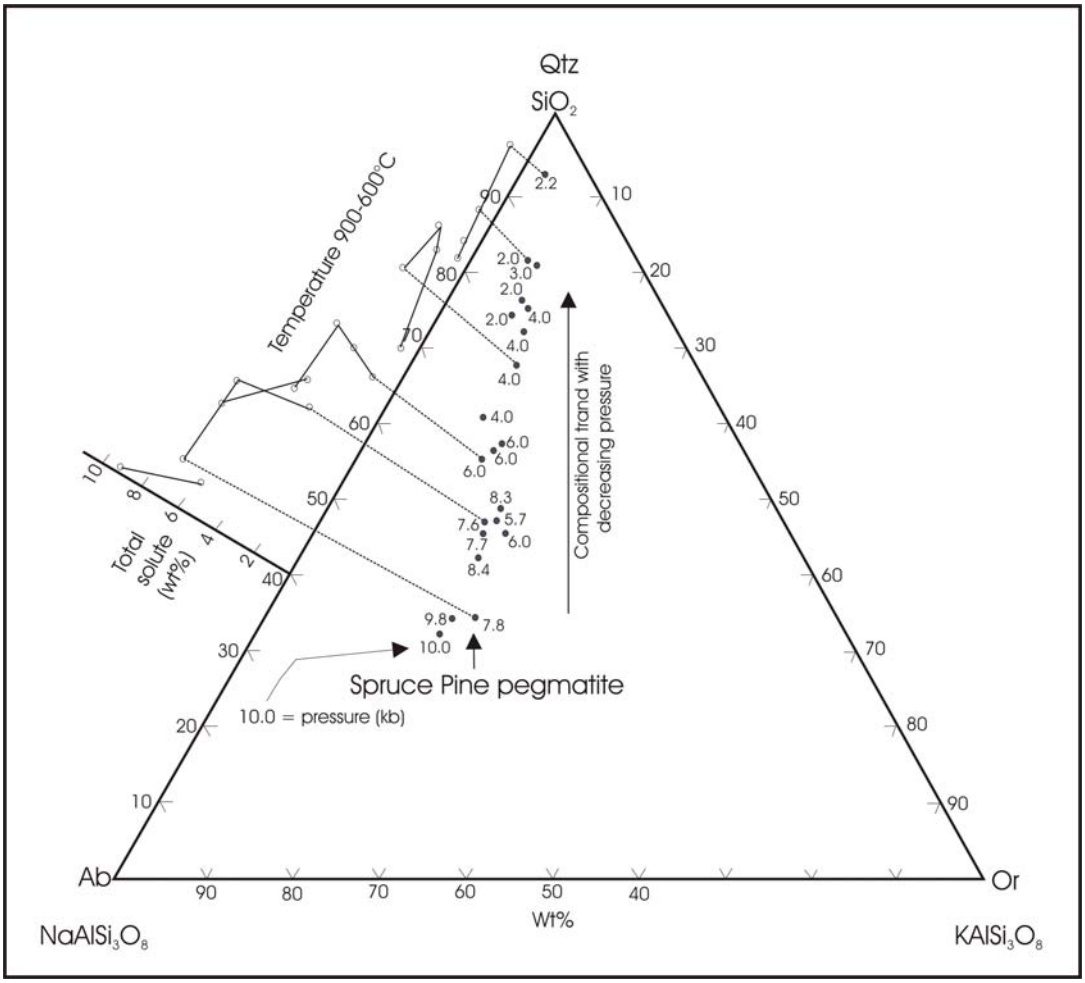

Fig. 1.7. Normalised compositions of aqueous fluid in equilibrium with a granitic pegmatite at pressures varying from 2 to 10 kbar and temperatures between 600 to 900°C. Pressure values are shown next to each point on the diagram. The auxiliary diagram on the left shows the approximate variation in the total solute content of the aqueous solutions as a function of pressure (redrawn after Burnham, 1967).

In addition to their ability to dissolve Na^{+}, K^{+}, and Si^{4+}, magmatic aqueous solutions can also transport significant amounts of Ca^{2+}, Mg^{2+}, and Fe^{2+}, as well as anionic substances, in particular Cl^{-}. The dissolved anions are important in ore-forming processes (Norton, and Cathles, 1973).

Magmatic aqueous solutions also contain a wide range of other constituents, some of which are easily detectable, with the reminder occurring only in trace amounts. These trace constituents are used to distinguish an ore-forming fluid from one that is likely to be barren. A significant amount of CO_2 is associated with magmatic fluids. The amount of sulphur in magmatic fluids is generally low because at high crustal levels SO_2 partitions into the vapour phase on boiling. The oxidised and reduced forms of sulphur are essentially mutually exclusive and exist either as the SO_4^{2-} complex (with S^{6+}) or as the reduced HS^{-} complex (with S^{2-}) (Burnham, 1997). Experimentally

measured fluid/melt partition coefficients of sulphur ranged from 47 under oxidising conditions (where SO_2 is the dominant sulphur species in the fluid) to 468 under reducing conditions, where H_2S dominates, (Keppler, 1999).
The oxidised I-type magmatic fluids tend to comprise sulphur as SO_4^{2-} which fractionates into the aqueous liquid phase. Porphyry Cu & Mo type deposits therefore, are associated with abundant sulphide minerals in the form of pyrite (FeS_2) and chalcopyrite ($CuFeS_2$).
S-type magmas, which are more reducing, because they equilibrated with graphite-bearing metasediments, exsolve aqueous solutions that contain mainly H_2S or HS^- and have lower total sulphur content. The presence of reduced sulphur species promotes the stability of sulphide minerals down to lower temperatures, such that the Sn & W oxide minerals (cassiterite, SnO_2 and scheelite, $CaWO_4$) associated with S-type granites tend to form early in the mineralising sequence of these systems (Burnham, 1997).
Recent analytical developments have allowed measurements of magmatic ore-forming fluids directly from the tiny volumes of fluid trapped in individual fluid inclusions providing some insights into the composition of both the aqueous liquid and vapour phases in granite ore-forming systems.
Ore-forming fluids can perhaps be best studied by examining the fluid inclusions (typically 5-30 μm in diameter) that exist particularly in quartz, but also in many other rock- and ore-forming minerals. An important source of information on dissolved volatiles in magmas is obtained through the analysis of glass inclusions trapped inside the crystals (Wallace et al., 2003). When melts crystallize, some crystals grow imperfectly, causing small blobs of melt to be trapped inside the crystals. If the magma erupts and cools rapidly, then these trapped melt inclusions quench to glass. Because the crystalline host for the inclusions is relatively rigid, they act as tiny pressure vessels and prevent the trapped melt from degassing, even though the bulk magma decompresses to surface pressure during eruption. For this reason trapped melt (glass) inclusions commonly retain their original dissolved volatiles. Melt inclusions are now routinely analyzed for many volatile species (H_2O, CO_2, S, Cl, F) using infrared and Raman spectroscopy, electron microprobe, and secondary ion mass spectrometry (SIMS). Studies of porphyry Cu and Mo systems have shown that the early generation of fluid trapped in primary fluid inclusions is characterized by high temperatures and high salinities, and also provides evidence of liquid-vapour phase separation, or boiling (Roedder, 1984). The presence of tiny minerals (daughter crystals) that precipitated from the fluid on cooling after it was trapped within the inclusion confirms the high salinities of these ore-forming fluids. The majority of these daughter crystals are identified as halite (NaCl) and to a lesser extent, sylvite (KCl). This also confirms that magmatic fluids contain significant amounts of K, Na, and Cl.
An accurate and complete assessment of porphyry Cu-related ore fluid composition is obtained from the quantitative analysis of individual fluid inclusions by laser-ablation inductively coupled plasma mass-spectrometry (LA-ICP-MS).
Figure 1.8 shows the results of LA-ICP-MS analysis of two coexisting fluid inclusions in quartz from the Bajo de la Alumbrera porphyry Cu-Au deposit (Ulrich et al., 2001). The two coexisting fluid inclusions, one a vapour-rich inclusion and the other a hypersaline liquid-rich inclusion containing several daughter crystals, indicate that the ore fluid was boiling during the time it was trapped.
Their analysis reflects the extent to which elements were partitioned between liquid and vapour, as well as the metal abundances in each. The plot shows that the majority of elements analysed partition preferentially (by a factor of about 10 to 20)

into the liquid rather than the vapour phase. In addition to the high concentrations of Na, K and Fe the liquid also contains significant quantities of Mn, Cu, Pb, and Zn in solution. Cu, however, behaves differently to the other metals in that it is preferentially fractionated into the vapour phase (Lowenstern et al., 1991).

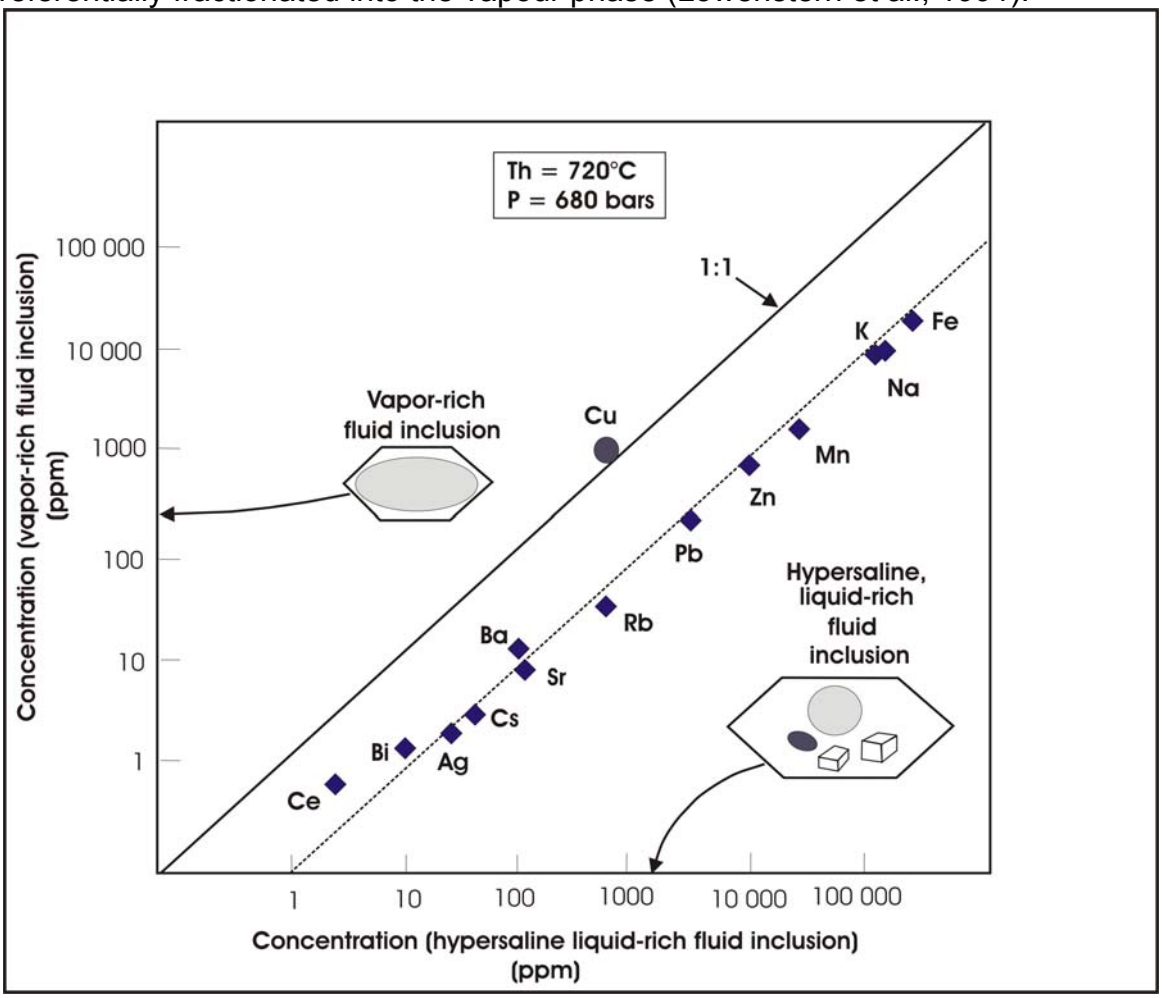

Fig.1.8. Plot of element concentrations in a vapour-rich fluid inclusion versus element concentration in a related hypersaline liquid-rich fluid inclusion. The two fluid inclusions analysed are shown next to their respective axes. The data pertain to the Bajo de la Alumbrera porphyry Cu-Au deposit in Argentina. The plot is redrawn after Ulrich et al., 2001.

After H_2O, CO_2 is the most common gas emanating from volcanic eruptions and its presence is important in a variety of ore-forming processes. Its solubility in felsic magmas is considerably lower than that of H_2O, and it dissolves as molecular CO_2 in normal felsic or mafic melts. In alkaline magmas, CO_2 will however, exists as carbonate ionic complexes in solution (Lowensterns, 2001). CO_2 solubilities will increase with pressure and magma alkalinity. In granitic melts CO_2 solubility is one order of magnitude lower than that of water solubility.

In felsic and mafic magmas CO_2 will exsolve much earlier than H_2O, partitioning preferentially into the vapour phase and therefore causing vapour-saturation at significant crustal depths, even to mid-crust (Lowensterns, 2001). This is also true for other low solubility gases like N_2, which will be associated with the vapour phase created by early CO_2 saturation or effervescence. The presence of CO_2 in an evolving aqueous fluid within crystallizing granite will promote immiscibility between vapour and saline liquid phases of the solution. Such processes can be very important during ore-forming processes since they promote the precipitation of

metals from solution (Lowensterns, 2001). Effervescence of CO_2 from the fluid will also promote certain types of alteration in the host rocks and increase the pH in the remaining fluid, further influencing ore-forming processes. A very important effect of CO_2 is the reduction in the solubility of silica and almost all other solutes in a hydrothermal fluid.

1.5. Pegmatites and their significance to granite-related ore-forming Process

Pegmatites are commonly regarded as rocks derived from magma that may have crystallized in the presence of a magmatic aqueous fluid. They are defined as very coarse-grained rocks, typically associated with granites and comprising the major rock-forming minerals. In addition they contain a wide variety of minor minerals of more exotic and semi-precious character, such as tourmaline (**Na**,Ca)(**Mg**,Fe^{2+},Fe^{3+},Al,Li)$_3Al_6(BO_3)_3Si_6O_{18}(OH)_4$; topaz, $Al_2SiO_4(F,OH)_2$, and beryl, $Be_3Al_2Si_6O_{18}$.

Pegmatites also contain concentrations of the large ion lithophile and high field strength elements, such as Sn, W, U, Th, Li, Be, B, Ta, Nb, Cs, Ce, and Zr. In the classification schemes for pegmatites the model by Cerny is particularly convenient because it separates them into characteristic metal assemblages that have an implied genetic connotation.

Two families of pegmatites are recognised, the Nb-Y-F suite associated with sub-alkaline to metaluminous (largely I-type) granites and the Li-Cs-Ta suite, also enriched in boron, and typically associated with peraluminous (dominantly S-type) granites (Cerny, 1991).

Pegmatites are spatially associated with the cupola zones of large granite intrusions and may be genetically linked to the most highly differentiated, water saturated portions of such bodies. Many pegmatites may however not be products of water-saturated granite crystallization.

There are other factors, in addition to the Jahns and Burnham model (1969) of H_2O-saturation, which need to be considered in order to fully understand the formation of pegmatites and their associated ore-deposits. D. London and co-workers (1990, 1992, and 1996) suggested that it is possible to generate pegmatites from H_2O under-saturated granitic melts by undercooling the magma below its normal liquidus temperature. Kinetic delays in the initiation of crystallization in felsic magmas that are rapidly undercooled means that melts persist in a metastable condition and result in non-equilibrium crystal growth. Pegmatitic features like mineral zonation, large grain size, variable textures, and highly fractionated chemistry, can be replicated experimentally in terms of the slow crystallization response to undercooling of granitic melts.

Boron and fluorine both individually and collectively, lower the granite solidus temperatures to below 500°C and increase the range of temperatures over which magmatic crystallization occurs. They also dramatically increase the solubility of H_2O in the melt and promote the crystallization of quartz (Johannes and Holtz, 1996).

Thomas et al., 2000, have studied the Sn-W-B-F-P pegmatite at Ehrenfriedersdorf in the Erzgebirge, Germany and came up with the following findings:

The fluid inclusions in these pegmatites are made up of coexisting silicate-rich H_2O-poor and silicate-poor H_2O-rich melts. On progressive reheating from 500°C to 700°C at 1 kbar pressure, the silicate-poor H_2O-rich phase became poorer in H_2O, whereas the former undergo a steady increase in water content (see **Figure 1.9**). At just above 700°C the two phases are effectively identical, with both containing about 20 wt% H_2O. This indicates that the two melts were originally a single homogeneous

melt. Even at low pressures (e.g. the Ehrenfriedersdorf pegmatites which crystallized at about 1 kbar) these B-F-P-rich pegmatites exhibit complete miscibility between silicate melt and aqueous fluid such that water can be regarded as infinitely soluble in this melt. On cooling below 700°C, immiscibility occurs to form two coexisting melts, i.e. one with very high water content and the other with low water content. The former, however, has a density, viscosity, and diffusivity that is more akin to an aqueous solution than to a silicate melt. Although its properties are water-like, it is by definition different from the exsolved H_2O fluid envisaged to have formed in the earlier Jahns-Burnham model.

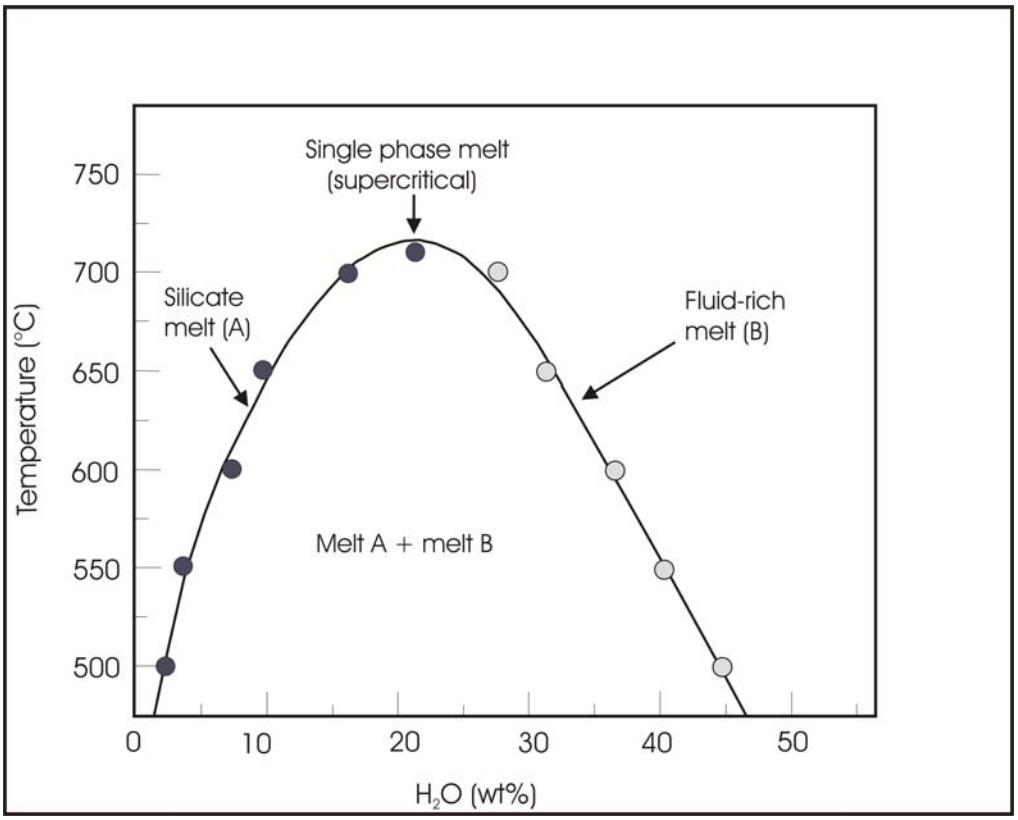

Fig.1.9. Plot of H_2O content versus temperature for rehomogenized (at 1 kbar) silicate-rich H_2O-poor melt (A) and silicate-poor H_2O-rich melt (B) inclusions from the Ehrenfriedersdorf pegmatite. The curve defines a solvus with a critical point at about 700°C and 20 wt% H_2O content (redrawn after Thomas et al., 2000).

It is apparent, therefore, that a magmatic aqueous phase has to be represented by a fluid that is more complex than simply exsolved H_2O. At low pressures and in the presence of significant concentrations of elements such as B, F, and P, granite melt solidus temperatures are significantly depressed and water solubility increases to such an extent that H_2O-saturation might not occur. In this case two immiscible melts may form, one of which is H_2O-rich and has physical properties akin to an aqueous solution with high solute content.

1.6. Fluid-melt trace element partitioning

The rise of magma to shallow levels of the earth's crust will inevitably result in saturation with respect to an aqueous fluid or vapour phase. The low density H_2O-fluid, together with entrained melt and crystals, will move to the apical portions of the

magma chamber (Candela, 1991). In an equilibrium situation, trace components of the magma must then partition themselves between melt, crystals, and H_2O-fluid. The extent to which trace components, such as metals, distribute themselves between these phases is a process that is potentially quantifiable in terms of partition coefficients (Candela and Holland, 1984 and 1986, Candela, 1989a, b, and 1992, and Candela and Piccoli, 1995).

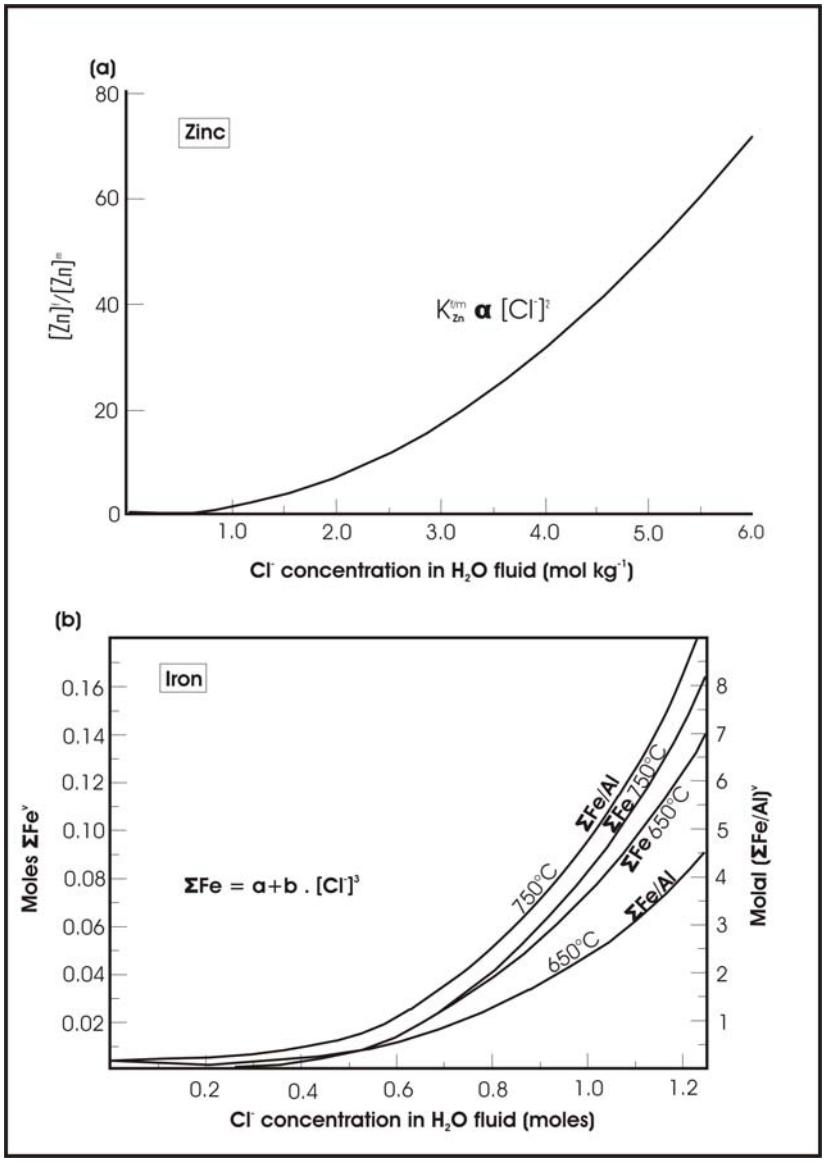

Fig.1.10. (**a**) The ratio of the concentration of Zn in H_2O-fluid to that in a granitic melt as a function of the Cl^- concentration. Experiments were carried out at various temperatures between 770 and 880°C and pressures between 1.4 and 2.4 kbar (after Holland, 1972). (**b**) The total Fe content and total Fe/Al ratio in H_2O-fluid that equilibrated with a granitic melt as a function of the Cl^- concentrations. Experiments carried out at temperatures of 650 and 750°C and a pressure of 2.0 kbar (after Burnham, 1967).

Classical experiments by Holland (1972), provide insight into why hydrothermal fluids are such efficient scavengers of metals and, therefore, so important in ore-forming processes. He showed that the solubility of many metals in a magmatic H_2O-fluid is strongly dependant on its Cl^- concentrations, in addition to other parameters such as temperature and pH. When an aqueous solution reacted with a granitic melt it was

observed that metals such as Zn, Mn, Fe, and Pb were strongly partitioned into the H_2O-fluid and that the ratio of metal concentration between melt and fluid was strongly dependant on the Cl^- concentration (see **Figure1.10a**). These experiments demonstrate quite clearly that certain metals will only readily dissolve in an aqueous solution if the later contains appreciable amounts of the chloride anion (Cl^-).

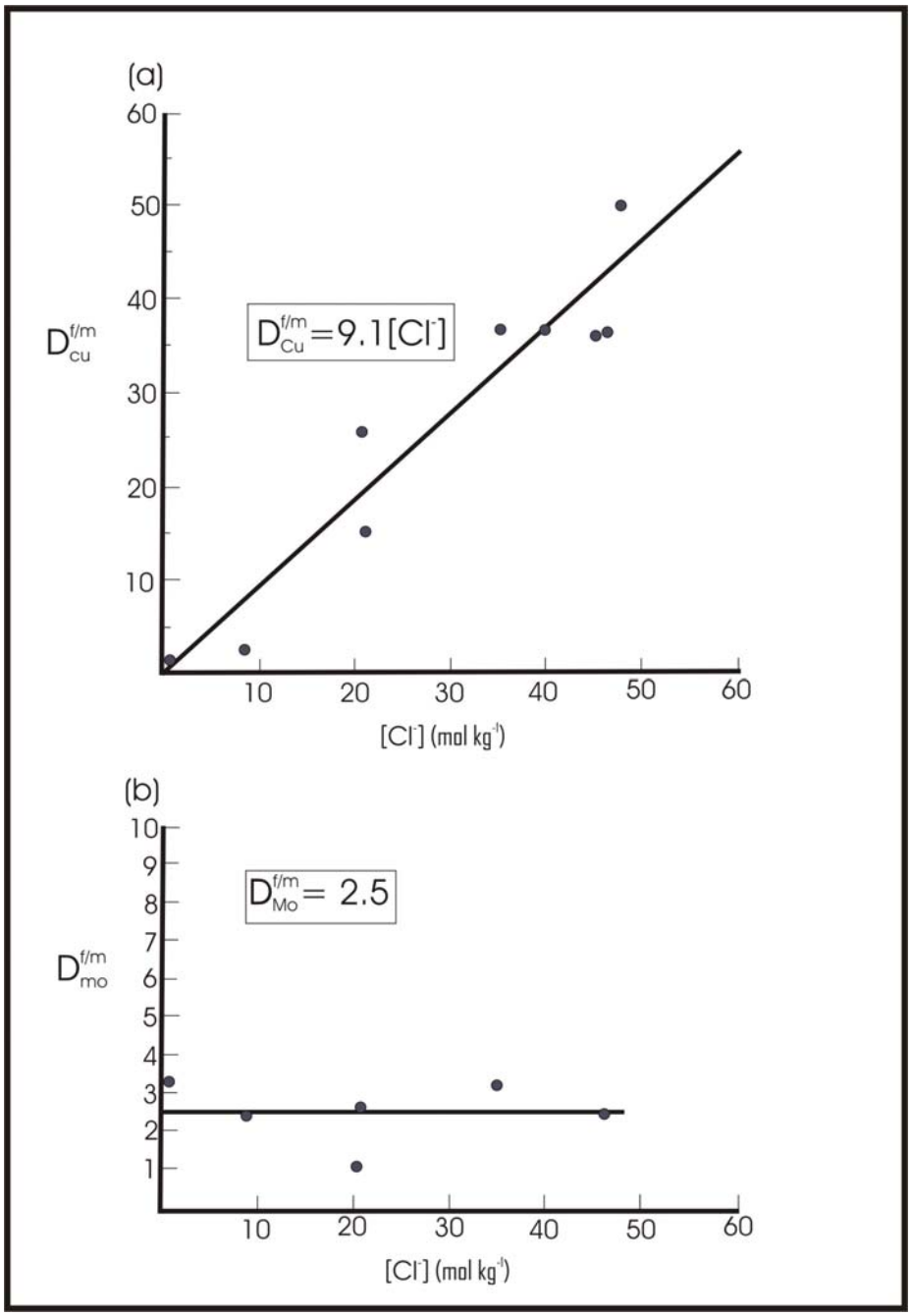

Fig.1.11. (**a**) The relationship between H_2O fluid/silicate melt partition coefficient for Cu and the Cl^- concentration of the aqueous fluid.
(**b**) The relationship between the H_2O fluid/silicate melt partition coefficient for Mo and the Cl^- concentration of the aqueous fluid (after Candela and Holland, 1984).

Burnham, 1967, showed that the total Fe content of the H_2O-fluid varies as a function of temperature, and is higher for any value of Cl^- at 750°C than it is at 650°C. This confirms the intuitive notion that solubility normally increases as a function of temperature. **Figure 1.10b** shows that the Al content in the fluid remains constant

(because the total Fe content changes in the same way as does the total Fe/Al ratio) and that it is not affected by the Cl^- concentration of the aqueous fluid. This further indicates that not all metals have their solubilities controlled by Cl^- concentrations in the fluid (although they may still be affected by the presence of other ligands) and that some metals will not at all partition into the aqueous phase.

Candela and Holland (1984) ran a series of experiments at 750°C and 1.4 kbar and were able to measure the extent to which Cu and Mo partition between granitic melt and a coexisting aqueous fluid containing both Cl^- and F^-. The results (see Figure **1.11a** and **b**) clearly demonstrate that Cu is a metal whose partitioning behaviour is strongly controlled by the Cl^- concentration of the fluid phase, whereas Mo remains unaffected by the latter.

D^{Cu}fluid/melt varies from about 1, for low salinity fluids, to about 50 at high salinities and is determined by the relationship

$$D^{Cu}\text{fluid/melt} = 9.1[Cl^-].$$

By contrast, although Mo is also preferentially partitioned into the H_2O-fluid (D^{Mo}fluid/melt = 2.5), its partition coefficient is fixed and remains constant irrespective of the Cl^- concentration. The partitioning behaviour of both Cu and Mo is unaffected by the presence of F^- in the aqueous solution.

The fluid-melt partitioning behaviour of W, like that of Cu and Mo is well constrained by the works of Keppler and Wyllie, 19991. Experiments suggest it has similar properties to those of Mo, but a lower partition coefficient (D^{Mo}fluid/melt = 1.0).
However, W also behaves as an incompatible element in terms of its crystal-melt partitioning behaviour in relatively reduced granitic magmas solidifying at some depth in the earth's crust. By contrast, Mo behaves in a more compatible manner in the same magma types such that fractionation will tend to result in increasing W/Mo ratios (Candela, 1992).

The crystal-melt partitioning behaviour of W also contrasts with that of Cu, which tends to act as a compatible element in virtually any magma composition (Candela and Holland, 1986).

The fluid-melt and crystal-melt partition coefficients play an important role in the distribution of metals in and around crystallizing granite plutons. These parameters, together with the granite type, depth of emplacement, and the timing of water-saturation relative to the crystallization sequence, can be used to explain the nature and origin of many magmatic-hydrothermal ore deposit types (Candela and Holland, 1986).

The partitioning of metals between a silicate melt and an exsolved H_2O-fluid is a complex matter. The extent to which metals are partitioned between melt and fluid is variable and is largely controlled by the Cl^- (and other ligand) concentration of the fluid which in an evolving system, itself changes continuously. Additional factors include temperature, pressure, the amount of water exsolved relative to the amount of water remaining in the silicate melt (i.e. when H_2O-fluid saturation is achieved during crystallization), and the oxygen fugacity (fo_2) of the silicate-fluid system.
Candela (1989a) has provided equations that quantify the distribution of a trace component between H_2O-fluid and the silicate melt for a first boiling situation. These

equations are applicable to those components whose partitioning does not change as a function of the ligand concentration of the fluid.

$$C_f^i = D_{f/m}^i \times C_o^i \left[1 - \left\{(1-F)C_o^w\right\}\right]^{D_{f/m}-1} \quad (1.3)$$

where C_f^i is the concentration of a trace component (i) in the H_2O-fluid at any instant in the evolution of the aqueous phase;
$D_{f/m}^i$ is the H_2O-fluid/silicate melt partition coefficient for the component (i);
C_o^i is the initial concentration of the component (i) in the silicate melt (defined at the instant of water saturation);
C_o^w is the initial concentration of water in the silicate melt (defined at the instant of water saturation); and
F is the ratio of the mass of water in the silicate melt (at any given instant after water saturation) to the initial mass of water in the silicate melt.

The concentration of the component (i) in the associated silicate melt (C_m^i) is simply given by:

$$C_m^i = \left[\frac{C_f^i}{D_{f/m}^i}\right] \quad (1.4)$$

Knowing the value of the partition coefficient ($D_{f/m}^i$), which changes as a function of pressure and hence, saturation water content, the concentration of a component such as chloride in an evolving aqueous phase, as well as in the associated silicate melt, can be calculated (see **Figure 1.12**, for the diagrammatic representations of Cl concentration-trends in an evolving silicate melt-H_2Ofluid system). The appearance of a magmatic aqueous fluid will typically result in the depletion of the volatile component in the melt (see **Figure 1.12b**) accompanied by a concomitant decrease of the same component H_2O-fluid (see **Figure 1.12a**), as the system evolves toward complete solidification (Candela, 1989).
Candela also observed that not all volatile components will act in the same way as the Cl. Fluorine, for instance, is predicted to have its concentration remain relatively constant during first boiling (see **Figure 1.12b**).

Metals (such as Cu) which bond strongly with Cl- in aqueous solution will tend to exhibit a partitioning behaviour that is similar to the one shown in the figure above. Their maximum concentration in the aqueous fluid occurs immediately after water saturation has been achieved. By contrast, metals such as Mo, which do not bond strongly with Cl^-, and are not, therefore, controlled by concentrations of this ligand, partition differently and may be most efficiently concentrated in the very last portions of the evolving H_2O-fluid phase. The contrasting behaviour of Cu and Mo in the magmatic-hydrothermal environments has been confirmed by direct experimental evidence.

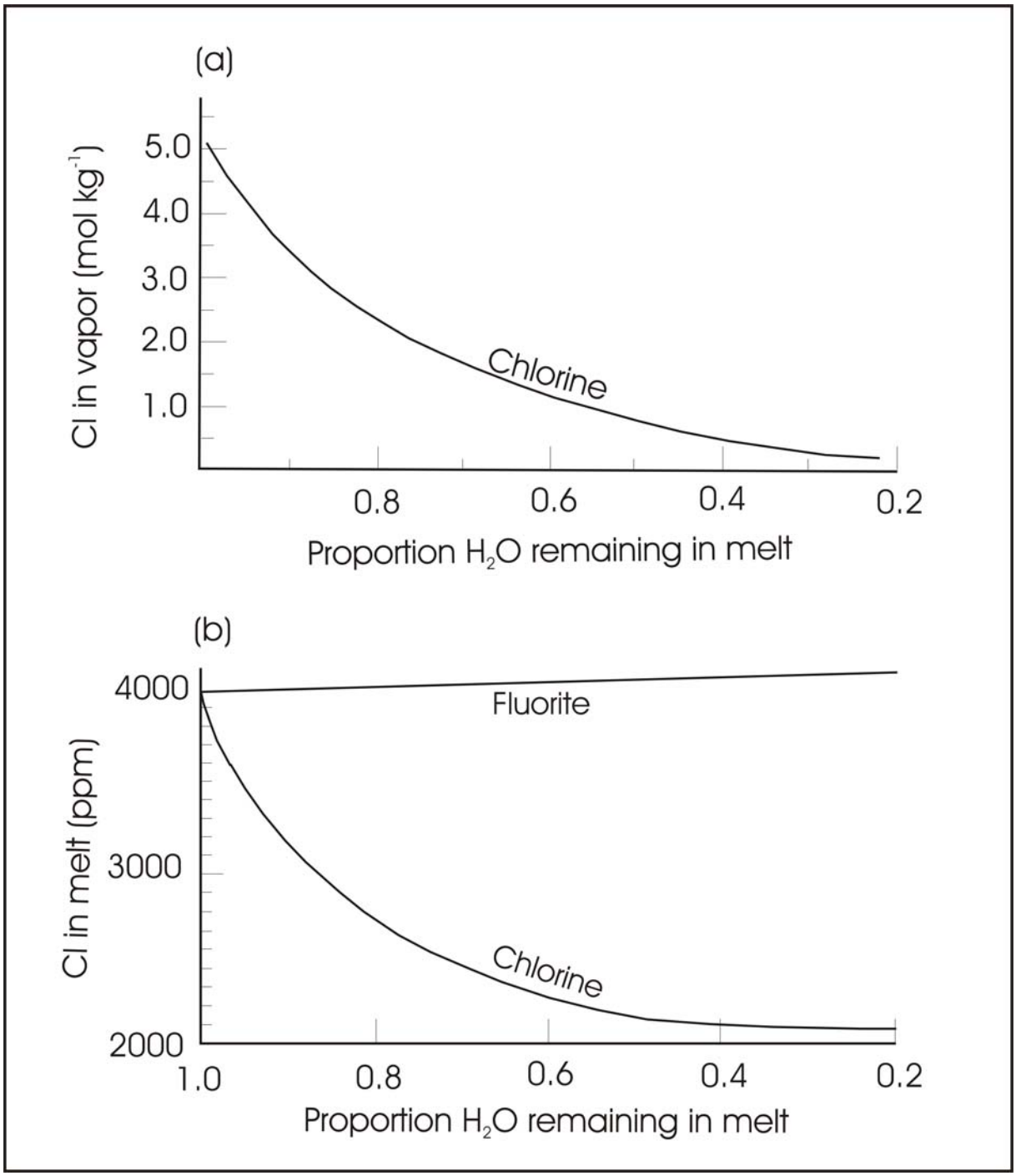

Fig.1.12. Calculated concentrations of Cl in (**a**) an aqueous fluid exsolved from a granitic magma, and (**b**) the residual magma itself, both as a function of the proportion of water remaining in the melt. A first boiling scenario is assumed, with the magma moving adiabatically upwards from 5.4 km depth (5 wt% H_2O at saturation) to the surface (1 wt% H_2O remains in the rock). $\mathbf{C^{Cl}_o}$ is assumed to 4000 ppm and $\mathbf{D^{Cl}_{fluid/melt}}$ is calculated to vary from 39 at the point of water saturation to 1 as the magma reaches the surface (after Candela, 1989b).

1.7. Water content and depth of emplacement of granites and their Relationships to ore-forming processes

Several ore deposits associated with granites, such as porphyry Cu and epithermal Au-Ag ores, are related to magma emplacement at high levels of the crust where H_2O-fluid production and hydrofracturing can take place. These types of deposits are commonly located in the volucanic or sub-volcanic environment and have formed as much from the action of surface-derived (or meteoric) water as they have from the circulation of magmatic waters (Strong, 1988).

Other deposit types, such as porphyry Mo and granitoid hosted Sn-W deposits, are generally associated with magmas emplaced at deeper levels in the crust. The depth of emplacement of granite magma, together with related parameters such as magma composition and initial water content, plays a very important role in determining the nature and origin of ore deposits associated with felsic igneous rocks.

In **Figures 1.13a** and **b** (after Strong, 1988), hypothetical zones of melting are shown for each of the three cases where the water required to initiate melting is supplied by the breakdown of muscovite, biotite, and amphibole. If sufficient melt is allowed to accumulate and then rise upwards in the crust along an adiabatic cooling path, each of these magmas would crystallize at different levels in the crust. Adiabatic upward movement of magma would involve cooling at a rate of about 1.5°C $kbar^{-1}$ and would approximately follow the steep curves that define mineral phase boundaries in the P-T space. Ideally magmas could rise upwards in the crust until they intersect the water-saturated granite solidus, by which time they have become completely solid and could not intrude any farther. S-type granite magmas would, therefore, be emplaced at mid-crustal depths (4-5 kbar), as indicated by the intersection of the muscovite breakdown curve with the water-saturated granite solidus. By contrast, intersection of the biotite or amphibole breakdown curves with the water-saturated granite solidus indicates that an I-type magma could move to much shallower crustal levels (1 kbar or less) before completely solidifying. **Figure 1.13b** is a schematical crustal profile showing the relationships between depth of emplacement and the metallogenic character of the various granite-related deposit types.

I-type magmas generated deep in the lithosphere usually form adjacent to subduction zones and commonly receive a contribution from mantle-derived mafic melts. They form at high temperatures (1000°C or more) and are relatively dry (water contents less than 3-4 wt %). They rise to shallow levels of the crust and may even extrude to form substantial volcanic structures. Such magmas will typically exsolve a magmatic vapour phase by first boiling, an event that will also promote hydrofracturing, brecciation, and the widespread circulation of hydrothermal solutions in and around the sites of magmatic activity. These are the environments in which porphyry Cu, as well as epithermal Au-Ag deposit types occur (Williams et al., 1997).

By contrast, S-type magmas are generated in the mid- to lower-crust by partial melting of a source rock that comprises a substantial proportion of metasedimentary material. These melts will form at relatively lower temperatures (around 700°C) and will initially comprise significant amounts of H_2O dissolved in the magma. Such magma will crystallize in the mid-crust and not too far from its site of generation, and will typically be barren.

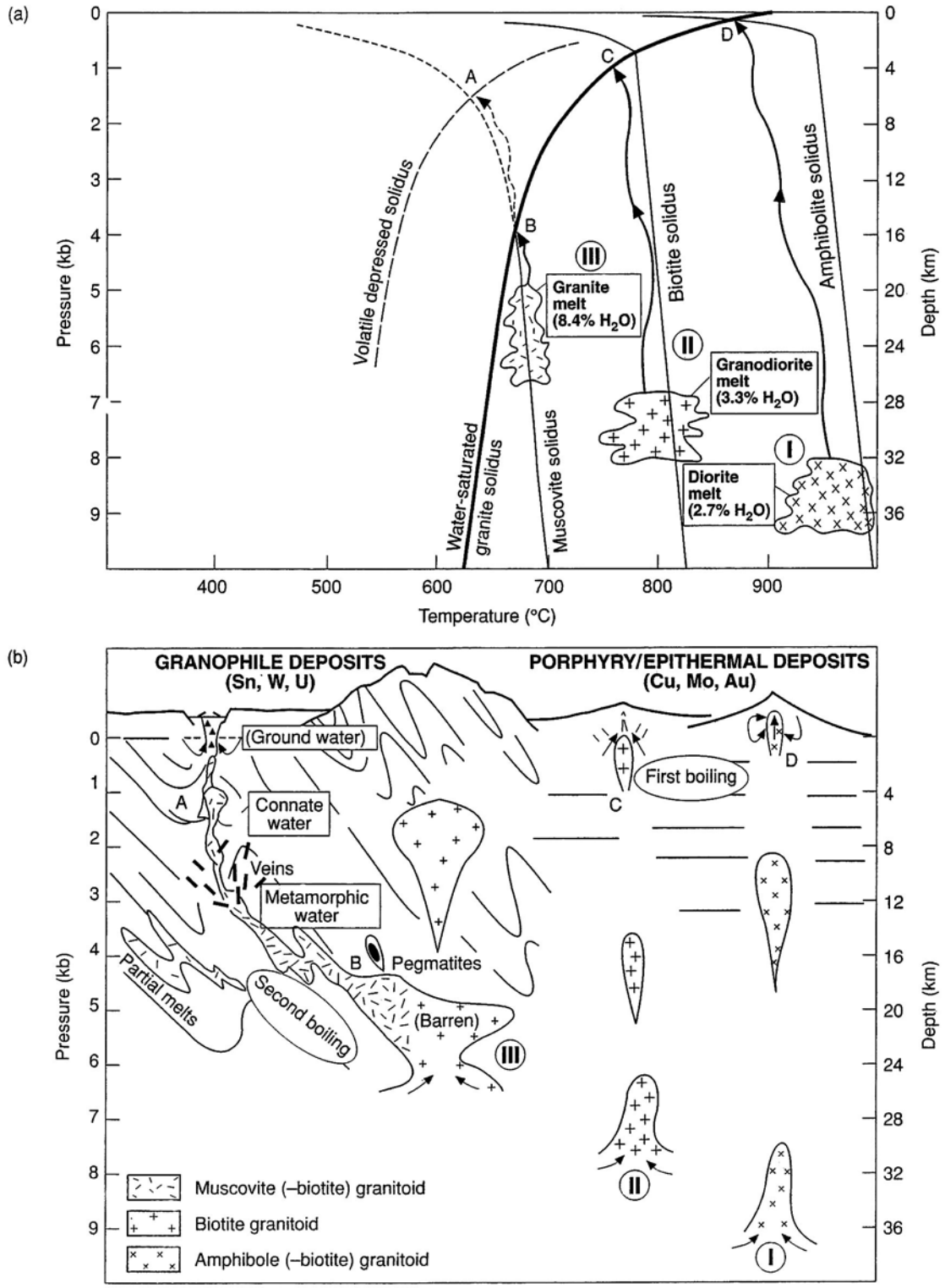

Fig.1.13. Strong's model showing the relationship between level of granite emplacement and metallogenic character. (a) Pressure-temperature plot showing the approximate conditions where fluid-absent melting of amphibole- (I), biotite- (II), and muscovite-bearing (III) protoliths would occur, and the expected levels in the Earth's crust to which melt fractions would rise adiabatically, as a function of the water-saturated solidus. (b) Schematic diagram illustrating the emplacement style and metallogenic character of granites formed under each of the conditions portrayed in part (a) (redrawn after Strong, 1988).

If substantial crystal fractionation occurs, however, incompatible trace elements will become concentrated in residual melts, and in those rocks representing the crystallized products of differentiated magma. H_2O-fluid saturation will also eventually occur in the residual magma by second boiling, to form pegmatites and related deposits. The concentration of volatiles, as well as elements such as B and P, will, together with exsolved water in the residual magma, depress the temperature of the water-saturated granite solidus to lower temperatures (500-600°C) such that the magma could continue its upward migration to higher levels in the crust. Fluid pressures would probably not be sufficient to fracture rocks at these depths, but other structural controls would nevertheless promote fluid circulation and it is in these environments that Sn greisen deposits, porphyry Mo deposits, polymetallic skarn ore deposits, and mesothermal veins might form.

1.8. Models for the formation of porphyry-type Cu, Mo and W deposits

Considerable progress has been made in understanding the processes that occur in a crystallizing granite intrusion in order to form genetically associated base metal deposits (Candela and Holland, 1984, 1986; Candela, 1989, 1991; Candela and Piccoli, 1995). Porphyry Cu (Mo-Au) deposits are probably the most well understood class of magmatic-hydrothermal deposits. As a generalization, porphyry Cu-Mo deposits are associated with arc related “calc-alkaline” or I-type magmas generated adjacent to Andean type subduction zones (Burnham and Ohmoto, 1980).
S-W deposits are more often associated with S-type granites that are derived by partial melting of the continental crust that would normally include a significant proportion of meta-sedimentary material. In certain settings these S-W deposits are also regarded as “porphyry-type” even though they may differ significantly in their geological characteristics from the Cu-Mo types (Rowins, 1999).

1.8.1. The origin of porphyry Cu-(Mo) and Porphyry Mo-(Cu) type deposits

The family of deposit types known as porphyry Cu-Mo ores can be subdivided into two groups, one in which Cu is the dominant exploitable metal (together with minor Mo and occasionally Au), and the other where Mo is the dominant exploitable metal (with minor Cu and sometimes W). These two groups are referred to as the Cu-(Mo) and the Mo-(Cu) porphyry types, respectively (Candela and Holland, 1984). Porphyry deposits are the world’s most important source of both Cu and Mo and, especially in the circum-pacific region, there are many world-class deposits that exploit these metals. Examples of these deposits include La Escondida, Chuquicamata and El Salvador in Chile; Bingham(Utah), San Manuel-Kalamazoo (Arizona) and Santa Rita (New Mexico) in the USA; Ok Tedi, and Panguana in Papua New Guinea; Lornex (British Columbia), and Valley Copper in Canada; Cerro Colorado in Panama; Cananea in Mexico and Coed-y-Brenin in the UK (Candela et al., 1999). As shown in **Figure 1.14**, both types of deposits are associated with the generation of oxidised I-type granite magmas associated with melting processes adjacent to subducted oceanic crust (Candela, 1989).

Cu-(Mo) can be explained in terms of a body of magma with a relatively low initial water content (inherited from the fluid absent melting of an amphibolitic protolith) rising to high levels in the crust before significant crystallization takes place. It is likely that some melt fractions from this high level magma chamber will be tapped off and extruded on the surface.
These fractions will crystallize to form volcanic and subvolcanic (porphyry) suits of rocks whose compositions will not be highly differentiated (i.e. granodioritic or rhyodacitic) because of the low degree of fractionation that has taken place prior to extrusion. Because the magma is emplaced at low load pressures the saturation water content will be relatively low and probably not significantly different from the initial water content. Vapor-saturation will, therefore, occur early in the crystallization sequence, essentially due to “first boiling”. Even though Cu is a compatible element in a crystallizing granitic melt (sequestration of Cu into accessory sulphide phases and biotite result in $D^{Cu}_{crystal/melt} > 1$), the lack of crystallization means that very little of the metal will have been removed from the melt by the time water-saturation occurs (Robb, 2005). The vapour phase, by contrast, is characterized by Cl^- concentrations and will, therefore, efficiently scavenge Cu from the silicate melt.

In this setting, however, the situation with respect to Mo is different. Mo is an incompatible element in a crystallizing granitic melt ($D^{Mo}_{crystal/melt} < 1$) but, because of the low degree of crystallization, its concentration in the residual magma will not have increased significantly prior to water saturation. On saturation, Mo will partition into the H_2O-fluid phase but, because its partition coefficient is relatively small and unaffected by the Cl^- concentration ($D^{Mo}_{fluid/melt} = 2.5$) it will never attain very significant concentrations in the fluid phase. In this setting, therefore, a high level granodioritic I-type magma will exsolve an aqueous phase that is highly enriched in Cu, but only moderately so in Mo, and form a typically porphyry Cu-(Mo) deposit (Robb, 2005).

A different scenario can be constructed for the formation of Mo-(Cu) porphyry deposits, where it is envisaged that the parental I-type magma might have originally contained a slightly higher initial water content (perhaps due to the fluid absent melting of a biotite-bearing protolith) than the Cu-dominant situation. As seen in **Figure 1.14**, this magma would not normally rise to the same shallow crustal levels as its drier equivalent. The saturation water content of the magma is also significantly higher in this situation and, consequently, a greater degree of crystallization needs to take place before water-saturation is achieved (in this case vapour-saturation might occur by second boiling). As the magma crystallizes so will Cu be extracted from the melt and end up distributed somewhat evenly throughout the rocks representing the marginal zones of the pluton. This Cu will not be available for partitioning into the aqueous fluid once saturation is achieved. Mo, on the other hand, is incompatible and its concentration will continue to increase in the residual melt. When saturation does occur, Mo will be concentrated even further into the H_2O-fluid phase because of its favourable partition coefficient. Although Cu will be strongly partitioned into the highly saline H_2O-fluid, its abundance in the melt is significantly depleted due the earlier crystal-melt sequestration and the vapour phase will not be significantly concentrated in Cu. The extraction of a melt fraction from a more deep-seated magma chamber will give rise to a pluton that is less likely to reach the surface and whose composition is more highly differentiated due to the greater degree of crystal fractionation prior to extraction. Porphyry-style mineralization associated with the circulation of a magmatic-hydrothermal fluid in and around such an intrusion may well

have Mo concentrations in excess of Cu, giving rise to Mo-(Cu) porphyry-type mineralization (Candela and Piccoli, 1995).

1.8.2. The origin of Porphyry W-type deposits

Candela (1992) emphasized the relationship that exists between W-rich porphyry-type deposits and the more reduced, ilmenite-bearing, S-type granites that crystallize at relatively deep levels of the earth's crust. In **Figure 1.14** its setting is illustrated under field (3).

Under oxidising conditions, such as those applicable to the I-type, magnetite-bearing granites, the efficiency of extracting W from a magmatic-hydrothermal system into an ore body is relatively low and therefore this metal is not a normal component of porphyry Cu-Mo deposits. Under reducing conditions, however, W behaves as an incompatible element in terms of its crystal-melt partitioning behaviour and its concentration will increase during crystal fractionation.

When a magma forms from the partial melting of a meta-sedimentary precursor, the melt formed will be relatively hydrous and will tend to crystallize relatively deep in the crust. Such a melt is likely to be peraluminous and relatively reduced since it will have equilibrated with meta-sedimentary material that might have contained organic carbon. The saturation water content under these conditions will be high and a significant degree of crystallization will occur before saturation is attained (by second boiling). Because W is incompatible under these conditions its concentrations will rise in the residual melt, whereas Mo concentrations will tend to decrease because it behaves in a more compatible way under reducing conditions. When the H_2O-fluid does exsolve it will interact with a highly differentiated melt that is significantly enriched in W. The fluid phase will scavenge some W but its relatively low partition coefficient ($D^{Mo}_{fluid/melt} \sim 1$) will ensure that most of the concentration is achieved prior to water saturation. The deposits that form in this setting will be associated with deep-level, highly differentiated S-type granites with metal concentrations dominated by W and only minor Mo.

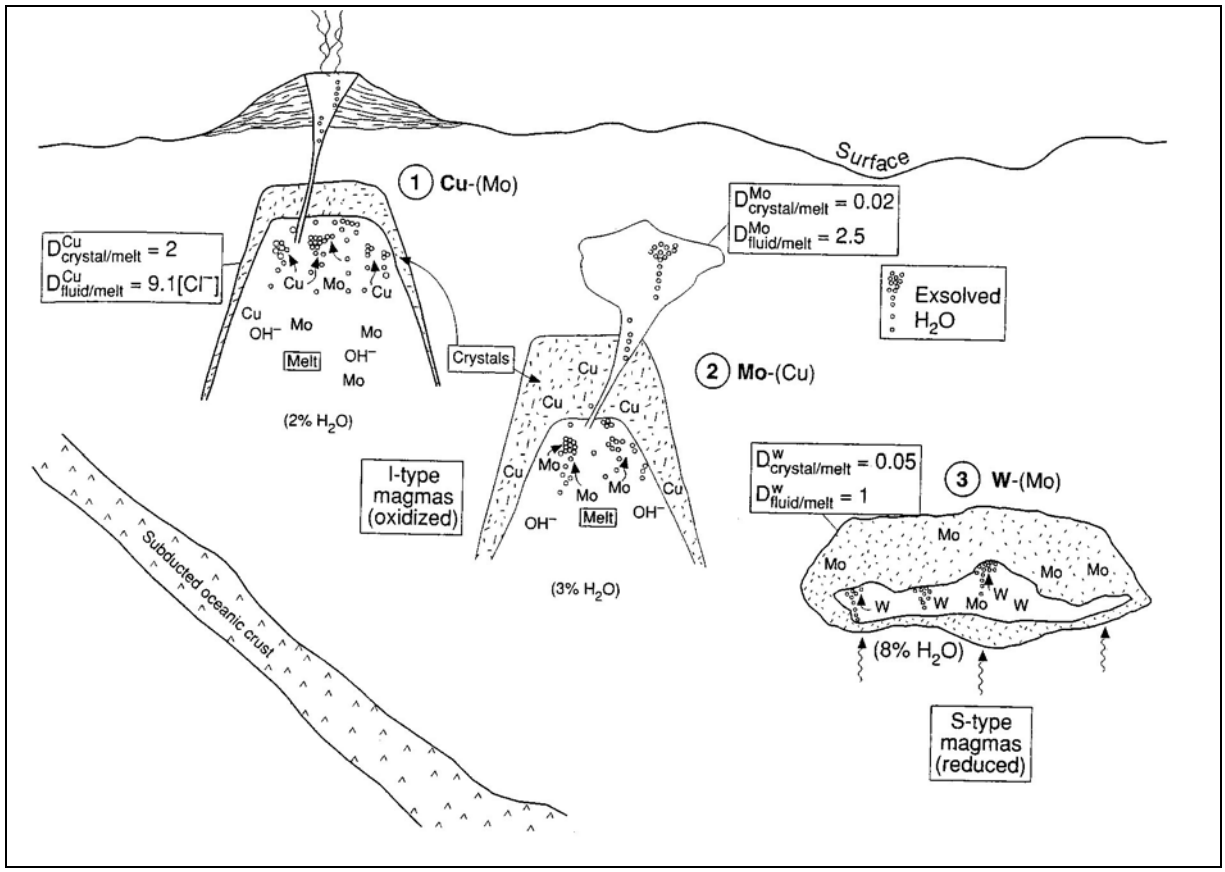

Fig.1.14. Schematic model for the formation of porphyry-type Cu, Mo, and W deposits (modified after the models of Candela and Holland, 1984; 1986; Strong. 1988; Candela, 1992).

These deposits often contain significant Sn mineralization to form the Sn-W porphyries. In this case the low oxidation state of the melt increases Sn solubility in the melt, as Sn^{2+} is much more soluble than Sn^{4+}. Therefore, Sn will partition less into crystalline phases and will become more concentrated in the residual melt (Linnen, et al., 1996). The elevated fluorine content in S-type granites enhances the solubility of the high field strength elements (HFSE), such as Sn, Nb, Ta, W, etc in the melt (Keppler, 1993). These elements therefore become enriched in the residual melts.

1.9. Fluid flow in and around the granite plutons

Most of the world's mineral resources occur in deposits formed as a result of the movement of hydrothermal solutions. These deposits form when solutions which have become charged with valuable components in a source region migrate to and through sites where part or all of the valuable components precipitate (Cathles, 1981). Understanding the flow patterns in and around the intrusion that forms the fluid source and the length of time that magmatic-hydrothermal fluids remain active subsequent to magma emplacement are of great importance with respect to the formation of magmatic-hydrothermal ore-deposits (Robb, 2005).

Fluid flow may be caused by heat supplied by repeated and sustained igneous intrusions at a fixed point in space, such as at mid-ocean spreading ridges and continental rifts. Fluid circulation may also be caused by the heat or hot volatiles from

a plutonic intrusion or by the heat of radioactive decay (Cathles, 1981). Fossilized fluid flow pathways are revealed by recognizing the effects of alteration and mineralization that a hydrothermal solution imposes on the rocks through which it circulates (Robb, 2005). The prediction of where such fluids have circulated is best achieved by modelling the thermal effects of an evolving fluid phase in terms of both conductive and convective heat loss in and around a theoretical intrusion. Attempts to model fluid flow around granite plutons have proven useful in predicting where optimal fluid flux, and hence mineralization, should be located in relation to the intrusion.

Cathles (1981) used a thermal modelling approach to demonstrate that intrusions cool very rapidly, at least in terms of a geological time scale. In **Figure 1.15**a model curves are plotted which relate the time for an intrusion to cool to 25% of its initial temperature, in relation to its size and geometry in space. For the case where a small intrusion cools by conduction of heat to the wall-rocks, solidification will be complete and magmatic-hydrothermal fluid circulation effectively over in about 105-106 years. If cooling is accompanied by convective heat loss caused by circulation of a hydrothermal fluid through a permeable network of fractures (such as would be the case if hydrofracturing had occurred) then such a pluton could be reduced to 25% of its initial temperatures within as little as 104 years. Thus, in a highly permeable system where fluid flow is maximized by fluid exsolution and hydrofracturing, heat loss will be very rapid and a single intrusion will not be able to sustain a geologically long-lived period of hydrothermal circulation. This feature could work against the development of a viable ore body, if it is considered that only magmatic fluids are responsible for ore formation. It should, however, be noted that mineralization in and around magmatic intrusions can also be the result of externally derived fluids and that these can circulate in response to other factors besides thermal gradients (Norton and Cathles, 1979).

Soon after the intrusion of a granitic body a substantial thermal anomaly is created for up to 2 or more km around the intrusion and an active system of circulatory fluid flow is set up from both the sides and top of the body. Aqueous solutions will then establish a convective cell where flow is upwards from the intrusion, and circulates back downwards at some distance away. These solutions could incorporate waters from the surrounding country rocks as well as the magmatic fluids derived from the cooling pluton itself. A fluid flux will be obtained around the intrusion from the gradients of the stream function which defines the streamlines (the closer together the streamlines, the greater the fluid flux, see **Figure 1.15**b).

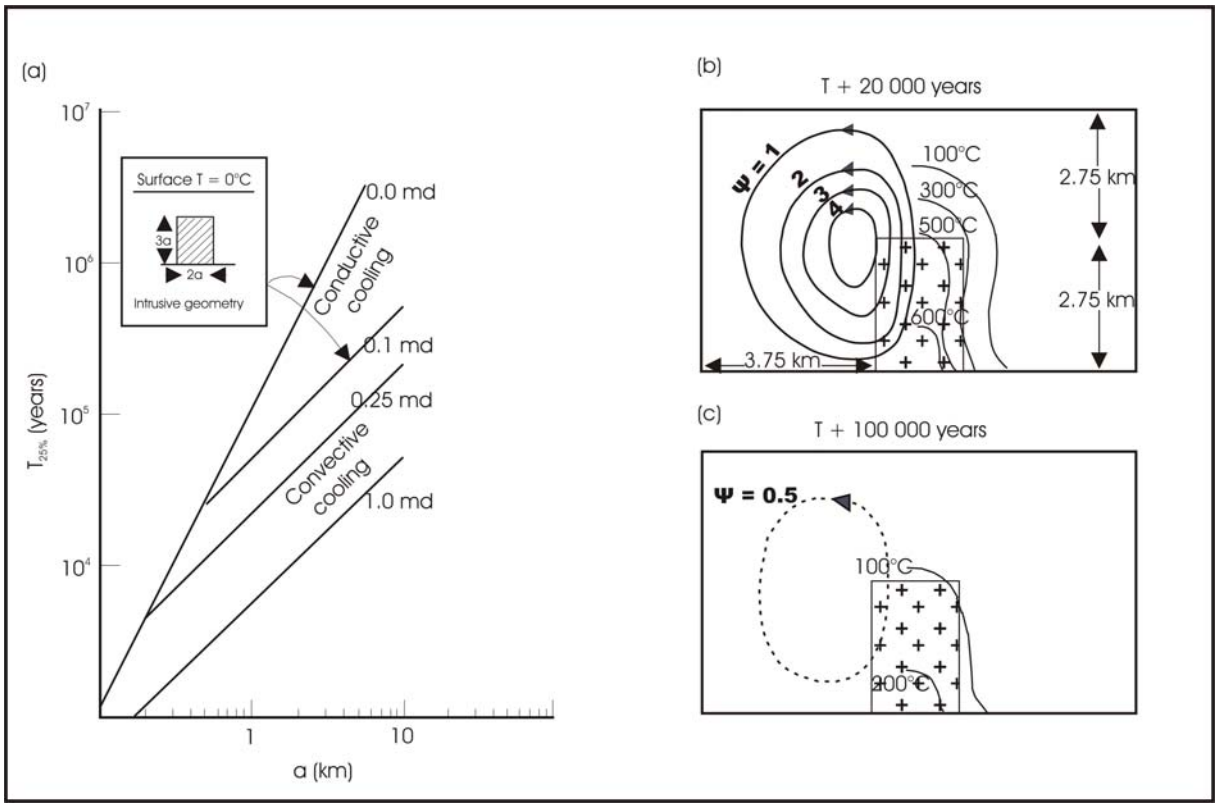

Fig.1.15. Models illustrating the thermal and fluid flow characteristics in and around a cooling igneous intrusive body. (a) Plot of time taken for the temperature of an intrusion to fall to 25% of its initial temperature as a function of the intrusion dimensions (a in km). Two situations, one where heat is lost by conduction alone (steep slopes) and another where a combination of conduction and convective heat loss occurs (shallow slopes), are shown. Permeabilities (in millidarcy, md) are shown for the two cases (after Cathles, 1981). (b) Thermal model showing fluid flow and temperatures in and around an intrusion some 20 000 years after emplacement. For clarity, streamlines (quantified in terms of the stream function Ψ) are shown on the left and isotherms on the right hand side, although the model is symmetric about the intrusion. The intrusion was initially at 750°C with a permeability of 0.07 md and the country rocks at 0°C with a permeability of 0.13 md. (c) Similar model for the situation 100 000 years after emplacement. Parts b and c are after Norton and Cathles, 1979.

Ore-forming events are likely to be short-lived in around small granite intrusions representing just a single pulse of magma. The ore bodies that form under these conditions are likely to be small and perhaps sub-economic. Larger, multi-episodic intrusions are required in order to create a system where a substantial magmatic-hydrothermal ore-body will form (Atkinson and Baker, 1986). An example of such ore-bodies includes the polymetallic (Sn-W-Cu-Pb-Zn) deposits of the Cornubian batholith in Cornwall and Devon, southwest England, where mineralized veins occur along the margins of individual granite plutons, extending out into the surrounding metasedimentary country rocks. Mineralization is also characterised by a pronounced regional zonation in the distribution of metals. These patterns can be explained in terms of the nature of fluid low in and around individual granite plutons, as well as the shape of the intrusions and the extent to which they have been exhumed.

1.10. Skarn deposits

The word “skarn” refers to the metasomatic replacement of carbonate rocks (limestone and dolomite) by calc-silicate mineral assemblages during either contact

or regional metamorphic processes (Meinert, 1992). Mineral deposits associated with skarn assemblages are referred to as skarn deposits, and are typically the product of contact metamorphism and metasomatism associated with intrusion of granite into carbonate rocks. Deposit types and metal associations grouped into the category of skarn deposits include W, Sn, Mo, Cu, Fe, Pb-Zn, and Au ores. The processes by which these metal deposits form are similar, namely granitoid emplacement and magmatic-hydrothermal activity, though at different levels in the crust. An association with granite intrusion cannot always be demonstrated, but is usually inferred.
The different metals found in skarn deposits are a product of differing compositions, oxidation state, and metallogenic affinities of the igneous intrusion (Einaudi et al., 1981; Misra, 2000). Figure 17 is a simple diagram relating granitoid compositions to skarn deposit type (after Meinert, 1992).

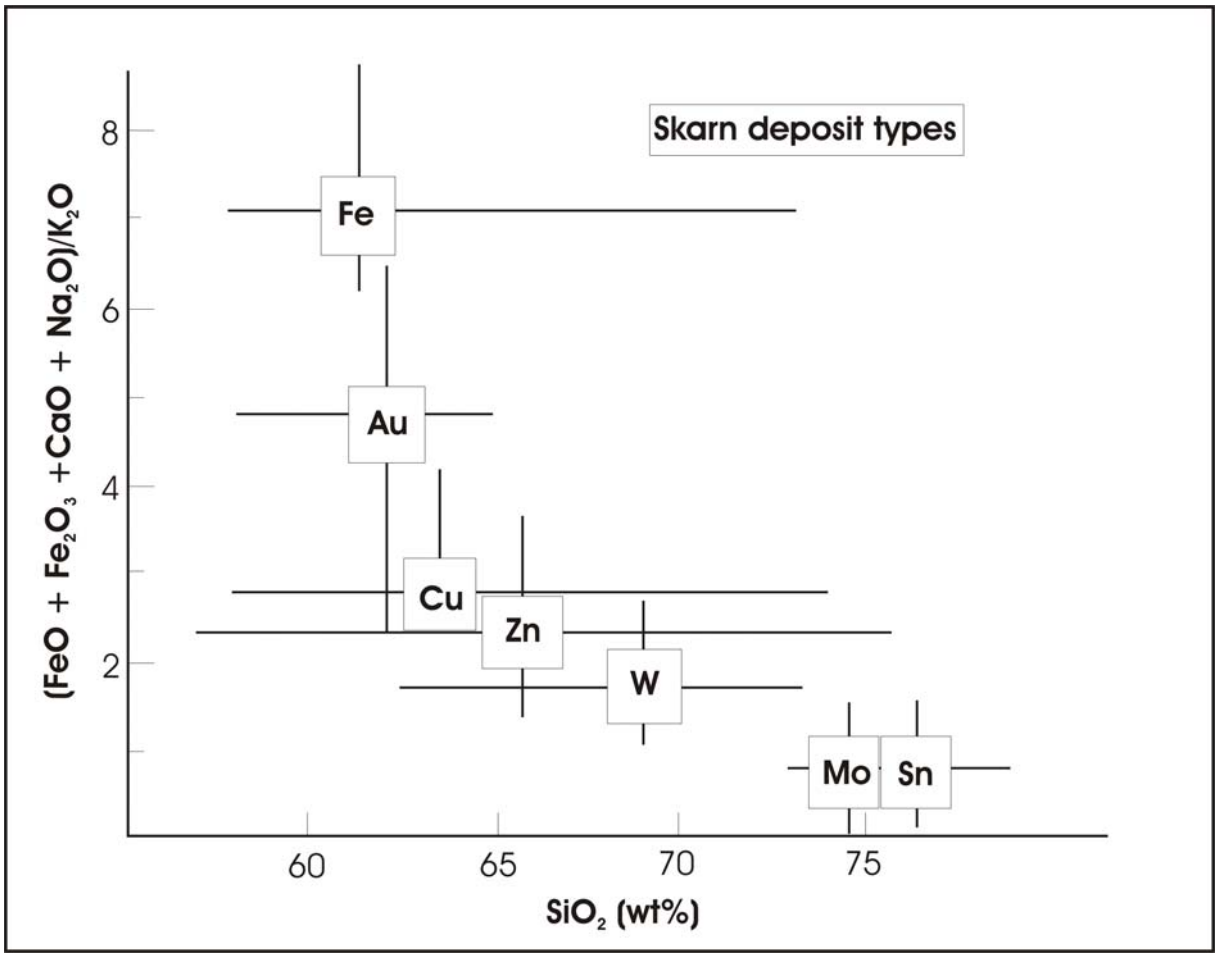

Fig.1.16. Plot of SiO_2 versus $[FeO+Fe_2O_3+CaO+Na_2O]/K_2O$ showing the relationship between the composition of igneous intrusion and the dominant metal in various skarn deposits (after Meinert, 1992).

As a general rule Fe and Au skarn deposits tend to be associated with magmas that are acidic to intermediate in composition. Cu, Pb, Zn, and W are linked to calc-alkaline, magnetite-bearing, oxidised (I-type) granitic intrusions, and Mo and Sn with more differentiated granites that might be reduced (S-type) and ilmenite-bearing (Meinert, 1992).
Skarn deposits can be classified into calcic or magnesian types, depending on whether the host rock is a limestone or dolomite. They are also described as either endo- or exo-skarns, depending on whether the metasomatic assemblage is internal

or external to the intruding pluton. Most of the large, economically viable skarn deposits are associated with calcic-exoskarns. Tungsten skarns produce the bulk of the world's W production and are typically associated with intrusion of calc-alkaline intrusions, emplaced relatively deep in the crust. Examples include the King Island mine of Tasmania and the MacTung deposit in the Yukon Territory of Canada.
Cu skarns, by contrast, are often associated with high level porphyry-style intrusions and many porphyry copper systems that intrude carbonate host rocks have copper skarns associated with them. A classic example is the Bingham district of Utah, USA, which contains both a huge porphyry Cu and the world's largest Cu skarn deposits (Einaudi, 1982). Au skarns associated with porphyry Cu mineralization are associated with emplacement of high level, oxidised, and magnetite-bearing granitoids. Other Au-specific skarn deposits, where Au occurs in association with a Bi-Te-As metal assemblage, are linked to more reducing, ilmenite bearing granitoid intrusions (Meinert, 2000). Fe skarns occasionally form large economically viable magnetite deposits, e.g. at Sverdlovsk and Sarbai in Russia, and are associated with more mafic gabbroic to granodioritic intrusions, typified by endoskarn alteration and sodium metasomatism (Einaudi et al., 1981).

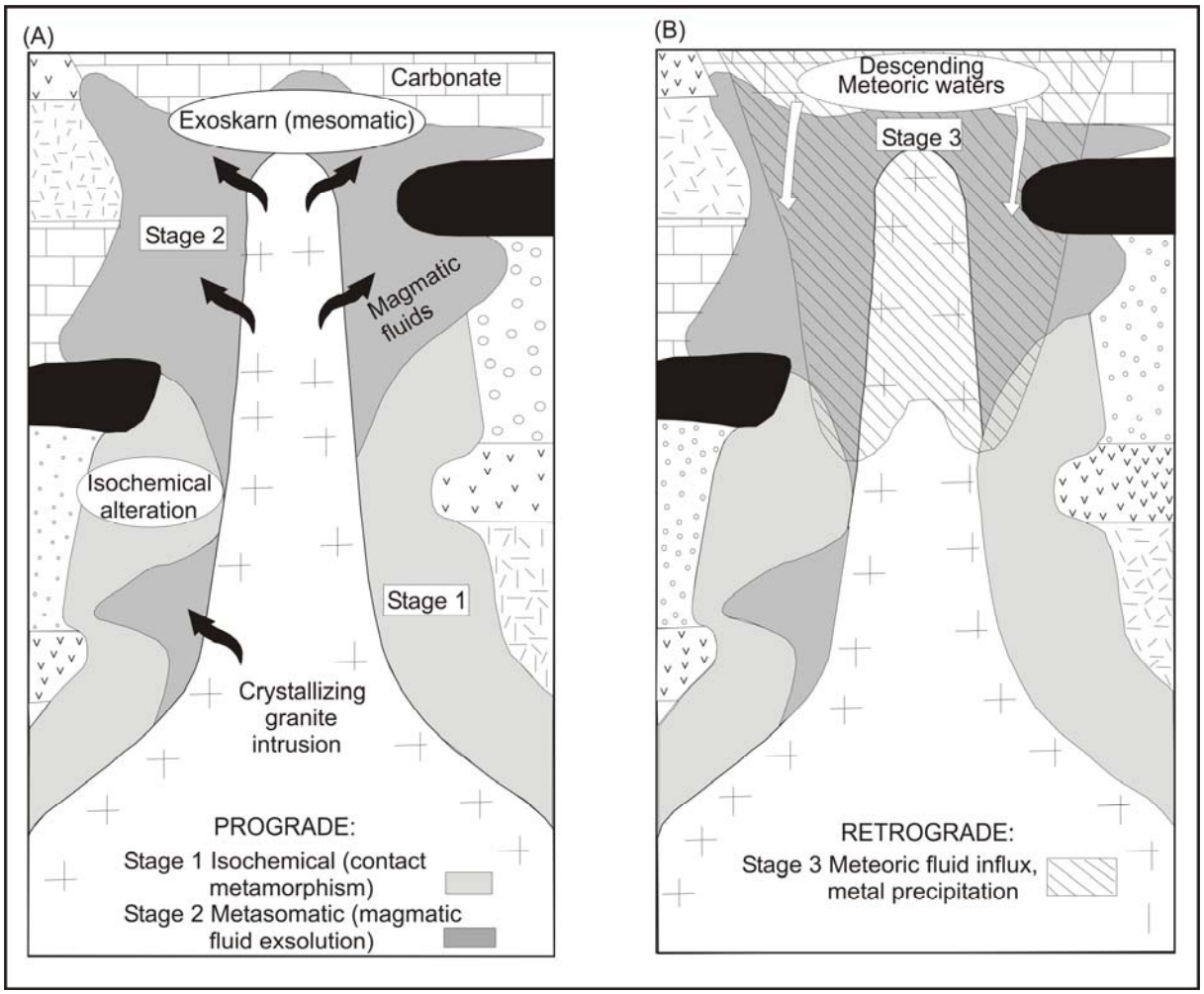

Fig.1.17. The evolution of intrusion-related skarn deposits showing the three sequential stages of formation. (a) Prograde stage, and (b) retrograde stage (modified after Corbett and Leach, 1998).

Sn skarns are generally associated with highly differentiated S-type (or ilmenite-bearing) granitoids, e.g. the Renison Bell mine in Tasmania.

Skarn deposits typically form as a result of three sequential processes (Einaudi et al., 1981; Meinert, 1992). As illustrated in **Figure 1.17**, these are 1) prograde-isochemical contact metamorphism during early stages of emplacement and crystallization, followed by 2) open system prograde-metasomatism and alteration during magmatic fluid saturation, and finally 3) the retrograde draw-down and mixing with meteoric fluids during cooling of the pluton.

During prograde-isochemical contact metamorphism the granite pluton intrudes the country rock whose sediments will be subjected to contact metamorphism and formation of a variety of hornfelsic textures. The mineral assemblages that form at this stage will reflect the composition of the litho-types within which they form. This is largely a thermal effect process although fluids as a product of prograde metamorphic reactions, and mainly CO_2 and H_2O, are likely to circulate. In dolomitic units mineral zonation approximates the sequence: garnet-clinopyroxene-tremolite-talc/phlogopite, reflecting increased distance and progressively more hydrous assemblages away from the intrusion. In limestone units the mineral zonation is garnet-vesuvianite + wollastonite-marble. Dehydration close to the pluton margins is important for increasing porosity of the source rocks as this facilitates fluid flow during later episodes of mineralization.

The second stage of skarn deposit formation involves H_2O-fluid and vapour saturation of the intruding magma (as a function of either first or second boiling or both). The fluid phase will then egress onto the surrounding contact metamorphic halo. At deeper crustal levels fluid flow is likely to be concentrated along discrete structural or bedding parallel conduits, whereas at higher levels fluid flow will be more pervasively distributed, perhaps due to hydrofracturing, in a broad halo in and around the granite cupola. The mineral assemblage will be similar as in the first stage, but alteration is more pervasive and coarser-grained, and will replace the earlier formed assemblage. Si, Al, and Fe, as well as other components will be introduced into the calcareous sediments by the aqueous magmatic fluid, while Ca, Mg, and CO_2 are locally derived and also introduced into the metasomatic system. Sulfide mineralization will not form at this stage, although magnetite and scheelite (in W skarns) do precipitate in the warning stages of prograde metasomatism.

During the third and final stage of skarn deposit formation all magmatic-hydrothermal systems undergo progressive cooling and decay of the high temperature magmatic fluid system. As fluids become progressively dominated by shallow meteoric waters, a series of complex retrograde reactions take place, as well as the precipitation of the main stages of base and precious metal, sulfide-related mineralization (Einaudi et al., 1981).

The retrograde alteration assemblages are superimposed onto earlier metamorphic and metasomatic minerals and, typically, this process is recognized by paragenetically late formation of epidote, biotite, chlorite, plagioclase, calcite, quartz (all after various garnet types), tremolite-actinolite, and talc (after pyroxenes) and serpentine (after olivine). Sulfide ore minerals, as well as magnetite and hematite, occur as disseminations, or veins, that cut across prograde assemblages.

Assemblages such as pyrite-chalcopyrite-magnetite characterise proximal settings, whereas bornite and sphalerite-galena are typically more distal in occurrence. The paragenetically late precipitation of most skarn-related ores suggests that metal precipitation is related to decreasing temperature of the ore fluids (and a resulting drop in solubilities), fluid mixing, or neutralization of the ore fluid by reaction with carbonate lithologies.

Mixing of magmatic ore fluid with the late meteoric components, and related redox reactions in the fluid, may be additional controls on the ore formation process.

1.11. Near-surface magmatic-hydrothermal processes, The "epthermal" family Au-Ag-(Cu) deposits

A large number of world-class gold deposits are associated with either active or geologically recent volcanic environments. These deposits are termed "epithermal", a term derived from Lindgren's (1933) classification of ore deposits and refers to those deposits that formed at shallow crustal levels, the "epizone". They form at temperatures between 160 and 270°C and at pressures equivalent to depths of between 50 and 1000m (Cooke and Simmons, 2000; Hedenquist et al., 2000). Two contrasting styles of mineralization are now recognized in epithermal deposits. They are referred to as high-sulfidation and low-sulfidation types. These terms refer specially to the sulphur fugacity in the ore fluid, the chemistry and pH of which also relates to the nature of alteration associated with each type. The two terms do not relate to the abundance of sulphur, as this is highly variable in each deposit type.

High- and low-sulfidation epithermal deposits are end-members of processes related to fluid evolution and circulation in and around volcanoes. High-sulfidation deposits occur in proximal settings and are commonly found within or close to the volcanic vent itself. The fluids involved with mineralization are, therefore, derived directly from the magma as a product of vapour and fluid-saturation and are usually boiling in the ore forming environment. The fluids are very acidic, pH~ 1-3, and oxidised, carrying the oxidised S^{4+} or S^{6+} species as SO^2, SO_4^{2-}, or HSO_4^- in solution. As the liquid boils SO_2 and CO_2 will be partitioned into the vapour phase, and the remaining liquid carries a surplus of H^+ making it very acidic (pH~1; Hedenquist et al., 2000). This acidic fluid is also capable of leaching most of the major elements from the host volcanic rocks or volcano-sedimentary rocks through which it circulates, resulting in vuggy textures and an advanced argillic style of alteration.

By contrast, low sulfidation deposits are associated with fluids that are similar to those involved with hotsprings and other geothermal manifestations in areas of enhanced heat flow. These fluids have equilibriated with their host rocks and generally comprise of a dominantly meteoric component, although it is likely that this will have been mixed with an evolved magmatic fluid if active volcanism is located nearby. Consequently, low sulfidation deposits may form within the volcanic edifice, especially during the warning stages of magmatic activity when draw-down of meteoric fluids is perhaps more likely. More typically, however, they may form at locations that are somewhat removed from the focus of volcanism. The fluid involved is near-neutral and has low salinities, but is also likely to have boiled in and around the zone of ore formation (Hedenquist et al., 2000).

Figure 1.18 shows schematically the characteristics of high- and low-sulfidation deposits and suggests a spatial and genetic link that exists between the two types. One area where both deposits occur in fairly close proximity to one another is in Kyushu, the southernmost island of Japan. It is also evident in this figure that there should be a genetic link between porphyry Cu-(Mo-Au) deposits formed in the sub-volcanic environment and high-sulfidation Au-Cu deposits at the surface. This link can be demonstrated in the case of the Lepanto epithermal Au-Cu and the far southeast porphyry Cu-Au deposits on Luzon in the Philippines (Arribas et al., 1995).

However, this spatial and generic link may, in most cases, not exist between the two types of deposits (Hedenquist et al., 2000). Many gold districts contain either low-sulfidation epithermal deposits (such as the major deposits in Nevada, USA, including Round Mountain, Comstock Lode, Midas, and Sleeper) or high-sulfidation deposits (such as many of the Andean deposits, including Yanacocha, Pierina, and El Indio-Tambo).

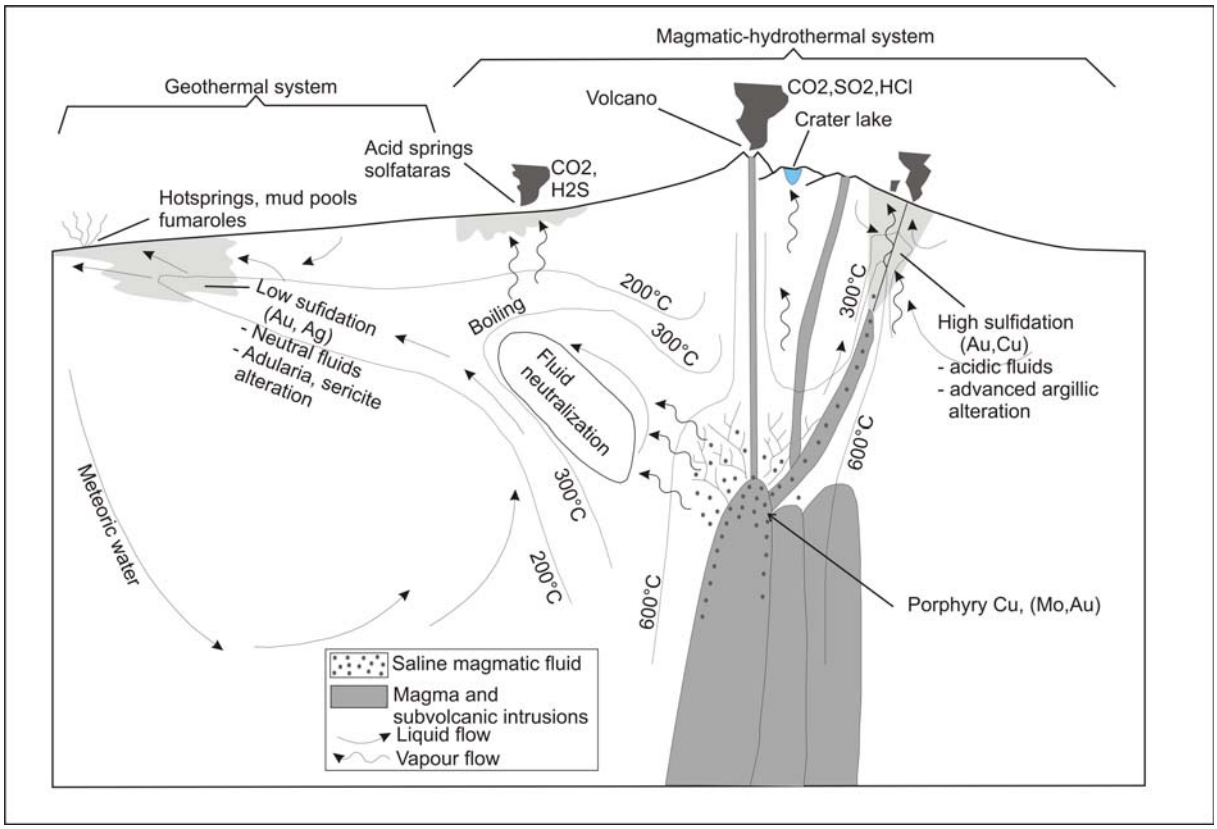

Fig.1.18. The geological setting and characteristics of high-sulfidation and low-sulfidation epithermal deposits. A genetic link between high-sulfidation epithermal Au-Cu and sub-volucanic porphyry type Cu-Au deposits is also suggested (after Hedenquist et al., 2000).

1.12. Conclusion

Magmatic intrusions and associated hydrothermal systems that occur along convergent plate margins, where oceanic crust is subducted under continental lithosphere, lead to the formation of volcanic arcs. This is the tectonic setting where most magma-related hydrothermal ore deposits are concentrated (Sawkins, 1990).

The flux of metals measured from some erupting volcanoes indicates that, given enough time and a concentration mechanismus, degassing magmas can exsolve sufficient amounts of metals to create an ore deposit (Cline, et al., 1991).
Evidence of association between magma and ore deposits comes from some correlations between the type of metal deposit and the composition of the associated magma, e.g. peralkaline intrusions with high K_2O or Na_2O can host ores of the lithophile elements such as Zr, Nb and the lanthanides, whereas more aluminous F-rich systems are typically associated with Sn, Mo and B ore bodies. Tin and W tend to be associated with reduced magmas (as indicated by the absence of magnetite), whereas Cu and Mo ore deposits tend to occur within more oxidised magmas, containing magnetite (Hedenquist & Lowenstern, 1994).
Within volcanic arcs, correlations exist between the tectonic environment and the metallogeny of an ore district.

Metals can enter magmas through a variety of pathways including; mantle melting, mass transfer from the subducting slab and melting of the crust. During partial melting of the mantle the metal sulphides will be partially consumed, to contribute metals to the basaltic liquids which will then ascend into the crust, both along mid-ocean ridges and at subduction zones. Subduction may contribute additional metals such as Cu and Zn to resulting arc magma, derived from hydrothermal mineralization of the subducted sea floor (Hedenquist & Lowenstern, 1994).

In terms of metal concentration, however, the source of metals may be less important than the magmatic processes that operate during the final ascent and differentiation of the magma. Crystallisation is one the main controls on the concentration of ore components in the magmas. The dominant minerals that crystallize in most igneous systems are silicates and oxides. Elements that partition into these minerals will have their concentrations lowered, whereas incompatible elements may become more concentrated in the residual melt (Robb, 2005).

Even after extensive crystallization, metal concentrations in magmas are still two or three orders of magnitude less than the grades of economic ores in the associated porphyry-style mineralization. Other processes are therefore necessary to concentrate metals from magma into an ore deposit. Magmas contain fluids during their ascent through the middle to the upper crust. At low pressures the residual magma reaches water saturation, at which point the fluids will exsolve from the magma taking with it some metals partitioned into it as chlorides, bisulphides and hydroxyacid complexes (Holland, 1972; Keppler & Wyllie, 1991 and Hemley & Hunt, 1992).

Most magmas will exsolve substantial quantities of water and CO_2, as the most dominant magmatic-hydrothermal fluids. Water has the ability to dissolve significant quantities of anionic substances, e.g. Cl^-, which in turn promotes the dissolution of other alkali and transition metal cations. The magmatic aqueous phase can exist as a

liquid, vapour, or homogeneous supercritical fluid. The process of H_2O-saturation can be achieved in two ways, either by decreasing the pressure of the system (called first boiling) or by progressive crystallization of magma (second boiling).

H_2O-saturation is relevant to ore-forming processes during the emplacement and crystallization of granitic magmas at moderate to shallow crustal levels. This environment gives rise to the formation of a wide variety of important ore deposit types including porphyry Cu and Mo deposits, polymetallic skarn ores, granite-related Sn-W deposits, and the family of volcanic-related epithermal Au-Ag-(Cu) deposit types.

Many metals will partition strongly into the liquid or vapour that forms on H_2O-saturation and, in such cases, mineralization accompanies the alteration of host rocks, both within and external to the intrusion (Hemley & Hunt, 1992). The formation of either Cu- or Mo-dominant porphyry deposits reflects a subtle interplay between the depth of intrusion of the granitic body (itself a function of the original water content), the timing of H_2O-saturation relative to the progress of crystallization, and the behaviour of metals during melt-fluid partitioning. Egress of fluids and vapour from the magma and their subsequent circulation are dependent on the permeability of the surroundings, and may be modified by boiling-related hydrofracturing.

Polymetallic skarn deposits reflect the interaction between the exsolved magmatic fluids from different types of granite and calcareous sediments (Robb, 2005). H_2O-saturation and boiling in volcanic environments, producing significant volumes of volatile-rich vapour, is conducive to the formation of epithermal deposits. High- and low-sulfidation epithermal deposits reflect end-members in a continuum of magmatic-hydrothermal processes that progressively incorporate more non-magmatic waters as the volcanic system wanes, or as one moves away from the volcanic centre (Rye, 1993).

2. DISTRIBUTION OF TRACE ELEMENTS BETWEEN BIOTITE AND HYDROUS GRANITIC MELTS

2.1. Aims

Formation of magmatic-hydrothermal ore deposits requires that ore trace elements, such as Cu, Ag, Mo and W, for example, are already concentrated in the magmatic melts during fractional crystallization. When a rock, at appropriate conditions of temperature and pressure, undergoes partial melting, trace elements will partition themselves between the melt phase and the solid residue of refractory minerals in a systematic manner. Some, the compatible, trace elements will prefer to be hosted by the minerals in the solid residue, whereas others, the incompatible, will opt to stay concentrated in the partial melt. In a similar way during fractional crystallization compatible trace elements that may still be available in the melt will again be taken up by the crystallizing mineral-assemblage leading to further concentration of the incompatible trace elements in the residual melt.

Thus enrichment of trace elements and their potential for ore-deposit formation is linked to their incompatibility during both anatexis and fractional crystallization. However, no element can be that perfectly incompatible and will thus possess a finite, albeit at times very little, solubility in the major rock-forming minerals.
Investigation of the origin of magmatic-hydrothermal mineral deposits requires modelling the behaviour of the concerned trace elements during fractional crystallization, which essentially demands obtaining information about the elements' mineral/melt partition coefficients, $D_i^{c/lq}$, thus the aim of this study.

$$D_i^{c/lq} = M_i^c / M_i^{lq} , \qquad (2.1)$$

where i is the element that partitions between the crystal phase, c, and the melt phase, lq. M_i^c and M_i^{lq} represents the trace element concentrations in the crystal and melt respectively.

D_i depends on a number of factors including the prevailing temperature and pressure conditions, the melt composition and the crystal composition.
Incompatible trace elements are characterised by very small values of D_i, usually less than one.

To understand the process of fractional crystallization of a granitic system one needs to know how its trace elements partitioned between the melt and the major and minor rock-forming minerals, including the micas, feldspars, pyroxenes, amphiboles, magnetite and allanite. Trace element partitioning studies have long been undertaken, especially on the partitioning of rare-earth elements between minerals and melts in basaltic systems. However, the biotite-melt partitioning data for trace elements in granitic systems is virtually lacking.
Biotite is one of the first minerals to crystallise out of the melt during fractional crystallisation. It is also one of the most abundant rock-forming minerals in granitic systems and contains, in its crystal lattice, sites for univalent, divalent and trivalent cations of different sizes. It therefore avails a large number of sites suitable for substitution of the crystal's major elements by some trace elements from the melt with appropriate ionic sizes and charges. It is for this reason that I investigated the

partitioning of trace elements between biotite and melt for a granitic system. The study investigates trace element partitioning for a single bulk composition but for a wide range of trace elements.

Selection of trace elements for this study was based on two criteria namely: (1) those elements relevant for the formation of economical ore deposits, e.g. Cu, Zn, Co, Ni, V, Cr, Ti, Mo, W, Nb, Ta, Zr, and Pb, and (2) trace elements whose partition-coefficient data can allow modelling the evolution of trace-element patterns during fractional crystallization, e.g. the lanthanides, Rb, Cs and Ba.

Knowledge of trace element abundances and their distribution in granitic systems in particular, can in principle be applied to reconstruct the entire evolution of the magma enabling successful and correct predictions of geological processes that gave rise to the formation of economically viable magmatic-hydrothermal ore deposits. The abundance of elements in a naturally occurring silicate melt (magma) can be used to constrain variables associated with the formation of a magma by partial melting and its subsequent evolution through processes such as fractional crystallisation. Integral to understanding the abundance of an element is the way in which it partitions between crystals and coexisting melt, hence the task of this study.

2.2. Experimental methods

In principle the investigation of a phase-equilibrium can be experimentally carried out by keeping a sample of known chemical composition under steady conditions of temperature and pressure for a certain period of time and subsequently bringing the entire system to room temperature (quenching), while keeping the pressure constant, in the shortest time possible. In this way most silicate systems will have their high-temperature and high-pressure state conditions frozen. Thus the melt in equilibrium with crystalline phases is abruptly solidified into glass. Various equipment for phase-equilibrium experimentation exists, the choice of which will depend on the specified conditions of temperature and pressure for a given experiment. They include the 1 atm.gas mixing furnaces, hydrothermal autoclaves (internally and externally heated), piston-cylinder-apparatus, multi-anvil-apparatus and the diamond cells (see **Figure 2.1**).

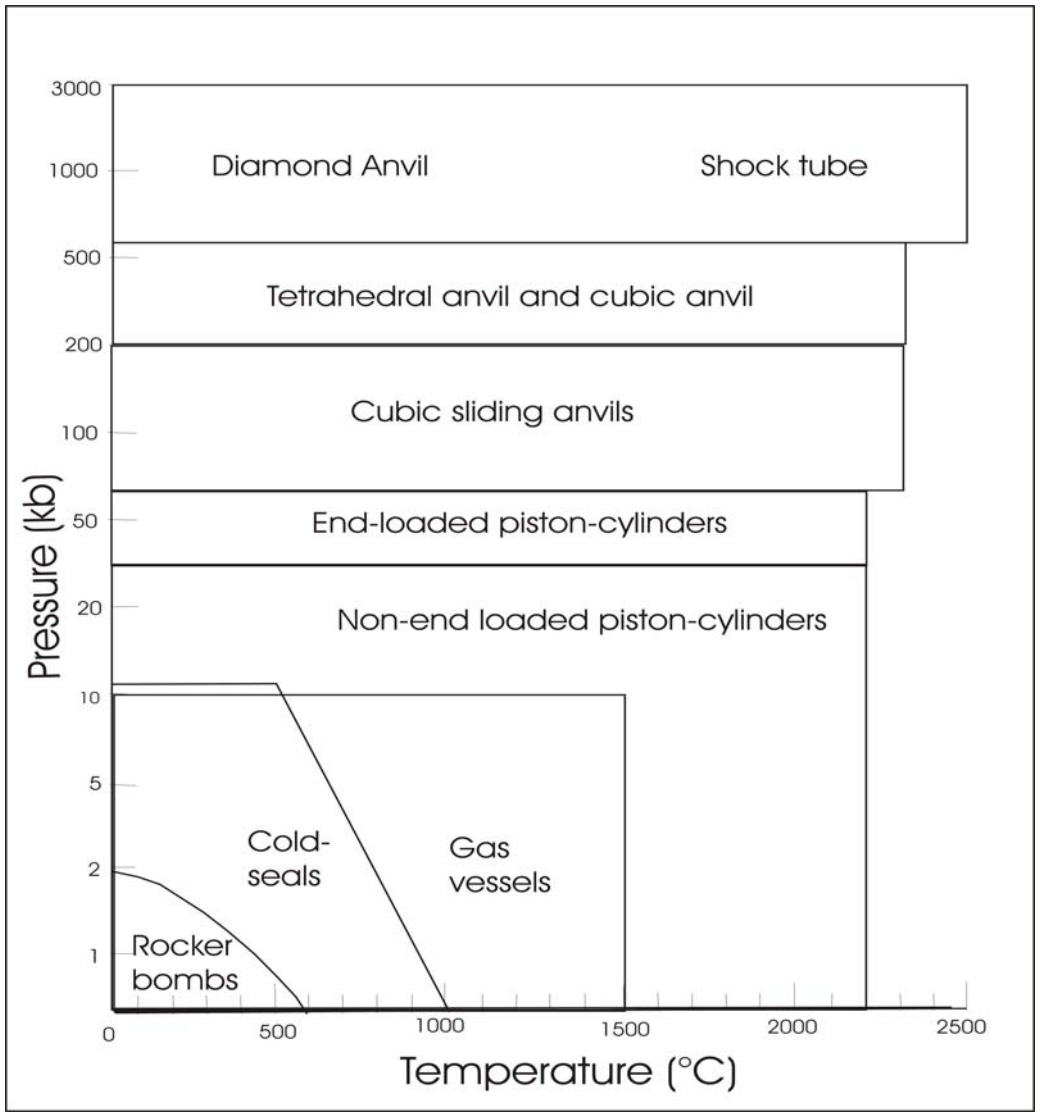

Fig. 2.1. Pressure and temperature fields for various equipment used for experimental investigations of phase equilibrium (redrawn from Holloway J R & Wood B J, 1988, simulating the Earth. Experimental Geochemistry. Boston, Unwin/Hyman).

Hydrothermal autoclaves, better known as “bombs” or “cold-seal vessels” are externally heated. This equipment employs gases or liquids (H_2O, Ar, CO_2) as a pressure medium. They operate optimally in a temperature and pressure range of 600-1000°C and 2-10 kbar (**Figure 2.1**).

In this study, phase equilibrium in silicate systems has been investigated by using externally heated hydrothermal autoclaves running at a constant pressure of 2 kbar and isothermal temperature in the range of 700-800°C, with H_2O as the pressure medium.

2.2.1. High-pressure equipment and technique

The equipment (**Figure 2.2**) consists of three units namely: 1) the pumping system, diagram (a), which generates the required high pressures using of two pumps (the air pump and the oil pump) and H_2O as a pressure medium. The generated pressure is then sent to the autoclaves, through pressure lines and a series of control valves. 2) A bank of cold-seals, diagram (b), in which prepared sample charges, in the form of capsules, are loaded and heated. 3) The temperature control unit for regulating the temperature inside the autoclaves and furnaces, through a series/number of thermocouples, see diagram (c). The integral operation of these three units simulates hydrothermal equilibrium processes and conditions similar to those in the earth’s crust and upper-mantle.

In this study, hydrothermal crystallization experiments were carried out in horizontal nimonic and Rene 41 cold-seal externally heated pressure vessels (EHPV), also called autoclaves, at a temperature range of 700-800 ± 10°C and a constant pressure of 2.0 ± 0.1 kbars, using water as a pressure medium. A variety of P-T conditions were contemporaneously investigated with a bank of cold-seal vessels. Typically 2 charges/capsules (see section 2.2.2, for sample and charge preparation) were simultaneously run in each experiment. The experimental-run temperature was continuously monitored using a K-type (Ni-CrNi) thermocouple located inside the autoclave and lying close to the sample charge/capsule (see **Figure 2.3**). The measured temperatures during the experiment are believed to be accurate to ± 10°C.

The loaded and assembled autoclave (see **Figure 2.3**) was first installed and connected to the pressure line. It was then pressurised cold to the target experimental pressure of 200 MPa, the pressure line closed off and left to stand for a day or two, as a test for possible pressure leakage. Pressure was monitored and measured with a gauge calibrated against a Heise-gauge.

When the autoclave was confirmed pressure-tight it was connected to the pressure line and its external heater (furnace) switched on. During the initial heating stage pressure increase was continually monitored and adjusted to remain close to the target pressure of 2 kbars as the temperature rose. Under normal circumstances the target experimental temperature could be reached and stabilised after about 30-45 minutes. The autoclave was then isolated from the pressure line and left to run at isobaric and isothermal conditions for 35-45 days.

Special care was taken to regularly keep the stability of the experimental conditions in check throughout the entire prescribed duration of the experiment by reconnecting the reaction vessels/autoclaves to the pressure line to make corrections for pressure losses or increases, remembering to close up or disconnect the vessels from the pressure line immediately after every check-up. Oxygen fugacity during the experiment was controlled by Ni-NiO buffer conditions achieved from the central Ni-metal rod in the autoclave together with water, as a pressure medium, lying next to the sample capsule.

All experiments were conducted as reverse-direction runs, i.e. the autoclaves were first heated to a higher temperature of about 830°C and held constant for two days to homogenize the components in the melt. This is called the preconditioning step of the experiment. The temperature was subsequently decreased in a single, isobaric step to the final run conditions, set for each reaction vessel.

At the end of the experiment the autoclave was reconnected to the pressure line, its external heating furnace switched off and quenched isobarically to room temperature in a stream of compressed air. The quenching operation was carried out in the shortest time possible (to minimise back reactions in the run products but also to avoid crystallisation of the melt during quenching) by sliding away the movable hot furnace to expose the autoclave to direct streams of cold compressed air, gushing out from the fully opened valve of the gas supply line. After about 15-25 minutes of cooling with compressed air the autoclave was dismounted from the pressure line assembly to be further cooled by cold running water in the laboratory water sink. The autoclave was finally dismantled to remove the sample capsule(s).

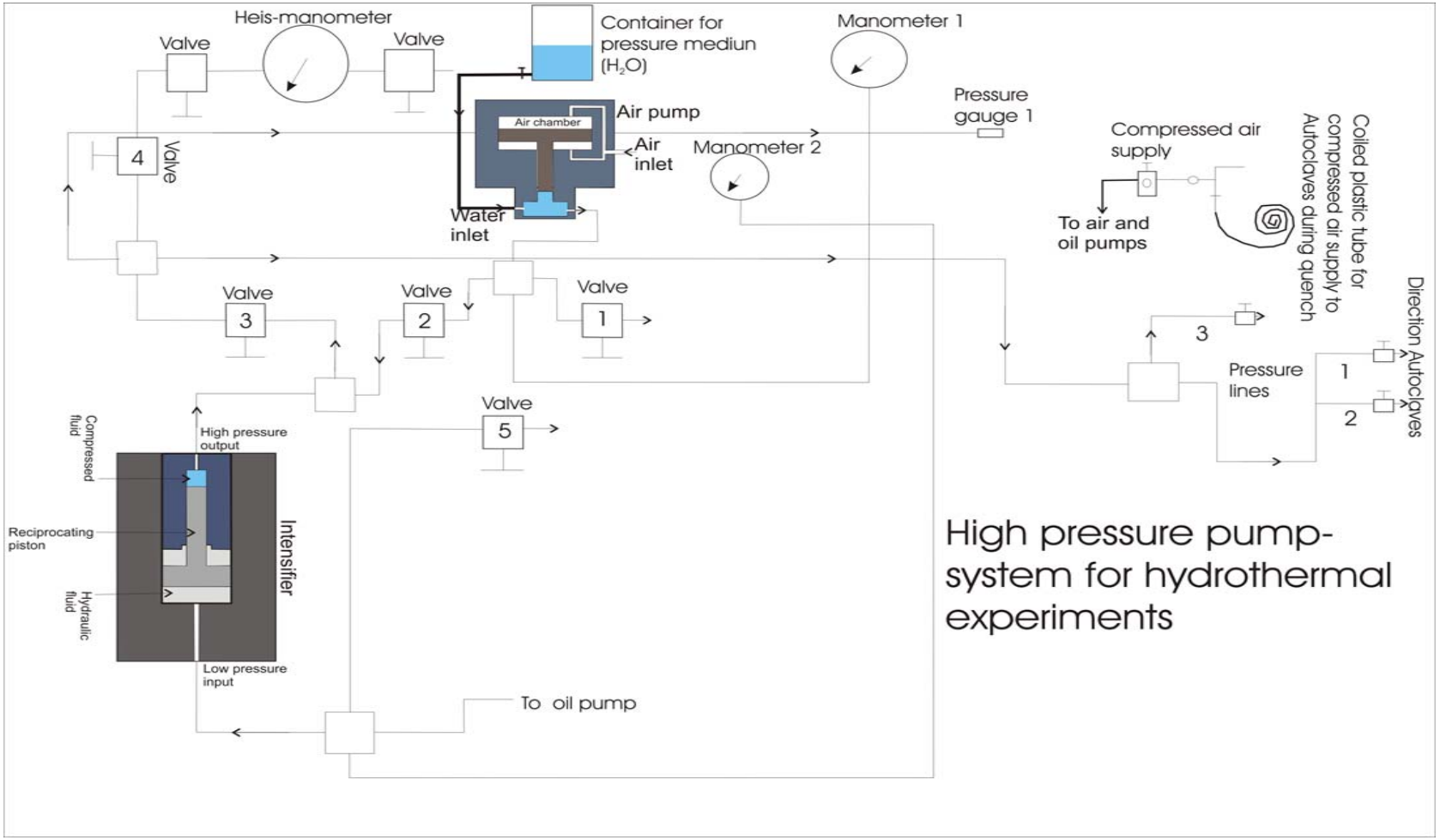

Fig. 2.2(a). Schematic diagram of the pressure-generating system for hydrothermal experimentation. The most important valves during the operation of the system include: No.1, the pressure release valve for the air pump, No.2, the valve to the intensifier, No.3, the valve to the autoclaves, and No.5, the pressure-release valve for the oil pump. See text for a brief description of the system.

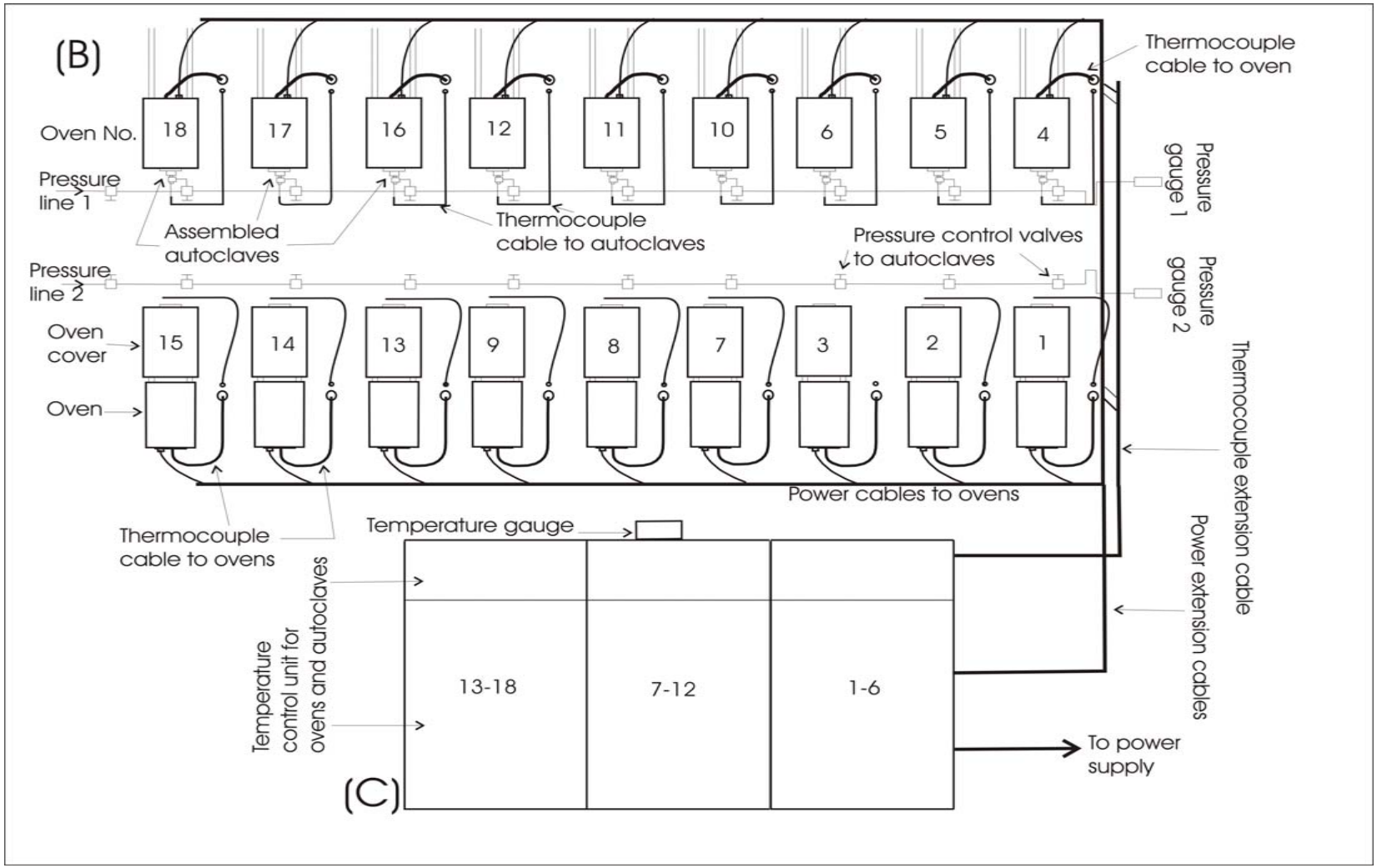

Fig. 2.2(b) Schematic overview of a bank of cold-seal systems, for hydrothermal experimentation. The numbers 1 to 18 indicate a series of furnaces/ovens used for the experiments as described in the text. The ovens (No. 4 -18) attached to pressure line 1 are assembled with autoclaves and in running mode. **(c)** Is a schematic front-view of the temperature control unit for the furnaces (ovens) and autoclaves. The numbers, e.g. 1-6, 7-12, and 13-18, show where on the control board each oven and autoclave can be monitored and regulated during the experimental run.

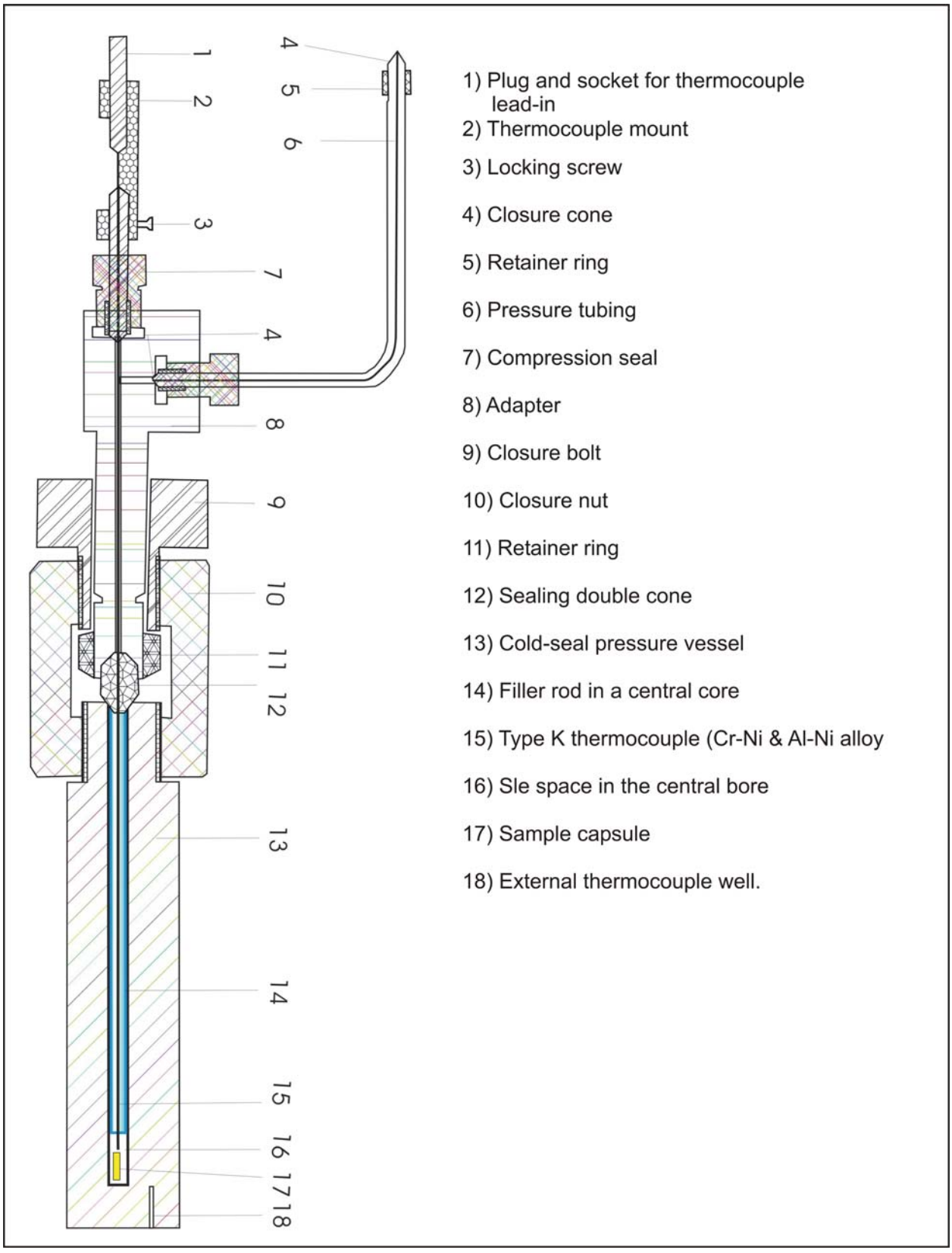

Fig. 2.3. Cross-section of a cold-seal vessel and closure assembly (Autoclave) Note that the thermocouple is installed and assembled inside the vessel and its end point lies just close to the sample charge, No. 17.

2.2.2. Starting materials (glasses) and preparation of capsules

2.2.2.1. Starting materials

The system Haplogranite-Anorthite-Biotite-H_2O was experimentally investigated to study the distribution of trace elements between biotite and the residual hydrous granitic melt in the temperature range of 700-800°C at a constant pressure of 2 kbar.
The starting materials, a series of synthetic silicate glasses, were composed of approximately 75.3 wt% haplogranite (35 wt% SiO_2, 40 wt% $NaAlSi_3O_8$ and 25 wt% $KAlSi_3O_8$), 8.4 wt% Anorthite ($CaAl_2Si_2O_8$), 15.3 wt% biotite ($K[Mg,Fe]_3[(OH)_2/AlSi_3O_{10}]$) with a 1:1 molar ratio of Mg/Fe, and 1 wt% of a selected set of trace element oxides, as a dopant (see **Table 2.1**). The trace elements were carefully selected to avoid peak interference during electron microprobe analysis of the starting materials (glasses) and the experimental run-products.
The composition of the haplogranite corresponds to the thermal minimum in the haplogranite system at P_{H2O} = 2 kbars (Tuttle and Bowen, 1958). Trace elements for this study were selected from 4 major groups of elements including 1) elements of the first transition metal series of the periodic table (V and Cr, 0.2 wt% each and Co, Ni, Cu, Zn, 0.5 wt% each, as oxides), 2) carbonates of the large lithophile elements (Rb, Cs, Sr and Ba, 0.5 wt% each), 3) oxides of the high-field strength elements (Mo, W, Nb, Ta, 0.2 wt% each, Pb 0.5 wt% and Zr 0.1 wt%) and 4) oxides of all the REE (La, Ce, Pr, Nd, Sm, Eu, Gd, Tb, Dy, Ho, Er, Tm, Yb and Lu, 0.2 wt% each).
The silicate glasses were carefully prepared by weighing, mixing and grinding commercially available reagent grade oxides and carbonates of appropriate purity (see **Table 2.1**) under ethanol in an automated electric-ball-mixer or grinder (called “Planetenkugelmuehle” in German) for about 30 minutes to produce a homogeneous mixture.

Table 2.1. Reagent grade oxides and carbonates used in the preparation of the experimental starting glass

Reagent-grade	Analytical-grade (%)	Manufacturer	Reagent-grade	Analytical-grade (%)	Manufacturer
SiO2	99.99	Chempur	ZrO_2	99.9	Chempur
$Al(OH)_3$	99.9	Merck	CeO_2	99.9	Aldrich
$Na_2(CO_3)$	99.9	Merck	Nb_2O_5	99+	Merck
$K_2(CO_3)$	99	Merck	Ta_2O_5	99.99	Chempur
$Mg(OH)_2$	99.9	Merck	MoO_3	99.5	Merck
$Ca(CO_3)$	99.5	Merck	WO_3	99.9	Chempur
FeO	99.5	Chempur	Lu_2O_3	99.9	Chempur
CuO	99	Chempur	La_2O_3	99.9	Chempur
ZnO	99+	Chempur	Pr_2O_3	99.9	Chempur
CoO	99.9	Aldrich	Nd_2O_3	99.9	Chempur
NiO	99	Chempur	Sm_2O_3	99.9	Chempur
TiO_2	99.5	Chempur	Eu_2O_3	99.9	Chempur
V_2O_5	98+	Chempur	Gd_2O_3	99.9	Chempur
Cr_2O_3	99	Chempur	Tb_4O_7	99.9	Chempur
$Rb_2(CO_3)$	99.9	Chempur	Dy_2O_3	99.9	Chempur
$Cs_2(CO_3)$	99.99	Chempur	Ho_2O_3	99.9	Chempur
$Ba(CO_3)$	99.99	Chempur	Er_2O_3	99.9	Chempur
$Sr(CO_3)$	99.999	Chempur	Tm_2O_3	99.9	Chempur
PbO	99.999	Aldrich	Yb_2O_3	99.9	Chempur

The mixture was left out to dry at room temperature for a few days after which it was again ground in a mortar and pestle to produce a relatively uniform fine powder. This powder was packed into a platinum crucible and slowly heated from room temperature to 1100°C in a furnace for about 48 hours to remove the carbonates from the mixture. The decarbonised sample was then removed from the furnace and left to cool down naturally. It was again crushed, ground and mixed by tumbling in the ball grinder to ensure thorough homogeneity of the powder and eventually melted in a platinum crucible at 1600°C in a high temperature furnace, within a relatively shorter period, 4 hours. The melt was heated isothermally at the maximum temperature of 1600°C for 2 hours and finally quenched in cold water to yield a hard dark, but lustrous silicate glass.

Small chips from this glass were reserved for electron microprobe analysis, to reveal the composition of the starting materials, while the rest was ground to relatively fine powder, preserved in clean and well labelled glass containers and later stored in air-tight desiccators, awaiting further experimentation.

The homogeneity and composition of the anhydrous glass samples were determined by multiple electron-microprobe analysis, using a JEOL 8900 (available in the University of Tuebingen) and a JEOL 8200 (from the Bayerisches Geoinstitut, University of Bayreuth) instruments that were operated at an accelerating voltage of 20 kV and a beam current of 70 nA with a beam diameter of 10-20 µm. Details of the compositions of all starting materials for all the relevant hydrothermal experiments in this project are listed in **Table 2.2**, which shows the theoretical target/nominal compositions of the starting material, as calculated from the weights of mixed components, and **Table 2.3**, which shows the bulk/actual compositions, as obtained from the electron-microprobe analysis of glass quenched from the melts of the starting materials.

Meanwhile pieces of gold tubes (25 mm long, 2.38 mm diameter and 0.13 mm wall thickness) for capsule preparation were cut from one-meter rods of gold tubes by marking the rods at regular space intervals of about 25 mm and using a sharp steel razor blade to make a smooth but shallow single line cut all round the tube, at every marked point, and finally breaking off individual pieces simply by applying a slight bending force. The Au-tubes were immersed in acetone and cleaned in an ultrasonic bath for about 5 minutes to loosen and dissolve obstinate stains of dirt in and around the tubes before being heated red-hot in an oven at 700°C for about 12 hours.

A few millimetres length from one end of each gold tube was crimped flat and its irregular edge freshly cut using a pair of pliers and scissors keeping the other end open. The crimped end of the tube was then completely sealed off by arc-welding. A number/label was engraved on one side of its flat surfaces, for future identification after the experimental run, and its empty weight taken and recorded.

Table 2.2. Nominal composition (weight %) of starting materials, calculated from the mixing ratios for each sample.

Sample Comp. wt%	**mca**	**MBO**	**MCO**	**MDO**	**M10**	**M20**	**M31**	**M32**
SiO_2	67.51	69.04	69.04	68.83	69.25	69.25	69.04	69.25
K_2O	4.65	4.75	4.75	4.74	4.77	4.77	4.75	4.77
Na_2O	3.49	3.57	3.57	3.56	3.58	3.58	3.57	3.58
Al_2O_3	13.78	14.10	14.10	14.05	14.14	14.14	14.10	14.14
CaO	1.65	1.69	1.69	1.69	1.70	1.70	1.69	1.70
MgO	1.95	2.00	2.00	1.99	2.00	2.00	2.00	2.00
FeO	3.48	3.56	3.56	3.55	3.57	3.57	3.56	3.57
CuO	0.50	0.50	-	-	-	-	-	-
ZnO	0.50	-	0.50	-	-	-	-	-
CoO	0.50	-	-	-	-	-	-	-
NiO	0.50	-	-	0.50	-	-	-	-
TiO_2	0.50	-	-	0.50	-	-	-	-
V_2O_5	0.20	0.20	-	-	-	-	-	-
Cr_2O_3	0.20	-	0.20	-	-	-	-	-
Gd_2O_3	-	-	-	-	0.20	-	-	-
Sm_2O_3	-	-	-	-	0.20	-	-	-
Ho_2O_3	-	-	-	-	-	0.20	-	-
Ta_2O_5	-	-	-	-	-	0.20	-	-
SrO	-	-	-	-	-	-	0.50	-
La_2O_3	-	-	-	-	-	-	0.20	-
Er_2O_3	-	-	-	-	-	-	-	0.20
Pr_2O_3	-	-	-	-	-	-	-	0.20
Total	99.42	99.41	99.41	99.41	99.40	99.40	99.41	99.40

Table 2.2. Continued….

Sample Comp. wt%	M40	M51	M52	M61	M62	M70	M71	M72	M83
SiO_2	69.25	69.04	69.04	69.25	69.04	68.83	69.11	69.25	69.25
K_2O	4.77	4.75	4.75	4.77	4.75	4.74	4.76	4.77	4.77
Na_2O	3.58	3.57	3.57	3.58	3.57	3.56	3.58	3.58	3.58
Al_2O_3	14.14	14.10	14.10	14.14	14.10	14.05	14.11	14.14	14.14
CaO	1.70	1.69	1.69	1.70	1.69	1.69	1.69	1.70	1.70
MgO	2.00	2.00	2.00	2.00	2.00	1.99	2.00	2.00	2.00
FeO	3.57	3.56	3.56	3.57	3.56	3.55	3.56	3.57	3.57
Lu_2O_3	0.20	-	-	-	-	-	-	-	-
Tm_2O_3	0.20	-	-	-	-	-	-	-	-
BaO	-	0.50	-	-	-	-	-	-	-
Yb_2O_3	-	0.20	-	-	-	-	-	-	-
Rb_2O	-	-	0.50	-	-	-	-	-	-
Nd_2O_3	-	-	0.20	-	-	-	-	-	-
Tb_2O_3	-	-	-	0.20	-	-	-	-	-
WO_3	-	-	-	0.20	-	-	-	-	-
PbO	-	-	-	-	0.50	-	-	-	-
Dy_2O_3	-	-	-	-	0.20	-	-	-	-
Cs_2O	-	-	-	-	-	0.50	-	-	-
CeO_2	-	-	-	-	-	0.20	-	-	-
Nb_2O_5	-	-	-	-	-	0.20	-	-	-
ZrO_2	-	-	-	-	-	0.10	-	-	-
Cs_2O	-	-	-	-	-	-	0.50	-	-
ZrO_2	-	-	-	-	-	-	0.10	-	-
Nb_2O_5	-	-	-	-	-	-	-	0.20	-
CeO_2	-	-	-	-	-	-	-	0.20	-
Eu_2O_3	-	-	-	-	-	-	-	-	0.20
MoO_3	-	-	-	-	-	-	-	-	0.20
Total	99.40	99.41	99.41	99.40	99.41	99.41	99.40	99.40	99.40

Table 2.3. Bulk composition (weight %) of starting materials (glasses), obtained by EMPA of glasses quenched from melts of the experimental samples .

Sample	**mca**	**MBO**	**MCO**	**MDO**	**M10**	**M20**	**M31**	**M32**
Comp. wt%	5 (pts)	7 (pts)	6 (pts)	6 (pts)	10 (pts)	15 (pts)	10 (pts)	15 (pts)
SiO_2	67.99	69.81	69.54	70.25	70.60	69.06	69.24	69.28
K_2O	4.102	4.71	4.693	4.738	4.792	4.742	4.938	4.713
Na_2O	3.242	3.21	3.530	2.997	3.444	3.494	3.473	2.489
Al_2O_3	15.41	14.70	13.83	13.75	13.86	13.62	14.07	14.96
CaO	1.762	1.82	1.695	1.743	0.182	1.712	1.772	1.875
MgO	1.732	1.43	1.423	1.459	1.993	1.991	2.032	1.985
FeO	3.106	3.60	3.537	3.588	3.507	3.529	3.618	3.699
CuO	**0.480**	**0.46**	-	-	-	-	-	-
ZnO	**0.514**	-	**0.502**	-	-	-	-	-
CoO	**0.502**	-	-	-	-	-	-	-
NiO	**0.465**	-	-	**0.425**	-	-	-	-
TiO_2	**0.525**	-	-	**0.504**	-	-	-	-
V_2O_5	**0.193**	**0.18**	-	-	-	-	-	-
Cr_2O_3	**0.180**	-	**0.190**	-	-	-	-	-
Gd_2O_3	-	-	-	-	**0.212**	-	-	-
Sm_2O_3	-	-	-	-	**0.214**	-	-	-
Ho_2O_3	-	-	-	-	-	**0.202**	-	-
Ta_2O_5	-	-	-	-	-	**0.202**	-	-
SrO	-	-	-	-	-	-	**0.640**	-
La_2O_3	-	-	-	-	-	-	**0.209**	-
Er_2O_3	-	-	-	-	-	-	-	**0.221**
Pr_2O_3	-	-	-	-	-	-	-	**0.233**
Total	100.20	99.91	98.95	99.45	98.80	98.55	99.99	99.46

Table 2.3. Bulk composition of starting materials (glasses) continued…

Sample	M40	M51	M52	M61	M62	M70	M71	M72	M83
Comp. wt%	6 (pts)	5 (pts)	10 (pts)	10 (pts)	10 (pts)	5 (pts)	10 (pts)	10 (pts)	8 (pts)
SiO_2	68.71	69.43	68.43	69.51	69.90	68.26	70.01	70.04	69.39
K_2O	4.730	4.742	4.888	4.766	4.670	4.972	4.769	4.760	4.771
Na_2O	3.607	3.432	3.305	3.633	3.525	3.592	3.323	3.304	3.595
Al_2O_3	13.68	13.74	14.16	13.81	13.81	14.47	13.36	13.90	13.59
CaO	1.745	1.700	1.827	1.723	1.653	1.768	1.732	1.694	1.680
MgO	2.000	2.020	2.204	2.000	1.990	2.050	2.049	1.970	2.055
FeO	3.717	3.526	3.826	3.687	3.489	3.564	3.509	3.483	3.619
Lu_2O_3	**0.216**	-	-	-	-	-	-	-	-
Tm_2O_3	**0.204**	-	-	-	-	-	-	-	-
BaO	-	**0.505**	-	-	-	-	-	-	-
Yb_2O_3	-	**0.214**	-	-	-	-	-	-	-
Rb_2O	-	-	**0.675**	-	-	-	-	-	-
Nd_2O_3	-	-	**0.215**	-	-	-	-	-	-
Tb_2O_3	-	-	-	**0.205**	-	-	-	-	-
WO_3	-	-	-	**0.180**	-	-	-	-	-
PbO	-	-	-	-	**0.456**	-	-	-	-
Dy_2O_3	-	-	-	-	**0.207**	-	-	-	-
Cs_2O	-	-	-	-	-	**0.501**	-	-	-
CeO_2	-	-	-	-	-	**0.227**	-	-	-
Nb_2O_5	-	-	-	-	-	**0.194**	-	-	-
ZrO_2	-	-	-	-	-	**0.297**	-	-	-
Cs_2O	-	-	-	-	-	-	**0.452**	-	-
ZrO_2	-	-	-	-	-	-	**0.434**	-	-
Nb_2O_5	-	-	-	-	-	-	-	**0.144**	-
CeO_2	-	-	-	-	-	-	-	**0.194**	-
Eu_2O_3	-	-	-	-	-	-	-	-	**0.206**
MoO_3	-	-	-	-	-	-	-	-	**0.182**
Total	98.60	99.31	99.54	99.51	99.70	99.89	99.64	99.49	99.09

2.2.2.2. Charge preparation

A tiny quantity of cold doubly distilled water (about 3-5.6µl) was first loaded into an empty sample tube using a micro syringe, taking note of the total weight. This was followed by loading the capsule with about 30-45 mg of the anhydrous glass powder, using a small funnel to direct the sample centrally into the tube and recording the new weight. The open end of the capsule was crimped shut, its edge cut smooth and even, and the weight recorded. The capsule was completely sealed off by arc-welding while suspended in an ice bath and its weight taken. The sealed capsules were tested for possible leakage by checking for weight losses after drying overnight in a low temperature oven at 150°C .

2.2.3. Investigation of run products

Following quench the capsules were cleaned and weighed to check for leaks or gains during the runs. They were then punched with a steel needle and the presence of water recorded. The capsules were put in a low temperature oven at 150°C for a few hours and afterwards reweighed to verify loss of free water. All capsules gained some minor weight during the experiments by the diffusion of Ni-metal from vessels and filler rods into the capsule walls, and in some cases into the capsule contents, causing some of the phases in the run products to suffer detectable contamination by Ni.
The dry capsules, somewhat flattened during the runs, were cut lengthwise along one edge and spread open to expose the run products, a little of which was ground to a fine powder in a mortar and pestle adding a few drops of acetone making a thick wet mixture that was spread uniformly over the surface of a glass slide and dried, in preparation for x-ray powder diffraction.
The rest of the run products were mounted in epoxy or crystal-bond and carefully polished first with a series of aluminium oxide powders of grain sizes ranging from 400–3 μm and subsequently with a series of diamond pastes of sizes 6–1 μm. The aim was to obtain high-quality polished surfaces of samples that would yield abundant information during subsequent qualitative and quantitative analytical methods of phase identification. Maximum care and attention plus through cleanliness was demanded and exercised at all stages of the sample polishing process.
The polished sections were washed clean in ethanol and distilled water and dried in preparation for reflected light microscopy, Raman spectroscopy and electron microprobe analysis.

2.2.3.1. Phase identification

A combination of methods including reflected light microscopy, x-ray powder diffractometry, Raman spectrometry and electron microprobe analysis was used for phase identification.

2.2.3.2. Reflected-light microscopy

Polished sections were examined with a standard reflected-light microscope to identify the phases available in the samples. Each phase exhibits a variety of characteristic properties that can be studied using the microscope using either the polarizer alone or with both the polarizer and analyser inserted. Properties studied using plane polarized light included colour, reflectance, bireflectance and reflection pleochroism, whereas anisotropism and internal reflections were observed under crossed polars.

The quality of polishing, including scratch and hardness of every phase, were rapidly and qualitatively examined under the microscope. Other properties studied were the structural and morphological form of each phase. This involves crystal form and habit, cleavage and twinning. With experience, all mineral products could be identified using reflected-light microscopy. To confirm the identifications achieved with the reflected-light microscope other quantitative methods including x-ray powder diffraction and electron microprobe analysis were subsequently employed.

2.2.3.3. X- ray powder diffractometry

This method is based on the phenomenon (by Max von Laue) that the wavelengths of x-rays and the lattice parameters of crystals are of the same order of magnitude and that x-rays are diffracted by crystal lattices. The instrument used was an x-ray powder diffractometer (Philips PW 1050/25 at the University of Tuebingen) equipped with a sensitive position detector and a curved germanium monochromator in Debye-Scherrer geometry. The diffractometer, consists of a goniometer (to measure the angular location in terms of 2θ for a diffraction peak), an x-ray counting device (for measuring of peak intensity), and an electronic readout system (see **Figure 2.3** and **2.4**).
The sample was prepared by grinding to a fine powder, which was then spread uniformly over the surface of a glass slide and left to dry in air.
The instrument is so constructed that, when clamped in place, the sample rotates in the path of a collimated x-ray beam while an x-ray detector, mounted on an arm, rotates about it to pick up the diffracted x-ray signals. When the instrument is set at the zero position, the x-ray beam is parallel to the base of the sample holder and passes directly into the x-ray detector. The slide mount and the counter are driven by a motor through separate gear trains such that, when the sample rotates an angle θ, the detector rotates through 2θ.

If the specimen has been properly prepared there will be thousands of tiny crystalline particles in random orientation. All possible reflections from atomic planes take place simultaneously and the x-ray detector maintains an appropriate geometrical relationship to receive each diffraction maximum separately. In practice, the sample, the x-ray detector and the reading device are activated simultaneously. If an atomic plane has an interplanar spacing (d) such that a reflection occurs at θ, there will be no evidence of this reflection until the counting tube has been rotated through 2θ. At this point the diffracted beam enters the x-ray detector, causing it to respond. The pulse thus generated is amplified and causes an electronic response on a vertical scale that represents the peak height. The angle 2θ at which the diffraction occurs is read on a horizontal scale. The heights of the peaks are directly proportional to the intensities of the diffraction effects. The 2θ positions of the diffraction peaks are tabulated by an online computer and the interplanar spacing giving rise to them are calculated using Bragg's law equation:

$$n\lambda = 2d \sin \theta \qquad (2.2)$$

where n = 1,2,3,… These are known as the first-, second-, third-order, etc., reflections and λ is the wavelength of the characteristic x-radiation.

Phase identification begins once a diffractometer tracing has been completed. This is a chart obtained over a 2θ region of about 6° to 80°, during a period of 45 minutes. The diffraction peaks are tabulated in a sequence of decreasing interplanar spacings (d), together with their relative intensities. Using a computer search technique (searching for comparable or identical diffraction patterns on the basis of the strongest lines or the largest interplanar spacings), the diffraction pattern of an unknown can be compared with records stored in the Powder Diffraction File (PDF) published by the International Centre for Diffraction Data (ICDD).

At least three 2θ values of the most intense peaks on the graph need be converted into d-values (see Table in appendix for the record of measurement). A variety of computer-

search programmes are available for indexing the planes using PDF Data. The analytical data is digitally processed by smoothing the diffractogram, making the underground corrections, removing the K-peaks, and doing the peak-search automatically. X-ray powder diffractometry was carried out on a number of samples prepared from run products obtained at different experimental temperatures to observe the effect of temperature on the development/intensities of the phases.

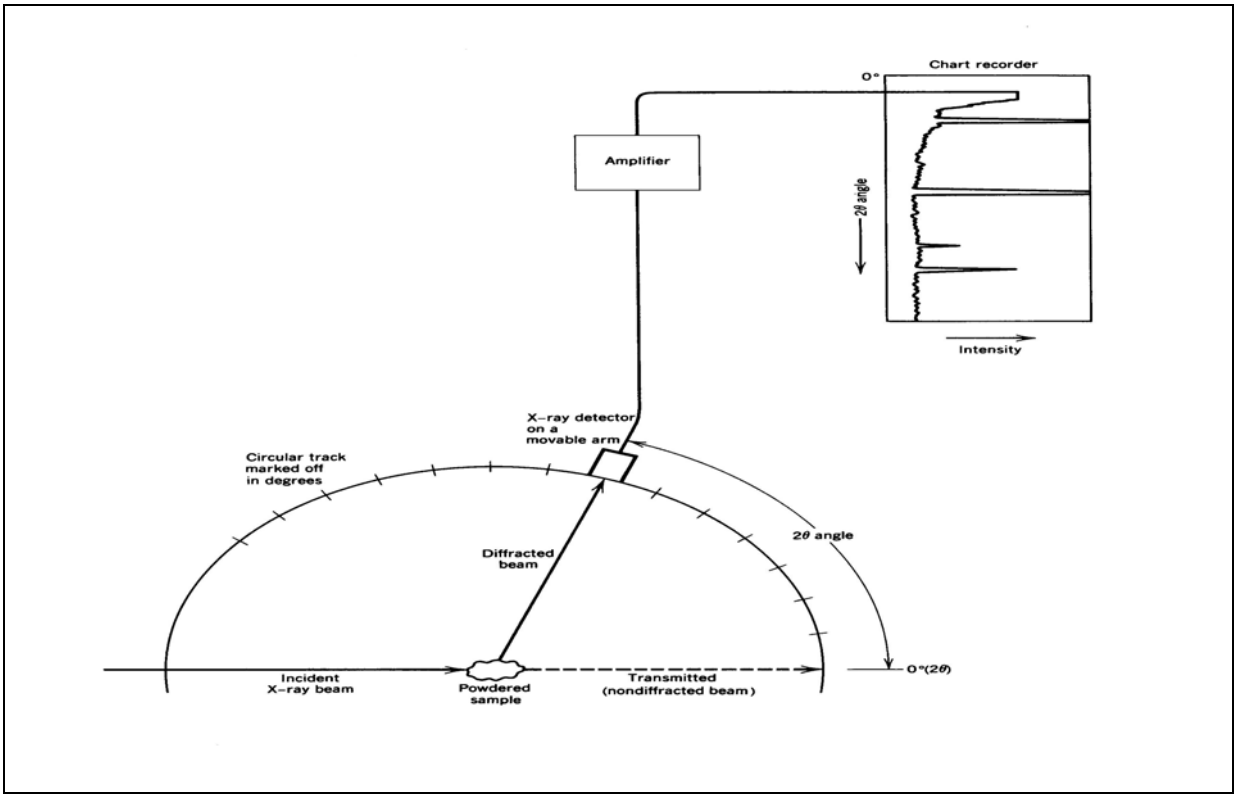

Fig.2.4. Schematic diagram showing some of the experimental configuration of an x-ray powder diffractometer.

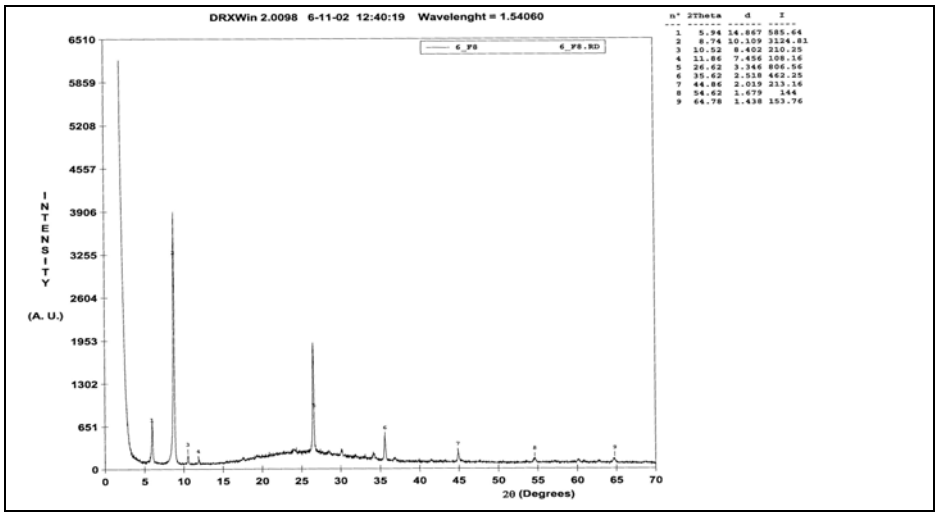

Fig. 2.5. A diffractometer tracing for the unknown that is to be identified. The x-ray radiation was produced by a Cu-target x-ray tube.

2.2.3.4. Electron microprobe analysis (EMPA)

Polished sections of the starting materials and run-products were carefully carbon coated in preparation for electron microprobe analysis. Anhydrous glasses from samples of the starting materials and hydrous residual glasses and crystalline phases from samples of run-products were analysed for wt% of their major and trace element oxides with a JEOL 8900 electron microprobe instrument at Tuebingen University and a JEOL 8200 at the Bayerisches Geoinstitut of the University of Bayreuth. To analyse both the anhydrous and hydrated residual glasses an accelerating voltage of 20 kV and a beam current of 70 nA with a probe-diameter of 20 µm was used. To minimize alkali volatility in these glasses counting times were reduced to 6 s on peak and 3 s on background for Na. At each spot of analysis the elements Na, K, and Al were analysed first to prevent beam-induced element migration effect (Morgan and London 1996). For the analysis of crystalline phases a focused beam, however, with the same conditions of accelerating voltage and beam-current as for glasses were used. The counting time for Na in crystalline phases was increased to 30 s for peak and 15 s for background. The other the elements experienced similar counting times for both glass and crystalline phases ranging from 30 s to 180 s for trace elements. Major elements were analysed with 30 s for peaks and 15 s for background. The analysis utilized synthetic crystalline and glass standards with TAP, PET, and LIF as the analysing crystals (see **Table 2.4**, for a complete list of standards and analysing conditions used for calibrating all the elements concerned). A few images of some experimental run-products of some samples were acquired using both backscattered and secondary electron signals.

Table 2.4. Standardization procedure used for electron microprobe analysis. BG and P stands for the time required for background and peak counts in seconds, respectively.

WDS CRYSTAL CONFIGURATION: 20 kV & 70 nA

Element	Crystal	Counting time		Standard	Element	Crystal	Counting time		Standard
		P	BG				P	BG	
Al	TAP	30	15	Plagioclase	Nb	PET	60	30	Li2Nb2O6
Na	TAP	30	15	Albite	Mo	PET	60	30	Mo (metal)
K	PET	30	15	Sanidine	Ta	LIF	60	30	Li2Ta2O6
Fe	LIF	30	15	Hematite	W	LIF	60	30	CaWO4
Si	TAP	30	15	Sanidine	Pb	LIF	60	30	Pb (metal)
Mg	TAP	30	15	Periclase	La	LIF	180	60	REE-La (gls)
Ca	PET	30	15	Bustamite	Ce	LIF	180	60	REE-Ce (gls)
Sr	TAP	60	30	SrTiO3	Pr	LIF	180	60	REE-Pr (gls)
Ba	PET	60	30	BaSO4	Nd	LIF	180	60	REE-Nd (gls)
Ti	PET	60	30	SrTiO3	Sm	LIF	180	60	REE-Sm (gls)
V	PET	120	60	V (metal)	Eu	LIF	180	60	REE-Eu (gls)
Cr	LIF	120	60	Cr (metal)	Gd	LIF	180	60	REE-Gd (gls)
Co	LIF	60	30	Co (metal)	Tb	LIF	180	60	REE-Tb (gls)
Ni	LIF	60	30	Ni (metal)	Dy	LIF	180	60	REE-Dy (gls)
Cu	LIF	120	60	Cu (metal)	Ho	LIF	180	60	REE-Ho (gls)
Zn	LIF	120	60	Zn (metal)	Er	LIF	180	60	REE-Er (gls)
Rb	PET	60	30	Pollucite	Tm	LIF	180	60	REE-Tm (gls)
Cs	PET	60	30	Pollucite	Yb	LIF	180	60	REE-Yb (gls)
Zr	PET	60	30	ZrO2	Lu	LIF	180	60	REE-Lu (gls)

2.2.3.5. Raman Spectroscopy

Raman spectroscopy was carried out at the University of Tuebingen on samples M32, M52, and M70 with an unusual phase that could not be otherwise identified. The equipment used was a LABRAN2 spectrometer equipped with a Peltier-cooled CCD detector and an optical microscope. An external Ar-laser with a frequency of 514 nm and He-Ne-laser with a frequency of 632.8 nm together with the software LabSpec **RXv2.08** were used for sample measurement. The spectra obtained from the unknown phase in the study samples were then compared with many other spetra from known mineral phases. The unknown phase was later identified to be allanite.

2.3. Experimental results

2.3.1. Phase assemblages

All experimental runs yielded homogeneous crystal phases and quenched melts. Major phases recognised in the run-charges include glass, biotite, amphibole (hornblende), pyroxene (clino-pyroxene), plagioclase, together with magnetite and allanite, as minor phases observed in some charges. As run-products these phases have been listed, for every charge, in the general results **Tables 2.11**, along with the biotite-melt partition coefficients for the trace elements (see section 2.3.2). The homogeneity of the phases, as assessed from the EMPA results' consistency, together with the regularity of the crystal-shapes, is an important indication for chemical equilibrium to have been established between the crystalline phases and the melts. In a few cases line profiles were measured across some large amphibole crystals and glass to determine the degree of chemical zoning, with the result that both phases are homogeneous and therefore in chemical equilibrium with one another.

2.3.1.1. Biotite

Biotite, the target phase of study for this project, was the dominant crystalline phase produced in all experimental runs. The biotites crystallised in these run charges contained Ni substituting for Mg and had an approximate composition: $(K_{0.7}Na_{0.1}Ca_{0.02})(Mg_{1.2}Fe_{0.6}Al_{0.6}Ni_{0.2})(Si_{3.4}Al_{0.6})O_{10}(OH)_2$. In most cases the crystals appear as thin platelets, which look like fibres, when cut across by polishing, occupying clearly outlined fields in the sample. The largest micas, about 5-8 μm width, could occasionally be observed in some charges whose run-temperatures ranged between 750-800°C. Lower temperature charges (700-750°C) produced biotite platelets or grains that are extremely tiny and could only be analysed with difficulty. Biotite was thoroughly analysed for its major and minor element composition, the results of which, together with those of coexisting glass analysis, have been used to calculate the partition coefficients for the trace elements which enter its crystal structure. **Figures 2.5a** and **b** are backscattered electron images of typical run-products (biotite and glass) and Table 2.5 lists the major-element oxide compositions of biotite, including its formula. Both quenched melts (glass) and biotite appear to be homogeneous within the accuracy of the electron microprobe analysis.
Results of x-ray diffraction analysis (see **Figure 2.6**) confirm the presence and predominance of the biotite phase in the samples at all experimental temperatures, with reflection peak positions at (001), (003), and (004). The reflections at (001) and (004) positions have highest and lowest intensities, respectively. Normally biotite reflects at several positions whose peaks could not be seen in this pattern as the samples seem to be strongly textured.

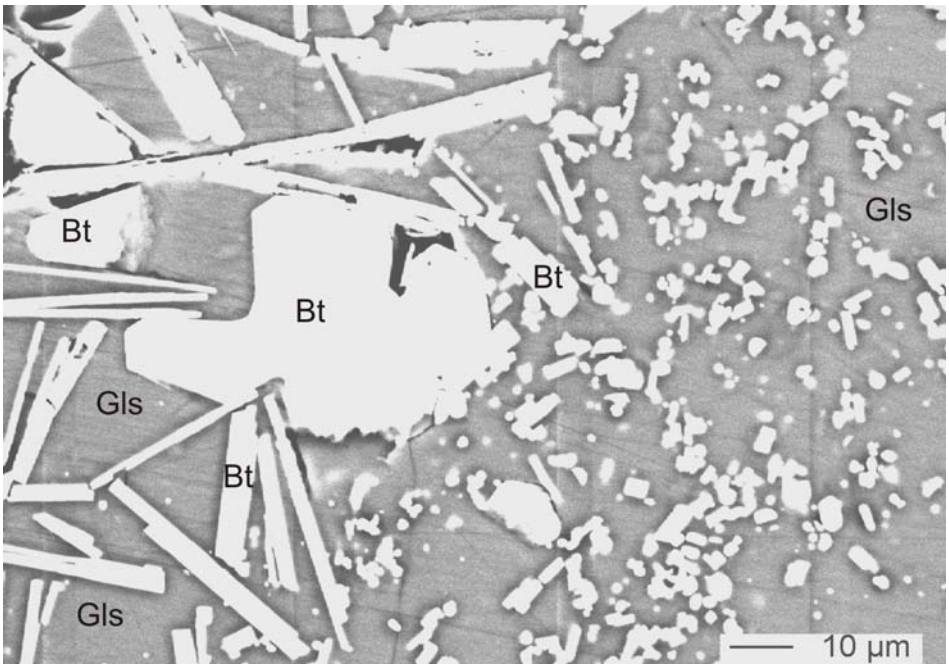

Fig. 2.6(a) Back-scattered electron image of a run-product of the crystal/melt partitioning experiment No. 25/800/MB0 at 2 kbar, 800°C and H_2O-saturated conditions for charge MB0. The large white crystals (centre left), including the long and short prismatic crystals are biotite (**Bt**) coexisting with glass (**Gls**). Note the cracks seen in the glass phase are caused by quenching of the sample.

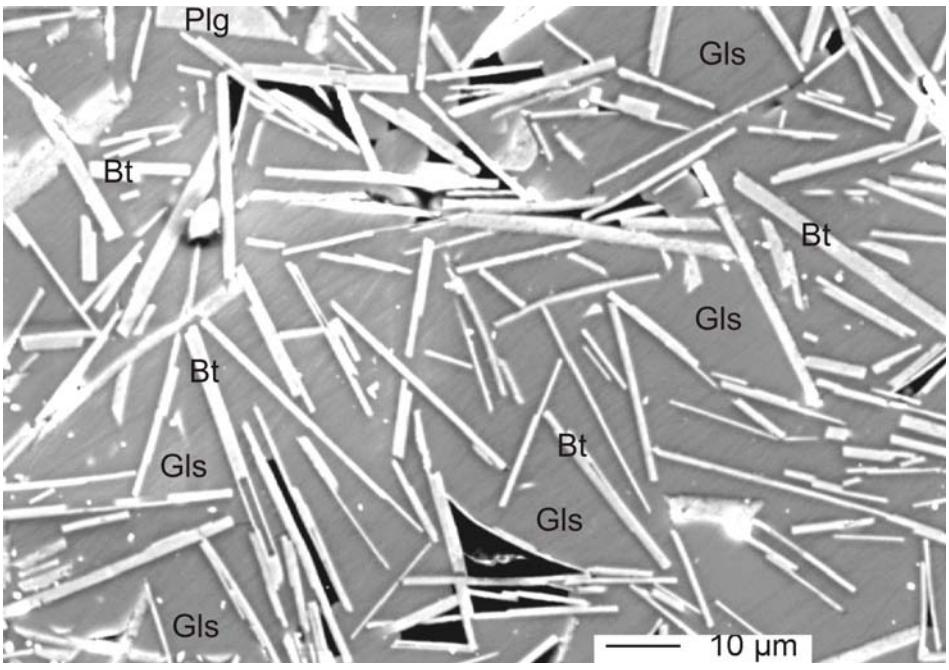

Fig. 2.6(b) Back-scattered electron image of a run-product of the crystal/melt partitioning experiment No. 32/800/M10 at 2 kbar, 800°C and H_2O-saturated conditions for charge M10. The long subhedral white crystals, including the short prismatic crystals are biotite (**Bt**) coexisting with glass (**Gls**). Top left is a plagioclase (**Plg**) grain, angular and light grayish filled with white bright inclusions of magnetite.

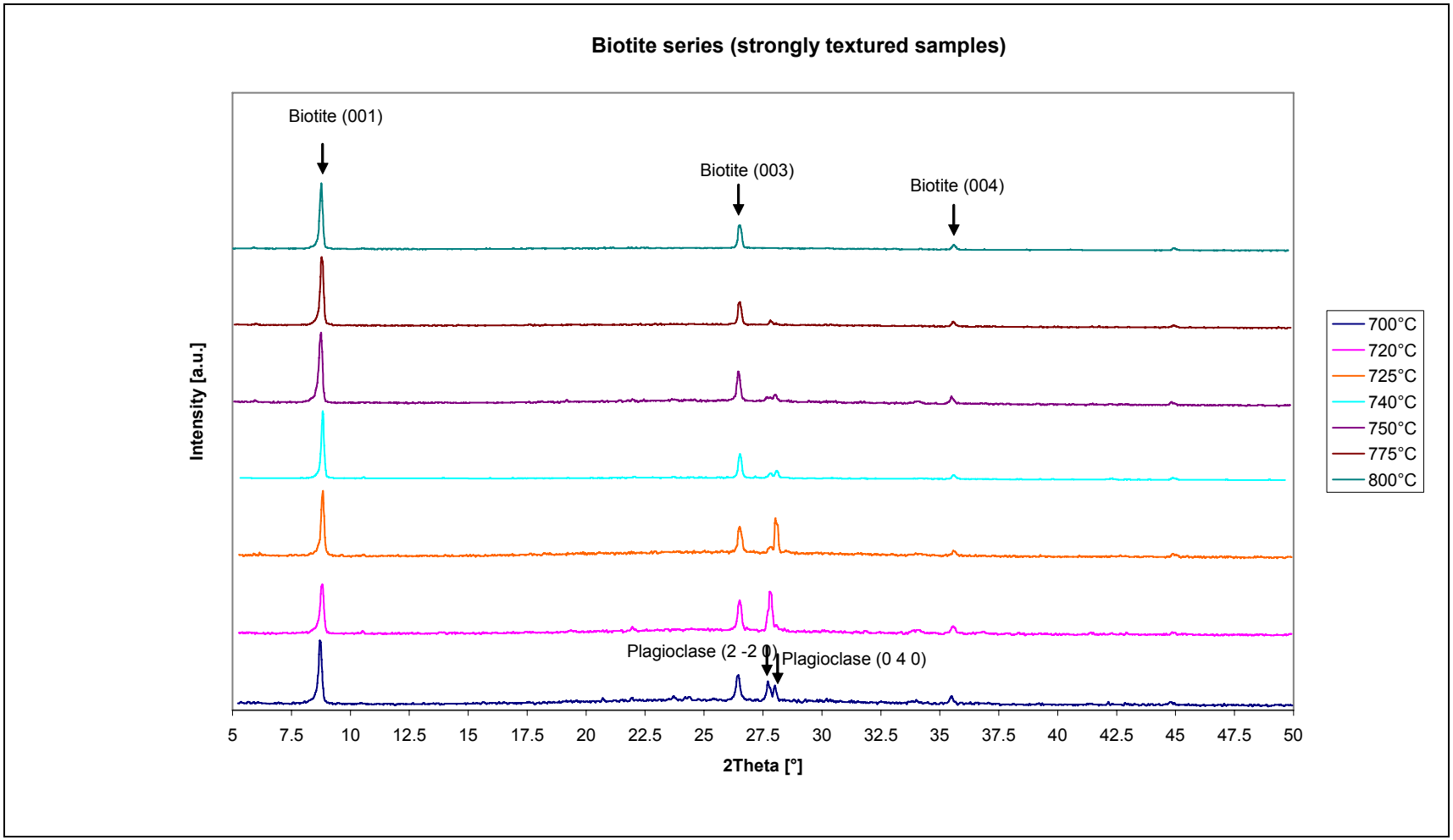

Fig. 2.7. XRD pattern for run-products at different temperatures. Peak positions 001, 003, and 004 are due to reflections from biotite. The reflection intensities decrease with increasing 2θ, i.e. 001 > 003 > 004. Temperature apparently has no effect on the biotite peak intensities. Peak positions (2 -2 0) and (0 4 0) are due reflections from plagioclase. The two peaks are resolved into one (0 4 0) whose intensity decrease with increasing temperatures. Analysis was carried out using a Philips PW 1050/25 automated x-ray diffraction system with 40 kV and 20mA. Cu Kα radiation with a tep size of 0.05° 2θ and a scan rate of 0.05°/4 sec was used for the analysis.

2.3.1.2. Allanite

Allanite was exclusively found in charges with the rare-earth elements, cerium, praseodymium, and neodymium, in charges that were run at 750-800°C. Its approximate composition reveals that it contains no Al in its tetrahedral site: $(Ca_{1.0}Nd_{0.8}K_{0.004}Na_{0.003})(Al_{1.6}Fe_{1.0}AMg_{0.4})(Si_{3.0}O_{12})(OH)$. The phase could clearly be observed under the microscope and in back-scattered electron images as large euhedral crystals, some larger than 100 µm in width. The oxide weight percent concentrations of some trace REEs in allanite were analysed at around 26 wt%, as seen from the results of chemical analysis (EMPA) for run products of samples M70, M32, and M52. It was also observed that in these charges, where allanite existed very little or no amphiboles were crystallised (see **Figure 2.7** and **Table 2.6**).

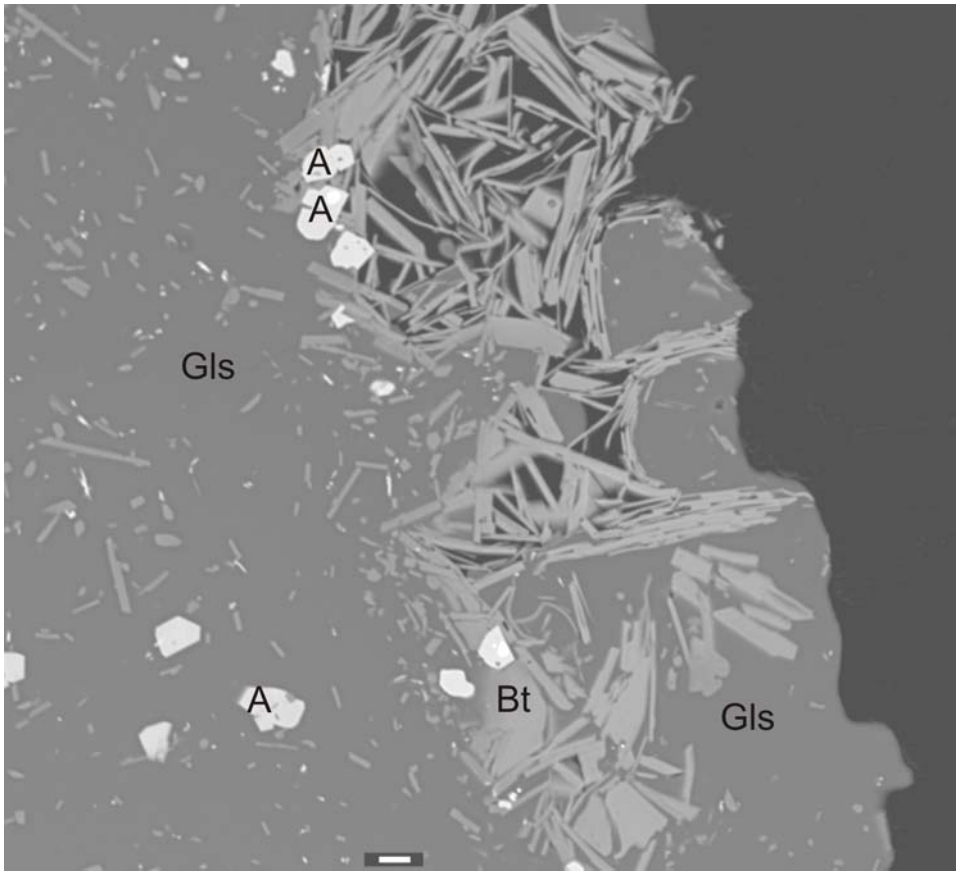

Fig. 2.8. Back-scattered electron image of a run-product of the crystal/melt partitioning experiment No. 70/800/M32 at 2 kbar, 800°C and H_2O-saturated conditions for charge M32. The white grains labelled **A** is allanite and its inclusions are magnetite crystal grains. **Bt** is biotite and **Gls** is glass. The scale bar is equivalent to 10 µm.

2.3.1.3. Amphibole

Amphibole of the hornblende type was found in all charges except those which contain allanite. The amphibole crystals are large and euhedral and contain a significant proportion of Al in the tetrahedral site. It has an approximate composition: $(Na_{0.4}K_{0.1})(Ca_{1.7}Fe_{0.3})(Mg_{3.3}Fe_{1.3}Al_{0.4})(Si_{7.0}Al_{1.0})O_{22}(OH)_2$. It formed in all sample charges ran under any given experimental conditions of temperature and pressure. The quantities produced in a given charge, however, decreased with decreasing temperature (see **Figure 2.8** and **Table 2.7**).

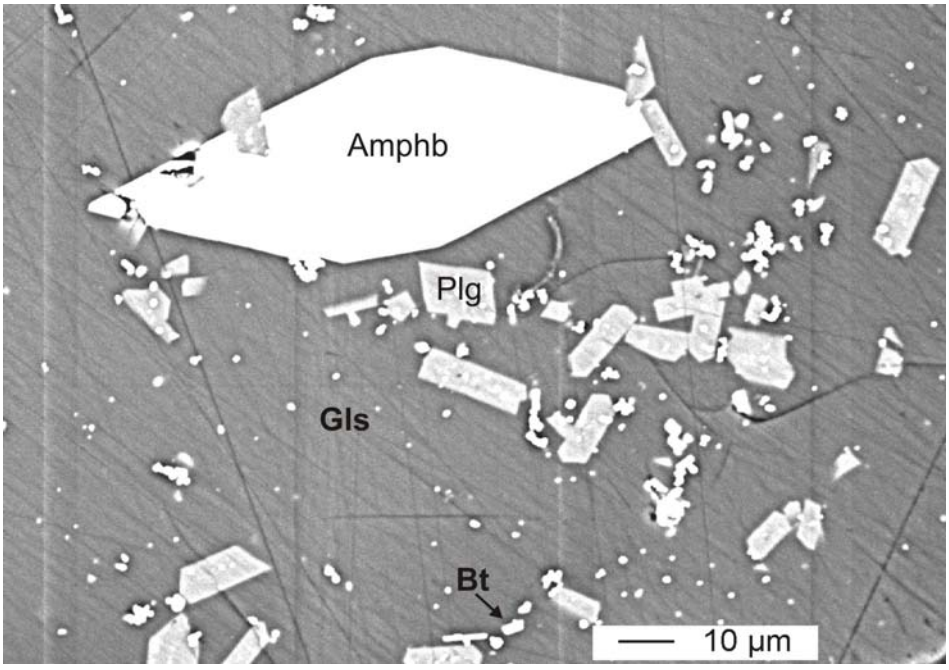

Fig. 2.9. Back-scattered electron image of a run-product from the crystal/melt partitioning experiment No. 30/800/M72 at 2 kbar, 800°C and H_2O-saturated conditions for charge M72. Note that the large amphibole (**Amphb**) crystal (white, upper-centre) is equant or euhedral and free of inclusions. Plagioclase (**Plg**) crystals (light gray) are also equant but often skeletal and inclusion-rich. Glass (**Gls**) is dark gray and bubble-free. The small white and lath-like grains spread all over the image are biotite and magnetite crystals. Magnetite and sometimes biotite grains appear as inclusions in the larger plagioclase crystals. Note that cracks in glass were caused by quenching.

2.3.1.4. Pyroxene

Pyroxenes found in the charges contained a high amount of Ca, with the general composition: $(Ca_{0.8}Na_{0.04}K_{0.02}Fe_{0.2})(Mg_{0.7}Al_{0.1}Fe_{0.2})(Si_2O_6)$. They are, therefore, clino-pyroxenes. They appeared in all charges, as thick euhedral crystals at high temperatures (800-750°C), and as thin long needles at lower temperatures. Their amount or volume content in the run-product decreased with decreasing temperature (see **Figure 2.9** and **Table 2.8**).

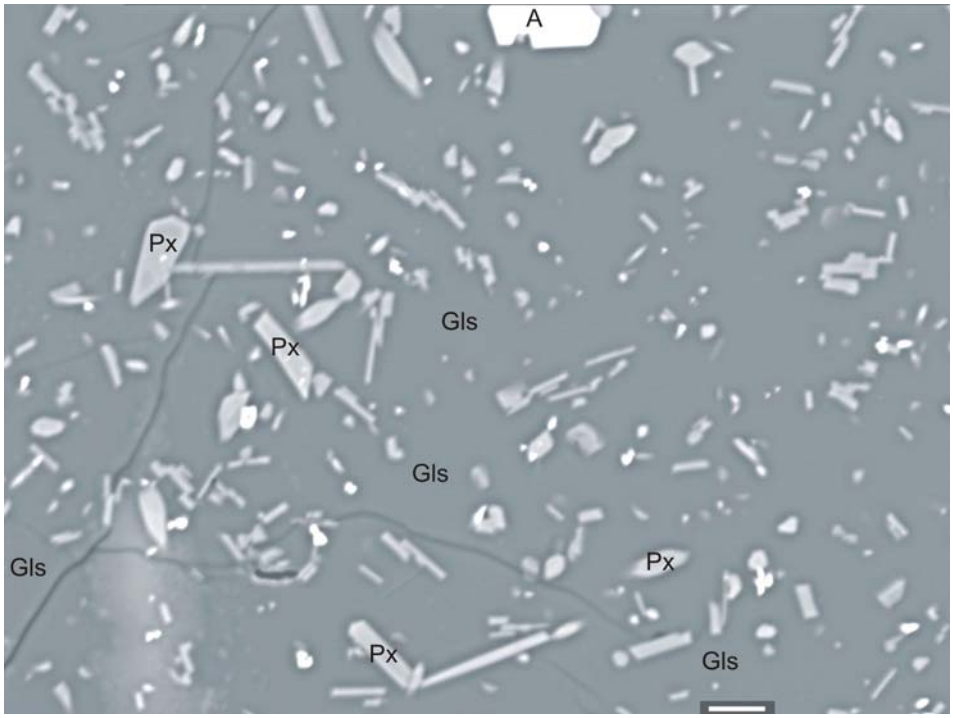

Fig. 2.10. Back-scattered electron image of a run-product from the crystal/melt partitioning experiment No. 38/800/M70 at 2 kbar, 800°C and H_2O-saturated conditions for charge M70. Note that the large pyroxene (**Px**) crystals (light gray) are sub-equant, and often inclusion-free whereas the large allanite (**A)** crystal (white, upper centre) is equant or euhedral. Glass (**Gls**) is dark gray and bubble-free. The small white grains spread all over the image are magnetite crystals.

2.3.1.5 Feldspars

Feldspars of the plagioclase type were observed in all run-products, appearing as large finger-like clusters disseminated throughout the sample. Their approximate composition is: $(Na_{0.6}Ca_{0.4})(Al_{1.3}Si_{2.7})O_8$. The crystals were all large and measurable at any experimental temperature conditions. This phase seem to occupy larger volumes of the sample charge at lower temperatures, making it difficult to find glass (residual melt) fields of analytical size (see **Figure 2.10** and **Table 2.9**).

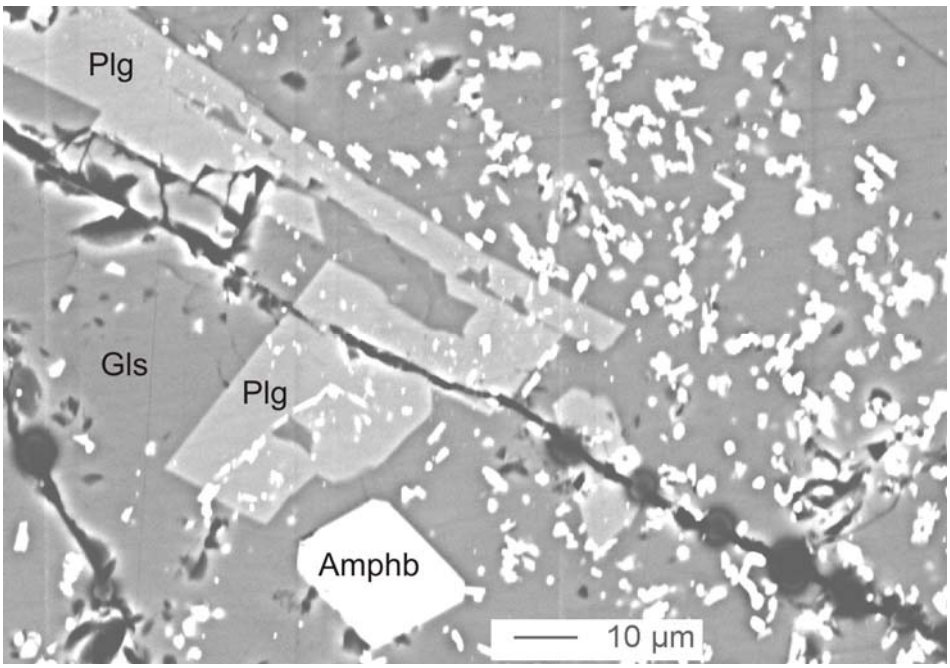

Fig. 2.11. Back-scattered electron image of a run-product from the crystal/melt partitioning experiment No. 65/800/M40 at 2 kbar, 800°C and H_2O-saturated conditions for charge M40. Note that the large plagioclase (**Plg**) crystal (light gray, centre upper left) is sub-equant, often skeletal and inclusion-rich whereas the large amphibole (**Amphb**) crystal (white, bottom centre) is equant or euhedral and free of inclusions. Glass (**Gls**) is medium gray and often containing bubbles and small fractures (dark irregular spots). The small white and lath-like grains spread all over the image are biotite crystals. Biotite and glass sometimes appear as inclusions in the large plagioclase crystals.

2.3.1.6. Magnetite

Magnetite was the only single accessory mineral that seem to have grown in all run charges at high temperatures. Its approximate composition is as follows: $(Fe_{0.85}Mg_{0.07}K_{0.004}Ca_{0.002}Na_{0.002})O(Fe_{1.9}Al_{0.14}Si_{0.01})O_3$. Its volume-fraction in the melt, however, decreased with decreasing temperatures. The magnetite grains appeared to be white, irregular in shape and highly reflecting as observed in the BSE image (see **Figure 2.11** and **Table 2.10**).

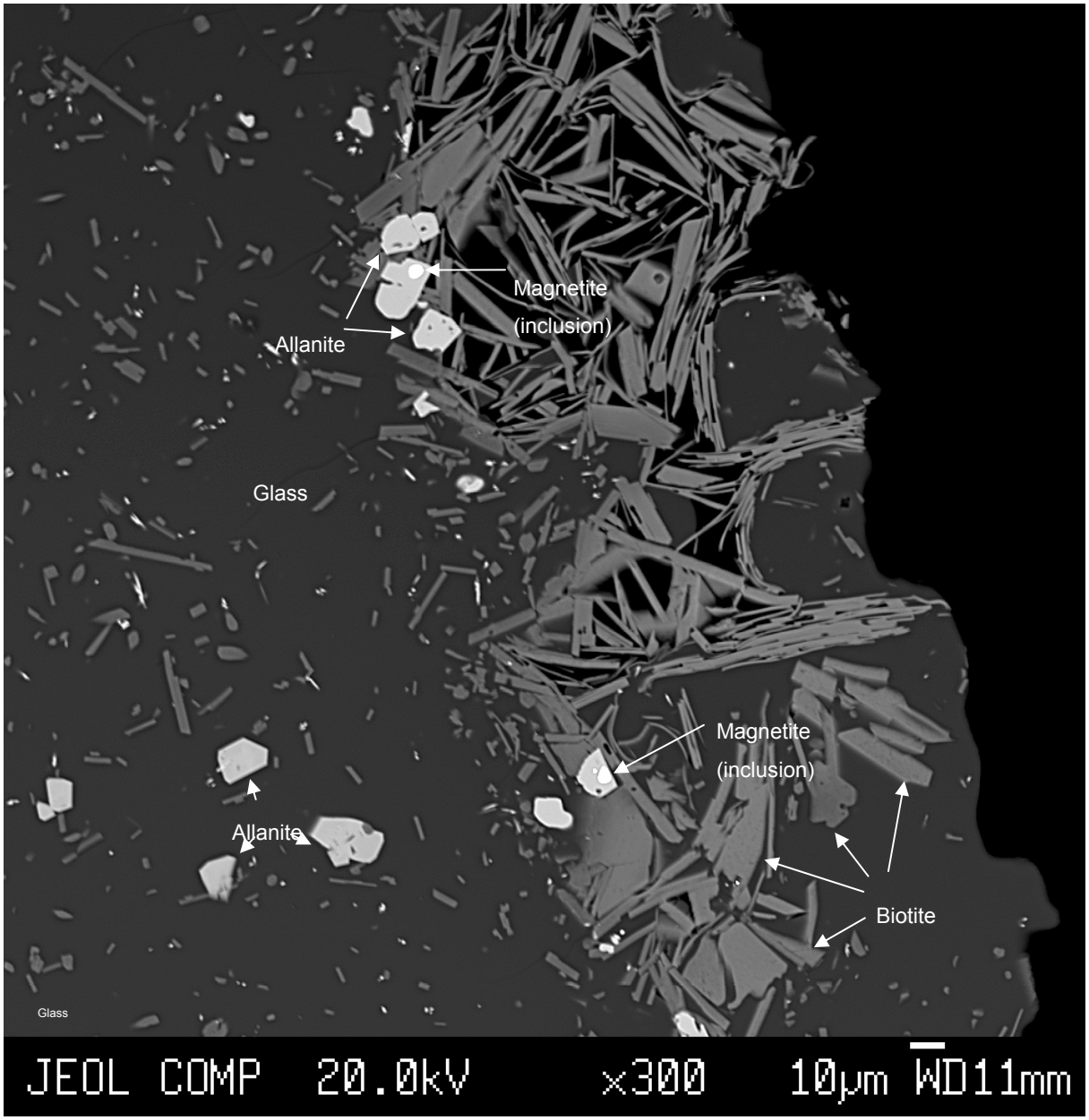

Fig. 2.12. Back-scattered electron image of a run-product of the crystal/melt partitioning experiment No. 70/800/M32 at 2 kbar, 800°C and H_2O-saturated conditions for charge M32. The light gray phase is allanite and its white inclusions are magnetite. The dark gray phase is biotite and the black phase is glass. The scale bar is 10 μm.

Table 2.5. EMPA average composition and formula of biotite.

Exp.No.	Al_2O_3	Na_2O	K_2O	FeO	SiO_2	MgO	CaO	NiO	Total	formula
M32/Bt**1**	16.02	0.587	7.98	10.99	44.28	16.36	0.267	0.09	96.57	$(K_{0.72}Na_{0.08}Ca_{0.02})(Mg_{1.71}Fe_{0.65}Al_{0.44}Ni_{0.01})(Al_{0.89}Si_{3.11})O_{10}(OH)_2$
M51/Bt**2**	14.75	0.644	7.65	11.85	44.62	16.23	0.204	0.84	96.80	$(K_{0.69}Na_{0.09}Ca_{0.02})(Mg_{1.71}Fe_{0.70}Al_{0.38}Ni_{0.05})(Al_{0.85}Si_{3.15})O_{10}(OH)_2$
M83/Bt**3**	14.68	0.653	8.00	14.85	43.98	12.91	0.143	1.47	96.69	$(K_{0.74}Na_{0.09}Ca_{0.01})(Mg_{1.39}Fe_{0.89}Al_{0.42}Ni_{0.09})(Al_{0.83}Si_{3.17})O_{10}(OH)_2$
M32/Bt**4**	14.88	0.551	7.75	10.83	44.72	15.56	0.197	1.71	96.19	$(K_{0.70}Na_{0.08}Ca_{0.01})(Mg_{1.65}Fe_{0.64}Al_{0.41}Ni_{0.10})(Al_{0.83}Si_{3.17})O_{10}(OH)_2$
M40/Bt**5**	15.17	0.548	7.41	12.26	43.42	13.75	0.388	1.85	94.79	$(K_{0.69}Na_{0.08}Ca_{0.03})(Mg_{1.49}Fe_{0.74}Al_{0.45}Ni_{0.11})(Al_{0.85}Si_{3.15})O_{10}(OH)_2$
M62/Bt**6**	14.40	0.678	7.62	12.28	44.32	13.43	0.205	2.70	95.62	$(K_{0.70}Na_{0.09}Ca_{0.02})(Mg_{1.45}Fe_{0.74}Al_{0.43}Ni_{0.16})(Al_{0.80}Si_{3.20})O_{10}(OH)_2$
MC0/Bt**7**	15.01	0.599	7.49	12.32	46.49	11.75	0.334	2.77	96.75	$(K_{0.68}Na_{0.08}Ca_{0.03})(Mg_{1.24}Fe_{0.73}Al_{0.54}Ni_{0.16})(Al_{0.71}Si_{3.29})O_{10}(OH)_2$
M52/Bt**8**	13.88	0.663	8.60	11.72	42.08	12.83	0.154	4.91	94.82	$(K_{0.82}Na_{0.10}Ca_{0.01})(Mg_{1.42}Fe_{0.73}Al_{0.35}Ni_{0.29})(Al_{0.87}Si_{3.13})O_{10}(OH)_2$
M20/Bt**9**	14.35	0.696	7.70	12.09	40.16	13.45	0.053	6.48	94.97	$(K_{0.74}Na_{0.10}Ca_{0.004})(Mg_{1.50}Fe_{0.76}Al_{0.28}Ni_{0.39})(Al_{0.99}Si_{3.01})O_{10}(OH)_2$
M61/Bt**10**	14.87	0.774	7.47	11.49	42.05	11.44	0.172	7.28	95.55	$(K_{0.71}Na_{0.11}Ca_{0.01})(Mg_{1.26}Fe_{0.71}Al_{0.41}Ni_{0.43})(Al_{0.89}Si_{3.11})O_{10}(OH)_2$
M70/Bt**11**	15.00	0.601	8.29	10.40	40.10	13.27	0.079	8.17	95.90	$(K_{0.79}Na_{0.09}Ca_{0.01})(Mg_{1.47}Fe_{0.65}Al_{0.31}Ni_{0.49})(Al_{1.01}Si_{2.99})O_{10}(OH)_2$
MD0/Bt**12**	15.73	0.625	8.38	9.62	38.12	12.77	0.025	8.71	93.98	$(K_{0.82}Na_{0.09}Ca_{0.002})(Mg_{1.45}Fe_{0.61}Al_{0.33}Ni_{0.53})(Al_{1.09}Si_{2.91})O_{10}(OH)_2$
M72/Bt**13**	14.01	0.727	7.50	9.28	43.12	10.51	0.154	9.96	95.26	$(K_{0.71}Na_{0.10}Ca_{0.01})(Mg_{1.16}Fe_{0.58}Al_{0.43}Ni_{0.60})(Al_{0.80}Si_{3.20})O_{10}(OH)_2$
M10/Bt**14**	15.69	0.869	7.17	10.59	40.37	9.98	0.016	10.42	95.10	$(K_{0.69}Na_{0.13}Ca_{0.001})(Mg_{1.12}Fe_{0.67}Al_{0.43}Ni_{0.63})(Al_{0.96}Si_{3.04})O_{10}(OH)_2$
M31/Bt**15**	15.10	0.882	6.92	9.43	42.71	7.98	0.129	10.58	93.73	$(K_{0.67}Na_{0.13}Ca_{0.01})(Mg_{0.90}Fe_{0.59}Al_{0.56}Ni_{0.64})(Al_{0.78}Si_{3.22})O_{10}(OH)_2$
MB0/Bt**16**	15.20	0.651	7.61	10.47	40.54	9.22	0.019	13.51	97.22	$(K_{0.73}Na_{0.09}Ca_{0.002})(Mg_{1.03}Fe_{0.66}Al_{0.38}Ni_{0.81})(Al_{0.96}Si_{3.04})O_{10}(OH)_2$

Table 2.6. EMPA Average composition and formula of allanite.

Exp.No.	Al_2O_3	Na_2O	K_2O	FeO	SiO_2	MgO	CaO	Er_2O_3	Pr_2O_3	Total	Formula
M32/ALNIT1	14.89	0.050	0.155	13.46	33.02	2.92	9.52	2.49	25.94	102.45	$(Ca_{0.92}Pr_{0.85}Er_{0.07}K_{0.02}Na_{0.01})(Al_{1.57}Fe_{1.01}Mg_{0.39})(Si_{2.96}O_{12})(OH)$
Exp.No.	**Al_2O_3**	**Na_2O**	**K_2O**	**FeO**	**SiO_2**	**MgO**	**CaO**	**Rb_2O**	**Nd_2O_3**	**Total**	
M52/ALNIT2	15.25	0.019	0.038	12.42	33.01	2.58	10.23	0.00	25.53	99.08	$(Ca_{1.00}Nd_{0.83}K_{0.004}Na_{0.003})(Al_{1.64}Fe_{0.95}Mg_{0.35})(Si_{3.01}O_{12})(OH)$
Exp.No.	**Al_2O_3**	**Na_2O**	**K_2O**	**FeO**	**SiO_2**	**MgO**	**CaO**	**Cs_2O**	**Ce_2O_3**	**Total**	
M70/ALNIT3	16.58	0.043	0.139	12.90	33.43	2.217	9.86	0.496	26.12	101.79	$(Ca_{0.94}Ce_{0.85}Cs_{0.02}K_{0.02}Na_{0.01})(Al_{1.73}Fe_{0.96}Mg_{0.29})(Si_{2.97}O_{12})(OH)$

Table 2.7. EMPA average composition and formula of amphibole

Exp.No.	Al_2O_3	Na_2O	K_2O	FeO	SiO_2	MgO	CaO	Total	formula
M20/AMPHB1	8.765	1.542	0.589	13.928	46.755	14.288	10.913	96.78	$(Na_{0.44}K_{0.11})(Ca_{1.73}Fe_{0.32})(Mg_{3.15}Fe_{1.40}Al_{0.45})(Al_{1.08}Si_{6.92})O_{22}(OH)_2$
M32/AMPHB2	7.634	1.343	0.507	12.749	47.628	15.870	11.060	96.79	$(Na_{0.38}K_{0.10})(Ca_{1.74}Fe_{0.37})(Mg_{3.48}Fe_{1.20}Al_{0.32})(Al_{1.00}Si_{7.00})O_{22}(OH)_2$
M40/AMPHB3	8.036	1.411	0.520	12.915	47.652	15.163	10.918	96.61	$(Na_{0.40}K_{0.10})(Ca_{1.72}Fe_{0.32})(Mg_{3.33}Fe_{1.27}Al_{0.40})(Al_{0.99}Si_{7.01})O_{22}(OH)_2$
M51/AMPHB4	7.646	1.359	0.569	12.524	48.412	15.510	10.961	96.98	$(Na_{0.39}K_{0.11})(Ca_{1.72}Fe_{0.31})(Mg_{3.38}Fe_{1.22}Al_{0.40})(Al_{0.92}Si_{7.08})O_{22}(OH)_2$
M61/AMPHB5	8.599	1.520	0.575	13.257	46.658	15.228	10.838	96.68	$(Na_{0.44}K_{0.11})(Ca_{1.72}Fe_{0.38})(Mg_{3.35}Fe_{1.26}Al_{0.39})(Al_{1.11}Si_{6.89})O_{22}(OH)_2$
M62/AMPHB6	8.142	1.436	0.510	14.508	47.312	14.747	10.484	97.14	$(Na_{0.41}K_{0.10})(Ca_{1.66}Fe_{0.41})(Mg_{3.24}Fe_{1.40}Al_{0.38})(Al_{1.03}Si_{6.97})O_{22}(OH)_2$
M71/AMPHB7	8.164	1.415	0.587	10.827	46.930	16.103	11.127	95.15	$(Na_{0.41}K_{0.11})(Ca_{1.77}Fe_{0.29})(Mg_{3.56}Fe_{1.05}Al_{0.39})(Al_{1.04}Si_{6.96})O_{22}(OH)_2$
M72/AMPHB8	7.887	1.394	0.506	12.947	46.900	14.934	10.767	95.34	$(Na_{0.40}K_{0.10})(Ca_{1.72}Fe_{0.33})(Mg_{3.32}Fe_{1.29}Al_{0.39})(Al_{1.00}Si_{7.00})O_{22}(OH)_2$
M83/AMPHB9	8.095	1.450	0.530	15.831	47.429	14.035	10.219	97.59	$(Na_{0.41}K_{0.10})(Ca_{1.61}Fe_{0.43})(Mg_{3.08}Fe_{1.52}Al_{0.40})(Al_{1.01}Si_{6.99})O_{22}(OH)_2$

Table 2.8. EMPA composition and formula of pyroxene.

Exp.No.	Al_2O_3	Na_2O	K_2O	FeO	SiO_2	MgO	CaO	Total	formula
M20/PYRX1	4.31	0.520	0.438	10.02	54.27	11.53	18.05	99.14	$(Ca_{0.72}Na_{0.04}K_{0.02}Fe_{0.14})(Mg_{0.64}Fe_{0.17}Al_{0.19})Si_{2.01}O_6$
M32/PYRX2	4.41	0.555	0.413	10.64	53.50	12.04	18.62	100.18	$(Ca_{0.74}Na_{0.04}K_{0.02}Fe_{0.16})(Mg_{0.66}Al_{0.17}Fe_{0.17})(Al_{0.02}Si_{1.98})O_6$
M40/PYRX3	3.39	0.424	0.332	11.83	54.13	13.07	17.34	100.51	$(Ca_{0.68}Na_{0.03}K_{0.02}Fe_{0.22})(Mg_{0.72}Al_{0.14}Fe_{0.14})(Al_{0.01}Si_{1.99})O_6$
M51/PYRX4	4.01	0.608	0.206	9.721	51.37	12.94	20.54	99.39	$(Ca_{0.83}Na_{0.04}K_{0.01}Fe_{0.13})(Mg_{0.72}Al_{0.11}Fe_{0.17})(Al_{0.07}Si_{1.93})O_6$
M51/PYRX5	4.00	0.606	0.379	10.24	52.62	12.44	19.21	99.50	$(Ca_{0.77}Na_{0.04}K_{0.02}Fe_{0.15})(Mg_{0.69}Al_{0.14}Fe_{0.17})(Al_{0.04}Si_{1.96})O_6$
M52/PYRX6	3.63	0.584	0.310	10.91	51.28	12.38	20.05	99.15	$(Ca_{0.81}Na_{0.04}K_{0.01}Fe_{0.14})(Mg_{0.70}Al_{0.10}Fe_{0.20})(Al_{0.06}Si_{1.94})O_6$
M61/PYRX7	3.81	0.542	0.314	10.25	52.21	12.28	19.47	98.86	$(Ca_{0.78}Na_{0.04}K_{0.02}Fe_{0.14})(Mg_{0.69}Al_{0.13}Fe_{0.18})(Al_{0.04}Si_{1.96})O_6$
M70/PYRX8	4.38	0.577	0.339	10.45	52.73	11.48	19.95	99.90	$(Ca_{0.80}Na_{0.04}K_{0.02}Fe_{0.12})(Mg_{0.64}Al_{0.15}Fe_{0.21})(Al_{0.04}Si_{1.96})O_6$
M72/PYRX9	3.37	0.569	0.213	10.81	50.82	12.58	19.55	97.91	$(Ca_{0.80}Na_{0.04}K_{0.01}Fe_{0.16})(Mg_{0.72}Al_{0.09}Fe_{0.19})(Al_{0.06}Si_{1.94})O_6$
M83/PYRX10	3.61	0.475	0.279	11.58	52.79	12.43	19.18	100.35	$(Ca_{0.76}Na_{0.03}K_{0.01}Fe_{0.17})(Mg_{0.69}Al_{0.12}Fe_{0.19})(Al_{0.04}Si_{1.96})O_6$

Table 2.9. EMPA composition and formula of plagioclase.

Exp.No.	Al_2O_3	Na_2O	K_2O	FeO	SiO_2	MgO	CaO	Total	formula
M10/PLG1	24.91	6.03	0.440	0.226	59.93	0.019	7.51	99.07	$(Na_{0.52}Ca_{0.36}K_{0.03})(Fe_{0.01}Mg_{0.001}Al_{1.32}Si_{2.69})O_8$
M20/PLG2	25.17	5.83	0.478	0.341	58.63	0.016	8.34	98.80	$(Na_{0.51}Ca_{0.40}K_{0.03})(Fe_{0.01}Mg_{0.001}Al_{1.34}Si_{2.65})O_8$
M40/PLG3	24.36	7.20	0.697	0.469	59.50	0.117	6.73	99.08	$(Na_{0.63}Ca_{0.33}K_{0.04})(Fe_{0.02}Mg_{0.01}Al_{1.30}Si_{2.69})O_8$
M61/PLG4	24.97	6.72	0.453	0.312	58.71	0.021	7.84	99.03	$(Na_{0.59}Ca_{0.38}K_{0.03})(Fe_{0.01}Mg_{0.001}Al_{1.33}Si_{2.65})O_8$
mca/PLG5	27.10	6.03	0.281	0.311	57.88	0.015	8.88	100.50	$(Na_{0.52}Ca_{0.42}K_{0.02})(Fe_{0.01}Mg_{0.001}Al_{1.42}Si_{2.58})O_8$

Table 2.10. EMPA average composition and formula of magnetite.

Exp.No.	Al_2O_3	Na_2O	K_2O	FeO_{total}	SiO_2	MgO	CaO	Total	
M32/MGST1	2.36	0.023	0.124	86.73	0.411	1.58	0.070	91.30	
M51/MGST2	2.83	0.028	0.134	84.88	1.556	1.19	0.094	90.72	
M61/MGST3	2.53	0.110	0.172	84.98	1.198	1.61	0.084	90.68	**Table part (a)**
M70/MGST4	3.02	0.027	0.092	86.31	0.304	1.23	0.059	91.05	
M71/MGST5	2.75	0.067	0.144	84.52	0.833	1.24	0.060	89.61	
M52/MGST6	2.44	0.053	0.128	86.64	0.513	1.01	0.061	90.85	

Exp.No.	Al_2O_3	Na_2O	K_2O	FeO	Fe_2O_3	SiO2	MgO	CaO	Total	Table part (b)	Formula
M32/MGST1	2.36	0.023	0.124	26.91	66.48	0.411	1.58	0.070	97.97		$(Fe^{2+}_{0.86}Mg_{0.09}K_{0.01}Ca_{0.003}Na_{0.002})O(Fe^{3+}_{1.90}Al_{0.11}Si_{0.02})O_3$
M51/MGST2	2.83	0.028	0.134	26.34	65.06	1.556	1.19	0.094	97.23		$(Fe^{2+}_{0.84}Mg_{0.07}K_{0.01}Ca_{0.004}Na_{0.002})O(Fe^{3+}_{1.86}Al_{0.13}Si_{0.06})O_3$
M61/MGST3	2.53	0.110	0.172	26.37	65.14	1.198	1.61	0.084	97.21		$(Fe^{2+}_{0.84}Mg_{0.09}K_{0.01}Ca_{0.003}Na_{0.01})O(Fe^{3+}_{1.86}Al_{0.11}Si_{0.05})O_3$
M70/MGST4	3.02	0.027	0.092	26.78	66.16	0.304	1.23	0.059	97.67		$(Fe^{2+}_{0.85}Mg_{0.07}K_{0.004}Ca_{0.002}Na_{0.002})O(Fe^{3+}_{1.90}Al_{0.14}Si_{0.01})O_3$
M71/MGST5	2.75	0.067	0.144	26.23	64.78	0.833	1.24	0.060	96.10		$(Fe^{2+}_{0.85}Mg_{0.07}K_{0.007}Ca_{0.002}Na_{0.005})O(Fe^{3+}_{1.88}Al_{0.13}Si_{0.03})O_3$
M52/MGST6	2.44	0.053	0.128	26.88	66.41	0.513	1.01	0.061	97.50		$(Fe^{2+}_{0.86}Mg_{0.06}K_{0.01}Ca_{0.003}Na_{0.004})O(Fe^{3+}_{1.91}Al_{0.11}Si_{0.02})O_3$

Note: EMPA does not differentiate between the chemical species FeO and Fe_2O_3. The result for Fe is therefore given as a total, in the form FeO; see part (a) of the table. In part (b) of the table FeO_{total} has been split into actual FeO and Fe_2O_3, in order to calculate the formula of magnetite. The structural formula of magnetite is given as Fe_3O_4 or $FeO.Fe_2O_3$. This means the molar mass of magnetite (231.5326) is simply the sum of the molar masses of FeO and Fe_2O_3 (i.e. 71.8444 + 159.6882). Therefore the weight percent concentration of FeO in part (b) is obtained by multiplying the corresponding result, FeO_{total}, in part (a) by 71.8444/231.5326 (i.e. ~ 0.31). Thus ~ 0.69 of FeO_{total} is the mass percent contributed by Fe_2O_3, however, still in form FeO. Therefore to obtain the weight percent value of Fe_2O_3 in part (b), the following conversion formula was used:

2 FeO + $\frac{1}{2} O_2$ ‹=› Fe_2O_3 i.e. 2 moles of FeO react with O_2 to yield 1 mole of Fe_2O_3.

Fe_2O_3 (wt%) = $\frac{0.69 \times FeO_{total} \times M_{Fe_2O_3}}{2 \times M_{FeO}}$ where $M_{Fe_2O_3}$ and M_{FeO} are the molar masses of Fe_2O_3 and FeO, respectively.

The factor 0.69 = $\frac{M_{Fe_2O_3}}{M_{Fe_3O_4}} = \frac{159.6882}{231.5326}$.

2.3.2. Partitioning of trace elements between biotite and silicate melts

Partition-coefficients ($D_i^{c/lq} = M_i^c/M_i^{lq}$, see definition in section 2.1), were calculated for each measured point in the biotite crystals using the average glass concentration, the results of which are listed in the general **Run-tables 2.11**. The results indicate that biotite has a stronger preference for hosting alkali and alkaline earth metals and transition metal elements than the rare earth elements of the lanthanide series. Thus the partition coefficients for the alkali, alkaline earths, and transition elements including the high field strength elements range from strongly compatible (e.g. $D_{Ni800°C} \sim 85$) to moderately compatible (e.g. $D_{Cu800°C} \sim 1.04$). Conversely the REEs are found to be incompatible in biotite, with the heavy and light REEs partitioning relatively more than the middle REEs. Therefore the biotite-melt partitioning description that follows has been divided into two parts; one part treats those trace elements belonging to the transition metals including the alkali and alkaline earths, and the other part describes the partitioning behaviour of the REEs in biotite.
Mineral-melt partitioning of trace elements can be accurately modelled with knowledge of elastic moduli for the host mineral, the charge and ionic radius of the substituent ions, along with the partitioning data for the major elements these ions replace. In the subsequent sections the Blundy and Wood version of the elastic strain model has therefore been applied to provide a framework for understanding the large variation in biotite-melt partition coefficients measured in this study.

Table 2.11. Run tables containing run-conditions and products (phases), concentrations of the trace element oxides (from EMPA), molar ratios of Fe and Mg in the phase biotite, and the biotite-melt partition coefficients of trace elements.

Run No.	Exp cond.& duration			Starting materials		Run products (phases)	Trace	Conc. (wt%) of element oxide				D.coefficient	
	T/°C	P/bar	t/days	components	wt%		elts	rsd glas	error (±)	Biotite	error (±)	Di	error (±)
	800	2	45	Hg,An,Bt,H_2O	99.65	**Biotite** (Fe 38, Mg 62),							
32/M10				Sm2O3	0.17	amphibole, plagioclase,	**Sm**	0.2194	0.0036	0.0116	0.0023	**0.0530**	0.0103
32/M10				Gd_2O_3	0.17	pyroxene and residual glass	**Gd**	0.1898	0.0148	0.0077	0.0010	**0.0404**	0.0053
	800	2	30	Hg,An,Bt,H_2O	99.63	**Biotite** (Fe 30, Mg 70),							
28/M20				Ho_2O_3	0.18	pyroxene, magnetite, plagioclase,	**Ho**	0.1373	0.0131	0.0097	0.0015	**0.0704**	0.0110
28/M20				Ta2O3	0.18	amphibole and residual glass	**Ta**	0.1332	0.0018	0.2506	0.0279	**1.8814**	0.2092
28/M20				Na2O			**Na**	2.4550	0.0532	0.6128	0.0476	**0.2496**	0.0194
28/M20				K2O			**K**	2.2975	0.0538	7.5280	0.1232	**3.2766**	0.0536
	800	2	40	Hg,An,Bt,H_2O	99.25	**Biotite** (Fe 41, Mg 59),							
29/M31				SrO	0.57	pyroxene and residual glass	**La**	0.0137	0.0012	0.0083	0.0013	**0.6037**	0.0921
29/M31				La_2O_3	0.18		**Sr**	0.1493	0.0096	0.0852	0.0100	**0.5709**	0.0670
	800	2	30	Hg,An,Bt,H_2O	99.59	**Biotite** (Fe 28, Mg 72),							
70/M32				Pr_2O_3	0.21	amphibole, magnetite, allanite,	**Pr**	0.0749	0.0012	0.0087	0.0018	**0.1162**	0.0243
70/M32				Er_2O_3	0.19	pyroxene and residual glass	**Er**	0.1028	0.0025	0.0977	0.0072	**0.9502**	0.0703
	800	2	40	Hg,An,Bt,H_2O	99.62	**Biotite** (Fe 34, Mg 66),							
65/M40				Tm_2O_3	0.18	pyroxene, magnetite,	**Tm**	0.1332	0.0070	0.0269	0.0100	**0.2017**	0.0751
65/M40				Lu_2O_3	0.19	amphibole and residual glass	**Lu**	0.1622	0.0079	0.5804	0.5804	**3.5783**	0.4515
65/M40				Na2O			**Na**	1.7580	0.1415	0.5478	0.1096	**0.3116**	0.0624
	800	2	40	Hg,An,Bt,H_2O	99.36	**Biotite** (Fe 30, Mg 70),							
71/M51				Yb_2O_3	0.19	pyroxene, magnetite,	**Yb**	0.1310	0.0223	0.0398	0.0210	**0.3038**	0.1602
24/M51				BaO	0.45	amphibole and residual glass	**Yb**	0.1304	0.0106	0.1383	0.0168	1.0606	0.1292
71/M51							**Ba**	0.4593	0.0025	0.8465	0.0613	**1.8429**	0.1334
24/M51							**Ba**	0.4605	0.0105	0.8019	0.0513	**1.7414**	0.1114

Hg = Haplogranite, An = Anorthite, Bt = Biotite. For all runs H2O = 11.10 wt%, An = 7.49 wt%, Bt = 13.68 wt%, Hg = 67.73 wt%

Table 2.11. continued …

Run No.	Exp cond.& duration			Starting materials		Run products (phases)	Trace	Conc. (wt%) of element oxide				D.coefficient	
	T/°C	P/bar	t/days	components	wt%		elts	rsd glas	error (±)	Biotite	error (±)	Di	error (±)
	800	2	35	Hg,An,Bt,H_2O	99.21	**Biotite** (Fe 34, Mg 66),							
20/M52				Nd_2O_3	0.19	pyroxene, magnetite,	**Nd**	0.0896	0.0039	0.0075	0.0010	**0.0837**	0.0112
20/M52				Rb_2O	0.60	allanite and residual glass	**Rb**	0.4001	0.0262	1.0498	0.0895	**2.6236**	0.2238
	800	2	35	Hg,An,Bt,H_2O	99.66	**Biotite** (Fe 34, Mg 66),							
31/M61				Tb_2O_3	0.18	pyroxene, magnetite, plagioclase,	**Tb**	0.1522	0.0083	0.0088	0.0016	**0.0578**	0.0108
31/M61				WO_3	0.16	amphibole and residual glass	**W**	0.0790	0.0218	0.1412	0.0156	**1.7877**	0.1976
	800	2	30	Hg,An,Bt,H_2O	99.41	**Biotite** (Fe 35, Mg 65),							
27/M62				Dy_2O_3	0.18	pyroxene,	**Dy**	0.1590	0.0033	0.0382	0.0089	**0.2402**	0.0561
27/M62				PbO	0.41	amphibole and residual glass	**Pb**	0.0250	0.0042	0.0205	0.0034	**0.8196**	0.1357
	800	2	45	Hg,An,Bt,H_2O	98.92	**Biotite** (Fe 29, Mg 71),							
38/M70				CeO	0.20	pyroxene, magnetite,	**Ce**	0.0601	0.0046	0.0164	0.0054	**0.2727**	0.0900
38/M70				Cs_2O	0.44	allanite and residual glass	**Cs**	0.4049	0.0123	0.2938	0.0093	**0.7257**	0.0231
38/M70				ZrO_2	0.26		**Zr**	0.0311	0.0027	0.0022	0.0014	**0.0709**	0.0459
38/M70				Nb_2O_5	0.17		**Nb**	0.1198	0.0091	0.4423	0.0414	3.6918	0.3456
	800	2	40	Hg,An,Bt,H_2O	99.21	**Biotite** (Fe 26, Mg 74),							
33/M71				Cs_2O	0.40	amphibole, magnetite,	**Cs**	0.0127	0.0037	0.0065	0.0007	**0.5132**	0.0558
33/M71				ZrO_2	0.39	pyroxene and residual glass	**Zr**	0.0328	0.0020	0.0137	0.0081	0.4162	0.2469
	800	2	40	Hg,An,Bt,H_2O	99.70	**Biotite** (Fe 33, Mg 67),							
30/M72				CeO	0.18	amphibole, pyroxene,	**Ce**	0.0212	0.0041	0.0078	0.0016	**0.3679**	0.0775
30/M72				Nb_2O_5	0.13	magnetite and residual glass	**Nb**	0.0218	0.0062	0.0110	0.0020	**0.5057**	0.0920
	800	2	35	Hg,An,Bt,H_2O	99.65	**Biotite** (Fe 39, Mg 61),							
67/M83				Eu_2O_3	0.18	amphibole and residual glass	**Eu**	0.1436	0.0028	0.0098	0.0014	**0.0679**	0.0097
67/M83				MoO3	0.16		**Mo**	0.0632	0.0016	0.0104	0.0021	**0.1646**	0.0328

Table 2.11. continued …

Run No.	Exp cond.& duration			Starting materials		Run products (phases)	Trace	Conc. (wt%) of element oxide				D.coefficient	
	T/°C	P/bar	t/days	components	wt%		elts	rsd glas	error (±)	Biotite	error (±)	Di	error (±)
	800	2	35	Hg,An,Bt,H_2O	93.24	**Biotite** (Fe 31, Mg 69),							
22/MA0				TiO_2	0.54	amphibole,	**Ti**	0.4175	0.0177	3.2271	0.4933	**7.7305**	1.1817
22/MA0				CoO	0.54	pyroxene and residual glass	**Co**	0.1116	0.0074	3.7771	0.4880	**33.8343**	4.3718
72/MA0							**Ti**	0.4871	0.0100	3.1714	0.4701	**6.5107**	0.9651
72/MA0							**Co**	0.1481	0.0264	4.9957	0.9263	**33.7295**	6.2542
	800	2	45	Hg,An,Bt,H_2O	99.44	**Biotite** (Fe 34, Mg 66),							
25/MB0				V_2O_3	0.16	amphibole,	**V**	0.0176	0.0043	0.5046	0.0267	**28.7510**	1.5210
25/MB0				CuO	0.40	pyroxene and residual glass	**Cu**	0.0036	0.0021	0.0038	0.0020	**1.0391**	0.5636
	800	2	30	Hg,An,Bt,H_2O	99.17	**Biotite** (Fe 31, Mg 69),							
69/MD0				TiO_2	0.45	amphibole,	**Ti**	0.1854	0.0256	2.4300	0.0823	**13.1048**	0.4436
69/MD0				NiO	0.38	pyroxene and residual glass	**Ni**	0.0259	0.0121	8.5457	0.3137	**330.3206**	12.1248
69/MD0				FeO			**Fe**	0.9012	0.0392	9.6786	0.2229	**10.7397**	0.2473
69/MD0				MgO			**Mg**	0.1728	0.0222	12.5543	0.1942	**72.6630**	1.1237
	800	2	45	Hg,An,Bt,H_2O	97.47	**Biotite** (Fe 38, Mg 62),							
02/mca				TiO_2	0.45	amphibole, plagioclase,	**Ti**	0.1094	0.0038	1.5381	0.1013	**14.0572**	0.9256
02/mca				V_2O_3	0.18	pyroxene and residual glass	**V**	0.0161	0.0078	0.3703	0.0205	**22.9600**	1.2695
02/mca				Cr_2O_3	0.18		**Cr**	0.0499	0.0315	0.0579	0.0332	**1.1606**	0.6651
02/mca				CoO	0.45		**Co**	0.0641	0.0094	2.1727	0.2697	**33.8959**	4.2082
02/mca				NiO	0.42		**Ni**	0.1224	0.0230	10.3000	0.6438	**84.1503**	5.2601
02/mca				CuO	0.38		**Cu**	0.0100	0.0007	0.0085	0.0021	**0.8500**	0.2121
02/mca				ZnO	0.47		**Zn**	0.0125	0.0050	0.0975	0.0151	**7.8110**	1.2137
02/mca				MgO			**Mg**	0.2149	0.0218	8.7200	0.3969	**40.5770**	1.8467
02/mca				FeO			**Fe**	1.0717	0.1085	8.7120	0.5251	**8.1294**	0.4900

Table 2.11. continued …

Run No.	Exp cond.& duration			Starting materials		Run products (phases)	Trace	Conc. (wt%) of element oxide				D.coefficient	
	T/°C	P/bar	t/days	components	wt%		elts	rsd glas	error (±)	Biotite	error (±)	Di	error (±)
	800	2	35	Hg,An,Bt,H_2O	99.38	**Biotite** (Fe 39, Mg 61),							
64/MC0				Cr_2O_3	0.17	amphibole, magnetite, allanite,	**Cr**	0.0211	0.0114	0.3370	0.0211	**15.9842**	0.9994
64/MC0				ZnO	0.45	pyroxene and residual glass	**Zn**	0.0246	0.0026	0.2082	0.0139	**8.4535**	0.5659
	775	2	30	Hg,An,Bt,H_2O	99.59	**Biotite** (Fe 36, Mg 64),							
73/M32				Pr_2O_3	0.21	amphibole, allanite,	**Pr**	0.0423	0.0045	0.0125	0.0051	**0.2955**	0.1196
73/M32				Er_2O_3	0.19	pyroxene and residual glass	**Er**	0.0449	0.0057	0.0895	0.0102	**1.9946**	0.2277
	775	2	35	Hg,An,Bt,H_2O	99.21	**Biotite** (Fe 35, Mg 65),							
75/M52				Nd_2O_3	0.19	pyroxene, magnetite,	**Nd**	0.0403	0.0048	0.0048	0.0037	**0.1197**	0.0913
75/M52				Rb_2O	0.60	allanite and residual glass	**Rb**	0.1333	0.0270	0.6444	0.0682	4.8351	0.5118
	775	2	35	Hg,An,Bt,H_2O	99.65	**Biotite** (Fe 36, Mg 64),							
83/M83				Eu_2O_3	0.18	pyroxene,	**Eu**	0.1450	0.0025	0.0100	0.0018	**0.0690**	0.0126
83/M83				MoO_3	0.16	amphibole and residual glass	**Mo**	0.0467	0.0052	0.0118	0.0015	**0.2526**	0.0318
	775	2	35	Hg,An,Bt,H_2O	99.66	**Biotite** (Fe 32, Mg 68),							
				Tb_2O_3	0.18	pyroxene,							
82M61				WO_3	0.16	amphibole and residual glass	**W**	0.0315	0.0075	0.0200	0.0046	**0.6349**	0.1455
	775	2	30	Hg,An,Bt,H_2O	99.41	**Biotite** (Fe 36, Mg 64),							
77/M62				Dy_2O_3	0.18	pyroxene,	**Dy**	0.0976	0.0009	0.0328	0.0222	**0.3355**	0.2279
77/M62				PbO	0.41	amphibole and residual glass	**Pb**	0.0403	0.0030	0.0265	0.0098	**0.6570**	0.2428
	775	2	40	Hg,An,Bt,H_2O	99.62	**Biotite** (Fe 45, Mg 55),							
61/M40				Tm_2O_3	0.18	amphibole and residual glass	**Tm**	0.0556	0.0037	0.0215	0.0120	**0.3867**	0.2162
61/M40				Lu_2O_3	0.19		**Lu**	0.0426	0.0009	0.0140	0.0057	**0.3286**	0.1328
	775	2	45	Hg,An,Bt,H_2O	99.44	**Biotite** (Fe 45, Mg 55),							
91/MB0				V_2O_3	0.16	amphibole, plagioclase,	**V**	0.0142	0.0088	0.5016	0.0107	**35.4202**	0.7540
91/MB0				CuO	0.40	pyroxene and residual glass							

Table 2.11. continued …

Run No.	Exp cond.& duration			Starting materials		Run products (phases)	Trace	Conc. (wt%) of element oxide				D.coefficient	
	T/°C	P/bar	t/days	components	wt%		elts	rsd glas	error (±)	Biotite	error (±)	Di	error (±)
	775	2	35	Hg,An,Bt,H_2O	99.38	**Biotite** (Fe 42, Mg 58),							
94/MC0				Cr_2O_3	0.17	amphibole, magnetite, allanite,	**Cr**	0.0112	0.0024	0.0622	0.0112	**5.5506**	0.9965
94/MC0				ZnO	0.45	pyroxene and residual glass	**Zn**	0.0142	0.0013	0.2182	0.0603	**15.4150**	4.2592
	775	2	45	Hg,An,Bt,H_2O	97.47	**Biotite** (Fe 38 , Mg 62),							
05/mca				TiO_2	0.45	plagioclase and residual glass	**Ti**	0.0825	0.0019	1.6916	0.0721	**20.5167**	0.8747
05/mca				V_2O_3	0.18		**V**	0.0115	0.0018	0.3801	0.0400	**33.1936**	3.4906
05/mca				Cr_2O_3	0.18		**Cr**	0.0254	0.0168	0.0495	0.0133	**1.9463**	0.5225
05/mca				CoO	0.45		**Co**	0.0502	0.0042	2.3011	0.0892	**45.8389**	1.7774
05/mca				NiO	0.42		**Ni**	0.1093	0.0320	9.2963	0.5011	**85.0267**	4.5836
05/mca				ZnO	0.47		**Zn**	0.1077	0.0021	0.1178	0.0063	**1.0941**	0.0582
				CuO	0.38								
	750	2	30	Hg,An,Bt,H_2O	99.59	**Biotite** (Fe 42, Mg 58),							
120/M32				Pr_2O_3	0.21	amphibole and residual glass	**Pr**	0.0200	0.0038	0.0089	0.0026	**0.4441**	0.1279
120/M32				Er_2O_3	0.19		**Er**	0.0611	0.0066	0.1373	0.0229	**2.2452**	0.3752
	750	2	35	Hg,An,Bt,H_2O	99.21	**Biotite** (Fe 29, Mg 71),							
102/M52				Nd_2O_3	0.19	pyroxene, plagioclase,	**Nd**	0.0282	0.0035	0.0079	0.0016	**0.2806**	0.0585
102/M52				Rb_2O	0.60	allanite and residual glass	**Rb**	0.1692	0.0130	0.6784	0.1056	4.0095	0.6242
	750	2	45	Hg,An,Bt,H_2O	97.47	**Biotite** (Fe 35, Mg 65),							
mca				TiO_2	0.45	amphibole, plagioclase,	**Ti**	0.0970	0.0065	2.0183	0.0564	**20.8076**	0.5811
mca				V_2O_3	0.18	and residual glass	**V**	0.0150	0.0000	0.5128	0.0079	**34.1867**	0.5279
mca				Cr_2O_3	0.18		**Cr**	0.0297	0.0124	0.0948	0.0253	**3.1938**	0.8525
mca				CoO	0.45		**Co**	0.0576	0.0047	2.6888	0.0642	**46.6797**	1.1153
mca				NiO	0.42		**Ni**	0.0780	0.0075	7.0475	0.3563	**90.3526**	4.5682
mca				CuO	0.38		**Cu**	0.0095	0.0007	0.0095	0.0007	**1.0000**	0.0744
mca				ZnO	0.47		**Zn**	0.1000	0.0039	0.0873	0.0165	**0.8725**	0.1648

Table 2.11. continued …

Run No.	Exp cond.& duration			Starting materials		Run products (phases)	Trace	Conc. (wt%) of element oxide				D.coefficient	
	T/°C	P/bar	t/days	components	wt%		elts	rsd glas	error (±)	Biotite	error (±)	Di	error (±)
	750	2	35	Hg,An,Bt,H_2O	99.65	**Biotite** (Fe 45, Mg 55),							
99/M83				Eu_2O_3	0.18	pyroxene, plagioclase,	**Eu**	0.1338	0.0004	0.0150	0.0039	**0.1121**	0.0289
99/M83				MoO3	0.16	amphibole and residual glass	**Mo**	0.0265	0.0047	0.0123	0.0033	**0.4646**	0.1230
	750	2	45	Hg,An,Bt,H_2O	99.44	**Biotite** (Fe 42, Mg 58),							
109/MBO				V_2O_3	0.16	amphibole, plagioclase,	**V**	0.0118	0.0007	0.5531	0.0817	**46.7408**	6.9077
109/MBO				CuO	0.40	pyroxene and residual glass	**Cu**	0.0026	0.0006	0.0048	0.0004	**1.8228**	0.1611
	700	2	45	Hg,An,Bt,H_2O	99.44	**Biotite** (Fe 48, Mg 52),							
127/MBO				V_2O_3	0.16	amphibole, plagioclase,	**V**	0.0139	0.0015	0.5383	0.0606	**38.8646**	4.3739
127/MBO				CuO	0.40	pyroxene and residual glass							
mca	720	2	45	Hg,An,Bt,H_2O	97.47	**Biotite** (Fe 46, Mg 54),							
mca				TiO_2	0.45	amphibole, plagioclase,	**Ti**	0.0730	0.0053	1.6622	0.2222	**22.7694**	3.0444
mca				V_2O_3	0.18	and residual glass	**V**	0.0109	0.0016	0.4912	0.0420	**45.0642**	3.8507
mca				Cr_2O_3	0.18		**Cr**	0.0432	0.0112	0.0968	0.0087	**2.2425**	0.2016
mca				CoO	0.45		**Co**	0.0326	0.0106	1.8900	0.0308	**57.9755**	0.9455
mca				NiO	0.42		**Ni**	0.0858	0.0074	5.9370	0.4816	**69.1689**	5.6108
mca				ZnO	0.47		**Zn**	0.0353	0.0118	0.2332	0.0063	**6.6000**	0.1774
				CuO	0.38								
	700	2	45	Hg,An,Bt,H_2O	97.47	**Biotite** (Fe 35, Mg 65),							
mca				TiO_2	0.45	amphibole, plagioclase,	**Ti**	0.0527	0.0094	1.5180	0.1096	**28.7909**	2.0796
mca				V_2O_3	0.18	pyroxene and residual glass	**V**	0.0103	0.0033	0.3800	0.0373	**37.0732**	3.6408
mca				Cr_2O_3	0.18		**Cr**	0.0289	0.0024	0.0685	0.0148	**2.3702**	0.5138
mca				CoO	0.45		**Co**	0.0279	0.0056	2.1700	0.1867	**77.9174**	6.7047
mca				NiO	0.42		**Ni**	0.0365	0.0157	14.1350	2.3939	**387.2603**	65.5867
mca				ZnO	0.47		**Zn**	0.0550	0.0084	0.0495	0.0214	**0.9003**	0.3897
				CuO	0.38								

BT = Analysis carried out from Bayreuth, TUE = analysis carried out from Tuebingen.

2.3.2.1. Transition metals, alkali and alkaline earth elements

A summary list of biotite/melt partition coefficients (D_i) for trace elements including transition metals, alkalis and alkaline earth elements is presented in **Table 2.12**. The table lists those elements which are particularly relevant for the formation of economical ore deposits, including Cu, Zn, Co, Ni, V, Cr, Ti, Mo, W, Nb, Ta, Zr, Pb, Rb, Cs and Ba. This is graphically shown in the corresponding **Figure 2.13**, depicting the variation of D_i with ionic radii (IR) of the trace elements concerned. The graphics shows the dependency of D_i on ionic charge and radius, in accordance with Brice's elastic strain model.

Table 2.12. Summary table for biotite-melt trace element partition coefficients and their ionic-radii (adapted from Shannon, 1976, for co-ordination 6)

Run No.	ion	IR (Å)	D_i	±	Run No.	ion	IR (Å)	D_i	±
28/M20	Na^{+}	1.020	0.2496	0.0194	02/mca	Ni^{2+}	0.690	84.1503	5.2601
65/M40	Na^{+}	1.020	0.3116	0.0624	69/MD0	Ni^{2+}	0.690	330.3206	12.1248
avrg	Na^{+}	1.020	0.2806	0.0409	25/MB0	Cu^{2+}	0.770	1.0391	0.5636
28/M20	K^{+}	1.380	3.2766	0.0536	02/mca	Cu^{2+}	0.770	0.8500	0.2121
69/MD0	K^{+}	1.380	2.1977	0.0451	avrg	Cu^{2+}	0.770	0.9445	0.3878
avrg	K^{+}	1.380	2.7372	0.0494	64/MC0	Zn^{2+}	0.740	8.4535	0.5659
20/M52	Rb^{+}	1.520	2.6236	0.2238	02/mca	Zn^{2+}	0.740	7.8110	1.2137
38/M70	Cs^{+}	1.670	0.7257	0.0231	avrg	Zn^{2+}	0.740	8.1323	0.8898
33/M71	Cs^{+}	1.670	0.5132	0.0558	25/MB0	V^{3+}	0.540	28.7510	1.5210
avrg	Cs^{+}	1.670	0.6194	0.0394	02/mca	V^{3+}	0.540	22.9600	1.2695
02/mca	Mg^{2+}	0.720	40.5770	1.8467	avrg	V^{3+}	0.540	25.8555	1.3953
69/MD0	Mg^{2+}	0.720	72.6630	1.1237	64/MC0	Cr^{3+}	0.620	15.9842	0.9994
avrg	Mg^{2+}	0.720	56.6200	1.4852	02/mca	Cr^{3+}	0.620	1.1606	0.6651
28/M20	Ca^{2+}	1.000	0.0164	0.0113	22/MA0	Ti^{4+}	0.610	7.7305	1.1817
29/M31	Sr^{2+}	1.180	0.5709	0.0670	72/MA0	Ti^{4+}	0.610	6.5107	0.9651
24/M51	Ba^{2+}	1.350	1.7414	0.1114	69/MD0	Ti^{4+}	0.610	13.1048	0.4436
71/M51	Ba^{2+}	1.350	1.8429	0.1334	02/mca	Ti^{4+}	0.610	14.0572	0.9256
avrg	Ba^{2+}	1.350	1.7922	0.1224	avrg	Ti^{4+}	0.610	10.3508	0.8790
27/M62	Pb^{2+}	1.190	0.8196	0.1357	38/M70	Zr^{4+}	0.720	0.0709	0.0459
69/MD0	Fe^{2+}	0.780	10.7397	0.2473	33/M71	Zr^{4+}	0.720	0.4162	0.2469
02/mca	Fe^{2+}	0.780	8.1294	0.4900	38/M70	Nb^{5+}	0.640	3.6918	0.3456
avrg	Fe^{2+}	0.780	9.4346	0.3687	30/M72	Nb^{5+}	0.640	0.5057	0.0920
02/mca	Co^{2+}	0.740	33.8959	4.2082	28/M20	Ta^{5+}	0.640	1.8814	0.2092
22/MA0	Co^{2+}	0.740	33.8343	4.3718	67/M83	Mo^{6+}	0.590	0.1646	0.0328
72/MA0	Co^{2+}	0.740	33.7295	6.2542	31/M61	W^{6+}	0.600	1.7877	0.1976
avrg	Co^{2+}	0.740	33.8199	4.9447					

Note: Averages (avrg) D_i-values have been used to plot **Figure 2.13**. Where two or more D_i-values exist for one element without an average value, means that all the listed Di-values for this particular element exist in the plot as well, e.g. Zr^{4+} and Nb^{5+}.

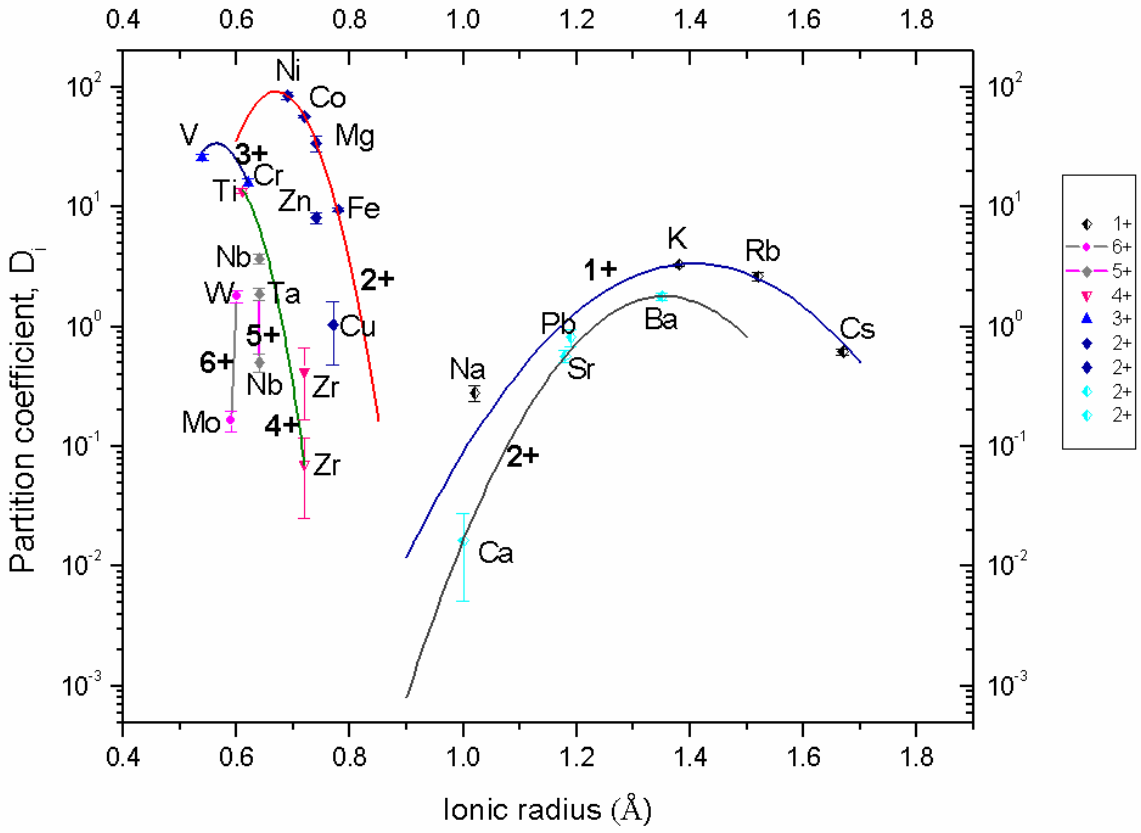

Fig. 2.13. Variation of biotite-melt partition coefficients with ionic radius. The Brice model fits of experimental biotite-melt partitioning data (**Table 2.12**) for isovalent cations of alkali earth, alkaline earth and transition metal elements to the lattice strain model curves, calculated using equation 2.9 (see text). See **Table 2.15** for the estimated lattice site parameters, D_o, r_o, and E_s. Note that the alkalis (Cs, Rb, K, and Na) and the alkaline earth elements (Ba, Sr, and Ca), including Pb partition into the interlayer site-K of biotite. Transition metal elements partition into the M2 site of the biotite crystal structure. Only the curves through 1+ and 2+ cations have been obtained by fitting the parabola, using a weighed non-linear least-squares regression to the Brice equation 2.9. The curves through 3+, 4+, 5+, and 6+ cations have been simply drawn as a guide for the eye. Note also that the curves become progressively tighter and displaced to lower r_o as the charge increase from 1+ to 2+ (K-site) and 2+ to 6+ (M2-site). Error bars denote 1 s.d. analytical uncertainty.

The graphics in **Figure 2.13** contains six curves, each representing the partitioning behaviour of a group of isovalent trace elements. The large alkali and alkaline earth elements plot to the centre-right, whilst the transition elements plot to left of the diagram.

In terms of site occupancy, the alkalis (Cs, Rb, and Na) and alkaline earths (Ba, Sr, and Ca), including Pb follow K into the largest interlayer site of the biotite crystal structure. The rest of the trace element groups, including the 2+ cations (Ni, Co, Zn, Cu, and Fe), the 3+ cations (V and Cr), the 4+ cations (Ti and Zr), the 5+ cations (Nb and Ta), and the 6+ cations (W and Mo) follow Mg into the M2 site, in a 6-fold co-ordination.

Some transition metal elements, especially the divalent cations, show deviations from the model curve, probably due to crystal field effects being significant. The deviation could also possibly arise from an unacceptable level of inaccuracy in determining the partition coefficients for some of these elements, particularly Cu and Zn, which were strongly absorbed by the gold capsule during the experimental runs. Biotite could, for instance, have crystallised in equilibrium with a high Cu concentration in the melt, but later during the run the residual melt lost almost all of its Cu content. This results in a higher partition-coefficient for Cu, as observed in some runs, with a correspondingly high analytical error.

Further, some elements, as observed from the experiments on the oxidation states of copper (see chapter 3), may exist in more than one valence state, e.g. Cu^{2+} and Cu^{+}. In this case the measured partition coefficient would be the sum of the partition coefficients for the two species.

Trace element cations of different sizes and charges in the silicate melt are able to substitute for major element cations that occupy either tetrahedral (Si, Al) or octahedral (Mg, Fe) or interlayer (K) lattice sites in the biotite crystal.

Heterovalent substitutions also require the presence of a charge-compensating defect (cation or anion) elsewhere in the lattice, which will also involve some degree of lattice strain. When, for instance, Mg is replaced by a cation of higher charge, the difference in charge will be compensated for by replacing several Si^{4+} cations by Al^{3+} cations, as many as required to achieve charge-balance at the site. There will be a decrease in the flexibility of a site with an increasing charge on the cation occupying that site. This could possibly be due to the shorter, stronger bonds of more highly charged cations, in addition to the increased size of the local tetrahedral units as Si^{4+} is replaced by Al^{3+} to maintain charge balance.

For example, the mechanism involves a trace ion entering the K-site (e.g. Ba^{2+} or Sr^{2+}, substituting for K^{+}). The cation, in this case, Ba^{2+}, has a charge which is different from that of the major ion (K^{+}) it is replacing. It will, therefore, form a charged defect in the crystal lattice. In order to maintain charge balance such substitutions must be compensated for by other substitutions, e.g.

1) $Ba^{2+} + Al^{3+} \leftrightarrow K^{+} + Si^{4+}$ (2.3)

2) $Sr^{2+} + Al^{3+} \leftrightarrow K^{+} + Si^{4+}$ (2.4)

2.3.2.2. Rare earth elements in biotite

A summary of the results of partition-coefficients of the REEs between biotite and melt is listed in **Table 2.13** and plotted against ionic radius in **Figure 2.14**. The graph, however, shows a partitioning pattern which cannot be explained by a substitution onto a single lattice site.

The REEs apparently partition into two crystallographic lattice sites of the biotite crystal (the K- and Mg-site). In going from left to right of the lanthanide series, the first four elements (i.e. La, Ce, Pr, and Nd) predominantly partition into the K-site. The next five elements (i.e. Sm, Eu, Gd, Tb, and Dy) show a mixed partitioning character in both the K and Mg-site, with Gd partitioning almost equally in both sites. The last five elements of the series will, like the first four, predominantly partition into the Mg-site.

The plot yields two distinct parabolas crossing each other in the mid-centre. This could imply that the partition-coefficients for the middle rare earth elements (MREEs, including Eu, Gd, Tb and Dy) can be estimated to be the sum of the D_i-values predicted from the two parabolas (see **Figures 2.15a** and **b**).

Table 2.13. Summary tables for biotite-melt partition coefficients for REEs and their ionic radii (adapted from Shannon, 1976)

Run No.	ion	IR (Å)	D_i	±
29/M31	La^{3+}	1.032	0.6037	0.0921
30/M72	Ce^{3+}	1.010	0.3679	0.0775
38/M70	Ce^{3+}	1.010	0.2727	0.0900
70/M32	Pr^{3+}	0.990	0.1162	0.0243
20/M52	Nd^{3+}	0.983	0.0837	0.0112
32/M10	Sm^{3+}	0.958	0.0530	0.0103
67/M83	Eu^{3+}	0.947	0.0679	0.0097
32/M10	Gd^{3+}	0.938	0.0404	0.0053
31/M61	Tb^{3+}	0.923	0.0578	0.0108
27/M62	Dy^{3+}	0.912	0.0407	0.0242
28/M20	Ho^{3+}	0.901	0.0704	0.0110
70/M32	Er^{3+}	0.890	0.9502	0.0703
65/M40	Tm^{3+}	0.880	0.2017	0.0751
71/M51	Yb^{3+}	0.868	0.3038	0.1602
24/M51	Yb^{3+}	0.868	1.0606	0.1292
61/M40	Lu^{3+}(1)	0.861	0.3922	0.2882
65/M40	Lu^{3+}(2)	0.861	3.5783	0.4515

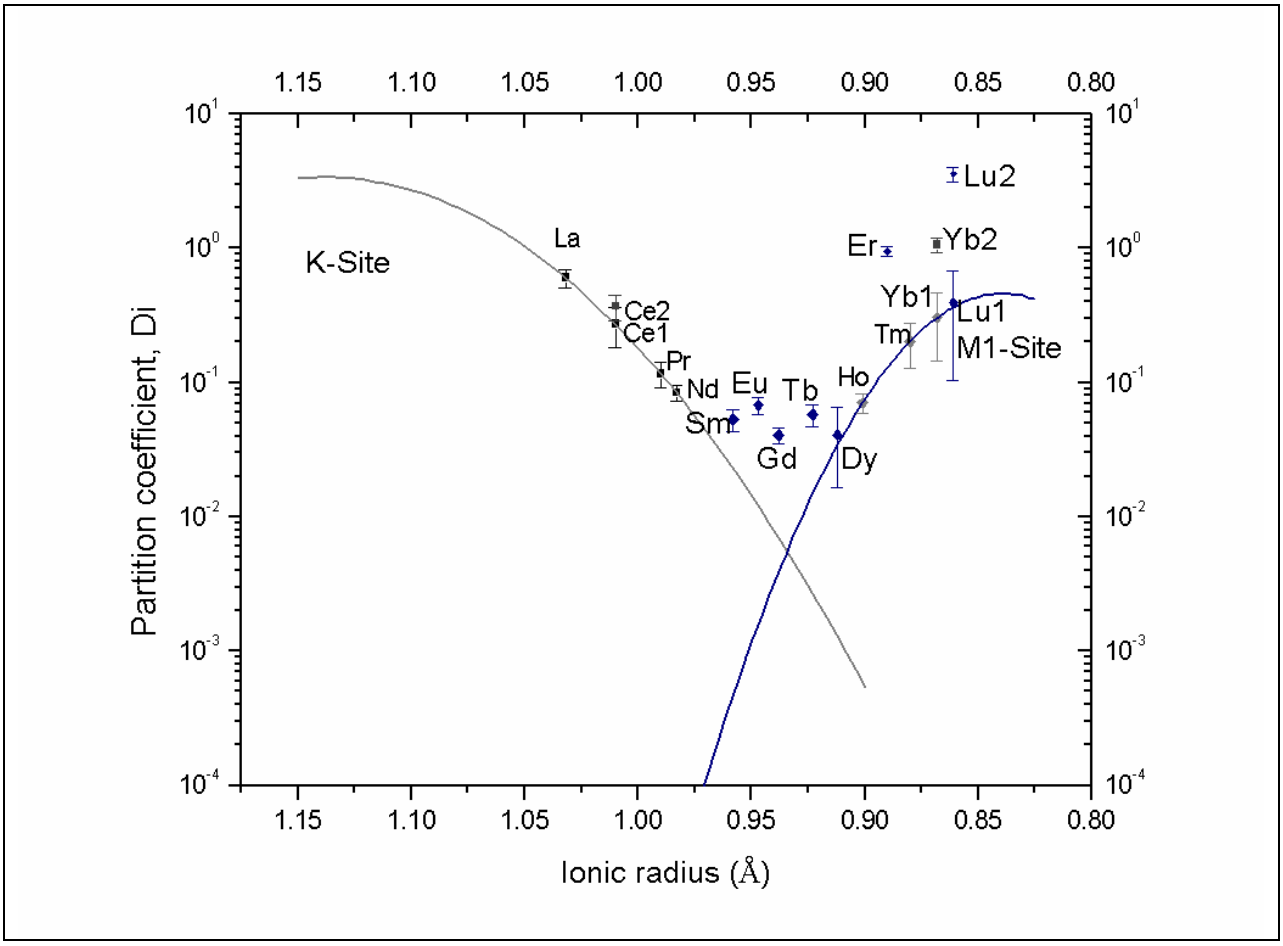

Fig. 2.14. Variation of biotite-melt partition coefficients with ionic radius for the rare earth elements. The model assumes two partitioning sites for the REEs in biotite, with the HREEs substituting in the M1-site and the LREEs in the K-site. The MREEs are assumed to partition in both sites. Therefore their effective partition coefficients are the sum of their partition coefficients in each site (see **Table 2.15** for the estimated lattice parameters, D_o, r_o, and E_s for each site).

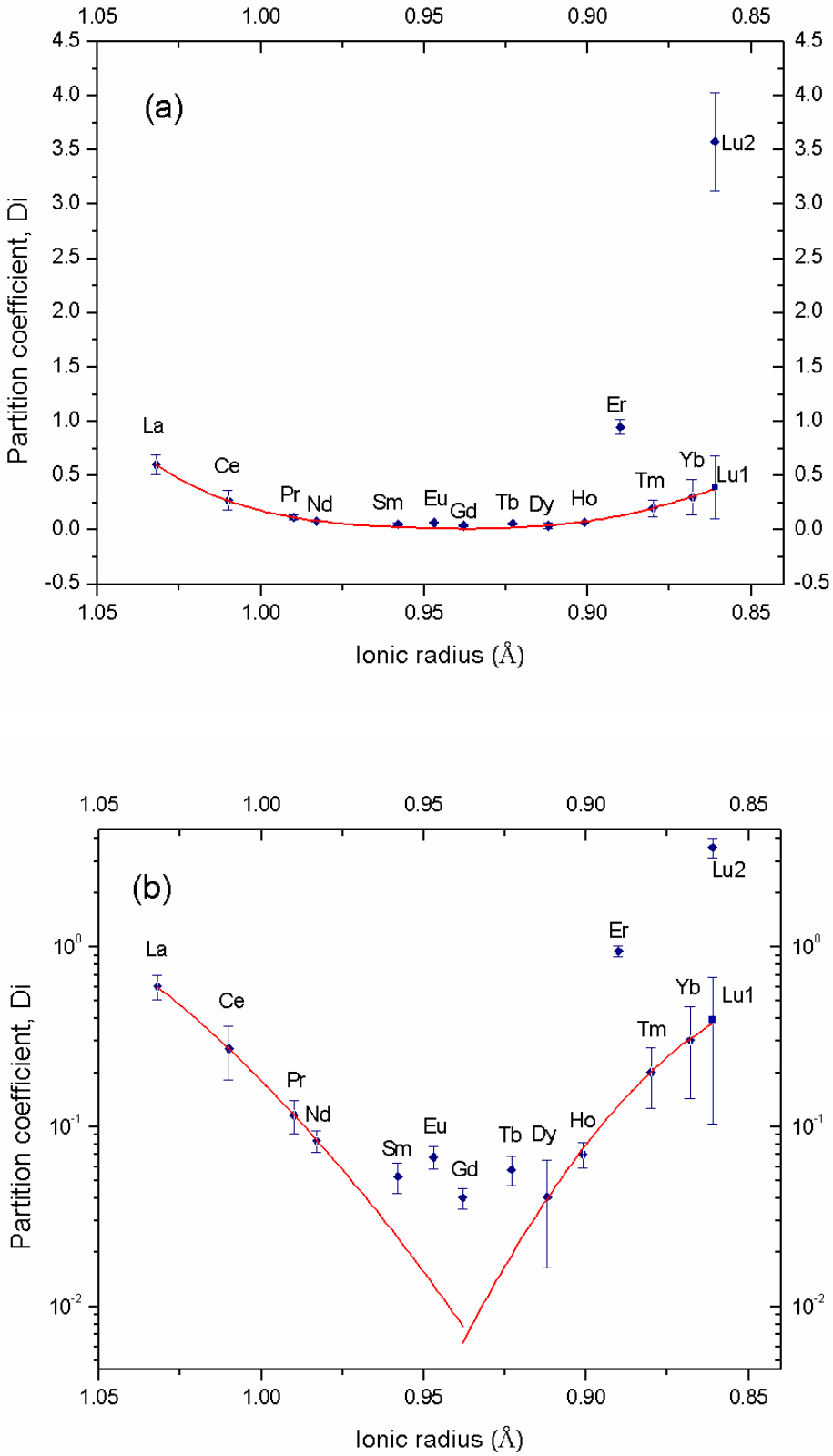

Fig. 2.15. Predicted (the curves) and measured biotite-melt partition coefficients of REEs. The two parabolas in **Figure 2.14** add up to yield the curve for the predicted partition coefficients. Diagrams (a) and (b) are linear-linear and log-linear plots of predicted and measured biotite-melt partition coefficients, respectively. The predicted curve is calculated from **equation (2.9)**.

This means, the MREEs are able to substitute almost equally in both lattice sites. The measured partition coefficients for these elements are therefore the sum of their partitioning behaviour in both sites. Substituting REE^{3+} into the K- and Mg-sites requires simultaneous substitution of another element in the neighbouring site, as already explained in the previous section, to achieve a charge balance of the structure.

1) $REE^{3+} + 2Al^{3+} \leftrightarrows K^{+} + 2Si^{4+}$. (2.5)
2) $REE^{3+} + Al^{3+} \leftrightarrows Mg^{2+} + Si^{4+}$. (2.6)

The REE data is consistent in showing the concave nature of the REE partition coefficient pattern, however, with anomalous peaks in the positions for the elements La, Dy and Er, falling significantly off the calculated or predicted trend curve of partition-coefficients (solid curve in **Figure 2.15**). One possible reason could be the intergrowth of biotite with allanite, which hosts most of the REEs as major constituents in its mineral structure. The measured partition coefficients could, in this case, be the average for both the biotite and its minute allanite inclusions. Another reason for the anomalous behaviour could possibly arise from the amounts of tetrahedral Al^{3+} cations substituting for Si^{4+}, possibly as a charge balancing mechanism, whilst the concerned REE partitioned into the K or M1 site. The graph illustrating the variation of partition-coefficients with tetrahedral Al^{3+} for the REEs yields a random scatter of points, implying no correlation between the two variables (see **Table 2.14** and **Figure 2.16**).

Table. 2.14. Relationship between biotite/melt partition coefficients of trace REEs and the number of moles of Al^{3+} ions in the tetrahedral site of the biotite crystal.

Run No.	Element	IR (Å)	Th .Al	±	Di (Å)	±
29/M31	**La**	1.032	0.720	0.096	0.604	0.092
38/M70	**Ce**	1.010	0.994	0.063	0.273	0.090
70/M32	**Pr**	0.990	0.825	0.096	0.116	0.024
20/M52	**Nd**	0.983	1.014	0.062	0.084	0.011
32/M10	**Sm**	0.958	0.958	0.034	0.053	0.010
67/M83	**Eu**	0.947	0.895	0.061	0.068	0.010
32/M10	**Gd**	0.938	0.941	0.085	0.040	0.005
31/M61	**Tb**	0.923	0.816	0.084	0.058	0.011
27/M62	**Dy**	0.912	0.620	0.087	0.036	0.012
28/M20	**Ho**	0.901	0.982	0.056	0.070	0.011
70/M32	**Er**	0.890	0.890	0.061	0.950	0.070
65/M40	**Tm**	0.880	0.607	0.179	0.202	0.075
71/M51	**Yb**	0.868	0.830	0.147	0.304	0.160
65/M40	**Lu**	0.861	0.818	0.064	3.578	0.452

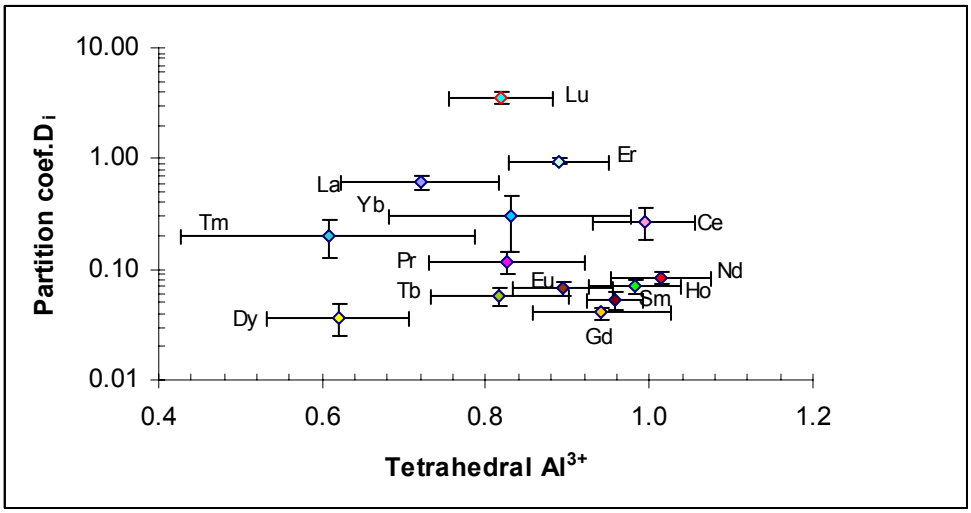

Fig.2.16. Variation of biotite-melt partition coefficients of REEs with their corresponding number of moles of Al^{3+} cations hosted in the tetrahedral site of the crystal (biotite). Note that there is apparently no correlation between the two variables.

Thus the anomalously high D_i-values for some REEs cannot be attributed to the corresponding amount of Al, the crystal hosts in its tetrahedral site.
It can also observed that biotite has two M-sites, the larger M1-site into which the HREEs partition and the small M2-site into which the rest of the transition metal elements partition.

2.3.2.3. Discussion of Brice model (lattice strain theory)

The lattice strain model is based on the long established observation that crystal-melt partition-coefficients for a series of isovalent cations show a near-parabolic dependence on cation radius (Onuma et al., 1968) see **Figure 2.17**.

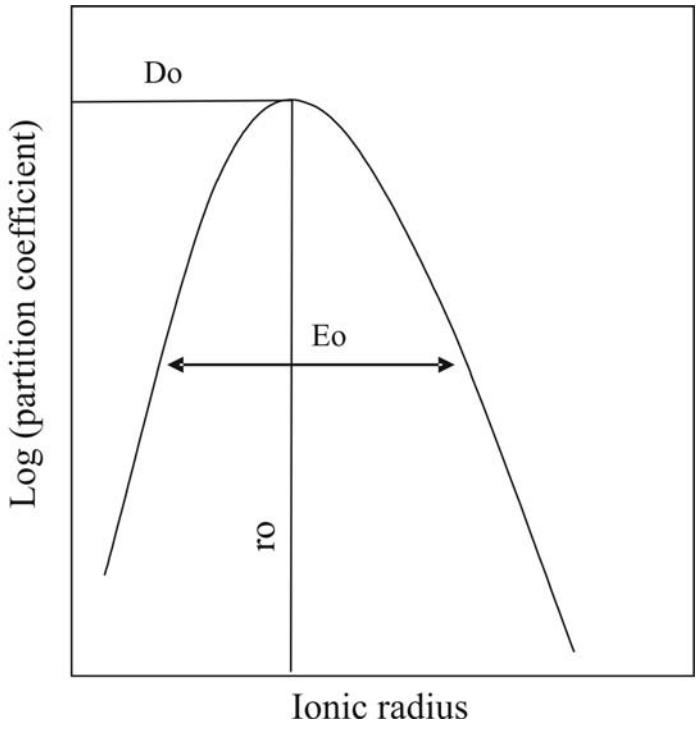

Fig. 2.17. Effect of ionic radius on mineral-melt partition coefficients of isovalent trace element cations. For an isovalent series of cations with charge n^+ and radius r_i entering a crystal lattice site M, the partition-coefficient, $D_{i(M)}$, can be described in terms of three parameters: $r_{o(M)}^{n+}$, the optimal radius of the crystal lattice site of substitution; $E_{s(M)}^{n+}$, the elastic response of the site (as measured by Young's Modulus) to the lattice strain caused by substitution of cations that are larger or smaller than the site size, and $D_{o(M)}^{n+}$, the strain-compensated partition-coefficient for an (ideal) cation that perfectly fits into the lattice site without strain, according to the equation:

$$D_i = D_{o(M)}^{n+} \times \exp\left[\frac{-4\pi N_A E_M^{n+}\left[\frac{1}{2} r_{o(M)}^{n+}\left(r_i - r_{o(M)}^{n+}\right)^2 + \frac{1}{3}\left(r_i - r_{o(M)}^{n+}\right)^3\right]}{RT}\right] \quad (2.7)$$

Where N_A is Avogardro's Number = $6.022 \times 10^{23} mol$. R is the gas constant and T the absolute temperature of the system.

The partitioning behaviour of any series of isovalent trace element cations between silicate minerals and their coexisting melts can be rationalised in terms of a physical model in which the size and elasticity of the crystal lattice sites play a critical role (Blundy and Wood, 1994). This is a quantitative model that describes the partitioning of trace elements as a function of pressure, temperature, bulk composition, and the elastic properties of the cationic site in which trace elements enter.

Qualitatively, the model rests on the property that substituting a cation with a different ionic radius than that of the major cation generates a strain energy that is proportional to a measure of the stiffness (Young's Modulus, E_s) of the cation-oxygen bonds in that site. If the substituting cation is larger than the major cation, it will exert a positive strain on the site. If, however, the substituting cation is smaller, it will exert a negative strain on the site.
Brice (1975) presented a mathematical expression for the strain for a perfectly spherical crystal lattice site:

$$\Delta G_{Strain}^{xtal} = 4\pi E_s N_A \left[\frac{r_o}{2}(r_o - r_i)^2 + \frac{1}{3}(r_o - r_i)^3 \right] \quad (2.8)$$

Where E_s is the Young's Modulus, N_A is Avogadro's number, r_o is the radius of the site, and r_i is the radius of the substituting cation.

The strain energy has a largely parabolic dependence on cationic radius, exhibiting a minimum strain when the substituting cation has identical radius to the site radius r_o.
Wood and Blundy (1994, 1997) showed that the partition coefficient of an element substituting into a given site is expressed as:

$$D_i = D_o \times \exp\left[\frac{-4\pi E_s N_A \left(\left(\frac{r_o}{2} \right)(r_o - r_i)^2 + \left(\frac{1}{3} \right)(r_o - r_i)^3 \right)}{RT} \right] \quad (2.9)$$

where R represents the gas constant, T is the absolute temperature, and D_o represents the partition coefficient of the major cation in that site, that is, the case in which the strain on that site is zero.

For a given charge, equation (2.9) represents a parabola, whose maximum is represented by D_o and whose curvature (or tightness) depends on Young's Modulus, E_s.

By fitting the experimentally determined D_i values to equation (2.9), best-fit values for D_o, E_s and r_o were obtained for each isovalent series of trace element ions (see **Table 2.15** for a summary of the regression lattice site parameters, as estimated from the experimental partitioning data).

Table 2.15. Lattice site parameters for the elastic strain model, as estimated from the partitioning data.

Phase	Lattice site	Elements	Charge	r_o (Å)	E_s (kbar)	D_o	Run T°C
Biotite	K	Alkali earth	1+	1.406 ± 0.022	370 ± 95	3.374 ± 0.194	800
	K	Alkaline earth	2+	1.356	650	1.794	800
	K	LREE	3+	1.137	3230	3.368	800
	M2	Transition	2+	0.670 ± 0.009	6840 ± 1320	91.341 ± 5.378	800
	M1	HREE	3+	0.839	13630	0.459	800

As observed from the model-fit curves and equation (2.9), E_s increases with increasing cationic charge and the higher the charge, the tighter the parabola. Qualitatively, this results from the fact that the higher the charge, the higher the coulombic anion-cation attraction and hence the stronger the bond. The actual height of each parabola depends on the equilibrium partition coefficient of the strain-free cation.

The importance of Wood and Blundy's formulations is two-fold. First they provide a simple physical explanation for the controls of trace-element partitioning. Second, they provide a means of predicting partition coefficients when experimental data is not available.

2.3.3. Partitioning of trace elements between allanite and melt

Trace element concentrations in allanite and coexisting melt together with their partition coefficients are listed in **Table 2.16**. As a run product, allanite is observed to have crystallised in only those samples doped with trace amounts of REEs in the starting mixtures. The REEs are highly compatible in allanite with their partition coefficients showing a considerable range in magnitude and range from ~ 390, for Ce, to about 40, for Er at the experimental conditions of 800°C and 2 kbar.

Allanite is known to incorporate large amounts of rare earth elements. This significantly affects the distribution of trace elements during late-stage fractional crystallisation and partial melting. It is for this reason that partition coefficients between allanite and silicate melt is an important control of trace elements in magmas during differentiation and therefore important parameters for geochemical modelling of petrogenetic processes. The fit-curve shows that all REEs partition compatibly in the octahedral Ca-site of the allanite crystal structure. It can be easily predicted from the model-fits, that allanite-melt partition coefficient for the REEs range from 15, for Lu, to about 420 for La, which almost ideally fits without strain into the Ca-site.

Table 2.16. Run tables containing experimental conditions and products, concentrations of trace-element oxides (EMPA), molar ratios of Fe and Mg in allanite, and the allanite-melt partition coefficients of trace elements.

Run No.	Exp cond.& duration			Starting materials		Run products (phases)	Trace	Conc. (wt%) of element oxide				D.coefficient	
	T/°C	P/bar	t/days	components	wt%		elts	rsd glas	error (±)	Allanite	error (±)	D	error (±)
	800	2	30	Hg,An,Bt,H_2O	99.59	**Allanite** (Fe 75, Mg 25),							
70/M32				Pr_2O_3	0.21	amphibole, magnetite, biotite,	**Pr**	0.0778	0.0076	26.4350	0.7439	**339.9640**	9.5664
70/M32				Er_2O_3	0.19	pyroxene and residual glass	**Er**	0.0716	0.0092	2.6030	0.2785	**36.3525**	3.8888
	775	2	30	Hg,An,Bt,H_2O	99.59	**Allanite** (Fe 73, Mg 27),							
73/M32				Pr_2O_3	0.21	amphibole, biotite,	**Pr**	0.0392	0.0057	25.6671	1.3133	**654.1368**	33.4692
73/M32				Er_2O_3	0.19	pyroxene and residual glass	**Er**	0.0435	0.0147	2.5404	0.2643	**58.3684**	6.0715
	800	2	35	Hg,An,Bt,H_2O	99.21	**Allanite** (Fe 75, Mg 25),							
20/M52				Nd_2O_3	0.19	pyroxene, magnetite,	**Nd**	0.0885	0.0063	25.5675	0.5600	**288.8983**	6.3279
				Rb_2O	0.60	biotite and residual glass							
	775	2	35	Hg,An,Bt,H_2O	99.21	**Allanite** (Fe 75, Mg 25),							
75/M52				Nd_2O_3	0.19	pyroxene, magnetite,	**Nd**	0.0402	0.0045	25.2738	0.7747	**628.5463**	19.2663
				Rb_2O	0.60	biotite and residual glass							
	750	2	35	Hg,An,Bt,H_2O	99.21	**Allanite** (Fe 71, Mg 29),							
102/M52				Nd_2O_3	0.19	pyroxene, plagioclase,	**Nd**	0.0240	0.0061	23.0900	0.3536	**962.8857**	14.7437
				Rb_2O	0.60	biotite and residual glass							
	800	2	45	Hg,An,Bt,H_2O	98.92								
38/M70				CeO	0.20	**Allanite** (Fe 78, Mg 22),	**Ce**	0.0678	0.0087	26.1156	0.6288	**385.4126**	9.2794
38/M70				Cs_2O	0.44	pyroxene, magnetite,	**Cs**	0.4682	0.0075	0.5042	0.0107	**1.0770**	0.0228
38/M70				ZrO_2	0.26	biotite and residual glass	**Zr**	0.0238	0.0112	0.0574	0.0367	**2.4111**	1.5402
38/M70				Nb_2O_5	0.17		**Nb**	0.1198	0.0152	0.0334	0.0138	**0.2793**	0.1149
38/M70							**Mg**	0.1607	0.0126	1.9920	0.1096	**12.3983**	0.6823
38/M70							**Fe**	1.0640	0.0485	12.6530	0.2771	**11.8919**	0.2604
38/M70							**K**	1.7127	0.1586	0.3250	0.0660	**0.1898**	0.0385
38/M70							**Na**	2.4975	0.1077	0.0172	0.0035	**0.0069**	0.0014
38/M70							**Ca**	1.5000	0.0367	9.7870	0.1471	**6.5247**	0.0981

Hg = Haplogranite, An = Anorthite, Bt = Biotite. For all cases H2O = 11.10 wt%, An = 7.49 wt%, Bt = 13.68 wt%, Hg = 67.73 wt%.

Table 2.17. Summary tables for **allanite-melt** partition coefficients of REEs and their ionic radii (adapted from Shannon, 1976)

Run No.	ion	IR (Å)	D_i	±	Run T
38/M70	Na^{1+}	1.020	0.0069	0.0014	800°C
38/M70	K^{1+}	1.380	0.1898	0.0385	800°C
38/M70	Cs^{1+}	1.670	1.0770	0.0228	800°C
70/M32	Ca^{2+}	1.000	6.5247	0.0981	800°C
20/M52	Mg^{2+}	0.720	12.3983	0.6823	800°C
70/M32	Fe^{2+}	0.780	11.8919	0.2604	800°C
38/M70	Ce^{3+}	1.010	385.4126	9.2794	800°C
70/M32	Pr^{3+}	0.990	339.9640	9.5664	800°C
73/M32	Pr^{3+}	0.990	654.1368	33.4692	775°C
20/M52	Nd^{3+}	0.983	288.8983	6.3279	800°C
75/M52	Nd^{3+}	0.983	628.5463	19.2663	775°C
102/M52	Nd^{3+}	0.983	962.8857	14.7437	750°C
70/M32	Er^{3+}	0.890	36.3525	3.8888	800°C
73/M32	Er^{3+}	0.890	58.3684	6.0715	775°C

2.3.3.1. Alkali earth elements in allanite

The alkali earth elements partition into the largest Cs site of the allanite crystal structure (see **Table 2.18**, for the lattice site parameters).

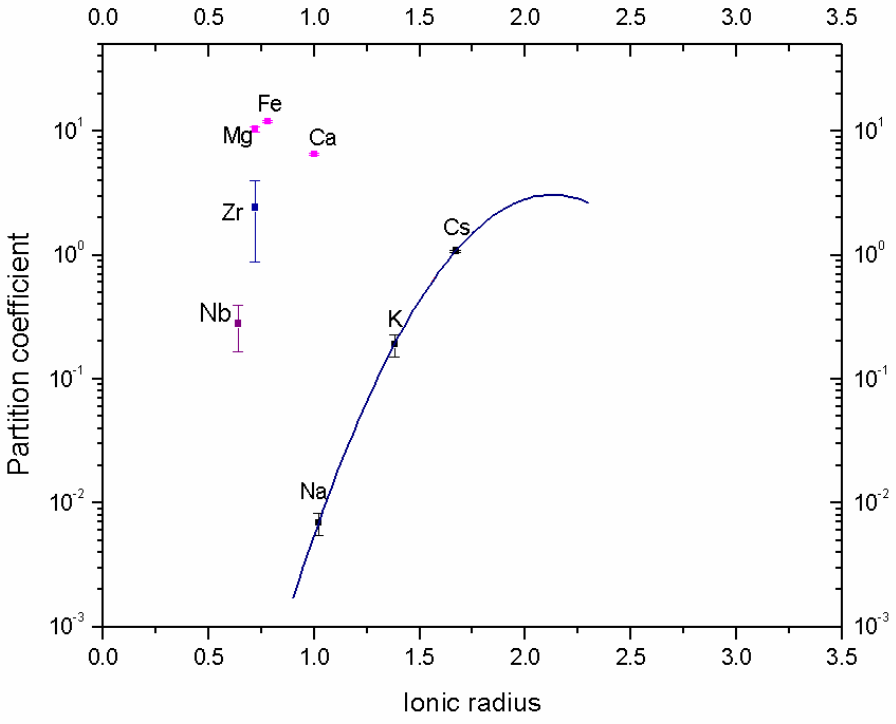

Fig. 2.18. Brice model fit of partition coefficient versus cation radius for alkali earth elements partitioning in allanite at 800°C and 2 kbar (see **Table 2.18**, for the lattice site parameters, D_o, r_o, and E_s).

2.3.3.2. Rare earth elements in allanite

The partitioning of all REEs in allanite was found to be highly influenced by temperature. In this study, partition-coefficients are seen to increase dramatically with falling temperatures, e.g. D_{Nd} ~ 290 at 800°C is almost doubled (~ 630) and tripled (~ 960) at 775°C and 750°C, respectively.

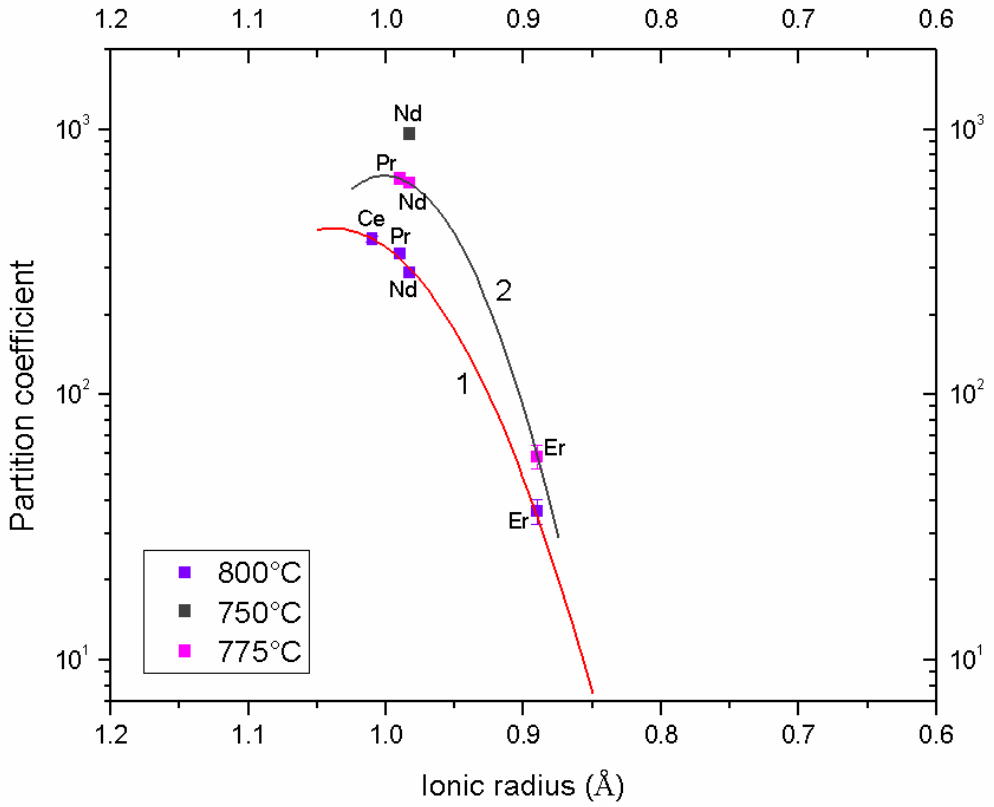

Fig. 2.19. Brice model fits of partition coefficients versus cation radius for REEs partitioning in allanite at 2 kbar, 800°C (curve 1), 775°C (curve 2), and 750°C (a single point for Nd). Partition coefficients for REEs in allanite are highly dependent on temperature. D_i increases and the optimal partitioning site radius, r_o, shifts to lower values with decreasing temperatures. See **Table 2.18** for the estimated site parameters.

Table 2.18. Lattice site parameters for the elastic strain model, as estimated from the partitioning data.

Phase	Lattice site	Elements	Charge	r_o (Å)	E_s (kbar)	D_o	Run T°C
	Ca	Alkali earth	1+	2.129	55	3.060	800
Allanite	Ca	REE	3+	1.038 ± 0.026	2610 ± 1170	423.377 ± 73.764	800
	Ca	REE	3+	1.001	4680	669.626	775

2.4. Geological implications of the partitioning data

2.4.1. Crystallisation and fractionation as ore-forming process

2.4.1.1. Batch crystallisation

A simple mathematical relation used to model the quantity of trace element variations (enrichment or depletion in the residual melt) during batch crystallisation is given by the equation:

$$\frac{C_{Lq}}{C_{Lq0}} = \frac{1}{D + F_{mlt}(1-D)} \qquad \text{(Shaw, 1970)} \qquad (2.10)$$

where C_{Lq0} is the initial concentration of the trace element in the original melt; C_{Lq} is the concentration of the trace element in the residual melt after some degrees (1-F_{mlt}) of crystallisation; D is the bulk partition-coefficient for the minerals that have crystallised from the melt; and F_{mlt} is the weight fraction of the melt remaining (i.e. residual melt).

Batch crystallisation requires that perfect equilibrium is obtained between the crystal phases and the residual melt during the entire crystallisation process, until physical removal and emplacement of the residual melt.

2.4.1.2. Enrichment/depletion of ore-metals in the residual melt

Results of quantitative calculations for the concentrations of trace ore-metal elements in the residual melt during cooling and progressive crystallisation of biotite in a synthetic granitic melt are listed in **Table 2.19** and graphically presented in **Figure 2.19**.

Table 2.19. Trace element distribution during batch crystallisation. Quantification of the degree of enrichment/depletion of a trace element in the residual melt expected after 5% (C_{Lq1}), 10% (C_{Lq2}), and 20% (C_{Lq3}) crystallisation of biotite. The concentration of the trace element in the original melt before the onset of crystallisation, C_{Lq0}, is equal to 1.

Biotite		Melt	Element:	Mo	Nb	Pb	W	Ta	Zn	Cu	Ti	Co	Ni
Xtl vol%	**(1-F_{mlt})**	**F_{mlt}**	**D_i:**	**0.164**	**0.536**	**0.936**	**1.788**	**1.888**	**8.453**	**11.253**	**14.04**	**37**	**84.15**
0	0.00	1.00	C_{Lq0}:	1.000	1.000	1.000	1.000	1.000	1.000	1.000	1.000	1.000	1.000
5	0.05	0.95	C_{Lq1}:	1.044	1.024	1.003	0.962	0.957	0.729	0.661	0.605	0.357	0.194
10	0.10	0.90	C_{Lq2}:	1.091	1.049	1.006	0.927	0.918	0.573	0.494	0.434	0.217	0.107
20	0.20	0.80	C_{Lq3}:	1.201	1.102	1.013	0.864	0.849	0.402	0.328	0.277	0.122	0.057

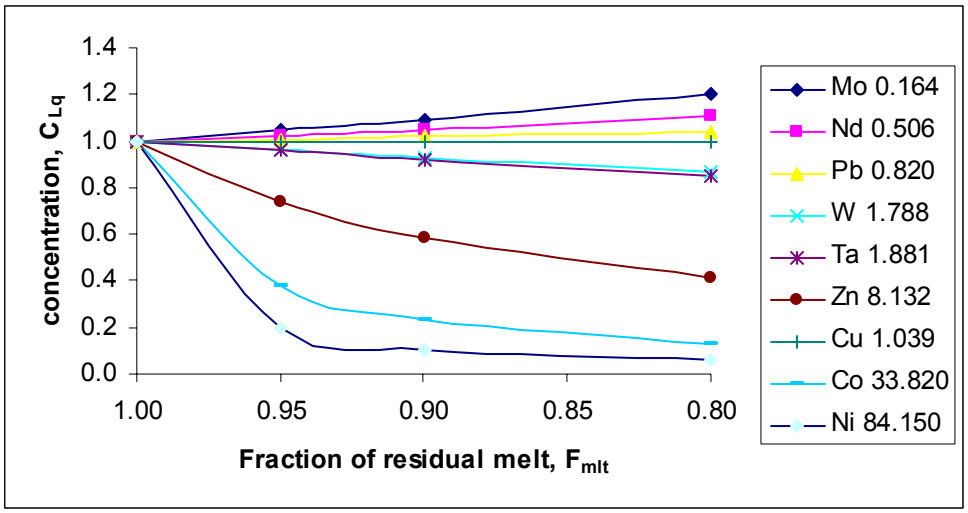

Fig. 2.20. Batch crystallisation model showing the degree of enrichment/depletion of ore-metal elements in the residual melt after 5% (C_{Lq1}), 10% (C_{Lq2}), and 20% (C_{Lq3}) crystallisation of biotite, as a function of the fraction of the remaining melt (F_{mlt}) using equation 1. See **Table 2.19** for the plotted data. Thus, compatible elements will be depleted whereas incompatible elements get enriched in the residual melt with progressive crystallisation of biotite from the granitic system.

Biotite is one of the first phases to crystallise during cooling of granite. Equation (2.10) has been used to quantify the amounts of ore-metals remaining in the residual melt, after crystallising 5, 10, and 20% of biotite (see results in **Table 2.19**). The degree of depletion increases with increasing compatibility of the trace-element with the early crystallising mineral assemblages. Compatible elements, Ni and Co, for instance, with high partition-coefficients, tend to be locked up in early formed rock-forming minerals (in this case biotite) and are typically not concentrated efficiently enough to form viable ore grade material. It is for this reason that there are no massive Ni and Co deposits associated with evolved granites. On the other hand, incompatible elements like Mo and Nb will be progressively enriched with increasing crystallisation of biotite. Batch crystallisation of biotite, however, does little to enrich or deplete the residual melt with elements whose partition coefficients are close to unity, e.g. Pb and Cu. Thus considerable amounts of Cu will remain in the melt even after crystallising/fractionating a lot of biotite (see Figure and **Table 2.19**). Eventually, at fluid saturation, a good proportion of Cu, still in the residual melt, will be extracted by the migrating hydrothermal fluids to be later concentrated and deposited as ore-deposits.

2.4.1.3. Enrichment/depletion of REEs in the residual melt

Contrary to the effect of batch crystallisation of biotite on ore-metals, REEs will be predominantly enriched in the residual melts with progressive cooling and crystallisation of the granitic system, since their partition coefficients are less than unity. This can be confirmed by the results of quantitative calculations listed in **Table 2.20** and graphically presented in **Figure 2.20**.

Table 2.20. Trace element distribution during batch crystallisation. Quantification of the degree of enrichment/depletion of a REE in the residual melt expected after 5% (C_{Lq1}), 10% (C_{Lq2}), and 20% (C_{Lq3}) crystallisation of biotite. The concentration of the REE in the original melt before the onset of crystallisation, C_{Lq0}, is equal to 1.

Biotite	melt	Element:	La^{3+}	Ce^{3+}	Pr^{3+}	Nd^{3+}	Ho^{3+}	Tm^{3+}	Yb^{3+}
		D_i:	**0.604**	**0.273**	**0.116**	**0.084**	**0.070**	**0.202**	**0.304**
xtl%	F_{mlt}	**$(1 - D_i)$:**	0.396	0.727	0.884	0.916	0.930	0.798	0.696
0	1.00	**C_{Lqo}:**	1.000	1.000	1.000	1.000	1.000	1.000	1.000
5	0.95	**C_{Lq1}:**	1.020	1.038	1.046	1.048	1.049	1.042	1.036
10	0.90	**C_{Lq2}:**	1.041	1.078	1.097	1.101	1.102	1.087	1.075
20	0.80	**C_{Lq3}:**	1.086	1.170	1.215	1.224	1.228	1.190	1.162

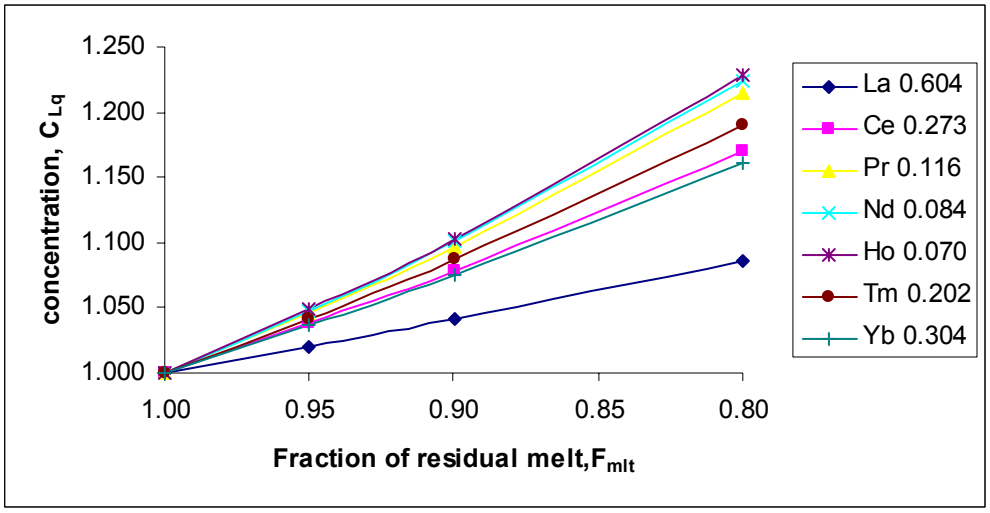

Fig. 2.21. A simple batch crystallisation model showing the degree of enrichment/depletion of REE in the residual melt relative to its concentration (C_{Lq0} = 1) in the original melt, as a function of the fraction of the remaining melt (F_{mlt}) using equation 1. See **Table 2.20**, for the plotted data.

2.4.1.4. Batch crystallisation of allanite

Allanite is an important accessory mineral in igneous systems because its crystallisation and fractionation leads to significantly low concentrations of the rare earth elements in the residual melts. Allanite/melt partition coefficients for REEs are anomalously high and a very small fraction of allanite crystallisation and fractionation may drastically deplete the melt of its rare earth content almost to zero (see **Table** and **Figure 2.21**).

Table 2.21. Trace element distribution during batch crystallisation. Quantification of the degree of enrichment/depletion of a REE in the residual melt expected after 5% (C_{Lq1}), 10% (C_{Lq2}), and 20% (C_{Lq3}) crystallisation of **allanite**. The concentration of the REE in the original melt before the onset of crystallisation, C_{Lq0}, is equal to 1.

Biotite	**melt**	**Element:**	**Cs^{1+}**	**Ce^{3+}**	**Pr^{3+}**	**Nd^{3+}**	**Er^{3+}**
		D_i:	**1.077**	**385.413**	**339.964**	**288.898**	**36.353**
xtl%	F_{mlt}	**$(1 - D_i)$:**	-0.077	-384.413	-338.964	-287.898	-35.353
0	1.00	**C_{Lq0}:**	1.000	1.000	1.000	1.000	1.000
5	0.95	**C_{Lq1}:**	0.996	0.049	0.056	0.065	0.361
10	0.90	**C_{Lq2}:**	0.992	0.025	0.029	0.034	0.220
20	0.80	**C_{Lq3}:**	0.985	0.013	0.015	0.017	0.124

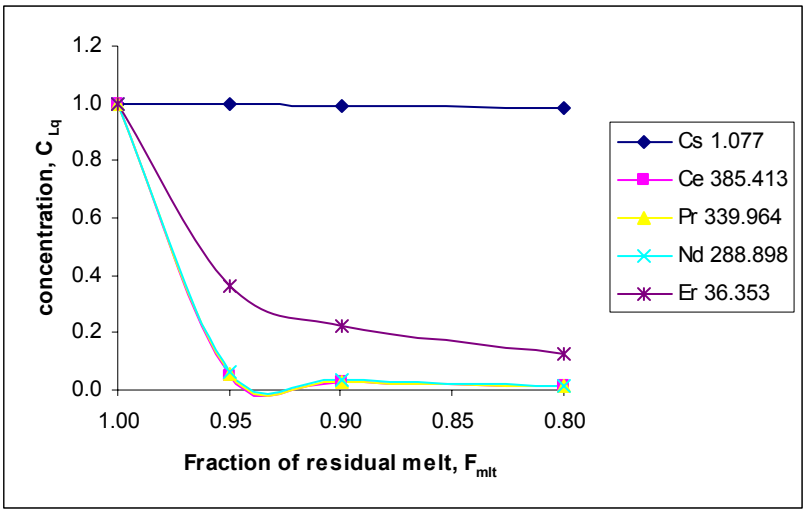

Fig. 2.22. A simple batch crystallisation model showing the degree of enrichment/depletion of REE in the residual melt expected after 5% (C_{Lq1}), 10% (C_{Lq2}), and 20% (C_{Lq3}) crystallisation of **allanite** as a function of the fraction of the remaining melt (F_{mlt}) using equation 2.10. The concentration of the REE in the original melt before the onset of crystallisation, C_{Lq0}, is equal to 1. See **Table 2.21**, for the plotted data.

2.4.1.5. Fractional crystallisation of biotite

A simple model that describes the distribution of trace elements in the residual magma during fractional crystallisation is mathematically expressed by the equation:

$$\frac{C_{Lq}}{C_{Lq0}} = F_{mlt}^{(D-1)} \quad \text{(Rollinson, 1993)} \tag{2.11}$$

This equation is also commonly known as the Rayleigh fractionation, where, like before, C_{Lqo} is the original concentration of trace element in the parental melt; D is the bulk partition coefficient of the fractionating mineral assemblage; F_{mlt} is the weight fraction of melt remaining.

In this situation, minerals accumulate on the floor, sides, and roof of the closed melt reservoir, stop their chemical exchange with the residual melt, and are essentially removed and isolated from the surrounding residual melt with only limited equilibration.

2.4.1.6. Enrichment/depletion of ore-metals in the residual melt

The extent of ore-metal enrichment and depletion during fractional crystallisation of a granitic melt is shown in **Table** and **Figure 2.22**. In comparison with batch crystallisation, fractional crystallisation has a more pronounced depleting effect from the melt for those elements with large values of partition coefficients. On the other hand incompatible elements and those whose partition coefficients are close to unity will be influenced in almost a similar manner by the two processes.

Table 2.22. Trace element distribution during **fractional crystallisation**. Quantification of the degree of enrichment/depletion of a trace element in the residual melt expected after 5% (C_{Lq1}), 10% (C_{Lq2}), and 20% (C_{Lq3}) crystallisation of biotite. The concentration of the trace element in the original melt before the onset of crystallisation, C_{Lq0}, is equal to 1.

Biotite	**melt**	**Element:**	**Mo^{6+}**	**Nb^{5+}**	**Pb^{2+}**	**W^{6+}**	**Ta^{5+}**	**Zn^{2+}**	**Cu^{2+}**	**Ti^{4+}**	**Co^{2+}**	**Ni^{2+}**
		D_i:	**0.165**	**0.506**	**0.820**	**1.788**	**1.881**	**8.132**	**1.039**	**13.581**	**33.820**	**84.150**
xtl%	F_{mlt}	**(D_i - 1):**	-0.835	-0.494	-0.180	0.788	0.881	7.132	0.039	12.581	32.820	83.150
0	1.00	**C_{Lqo}:**	1.000	1.000	1.000	1.000	1.000	1.000	1.000	1.000	1.000	1.000
5	0.95	**C_{Lq1}:**	1.044	1.026	1.009	0.960	0.956	0.694	0.998	0.524	0.186	0.014
10	0.90	**C_{Lq2}:**	1.092	1.053	1.019	0.920	0.911	0.472	0.996	0.266	0.031	0.000
20	0.80	**C_{Lq3}:**	1.205	1.117	1.041	0.839	0.821	0.204	0.991	0.060	0.001	0.000

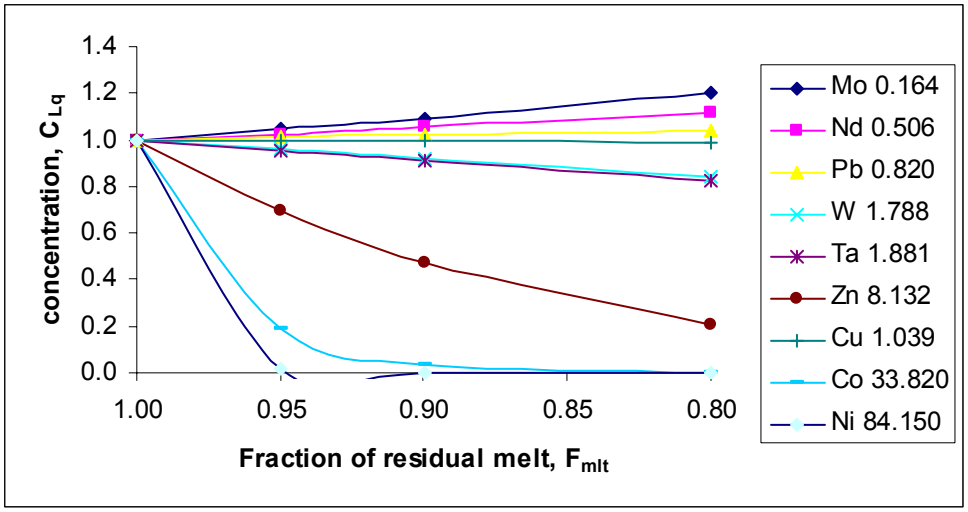

Fig. 2.23. Fractional crystallisation model showing the degree of enrichment/depletion of ore-metal elements in the residual melt after 5% (C_{Lq1}), 10% (C_{Lq2}), and 20% (C_{Lq3}) crystallisation of biotite as a function of the fraction of the remaining melt (F_{mlt}) using equation 2.11. See **Table 2.22** for the plotted data.

2.4.1.7. Enrichment/depletion of REEs in the residual melt

The enrichment of REEs in the residual melt during fractional crystallisation creates a similar trend pattern like that of batch crystallisation, although the elements will be a little more concentrated (see **Table** and **Figure 2.23**).

Table 2.23. Trace element distribution during fractional crystallisation. Quantification of the degree of enrichment of a REE in the residual melt expected after 5% (C_{Lq1}), 10% (C_{Lq2}), and 20% (C_{Lq3}) crystallisation of **biotite**. The concentration of the REE in the original melt before the onset of crystallisation, C_{Lq0}, is equal to 1.

Biotite	**melt**	**Element:**	La^{3+}	Ce^{3+}	Pr^{3+}	Nd^{3+}	Ho^{3+}	Tm^{3+}	Yb^{3+}
		D_i:	**0.604**	**0.273**	**0.116**	**0.084**	**0.070**	**0.202**	**0.304**
xtl%	F_{mlt}	**$(D_i - 1)$:**	-0.396	-0.727	-0.884	-0.916	-0.930	-0.798	-0.696
0	1.00	**C_{Lq0}:**	1.000	1.000	1.000	1.000	1.000	1.000	1.000
5	0.95	**C_{Lq1}:**	1.021	1.038	1.046	1.048	1.049	1.042	1.036
10	0.90	**C_{Lq2}:**	1.043	1.080	1.098	1.101	1.103	1.088	1.076
20	0.80	**C_{Lq3}:**	1.092	1.176	1.218	1.227	1.231	1.195	1.168

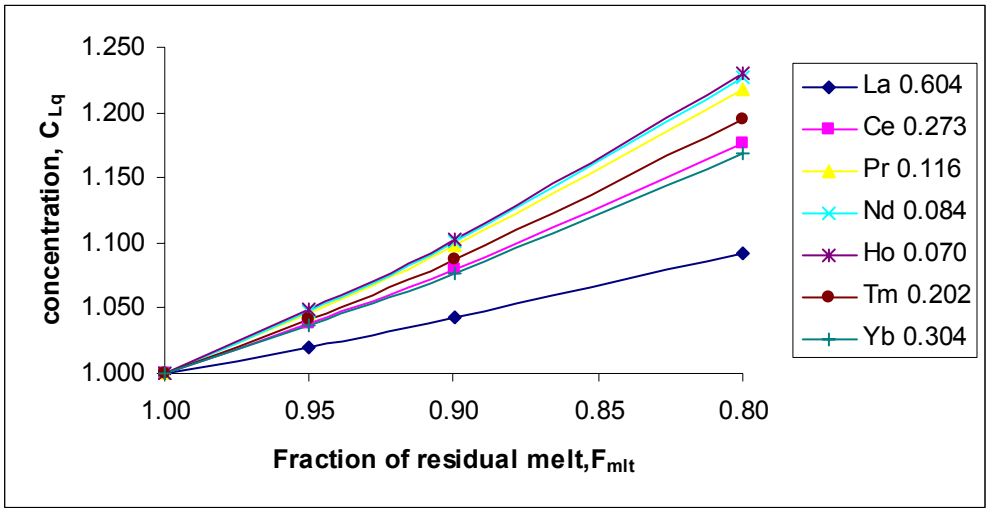

Fig. 2.24. A simple fractional crystallisation model showing the degree of enrichment of REE in the residual melt after 5% (C_{Lq1}), 10% (C_{Lq2}), and 20% (C_{Lq3}) crystallisation of **biotite**, as a function of the fraction of the remaining melt (F_{mlt}) using equation 2.11. See **Table 2.23**, for the plotted data.

2.4.1.8. Fractional crystallisation of allanite

Crystallisation and fractionation of allanite rapidly and completely depletes the melt of its REE content after as little as 5% crystallisation (see **Table** and **Figure 2.24**).

Table 2.24. Trace element distribution during fractional crystallisation. Quantification of the degree of depletion of a REE in the residual melt expected after 5% (C_{Lq1}), 10% (C_{Lq2}), and 20% (C_{Lq3}) crystallisation of **allanite**. The concentration of the REE in the original melt before the onset of crystallisation, C_{Lq0}, is equal to 1.

Biotite	**melt**	**Element:**	**Cs^{1+}**	**Ce^{3+}**	**Pr^{3+}**	**Nd^{3+}**	**Er^{3+}**
		D_i:	**1.077**	**385.413**	**339.964**	**288.898**	**36.353**
xtl%	F_{mlt}	**(D_i - 1):**	0.077	384.413	338.964	287.898	35.353
0	1.00	**C_{Lqo}:**	1.000	1.000	1.000	1.000	1.000
5	0.95	**C_{Lq1}:**	0.996	0.000	0.000	0.000	0.163
10	0.90	**C_{Lq2}:**	0.992	0.000	0.000	0.000	0.024
20	0.80	**C_{Lq3}:**	0.983	0.000	0.000	0.000	0.000

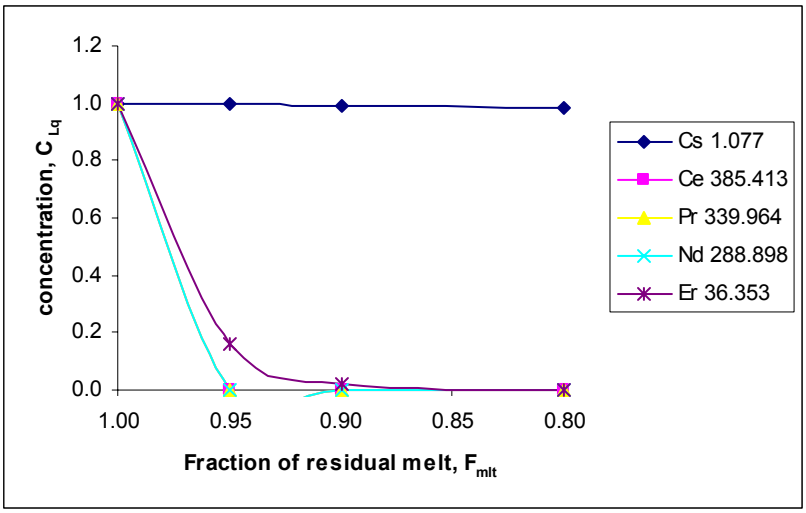

Fig. 2.25. A simple fractional crystallisation model showing the degree of enrichment/depletion of REE in the residual melt expected after 5% (C_{Lq1}), 10% (C_{Lq2}), and 20% (C_{Lq3}) crystallisation of **allanite** as a function of the fraction of the remaining melt (F_{mlt}) using equation 2.11. The concentration of the REE in the original melt before the onset of crystallisation, C_{Lq0}, is equal to 1. See **Table 2.24**, for the plotted data.

3. SPECIATION AND OXIDATION STATE OF COPPER IN SILICATE MELTS

3.1. Aims

The partitioning of trace elements between rock-forming minerals and residual melts during fractional crystallization in a granitic system, at any equilibrium conditions of temperature and pressure, is significantly controlled by the prevailing oxidation state of the elements. Copper, for example, occurs in two oxidation states (i.e. Cu^{1+} and Cu^{2+} cations) with different ionic radii and charge and will each consequently partition differently between the silicate melt and crystals in equilibrium. This implies that the different oxidation states of the same element result in different mineral/melt partition coefficients. Similarly, at magmatic fluid saturation the elements' fluid/melt partitioning will largely depend on the oxidation states of the trace elements involved. It is, therefore, important to know the oxidation state of the prevailing copper species in silicate melts under geologically reasonable conditions.

For a melt of fixed composition, the fugacity of oxygen controls the redox ratio of copper (i.e. Cu^{2+}/Cu^{1+}) in the silicate melt. This phenomenon has already been studied, e.g. by Canil, 2004, for the redox ratios Cr^{2+}/Cr^{3+} and V^{2+}/V^{3+}. The olivine/melt partition coefficients for chromium and vanadium were found to be very sensitive to changes in oxygen fugacity.

In this study silicate melts from a wide range of compositions were investigated, including granites, alkali basalt, tholeiite and andesite, as these are compositions well known for their geological relevance as far as magmatic-hydrothermal ore-deposit formation is concerned. In addition, this choice avails one the opportunity to observe experimentally how the physical-chemical properties of a melt change with composition. By varying the molar ratios (Na+K)/Al for the haplogranite changes in the speciation and oxidation state of copper can be easily observed from changes in colour intensity of the glasses quenched from melts.

As regards to the structure of silicate melts, metal cations may be divided into two categories: network-formers and network-modifiers (Bottinga et al., 1972). Network-forming cations occur in tetrahedral coordination in various polymers or units in the melt, whereas the network-modifiers connect such units together. Network-formers include mostly tetrahedrally coordinated cations like Si^{4+}, Al^{3+}, Fe^{3+} and more rarely B^{3+}, P^{3+}, and Ti^{4+}, among others. In the case of AlO_4 and $Fe^{3+}O_4$ tetrahedra, each tetrahedron has a -1 formal charge. Charge balancing requires that a monovalent cation or half a divalent cation be associated with the negatively charged tetrahedron. Typical charge-balancing cations in silicate minerals and melts are K^+ and Na^+, as in alkali feldspars, and Ca^{2+}, in anorthite. Silica, SiO_2, is the simplest chemical compound relevant to the structure of magmatic liquids. Structural information indicates a three dimensional interconnected structure of vitreous SiO_2 (Soules, 1979). In this structure, nearly all the oxygen atoms act as bridges between two silicon atoms which are in tetrahedral coordination with oxygen. Oxygen in such a structural position is referred to as "bridging oxygen" (BO).

The addition of alkali or alkaline-earth oxides to silica melt results in the formation of nonbridging oxygen atoms (NBO). Such oxygen atoms are bonded to both network-modifying metal cations and tetrahedrally coordinated cations in the silicate network. Metal cations act, therefore, as links between the various anionic structural units with the tetrahedrally coordinated cations that occur in the melt. Alkali and alkaline earth oxides are known to act as depolymerising agents on the silicate tetrahedral network structure. The degree of polymerization of a silicate melt is often expressed as the ratio of nonbridging oxygens per tetrahedrally coordinated cations (NBO/T). Thus, a three-dimensionally interconnected structure has NBO/T = 0, a sheet has NBO/T = 1, a chain or a single ring has NBO/T = 2, a dimer has NBO/T = 3, and a monomer has NBO/T = 4.

3.2. Experimental methods

3.2.1. Sample synthesis

3.2.1.1. Starting materials and preparation of glass samples

Starting materials consisted of seven synthetic silicate glass types prepared from powders of reagent-grade oxides and carbonates, with compositions equivalent to those of average magmatic compositions for a series of haplogranites (4 types), tholeiite, alkali-basalt, and andesite. Each glass type was doped with 1.0 wt % CuO. With regard to the haplogranites, a series of bulk compositions were prepared with varying molar ratios of $(Na_2O+K_2O)/Al_2O_3$, the inverse of aluminium saturation index (ASI). Thus, the haplogranite sample series prepared included $[Na_2O+K_2O]/Al_2O_3$ =1.0, 1.5, 2.0, and 2.5. ASI is a molar ratio usually employed to quantify the degree of polymerization in the silicate melts. The aluminium saturation index was varied quite significantly over the chosen range of bulk haplogranite compositions keeping the SiO_2 content and the molar ratio Na_2O/K_2O relatively constant. In terms of the degree of polymerization, these bulk compositions represent a wide range of naturally occurring melts.

The starting materials for the haplogranites (HPG1, HPG15, HPG2, and HPG25) were prepared by weighing and mixing appropriate amounts of reagent-grade oxides, carbonates and hydroxides (Na_2CO_3, K_2CO_3, SiO_2 and $Al(OH_3)$. Each type of haplogranite was doped with a trace amount of Cu (1.0 wt%), as CuO. The mixtures were then ground in turn under acetone in an automated electric ball mixer/grinder (Planetenkugelmuehle) for about 30 minutes to produce homogeneous mixtures, taking care to thoroughly clean the mixing equipment in between, to avoid contamination. The mixtures were first left to dry slowly in free-air at room temperature and subsequently overnight in a low temperature oven at 150°C. The dried, but still hot, mixtures were allowed to cool under vacuum in a desiccator, before being ground to homogeneous fine powders. The powdered mixtures were, in turn, packed into alumina crucibles and put in a furnace to slowly decarbonise at 1100°C for about 24 hours and later quickly heated to melt at 1400°C over 4 hours. The melt was kept at this temperature for 2 hours and finally quenched into glass. These preliminary glasses were crushed into small grains, reground into fine powders as before, and then heated to melt at 1600°C. The melt was kept at this temperature for 2 hours before being quenched to yield glasses of the starting materials (see chapter 2, section 2.2.2, for further details of glass preparations). In addition to the ASI-series of haplogranite glasses, glasses of andesite (ANDS), tholeiite (THLT) and alkali-basalt (ALKB) compositions were also prepared in a similar manner as outlined above. In this case, however, additional component oxides (i.e. CaO and MgO) were included in the mixtures. Iron oxides (i.e. FeO and Fe_2O_3), which often occurs in natural samples, were replaced by MgO and Al_2O_3 respectively and TiO_2 was ignored (see **Table 3.1**, for nominal compositions of starting materials). As before, the oxides Na_2O, K_2O, CaO, MgO, and Al_2O_3 were calcinated from reagent-grade carbonates and hydroxides, including Na_2CO_3, K_2CO_3, Ca_2CO_3, $Mg(OH)_2$ and $Al(OH)_3$.

Table 3.1. Nominal compositions of the starting materials for copper speciation experiments. Some oxides were obtained from calcinations of their respective carbonates and hydroxides, as described in the text.

Sample	ANDS	ALKB	THLT	HPG1	HPG15	HPG2	HPG25
wt%							
SiO_2	58.84	48.39	52.24	77.90	77.90	77.90	77.90
Na_2O	3.53	3.31	2.30	4.68	5.80	6.59	7.18
K_2O	1.65	1.14	0.42	4.19	5.19	5.90	6.42
Al_2O_3	20.60	21.33	15.82	12.23	10.11	8.61	7.50
MgO	7.48	14.88	17.40	0.00	0.00	0.00	0.00
CaO	6.90	9.95	10.82	0.00	0.00	0.00	0.00
CuO	1.00	1.00	1.00	1.00	1.00	1.00	1.00
Total	100.00	100.00	100.00	100.00	100.00	100.00	100.00

Note: Data for chemical compositions of andesites, alkalibasalts, and tholeiites was taken from LeMaitre, 1976. Sample names are written in brevity, i.e. HPG1, HPG15, HPG2, HPG25 = Haplogranites, with nominal molar ratios (Na+K)/Al = 1.0, 1.5, 2.0, and 2.5 ; ANDS = andesite, THLT = tholeiite and ALKB = alkalibasalt.

Images of experimental starting glasses can be seen in **Figure 3.6**. Among those representing the haplogranite series, (i.e. HPG1, HPG15, HPG2, and HPG25) it was observed that the blue colour of glass becomes progressively more intense as the molar ratio $\frac{Na+K}{Al}$ in the sample increases. Similarly the blue-greenish colour is most intense in glass of andesitic (ANDS) composition becoming less and least intense in alkalibasalt (ALKB) and tholeiite (THLT) glass, respectively.

For each composition an adequate amount of glass-material was prepared and apportioned for the following investigations:

(i) electron microprobe analysis (EMPA),
(ii) optical spectrometry,
(iii) density determination,
(iv) oxygen fugacity experiments with a vertical tube (gas-mixing) furnace, and
(v) preparation of glass standards.

3.2.1.2. Chemical composition of samples

A small fragment from each type of glass composition (HPG1, HPG15, HPG2, HPG25, ANDS, ALKB, and THLT) was mounted in crystal bond on a glass slide and polished, as before, with a series of aluminium oxide powders of varying grain sizes and subsequently with diamond paste of grain size 1.0 µm to obtain a fine smooth surface of high-quality polish. The polished sections were washed clean in ethanol and distilled water and then left to dry, first in free air at room temperature, for a few days, and later in dry air-free conditions in desiccators.
The dried sections were carbon-coated and analysed with a JEOL8900 electron microprobe at the University of Tuebingen, following the same procedure, as already described in chapter 2, sub-section 2.2.3.3, to determine the bulk compositions of

each glass type. The results of this analysis (see **Table 3.2**) are the bulk chemical compositions of the starting materials which were used for the subsequent oxygen fugacity experiments.

Table 3.2. 10 point averages from the EMPA of silicate glasses. These are the bulk compositions of starting materials (glasses) for copper speciation experiments.

Sample	ANDS	ALKB	THLT	HPG1	HPG15	HPG2	HPG25
wt%							
SiO_2	60.06	49.78	51.11	80.49	80.60	79.72	81.00
Na_2O	3.61	3.35	2.56	2.07	3.27	4.43	4.85
K_2O	1.36	0.98	0.33	3.42	4.33	4.89	5.18
Al_2O_3	19.98	20.84	14.45	12.03	10.82	8.88	7.75
MgO	7.53	14.87	18.69	0.00	0.00	0.00	0.00
CaO	7.08	10.36	10.71	0.00	0.00	0.00	0.00
CuO	0.938	0.708	0.684	0.315	0.344	0.813	0.843
Total	100.56	100.89	98.53	98.33	99.36	98.73	99.62

Table 3.3. Comparison of the molar ratios (Na+K)/Al) in glasses and raw mixtures.

Compostion	THLT	ALKB	ANDS	HPG1	HPG15	HPG2	HPG25
(Na+K)/Al (Molar)							
Nominal composition (mixture)	0.27	0.31	0.37	1.00	1.50	2.00	2.50
Bulk composition (glass)	**0.32**	**0.32**	**0.37**	**0.60**	**0.93**	**1.42**	**1.75**
NBO/T (glass)	**1.28**	**1.02**	**0.50**	**0.020**	**0.07**	**0.13**	**0.15**

Note: The molar ratios (Na+K)/Al in the original mixtures for ANDS, ALKB, and THLT are retained in the glass. Therefore the calculated values in glass are similar to those calculated for their corresponding nominal mixtures. This is not the case for the haplogranites. The values of molar ratios (Na+K)/Al in glasses are significantly less than the values calculated for the nominal mixtures in **Table 3.1**. This is because Na and K are volatile elements and most likely small amounts would be lost by heating during glass preparation. It is also evident that glasses HPG1, HPG15, and (HPG2 & HPG25) are peraluminous, subaluminous, and peralkaline, respectively. NBO/T decreases from 1.28 for THLT to 0.02 for HPG1 and again increases with increasing Na+K/Al ratio in the haplogranites to 0.15 for HPG25.

3.2.1.3. Determination of the density of silicate glasses

The density of anhydrous silicate melts/glass is dependent on the ratio of network-forming to network-modifying species. Silicate melts rich in SiO_2, Al_2O_3, and the associated oxides of the charge-balancing cations have lower densities than relatively SiO_2-poor and MgO-, and CaO-rich melts.

In this study the densities of different silicate glasses under ambient conditions were determined using a pycnometer. This is a specific gravity bottle or standard flask for measuring and comparing the densities of liquids and solids. The pycnometer used was made of boron-silicate glass (maximum volume 50 ml) with a side capillary tube

and a ground thermometer with a measuring range of 10-40°C.

Procedure

A mass (m_1) of carefully selected homogeneous and bubble-free glass grains from each silicate glass type was precisely measured using sensitive laboratory scales. This was followed by measuring weight (m_2) of the pycnometer filled with distilled water at room temperature, approximately 20°C. Finally the pre-weighed glass sample grains were carefully introduced into a dry, empty pycnometer using a pair of forceps. It was then filled with water and the mass (m_3) measured.
This procedure can be summarised as follows:

1. mass of the glass sample, m_1,
2. mass of pycnometer + H_2O, m_2,
3. mass of pycnometer + sample + H_2O, m_3,
4. mass of the H_2O displaced by sample, m (H_2O),
5. volume of the displaced water = volume of the sample, V (H_2O), and
6. density of the sample, ρ (Spl) = m_1/V (H_2O).

Steps 4 to 6 are calculated as follows:

4. m (H_2O) = $m_1 + m_2 – m_3$,

5. V (H_2O) = ($m_1 + m_2 – m_3$) / ρ (H_2O)

7. ρ (Spl) = m_1 / V (H_2O).

It should be observed that during the experiment no air-bubbles remained in the water filled pycnometer and that its entire outer surface was carefully wiped dry. All measurements had to be done at the same temperature such that the volume of the pycnometer remained constant.

The density of water at 20°C, ρ (H_2O) = 0.9982 g/ml

Tables 3.4 shows the results of density determination for the experimental silicate glass of tholeiite composition. A similar procedure was followed to determine the densities of other silicate glasses including andesite, alkalibasalt, haplogranite (1.0), haplogranite (1.5), haplogranite (2.0), and haplogranite (2.5).

Table 3.4. Determination of the density of a tholeiite glass using a pycnometer

T_w = 20°C and ρ_w = 0.9982 g/cm3						
No.	m_1 [g]	m_2 [g]	m_3 [g]	m [g]	V [cm^3]	ρ_s [g/cm^3]
1	0.5376	88.5896	88.9251	0.2021	0.2025	2.6553
2	0.5375	88.5898	88.9252	0.2021	0.2025	2.6548
3	0.5378	88.5894	88.9250	0.2022	0.2026	2.6550
4	0.5375	88.5895	88.9249	0.2021	0.2025	2.6548
5	0.5377	88.5896	88.9251	0.2022	0.2026	2.6545
Average	0.5376	88.5896	88.9251	0.2021	0.2025	**2.6549**
No.	ρ_s [g/cm^3]	v [g/cm^3]	v^2 [g^2/cm^6]			
1	2.6553	-0.0004	1.45E-07			
2	2.6548	0.0001	1.27E-08			
3	2.6550	-0.0001	3.06E-09			
4	2.6548	0.0001	1.27E-08			
5	2.6545	0.0004	1.92E-07			
Σv^2			3.66E-07			
	Σv^2	n	n(n - 1)	$\Sigma v^2/[n(n-1)]$	$\sqrt{\{\Sigma v^2/[n(n-1)]\}}$	
	3.66E-07	5	20	1.82969E-08	**0.0001**	

The densities of the other glass-types were similarly determined. **Table 3.5** shows results of the determined densities for the seven experimental glass types.

Table 3.5. Summary table for densities of experimental glasses

Glass type	Density, ρ_s[g/cm^3]	
	ρ_s	±
Tholeiite	**2.65485**	0.00014
Alkalibasalt	**2.62480**	0.00009
Andesite	**2.46618**	0.00033
Haplogranite (2.5)	**2.55013**	0.00006
Haplogranite (2.0)	**2.42401**	0.00016
Haplogranite (1.5)	**2.25505**	0.00039
Haplogranite (1.0)	**2.01473**	0.00021

3.2.1.4. Preparation of standards for Cu^{2+} in glass

Glasses allotted for standard preparation (see section 3.2.1.1) were crushed and ground into relatively fine powder and a few Pt/Rh capsules, at least three for each composition, prepared to hold the samples.

Capsule tubes made of Pt/Rh alloy material with dimensions 10 mm L, 5 mm OD and 0.3 mm wall thicknesses were used. One end of each tube (~ 1.5 mm length) had some of its inside wall-material hollowed out, reducing the wall thickness to ~0.2 mm while the other end of the tube was left with its normal wall thickness (0.3 mm). Each tube was supplied with two caps made of different materials (pure Pt and Pt/Rh). The Pt cap was adapted to give a perfect seal when fixed to the end of the tube with its inner wall hollowed out. This side was considered to be the top end of the capsule. The second cap made of the same alloy material as the tube (i.e. Pt/Rh) was arc-welded to the other end of the capsule.

Each empty capsule with one end still open was immersed in acetone and cleaned in an ultrasonic bath for about 5 minutes, after which it was packed to the brim with experimental glass samples in powder form. For each glass type a minimum of three capsules were prepared and clearly labelled for future identification. The loaded capsules were then carefully placed upright on an alumina plate and put into a high temperature furnace and heated to about 1200°C over 2 hours. This allowed the filled materials to shrink to a lower level leaving enough empty space for additional refills of same glass powders. The capsules were finally heated to 1400°C to melt the samples into homogeneous liquids which quenched to yield perfect short glass columns of about 4 mm from the bottom of the tube, leaving a clear empty space of about 4.5 mm length above the quenched glass material.

Approximately 2.45 mg of PtO_2 in powder form was added to the top of each glass column in the capsule. The capsule was finally closed with the top cap and carefully sealed off by arc-welding, using liquid N_2 to cool its top and bottom parts, to prevent excessive loss of O_2 from the heat sensitive PtO_2 reagent-grade powder. The completely sealed capsules were again placed on the alumina plate, standing the other way round, such that the PtO_2 powder was at the bottom of the tubes. In this way the released O_2 could quickly and thoroughly diffuse through the entire glass sample column during the heating process. The alumina plate holding the sample capsules was put carefully into the furnace and heated to 1250°C, over about 2 hours. The samples were kept at this temperature for half an hour before quenching. This enabled the released O_2 gas to uniformly diffuse through the entire molten glass material in the capsule, allowing all the free Cu^{+} ions in the melt to convert into Cu^{2+} ions by oxidation in a pure oxygen atmosphere (~ 20-30 bars of oxygen pressure), produced by the thermal decomposition of PtO_2.

$$PtO_2(s) \rightarrow Pt\ (s) + O_2(g) \qquad (3.1)$$

This process was confirmed by the intense blue/green colour of the resulting glass product. After the heating and quenching processes successful capsules were easily recognised by having one end bulging out due the accumulation of excess oxygen pressure in the perfectly sealed capsule. Any capsule with both ends still flat after the

heating process was considered dead i.e. was not perfectly sealed to confine the O_2 gas during the heating. **Figure 3.1** illustrates the entire procedure of standard preparation diagrammatically.

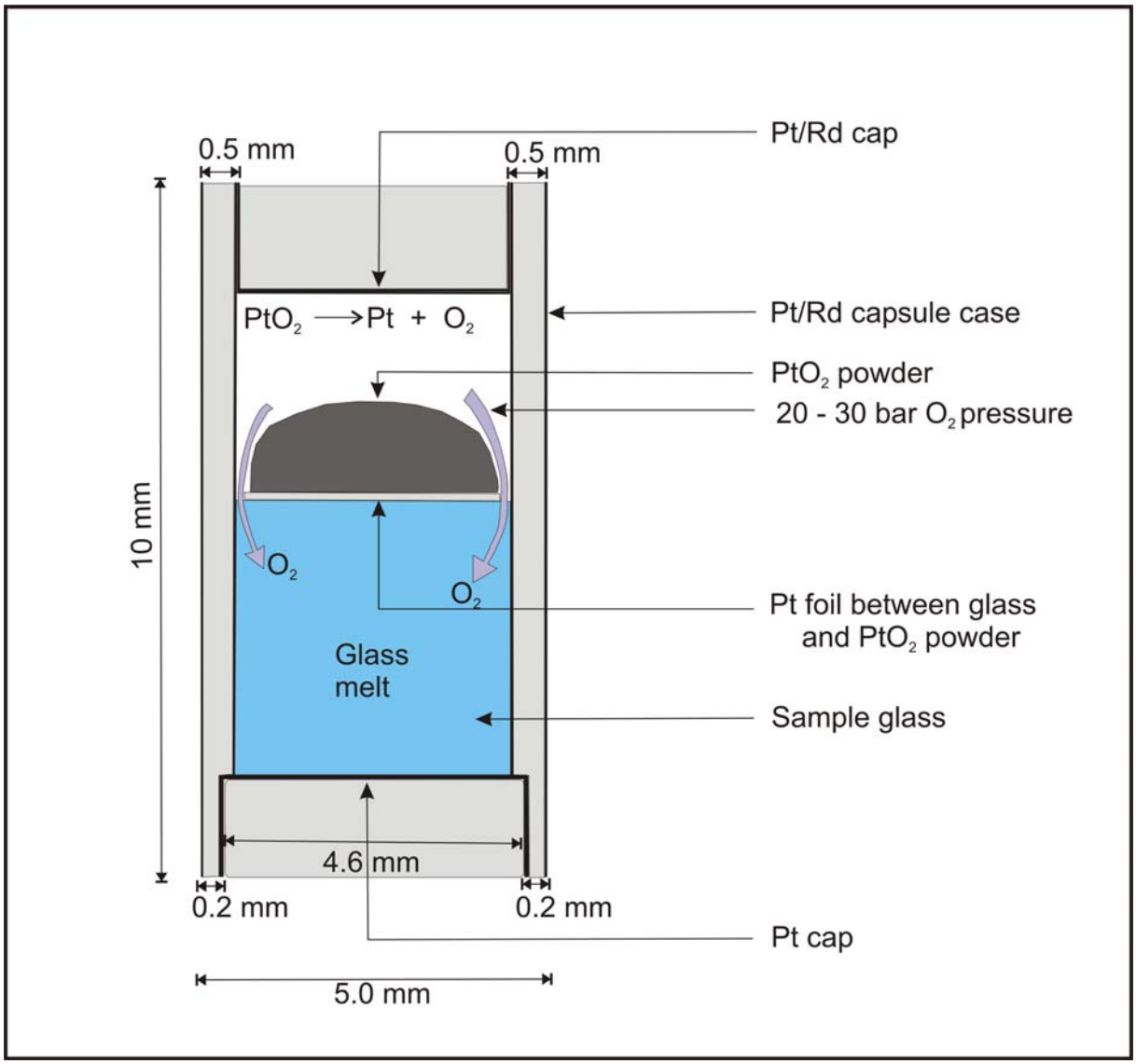

Figure 3.1. Cross-section of a Pt/Rh capsule loaded with a glass sample (blue) and PtO_2 (black). The column of sample glass is ~ 4 mm length and the PtO_2 powder weighs between 2.4 and 3.0 mg. When the sealed capsule is heated to 1250°C over two hours PtO_2 will decompose into Pt and O_2. An oxygen pressure between 20 – 30 bars develops in the empty space of the capsule and O_2 will diffuse through the molten glass material, oxidising all the Cu^{1+} species into Cu^{2+}. This reaction process is confirmed by a deep blue colour of the run products when the capsule is cut open. This is the standard glass. See text for further details of standard preparation.

The successful capsules were carefully cut open to extract the glass fragments or columns. The recovered samples were doubly polished, in preparation for optical spectroscopy (NIR spectroscopic analysis).
Glasses prepared in this way served as standards to determine the Cu^{2+}/Cu^{+} ratio in glasses reduced under different conditions of temperature and oxygen fugacity,

obtainable in the gas-mix furnace, as a result of a controlled steady flow of pure CO_2 gas or H_2/CO_2 gas-mixtures heated at a fixed temperature (see section 3.2.1.5).

Under the above given conditions of standard preparation, PtO_2 broke down to Pt producing O_2 (see equation 1) at a partial pressure corresponding to log fo_2 = +1.48, assuming an oxygen pressure of 30 bars in the melt atmosphere.

3.2.1.5. Gas-mixing furnace

Oxygen fugacity (fo_2) is an important intensive parameter, which often controls the stability of minerals and mineral assemblages and governs the evolution of magma and ore-forming hydrothermal solutions (I-Ming Chou, 1987). Gas-mixing techniques are the most commonly used methods for conveniently controlling oxygen fugacities in high temperature experiments conducted at approximately 1 bar pressure. Gas mixtures most often used are (CO_2/CO) or (CO_2/H_2) and their most common purpose is to specify the oxygen fugacities of the material being investigated at high temperature (Huebner, 1987). Gas-mixing techniques were originally developed to help determine the phase equilibria of oxides and silicates encountered in smelting iron ore and making steel (Muan and Osborn, 1965). Geoscientists have adopted these techniques to study the redox reactions among the phases that occur in natural, multicomponent systems and their synthetic analogues. The technique is now an essential aid to material scientists and geophysicists who need to maintain a single phase at a constant, known oxygen fugacity during physical property measurements or when they need to control the oxygen fugacity of a crystallizing melt.

3.2.1.6. The technique

CO_2 and H_2 gases from pressurised cylinder-tanks were allowed to flow through a system of control valves into a mixing chamber, where they were homogeneously mixed in known volumetric proportions, by means of programmable mass flow controllers and meters installed in the gas train line. The mixture was then allowed to flow through the copper pipe line into the hot preheated furnace, and finally exhausted into the open atmosphere (see gas-flow diagram and the oxygen fugacity sensor assembly unit **Figures 3.2** and **3.3**). The furnace is centrally equipped with a vertical ceramic muffle tube of appropriate hollow-diameter into which the samples and the oxygen sensor assembly are installed. The ceramic muffle tube is vertically and centrally installed in the furnace body with its upper and lower portions cooled by cold tap-water circulating through the attached cooling-jackets. The gas mixture is assumed to have equilibriated by the time it reaches the samples, usually located at the hottest spot of the furnace. The samples were hanged on Pt-wire loops attached to the alumina rods of the oxygen sensor assemblage. The type of gas to be mixed was chosen such that, at furnace temperature and pressure, an invariant equilibrium would develop and the fugacity to be controlled would therefore be defined.

In this study I carried out a series of experimental runs to investigate the effect of oxygen fugacity on the redox ratio of copper (Cu^{2+}/Cu^{+}) in a silicate melt, at various equilibrium temperatures. The runs were conducted in a GERO furnace (type: HTRV 70-250/16”), modified for gas mixing experiments.

Oxygen fugacity (fo_2) inside the furnace atmosphere (1 bar total pressure) was imposed by the CO_2/H_2 gas mixtures of varying ratios using mass flow controllers, T1 and T2, and an MKS programmable flow meter (type: PR 4000). The gas-mixture entered the furnace (entrance at the top) through a copper pipeline or conduit to occupy the entire furnace space and eventually exited into the free-atmosphere through a similar conduit at the bottom of the furnace.

Six sets of experimental runs were carried out using the following gas mixtures (arranged in order of increasing potential to reduce Cu^{2+} to Cu^{1+} ions) to control the oxygen fugacity inside the furnace:

1) Air (0.21 O_2) in a normal heating furnace
2) pure CO_2 gas flowing at a steady rate of 100CCM/sec,
3) CO_2/H_2 mixture in the ratio 400 CCM CO_2 to 2 CCM H_2,
4) CO_2/H_2 mixture in the ratio 200 CCM CO_2 to 2 CCM H_2,
5) CO_2/H_2 mixture in the ratio 200 CCM CO_2 to 6 CCM H_2, and
6) CO_2/H_2 mixture in the ratio 200 CCM CO_2 to 20 CCM H_2.

The fo_2 imposed by the CO_2 gas or CO_2/H_2 gas-mixtures in the furnace atmosphere, at a range of equilibrium temperatures (1200-1400°C), was measured in volts with an OMEGA voltmeter (type: HH M31) connected by Pt-wires to the Y-doped ZrO_2 oxygen sensor assembly installed into the furnace through the central upper-ceramic core lid (**Figure 3.3**). The measured voltage was then converted into fo_2 by applying equation (2).

Using the above stated ratios of gas-mixtures fo_2 was controlled at values of log fo_2 between ~ -2.72 (for pure CO_2 at 1400°C) and -9.61 (for CO_2/H_2 = 200/200 at 1200°C), see **Table 3.6**.

Table 3.6. Gas-mixtures and the log fo_2 they impart in the furnace at any fixed equilibrium temperature and pressure (1 atm)

Gas mixture	mix-ratios	log fo_2(1400°C)	log fo_2(1350°C)	log fo_2(1300°C)	log fo_2(1250°C)	log fo_2(1200°C)
Air	0.21O_2	-0.68	-0.68	-0.68	-0.68	-0.68
CO_2	pure	-2.72	-2.78	-2.88	-2.92	-2.99
CO_2/H_2	400/2	-3.83	-4.30	-5.06	-5.60	-6.04
CO_2/H_2	200/2	-4.73	-5.07	-5.52	-6.13	-6.93
CO_2/H_2	200/6	-5.53	-6.05	-6.80	-7.68	-8.33
CO_2/H_2	200/20	-7.38	-7.84	-8.37	-8.96	-9.61

Note: see equations (3.2) and (3.3) for the calculation of fo_2.

Two samples of glass materials could be run simultaneously. Each sample was wrapped in a Pt-foil, suspended on Pt-wire loops attached to the alumina rod supporting the thermocouple, and held close to the hottest central spot of the furnace. The samples were then isothermally heated at a given temperature for between 12 and 24 hours. The molten samples were held on the loops by surface tension and the high viscosity of the melts. The sample temperature was measured by an S-type thermocouple located just next to the hanging samples in the central and hottest part of the furnace. At the end of the experimental run the samples were quenched in air by slowly taking the charge out of the furnace (avoiding damage of the ceramic rods by thermal shocks). The samples cooled down to room temperature within a few minutes.

For every ratio of gas-mixture, a series of isothermal runs (in steps of 50°C from 1400 to 1250°C) were conducted for glass samples of haplogranitic, basaltic, tholeiitic and alkalibasaltic compositions.

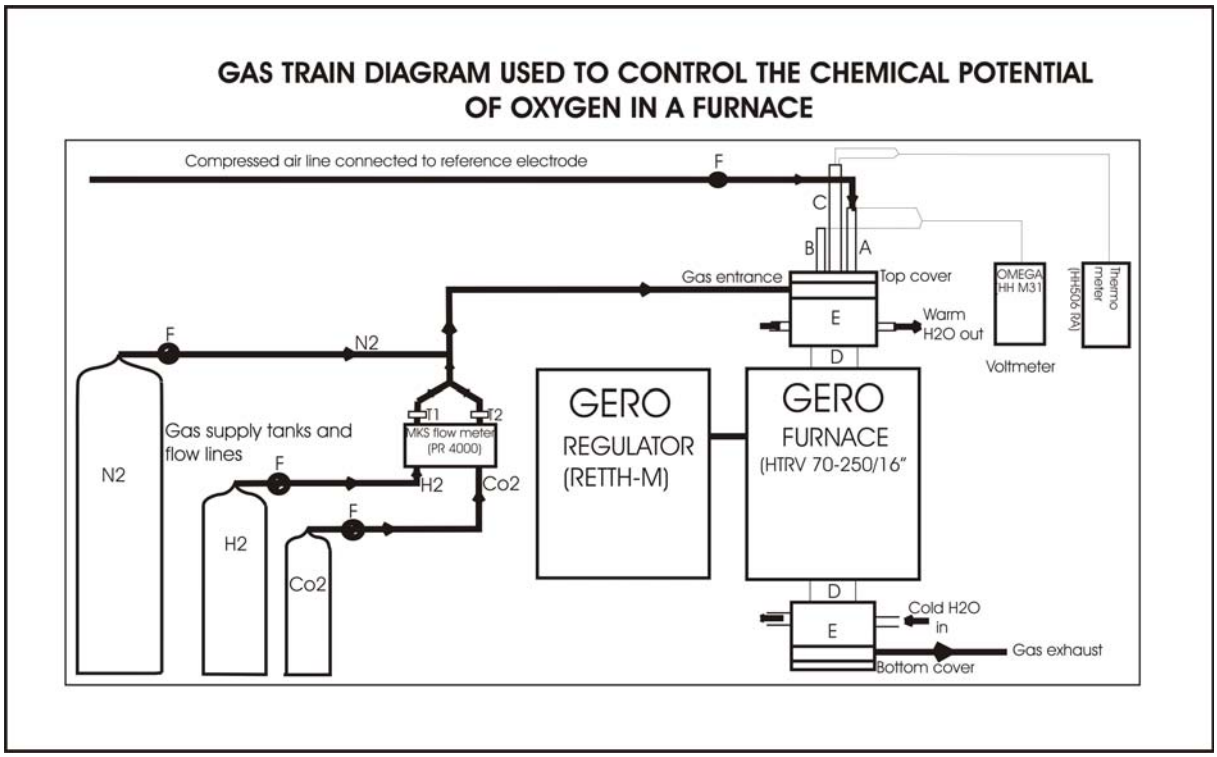

Fig. 3.2. Schematic representation of the conceptual design and integration of the gas-mixing-furnace system and the associated instrumentation. T1 and T2 are mass flow controllers; F: gas pressure control valves and gauges attached to the pressurised gas supply cylinder tanks. D is the furnace's central alumina rod, into which the sample and the oxygen sensor assembly are inserted and fixed in position by rings and screws in the top cover (see oxygen sensor diagram below); E: water-circulating jackets attached to the outer ends of the central ceramic rod and through which cold water from the water supply source is allowed to flow so as to cool the system. A, B, and C are alumina rods supporting both the zirconia sensor and the thermocouple wires assembled onto the furnace's central rod cover or lid (see oxygen sensor assembly diagram below).

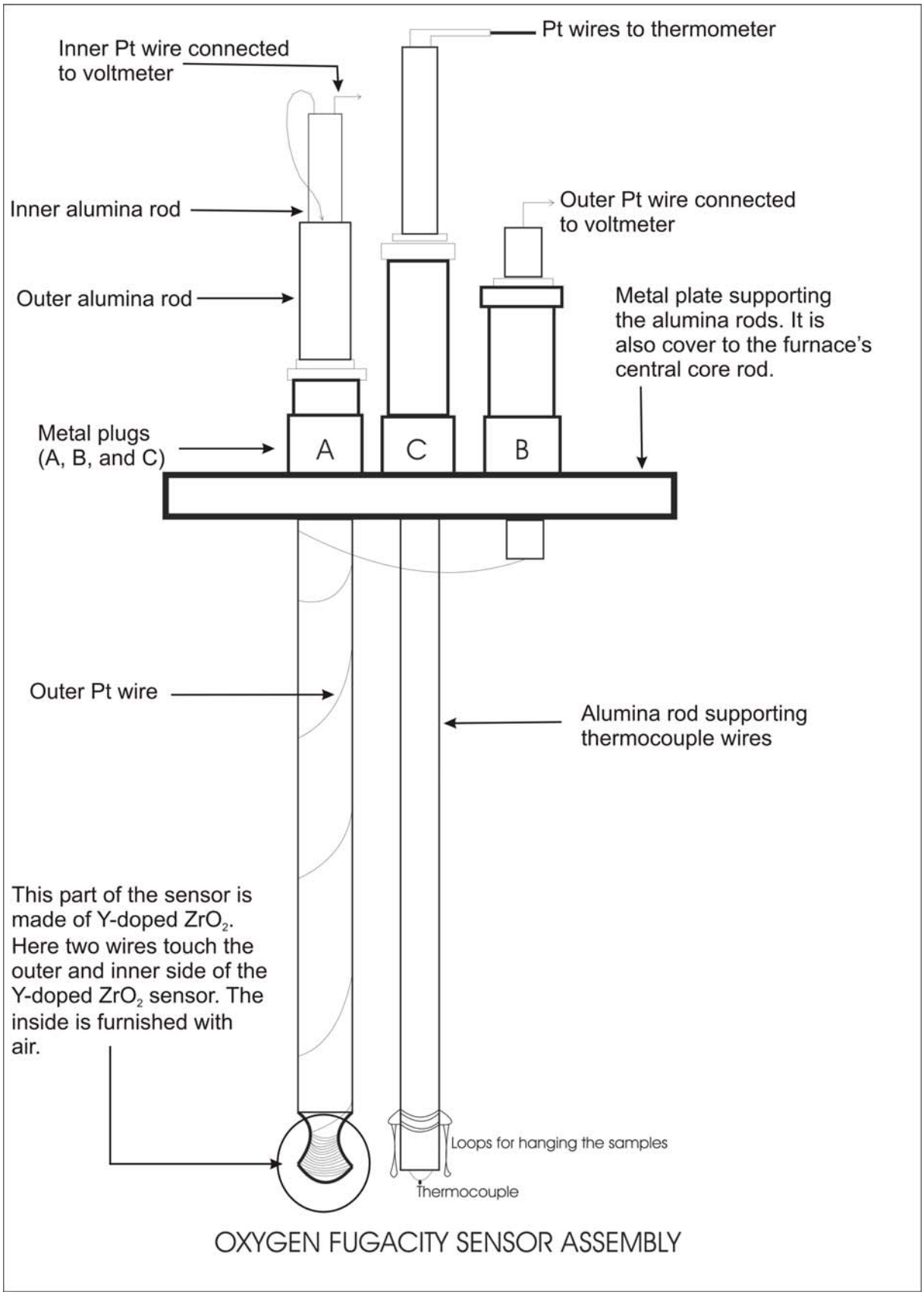

Fig. 3.3. Details of an oxygen sensor assembly.

The measured voltage of the oxygen sensitive electrode was converted into oxygen fugacity (in bar) using the following formula:

$$E = 2.303 \times \left(\frac{RT}{4F} \right) \log_{10} \left[\frac{p_{O_2}}{p_{ref}} \right] \quad (3.2)$$

Or

$$E = 0.0496T \log_{10} \left[\frac{p_{O_2}}{p_{ref}} \right] \quad (3.3)$$

Where E = the experimentally measured e.m.f. in V eqn (3.2) or mV eqn (3.3),
R = gas constant (8.314 J/Kmol),
T = absolute temperature in Kelvin (K),
F = Farady constant (9.649×10^4 C/mol),
p_{O_2} = partial pressure of oxygen (fo_2) in the cell, to be determined, and
p_{ref} = the partial pressure of oxygen for a reference gas, in this case air, with a constant oxygen content of 20.9 Vol%.
p_{O_2} and p_{ref} are given in bars. Thus p_{ref} ~ 0.21 bar.

For each gas or mixed gas-ratio (i.e. air, CO_2(pure), CO_2/H_2 = 400/2, 200/2, 200/6, and 200/20) tables were prepared in which the following experimental details were registered:

1) the composition or type of glass (i.e. HG15, HG2, HG25, ALKB, ANDS, and THLT),
2) the equilibrium temperature of the experimental run (i.e. 1250, 1300, 1350, and 1400°C),
3) the e.m.f. (mV) and later converted into fo_2 (in bars). This was measured after the experiment had reached and stabilised at the run target temperature,
4) the duration of the experimental run, in hours, and
5) the colour of the reduced glass, as a final remark.

After quenching, individual charges were mounted in crystal-bond and doubly polished glass slabs prepared (using alumina powder of grain sizes 400, 12, and 3μm-diameter) for optical spectroscopy.

3.2.1.7. Measures taken to avoid explosion hazards

The gas mixtures, CO_2/H_2, are highly inflammable at the high experimental temperature conditions. Care was therefore taken to avoid explosive accidents in the laboratory by flushing the entire system with N_2 gas before starting and stopping each experimental run. Cold water was left to circulate continuously through the cooling jackets during and after the experimental run, and was only turned off when the entire system had cooled to room temperature. The window close to the furnace was kept open or half open during and after the run to ensure that cold fresh air in the room, and particularly around the hot furnace, was continually replenished. As a final safety measure, a small handy fire extinguisher was always kept on standby, installed on the laboratory wall close to the equipment.

3.2.2. Optical spectrometry

Optical spectroscopy is based on absorption processes in the infra-red, visible, and ultraviolet regions of the electromagnetic spectrum of radiation.

In this study optical spectroscopy was used to establish the presence and quantity of Cu(II) ions in silicate glasses as electron microprobe analysis simply gives total copper content in a given sample (i.e. Cu_{total} = Cu^{+} + Cu^{2+}) and does not differentiate between Cu^{2+} and Cu^{+} oxidation states. This is the best analytical method since it will only be sensitive to Cu^{2+} cations, which cause an absorption peak in the near infra-red region of the electromagnetic spectrum. Tails of this absorption band extend into the visible range of the spectrum to cause the green or blue colour of the copper-bearing glasses, whilst Cu^{+} ions do not impart any colour to the glasses in which they exit. Consequently, optical spectroscopy enables the concentration of Cu^{2+} cations in the concerned glass (or silicate melt) type to be quantitatively determined. Since the total amount of copper (Cu_{total}) is known (from the results of EMPA), the concentration of Cu^{+}, and hence the oxidation state ratio (Cu^{2+}/Cu^{+}), for a given glass type at any given equilibrium conditions of temperature and pressure can be easily estimated.

3.2.2.1. Spectrometer

The instrument used to measure the infrared absorption spectra in this study was the Bruker IFS 125 HR Fourier-Transform-Spectrometer (FTIR). This technique uses the Fourier transform methods to mathematically de-convolute individual absorptions at particular energies or frequencies from data containing all such energies which were recorded as an interference pattern. The chief advantage of using Fourier transform techniques in spectroscopy is that the whole of the spectrum is recorded at the same time. So for the time it takes to scan through the complete spectrum sequentially, a number of interferograms can be recorded and added together to improve the signal-to-noise ratio. As a series of scans are added the random noise is reduced in intensity and the signals due to peaks are reinforced. In this way the more scans recorded the better the signal-to-noise ratio (S/N) in the final spectrum, such that after n scans the S/N has increased by $\sqrt{n}$.

Figure 3.4 shows a schematic diagram of a Michelson interferometer, which is permanently aligned with the spectrometer. The spectrometer is also equipped with a Bruker IR microscope containing all-reflecting cassegranian optics that allow measurements of small areas with apertures down to 10 µm. Measurements were carried out in the near infrared region using a tungsten light source, a CaF_2 beam-splitter and a highly sensitive narrow-band MCT detector.
For each absorption spectrum 100 scans were accumulated with 4 cm^{-1} resolution.

The spectrometer was connected to a computer so that data could be stored and manipulated electronically. This facilitates smoothing noise data, removing background peaks, and making the measurement of spectroscopic parameters, such as peak positions and relative intensities or absorptions (A), much easier.

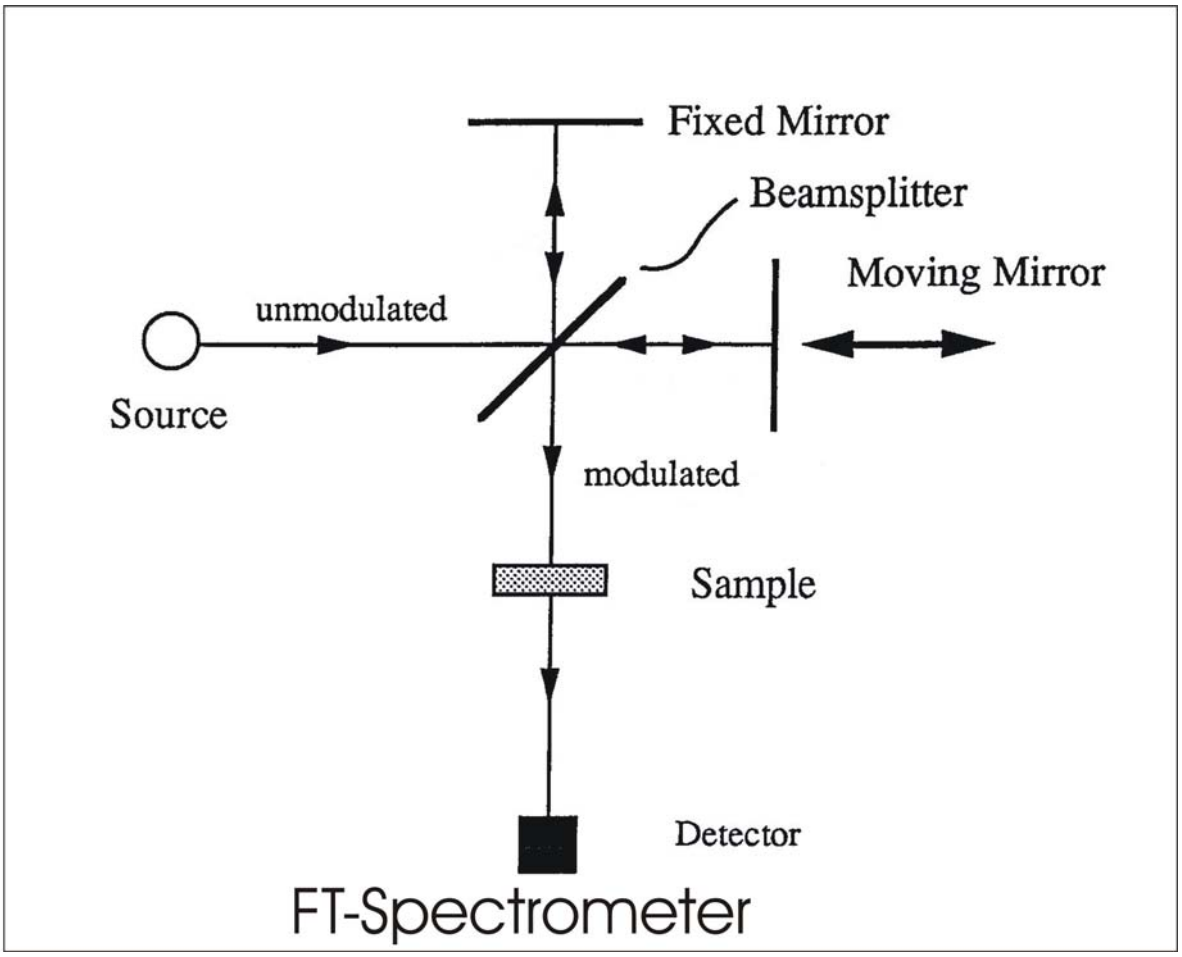

Fig. 3.4. A schematic diagram of the Michelson interferometer used in Fourier Transform Infrared Spectrometers.

3.2.2.2. Optical absorption measurements

From the starting synthetic glasses of each composition (see section 3.2.1) three categories of glass samples were prepared for spectroscopic measurements.

The first category involved glasses that had been re-fused in air at atmospheric pressure conditions at temperatures ranging from 1250 – 1400°C. This consists of glass samples from haplogranites with molar ratio (Na+K)/Al = 0.60, 0.93, 1.42, and 1.75 including glasses of andesitic, alkalibasaltic and tholeiitic compositions.

The second category of glass samples was those that had been re-fused at the same pressure and temperature ranges as above but under different reducing conditions obtained by providing a constant atmosphere of pure CO_2 gas or mixtures of H_2/CO_2 gases in the volume ratios ($H : CO_2$) of 1 : 200, 1 :100, 1 : 33, and 1 :10, from the gas-mixing equipment. Gas atmospheres, depending on temperature and amount of gas or gas mixtures steadily flowing through the gas-mixing furnace, imparted different oxygen fugacities to glass that was being re-fused (see section 3.2.1.5), yielding quenched glasses with different levels of copper reduction, as seen from the varying colour of the product glasses.

The third and final category of glass samples for spectroscopic measurements were those that had been prepared as standards for each glass composition (see section 3.2.1.4).

Homogeneous and bubble-free transparent glasses from each of the three categories were selected and doubly polished to flat discs with an appreciable, uniform thickness (**d**) and adequately large plain surface-areas. Optical absorption of each dust-free polished glass was measured by putting the disc on a metallic (bronze) rectangular plate with a triangular opening in the mid-centre. The disks (one at a time) were carefully laid on the plate across the triangular opening by means of a pair of forceps. The plate was then carefully placed on the stage of the Bruker IR microscope attached to the spectrometer, with the sample disc lying directly in the centre of the IR beam path.
Before taking IR absorption measurements, normal microscopic procedure was carried out to focus and select a clean and clear sample field, suitable for NIR exposure. During the measurement an absorption spectrum was simultaneously drawn on the computer screen, from which both the wavenumber at peak position of the absorption band and the absorbance, **A**, of the measuring sample could be determined (see Figure 3.5, the sample FTIS spectrum). The absorbance, **A**, of the glass sample was then calculated according to Lambert Beers law equal to:

$$\mathbf{A = cd\varepsilon} \qquad (3.4)$$

Where **c** is the concentration of the colouring ion, Cu^{2+}, **d** is the thickness of the glass sample in the light beam and **ε** is the extinction coefficient of the colouring ion, i.e. Cu^{2+}.

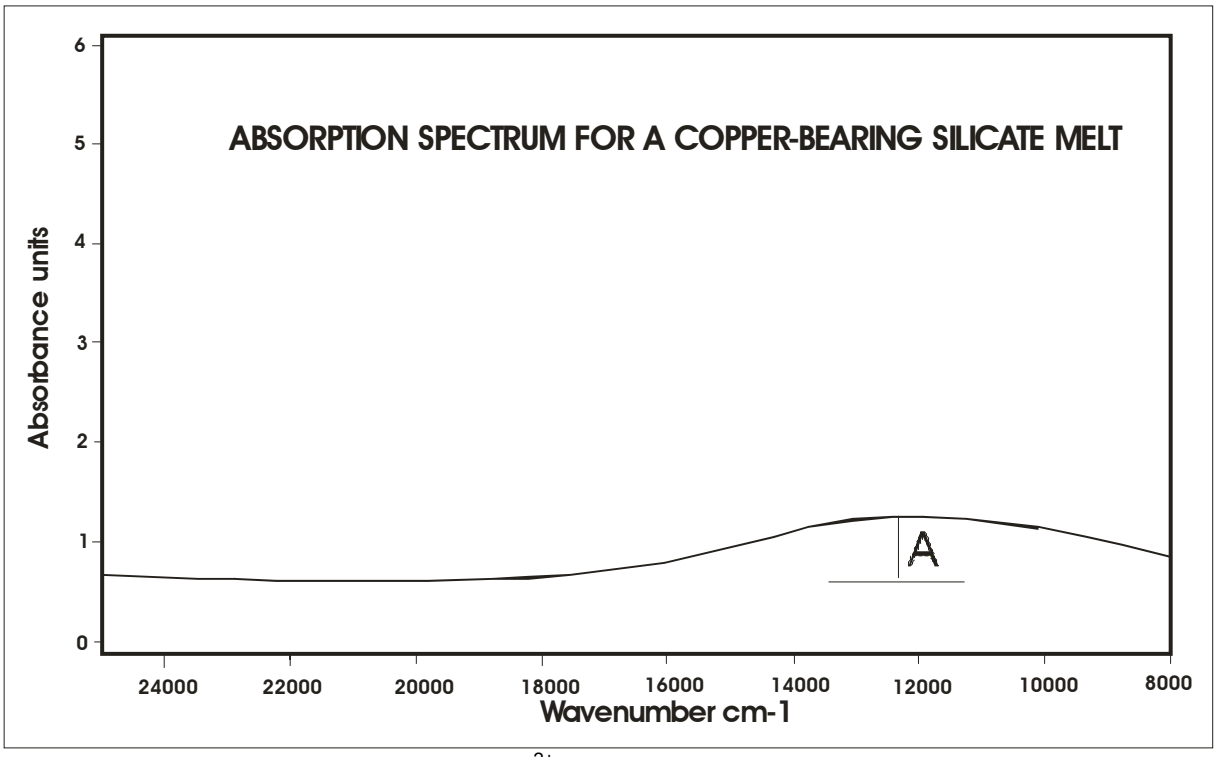

Fig.3.5. Absorption spectrum due to Cu^{2+} ions in silicate glass. The curve is an absorption spectrum of a doubly polished glass sample (from this study) quenched from a copper-bearing silicate melt at 1400°C.

3.3. Results and discussion

Analytical results of spectroscopic investigations on the doubly polished glass disks together with their corresponding experimental run conditions are listed in **Table 3.9**. The optical property spectroscopically measured (in the NIR region) was the absorbance (**A**) of glass samples, from a range of compositions, which had previously been experimentally treated/reduced under different conditions of temperature and oxygen fugacity (see section 3.2.1.5). These glasses contain both species of copper (i.e. Cu^{1+} and Cu^{2+}) in different proportions, depending on the experimental conditions under which the glasses were treated. Cu^{2+} ions are responsible for the blue colour in glass. The more intense the blue colour the higher the concentration of Cu^{2+} ions in a given glass sample.

Theoretically, Cu^{2+} in a silicate melt is related to Cu^{1+} according to the following equation:

$$Cu^{+} + \frac{1}{4}O_2 \Leftrightarrow Cu^{2+} + \frac{1}{2}O^{2-} \tag{3.5}$$

The equilibrium constant K for this reaction can be obtained by the relation

$$K = \frac{a\left(O^{2-}\right)^{\frac{1}{2}} \times a\left(Cu^{2+}\right)}{a\left(Cu^{+}\right) \times f\left(O_2\right)^{\frac{1}{4}}} \tag{3.6}$$

where a is the activity of the corresponding ionic species in equation (3.5) and f is the fugacity of oxygen of the system at a given equilibrium temperature, T.

Assuming that the activity a of O^{2-} in the melt remains constant during the reaction, and that the activities of Cu^{2+} and Cu^{+} species are proportional to their respective concentrations, c, K will be proportional to K^*, a new equilibrium constant. Thus,

$$K^* = \frac{c\left(Cu^{2+}\right)}{c\left(Cu^{+}\right) \times f\left(O_2\right)^{\frac{1}{4}}} \tag{3.7}$$

Equation (7) can be rearranged to state the redox ratio (Cu^{2+}/Cu^{+}) at the subject:

$$\left(Cu^{2+}/Cu^{1+}\right) = f(O_2)^{\frac{1}{4}} \times K^* \tag{3.8}$$

This equation predicts the Cu^{2+}/Cu^{1+} ratio to increase linearly with the fourth root of the oxygen fugacity in the silicate melt. Consequently,

$$Log\left(Cu^{2+}/Cu^{1+}\right) = \frac{1}{4}\log f(O_2) + \log K^* \tag{3.9}$$

A plot of log (Cu^{2+}/Cu^{1+}) against fo_2 should therefore be expected to give a straight line graph with a gradient of $1/4$.

In the experimental samples, the concentration (**c**) of Cu^{2+} ions, which are

responsible for optical absorption glass, can be calculated for each composition by rearranging equation (4) as follows:

$$\mathbf{A/(d.\varepsilon) = c} \qquad (3.10)$$

ε, the extinction coefficient was obtained using glass standards (see section 3.3.1) whose entire copper content is assumed to be Cu^{2+}, after the reaction with PtO_2 (section 3.2.1.4). The Cu^{2+} concentrations in glass standards are, therefore, assumed to be equal to the analytical concentrations of copper obtained from EMPA of counterpart glasses before the experimental runs.

The concentration of Cu^{+} in a given glass sample was obtained by taking the difference between the concentration of Cu^{2+} in the counterpart glass standards (see section 3.2.1) and that of the measuring glass sample, obtainable from equation (3.10). This enabled the calculation of the speciation ratio (Cu^{2+}/Cu^{+}) as seen in the results Table 3.9.

Logarithms of the redox ratio (Cu^{2+}/Cu^{+}) and oxygen fugacity (fo_2), at any given equilibrium conditions of temperature, are the two most important elements of the results table used to characterise the oxidation state of copper existing in melts of various compositions at different experimental conditions.

It was observed that glass discs belonging to standard glass samples yielded the maximum values of absorbance (**A**) for each glass composition. When glass discs of same composition and similar thickness, are run at the same temperature but varying redox atmospheres, results show that their **A**-values tend to decrease in the following order:
PtO_2 > air > pure CO_2 > CO_2/H_2 = 400/2 > CO_2/H_2 = 200/2 > CO_2/H_2 = 200/6 > CO_2/H_2 = 200/20.
This observation could also be easily confirmed from the glass colours which, in a similar manner, declined in intensity from deep blue/green through pale blue/green to colourless, across the same order of oxidising/reducing environments outlined above.

Generally the maximum absorption band due to Cu^{2+} ions appeared at ~ 13000 cm^{-1} (wavenumber) for glass samples belonging to andesite, alkalibasalte, and tholeiite, and ~ 12500 cm^{-1} for glass samples of the haplogranite series.

Peraluminous haplogranite glass (glass sample HPG1 with molar ratio (Na+K)/Al = 0.60) entirely contained Cu^{1+} ions, which could not be converted into Cu^{2+} ions even at the most oxidising conditions with PtO_2. It was therefore not necessary to carry out any further experiments on this sample using reducing gas mixtures, since all the copper in this sample happens to exist only in the reduced form, Cu^{1+} (see **Figures 3.6** and **3.7**). **Figure 3.8** shows NIR-Cu^{2+} spectra for all silicate glass compositions prepared in air at 1600°C, as starting materials for the reduction experiments.
Figures 3.9(**a**) and (**b**) show NIR-Cu^{2+} spectra for all the glass standards and a series of alkalibasalt glass samples at different oxygen fugacity at 1300°C, respectively.

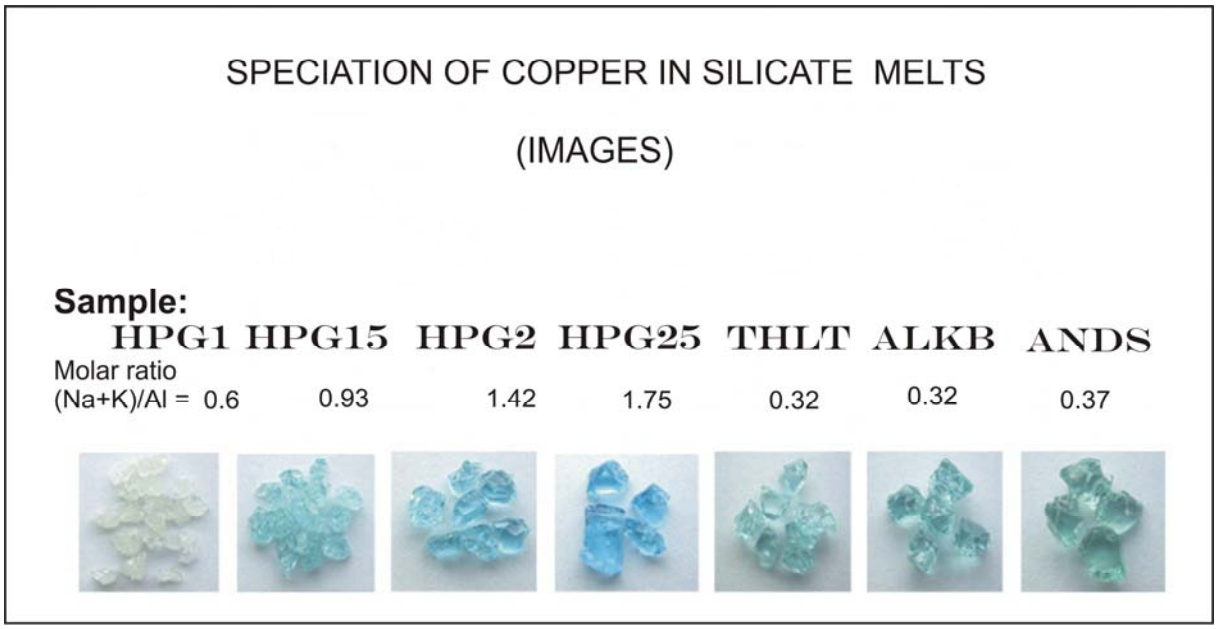

Figure 3.6. Colour gradation in glasses quenched from silicate melts (at 1500°C in air) with different ASI and composition. The nominal mixtures were all prepared with the same initial concentrations of Cu, as 1 wt% CuO. In all glasses, except HPG1, copper occurs in two oxidation states (i.e. Cu^{+} and Cu^{2+}). Cu^{+} is colourless and Cu^{2+} is blue. Therefore the intensity of the blue/green colour seen in these glasses is an indication of the amounts of Cu^{2+} ions a given sample contains. Sample HPG1, however, contains all its copper in a reduced form (Cu^{1+}). Glass in this sample is, therefore, observed to be colourless. The gradation of colour intensity in other glasses is observed to change with ASI, a parameter that influences the degree of polymerisation in the melt. For instance, among the haplogranite series, sample HG1 is the most polymerised and HPG25, the least polymerised glass. Polymerisation, in this case, could be used as an indicator for the amounts of Cu^{2+} ions contained in each glass-type, i.e. Cu^{2+} concentration increase with decreasing levels of polymerisation in silicate melts.

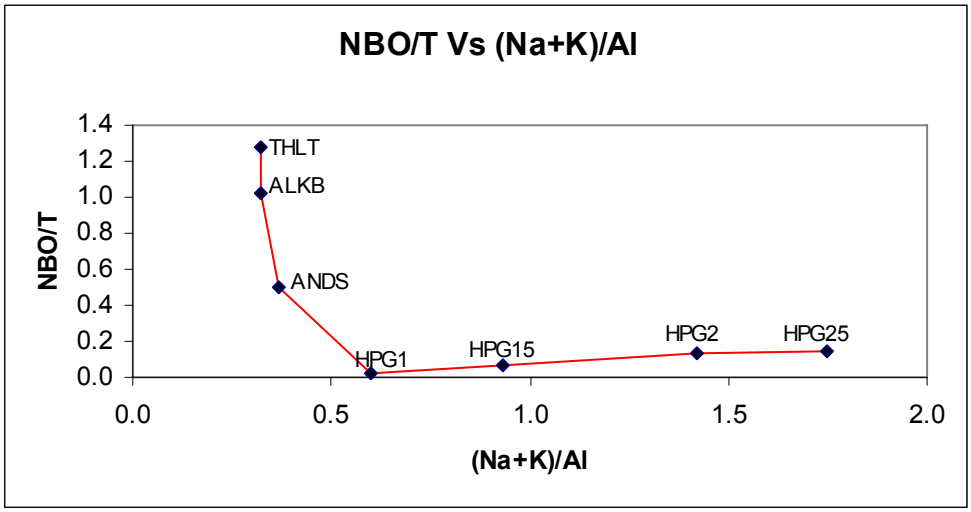

Fig. 3.7. Variation of the ratio of non-bridging oxygen atoms per tetrahedral atom (NBO/T) with the reciprocal ASI. Note: NBO/T ratio has influence over many physical-chemical and optical properties of silicate melts, e.g. optical absorption and density of the experimental glasses apparently increase with increasing NBO/T ratio.

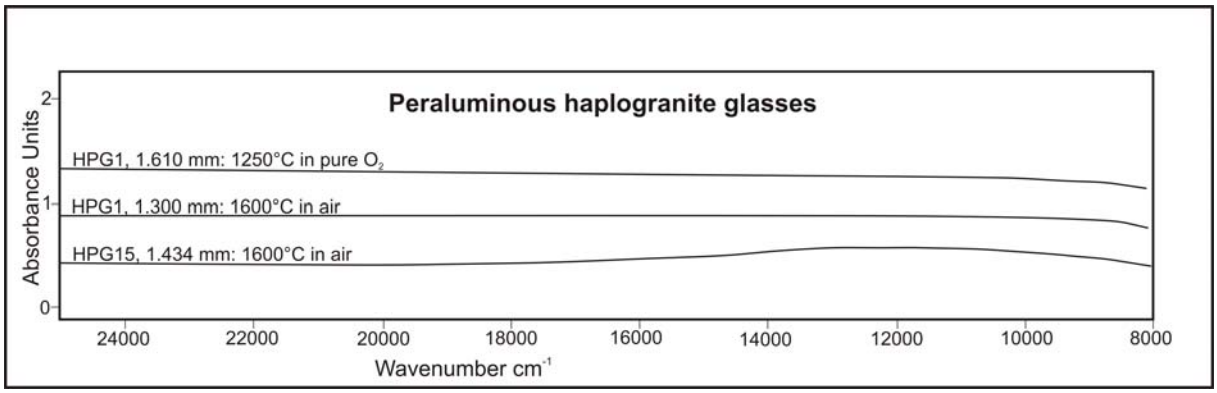

Fig. 3.8. Copper in peraluminous haplogranites is a special case. In this figure the middle spectrum belongs to sample HPG1 prepared at 1600°C in air. This spectrum shows there is no presence of Cu^{2+} ions in the glass to cause an absorption peak. The uppermost spectrum belongs to the same sample (HPG1), however, prepared under the most oxidising conditions (i.e. the sample was heated in PtO_2 at 1250°C, enclosed in a Pt-capsule). Similarly there is no evidence for Cu^{2+} ions in this sample, as well. This implies that copper in peraluminous granites only exist in one oxidation state as Cu^{1+} even at the most oxidising conditions.
The lowermost spectrum (drawn for comparison) belongs to sample HPG15, a sub-aluminous haplogranite. Unlike the HPG1 spectra, there is an absorption maximum in this spectrum due to the presence of Cu^{2+} in the sample.

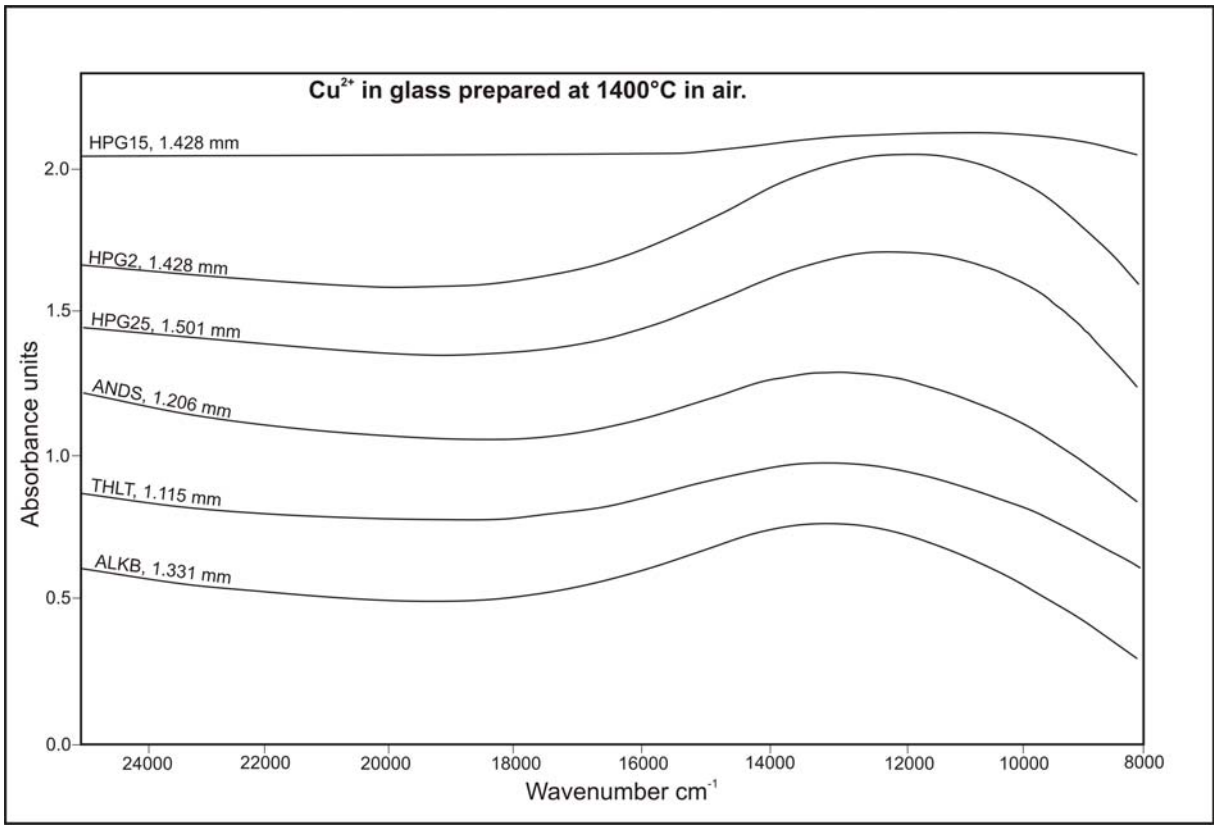

Fig.3.9. NIR Cu^{2+} spectra for original (starting) glasses prepared in air at 1600°C, with varying molar ratios of (Na+K)/Al, also known as the agpatic index **(AI)**. **AI = 0.32, 0.32, 0.37, 1.75, 1.42,** and **0.93,** for ALKB, THLT, ANDS, HPG25, HPG2, and HPG15, respectively.

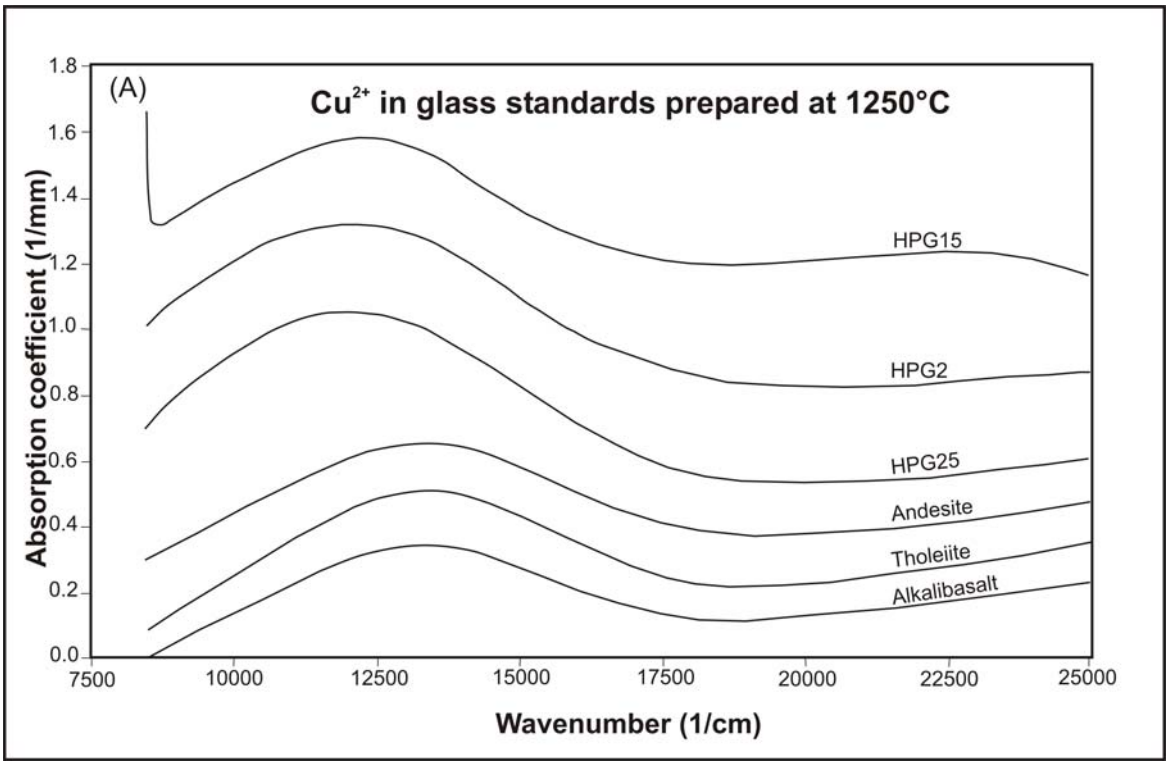

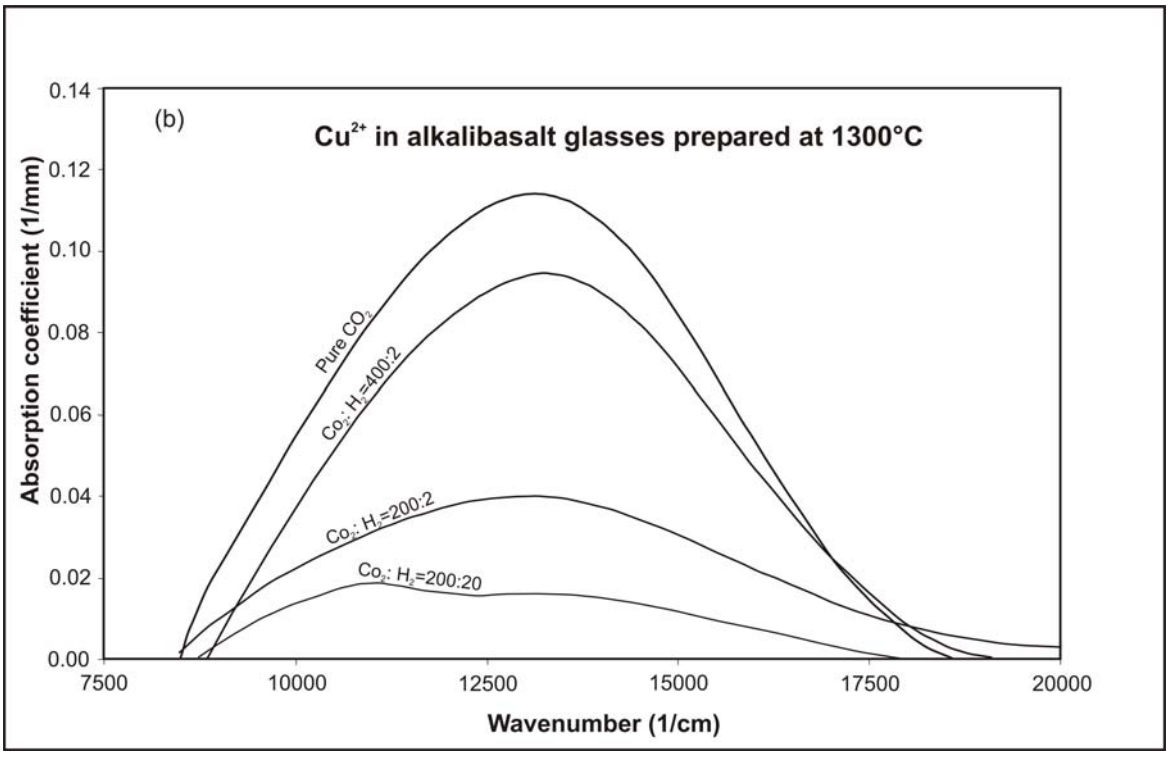

Fig. 3.10. See figure caption on the next page.

Fig. 3.10(a). Spectra of Cu^{2+} in standard glasses, including alkalibasalt (s. STD12), tholeiite (s. STD13), andesite (s. STD10), haplogranite25 (s. STD1), haplogranite2 (s. STD7), and haplogranite15 (s. STD9). Note: glasses HPG25 and HPG2 represents peralkaline granite melts with agpaitic index **(AI)** 1.75 and 1.42, respectively. Glass HPG15 represents a sub-aluminous granite melt with AI = 0.93. All spectra have been normalised to 1mm glass thickness. AI = (Na+K)/Al, a molar ratio.

Fig. 3.10(b). A series of Cu^{2+} spectra for alkalibasalt glasses prepared at 1300°C in different oxygen atmospheres, provided by pure CO_2 and a series CO_2/H_2 mixed gases with varying ratios. Note that the reducing power of the gas atmospheres decreases in the following order: CO_2/H_2 = 200/20 (s. ALKB103) > 200/2 (s.ALKB1003) > 400/2 (s. ALKB2002) > pure CO_2 (s. ALKB3).

3.3.1. The extinction coefficient, ε, of Cu^{2+}

In order to determine **ε**, the extinction coefficient of the Cu^{2+} ions for the various experimental glass compositions (haplogranites, andesite, tholeiite, and alkali-basalt), standard glasses prepared under 30 bar of O_2 were used. It was assumed that all the Cu^{+} ions in the silicate melt were oxidised to Cu^{2+} ions in the process of standard preparation. This was confirmed by observing a strong blue/green colour of the quenched glass after the experiment. The concentration, **c**, of copper in this sample was then assumed to be entirely that of Cu^{2+} ions and the same as that of total copper in the starting material, obtained from the results of microprobe analysis of the original glass.
From equation (10),

$$\varepsilon = A/cd \qquad (3.11)$$

In equation (4) above **A** was obtained directly from spectroscopic measurement by subtracting the magnitude at the base from that at the peak of the absorption spectrum and **d**, the thickness of the glass sample, was measured directly by means of a digital micro-meter. The concentration, **c**, is calculated from the density, **ρ**, and the EMPA (wt%) values of CuO in the concerned glass standard (see **Tables 3.2** and **3.5**).

Table 3.7. Measured Extinction, **A,** and thickness, **d,** of glass standards.

Run No.	Comp	Gas mixture	Thickness mm	f_{O2}. bar	T_{eq} °C	A	Band position cm^{-1}	Colour
STD13	THLT	pure O_2	1.445	30	1250	0.555	13141	blue-green
STD12	ALKB	pure O_2	1.859	30	1250	0.557	13038	blue-green
STD10	ANDS	pure O_2	2.145	30	1250	0.725	13141	blue-green
STD11	HPG1	pure O_3	1.312	30	1250	0.076	8308	colourless
STD9	HPG15	pure O_2	1.607	30	1250	0.520	12524	blue
STD7	HPG2	pure O_2	2.158	30	1250	0.834	12250	blue
STD1	HPG25	pure O_2	1.900	30	1250	0.793	12241	blue

Note: pure O_2 is obtained from the break-down of PtO_2 as described in text.

Table 3.8. Calculated extinction coefficient, **ε**, of glass standards.

sample	Density(glass)	Concentration Cu^{2+} in glass					thickness	Extinction	extinction coeff.
	ρ (g/cm3)	CuO(wt%)	Cu^{2+}(wt%)	(g/cm^3)	(mol/cm^3)	**c** (mol/l)	**d** (cm)	**A** (unitless)	**ε** (l/mol.cm)
ALKB	2.6250	0.708	0.566	0.0148	2.34E-04	2.34E-01	0.1859	0.557	**1.28E+01**
THLT	2.6550	0.684	0.546	0.0145	2.28E-04	2.28E-01	0.1445	0.555	**1.68E+01**
ANDS	2.4662	0.938	0.749	0.0185	2.91E-04	2.91E-01	0.2145	0.725	**1.16E+01**
HPG1	2.0147	0.315	0.252	0.0051	7.98E-05	7.98E-02	0.1312	0.076	**7.26E+00**
HPG15	2.2550	0.344	0.275	0.0062	9.75E-05	9.75E-02	0.1607	0.520	**3.32E+01**
HPG2	2.4240	0.813	0.649	0.0157	2.48E-04	2.48E-01	0.2158	0.834	**1.56E+01**
HPG25	2.5500	0.843	0.673	0.0172	2.70E-04	2.70E-01	0.1900	0.793	**1.54E+01**

3.3.2. Oxidation states of copper in silicate melts

Results of the redox ratio (Cu^{2+}/Cu^{+}) and oxygen fugacity fo_2 (calculated as logarithms) for glass of varied compositions and experimental run temperatures ranging from 1250 – 1400°C are summarised in **Table 3.9**(1-6) and graphically presented in **Figures 3.11** and **3.12**. The graphs show a linear relationship between the logarithms of the redox ratios and oxygen fugacities for glass of a given composition at any given temperature. At a fixed temperature, log (Cu^{2+}/Cu^{+}) increases proportionally with log fo_2 to yield a straight line curve with its gradient in the range 0.24 – 0.26, which is in close agreement with the theoretical value, 0.25.
The effect of temperature on speciation as a function of oxygen fugacity was investigated by plotting all temperatures in one diagram for glass of the same composition (see **Figures 3.11**(a-f). The lines of fit are nearly parallel to one another, with the lowest and highest temperature curves lying uppermost and lowermost, respectively. At a fixed log fo_2 the speciation ratio Cu^{2+}/Cu^{+} increases with decreasing temperature, for glass of same composition.

Similarly the effect of composition on the speciation ratio, Cu^{2+}/Cu^{+}, as a function of fo_2 was investigated by plotting all compositions experimentally run at same temperature in one diagram (see **Figure 3.12**(a-d).

Generally at any given temperature and log fo_2 the ratio Cu^{2+}/Cu^{+} varies in the following order: HPG ≥ ANDS > ALKB ≥ THLT. Among the haplogranite series, the order of magnitude of the speciation ratios was observed to change with temperature as follows:

at 1400°C HPG15> HPG2> HPG25; at 1350°C, HPG2> HPG15> HPG25; at 1300°C, HPG25> HPG2> HPG15; and at 1250°C, the order is HPG2> HPG25> HPG15.

A similar effect was also observed for glass of tholeiite and alkalibasalt compositions, with the tholeiite curve lying significantly above that of the alkalibasalt at 1300°C. At 1350°C, however, there is hardly any variation in the redox ratio between tholeiite and alkalibasalt at any oxygen atmosphere and the two curves are seen to have merged into one another and trending as a single line.

The speciation of copper in silicate melts of haplogranites and andesites is, at any given oxygen fugacity, almost similar at lower temperatures but will, however, be significantly varied at higher temperatures, with andesites exhibiting lower speciation ratios.

Table 3.9(1). Synthesis relations for **tholeiite** (THL) glass samples containing a trace amount of Cu and their spectroscopic data for Cu^{2+} ions in the resulting silicate glasses.

Sample No	Atmosphere	T_{eq} (°C)	Duration (hrs)	Thickness of sample (mm)	fo_2 bar	Absorption (A)	Band position cm^{-1}	concntration of Cu species in glass			log fo_2	log (Cu^{2+}/Cu^{1+})	Colour	remarks
								Cu^{2+}(mol/l)	Cu^{+}(mol/l)	Cu^{2+}/Cu^{+}				
STD13	pure O_2	1250	4.00	1.445	3.00E+01	0.555	13141	0.229	0.000		1.477		blue-green	ok
THLA1	air with 0.21O_2	1400	4.00	1.542	2.10E-01	0.550	13038	0.212	0.016	13.016	-0.678	1.114	clear green	nu
THLA2	air with 0.21O_2	1350	4.00	1.543	2.10E-01	0.604	12833	0.233	-0.004	-53.170	-0.678		intense green	nu
THLA3	air with 0.21O_2	1300	4.00	1.461	2.10E-01	0.531	13175	0.216	0.012	17.615	-0.678	1.246	cloudy green	nu
THL1	pure CO_2	1400	20.50	1.289	1.91E-03	0.035	11667	0.016	0.212	0.076	-2.719	-1.119	colourless	ok
THL2	pure CO_2	1350	20.00	1.435	1.66E-03	0.126	12250	0.052	0.176	0.296	-2.780	-0.528	pale green	ok
THL3	pure CO_2	1300	20.00	1.104	1.31E-03	0.220	13313	0.119	0.110	1.078	-2.883	0.033	pale green	ok
THL2000	CO_2/H_2 = 400/2	1400		ms	1.47E-04	ms					-3.833			ms
THL2001	CO_2/H_2 = 400/2	1350	14.00	1.831	5.00E-05	0.065	10471	0.021	0.207	0.102	-4.301	-0.992	colourless	ok
THL2002	CO_2/H_2 = 400/2	1300	13.50	1.662	8.69E-06	**nm**					-5.061		pale green	**nm**
THL1002	CO_2/H_2 = 200/2	1400	10.00	1.594	1.88E-05	0.015	10518	0.006	0.223	0.025	-4.726	-1.600	colourless	ok
THL1003	CO_2/H_2 = 200/2	1350	11.50	1.469	8.43E-06	0.047	12896	0.019	0.210	0.091	-5.074	-1.042	pale green	ok
THL1004	CO_2/H_2 = 200/2	1300	11.00	1.491	3.01E-06	**nm**					-5.521		pale green	**nm**
THL331	CO_2/H_2 = 200/6	1400	12.00	1.482	2.96E-06	**nm**					-5.529		colourless	**nm**
THL332	CO_2/H_2 = 200/6	1350	14.00	1.347	8.94E-07	**nm**					-6.049		colourless	**nm**
THL333	CO_2/H_2 = 200/6	1300	18.00	0.991	1.59E-07	**nm**					-6.799		cloudy white	**nm**
THL100	CO_2/H_2 = 200/20	1400		ms	4.21E-08	ms					-7.376			ms
THL101	CO_2/H_2 = 200/20	1350	13.00	1.977	1.44E-08	0.012	13343	0.004	0.225	0.016	-7.842	-1.794	colourless	ok
THL102	CO_2/H_2 = 200/20	1300	12.00	1.621	4.24E-09	0.030	10683	0.011	0.218	0.051	-8.373	-1.296	colourless	ok

Note: nu = not used, sample data was not used for the subsequent calculations and graphics due to measuring errors.
ms = missing, sample was not available for spectroscopic measurement.
nm = not measured, sample is available but for some unspecified reasons was not measured or is still waiting to be measured.
ok = okay, sample was measured and data used in the subsequent graphics.

Table 3.9(2). Synthesis relations for **alkalibasalt** (ALKB) glass samples containing a trace amount of Cu and their spectroscopic data for Cu^{2+} ions in the resulting silicate glasses.

Sample No.	Atmosphere	Duration (hrs)	T_{eq} °C	fo_2 bar	Thickness of sample (mm)	Absorption (A)	Band position cm^{-1}	concentration of Cu species in glass			log fo_2	log (Cu^{2+}/Cu^{1+})	Colour	remarks
								Cu^{2+}(mol/l)	Cu^{+}(mol/l)	Cu^{2+}/Cu^{+}				
STD12	pure O_2	4.0	1250	3.00E+01	1.859	0.557	13038	0.234			1.48		blue-green	std
ALKBA1	air with $0.21O_2$	2.0	1400	2.10E-01	1.522	0.437	13028	0.224	0.010	23.159	-0.68	1.365	clear green	nu
ALKBA2	air with $0.21O_2$	2.0	1350	2.10E-01	1.483	0.513	13004	0.270	-0.036	-7.455	-0.68		intense green	nu
ALKBA3	air with $0.21O_2$	2.0	1300	2.10E-01	1.446	0.440	13107	0.238	-0.004	-63.823	-0.68		cloudy green	nu
ALKBA4	air with $0.21O_2$	2.0	1250	2.10E-01	ms	ms					-0.68			ms
ALKB1	pure CO_2	20.0	1400	1.91E-03	1.400	0.063	12696	0.035	0.199	0.177	-2.72	-0.753	colourless	ok
ALKB2	pure CO_2	20.0	1350	1.66E-03	0.932	0.067	13084	0.056	0.178	0.316	-2.78	-0.501	colourless	ok
ALKB3	pure CO_2	20.0	1300	1.31E-03	1.353	0.182	13141	0.105	0.129	0.815	-2.88	-0.089	pale green	ok
ALKB4	pure CO_2	20.0	1250	1.19E-03	0.973	0.273	13097	0.219	0.015	14.810	-2.92	1.171	pale green	nu
ALKB2000	CO_2/H_2 = 400/2		1400	1.47E-04	ms	ms					-3.83			ms
ALKB2001	CO_2/H_2 = 400/2	14.0	1350	5.00E-05	1.789	0.052	13226	0.023	0.211	0.107	-4.30	-0.969	pale blue	ok
ALKB2002	CO_2/H_2 = 400/2	13.5	1300	8.69E-06	1.603	0.143	13226	0.070	0.164	0.424	-5.06	-0.372	pale green	ok
ALKB2003	CO_2/H_2 = 400/2	14.0	1250	2.53E-06	1.494	**nm**					-5.60		pale green	**nm**
ALKB1001	CO_2/H_2 = 200/2	10.0	1400	1.88E-05	1.568	0.026	13155	0.013	0.221	0.059	-4.73	-1.232	colourless	ok
ALKB1002	CO_2/H_2 = 200/2	11.5	1350	8.43E-06	1.645	0.042	13155	0.020	0.214	0.093	-5.07	-1.031	pale green	ok
ALKB1003	CO_2/H_2 = 200/2	11.0	1300	3.01E-06	1.549	0.055	13155	0.028	0.206	0.134	-5.52	-0.871	pale green	ok
ALKB1004	CO_2/H_2 = 200/2		1250	7.44E-07	ms	ms					-6.13			ms
ALKB331	CO_2/H_2 = 200/6	12.0	1400	2.96E-06	2.152	**nm**					-5.53			**nm**
ALKB332	CO_2/H_2 = 200/6	18.0	1350	8.94E-07	1.707	**nm**					-6.05			**nm**
ALKB333	CO_2/H_2 = 200/6	14.0	1300	1.59E-07	1.461	**nm**					-6.80			**nm**
ALKB334	CO_2/H_2 = 200/6		1250	2.11E-08	ms	ms					-7.68			ms
ALKB101	CO_2/H_2 = 200/20		1400	4.21E-08	ms	ms					-7.38			ms
ALKB102	CO_2/H_2 = 200/20	13.0	1350	1.44E-08	1.867	0.010	11954	0.004	0.230	0.018	-7.84	-1.740	colourless	ok
ALKB103	CO_2/H_2 = 200/20	12.0	1300	4.24E-09	1.626	0.019	12143	0.009	0.225	0.041	-8.37	-1.392	colourless	ok
ALKB104	CO_2/H_2 = 200/20		1250	1.09E-09	ms	ms					-8.96			ms

See notice in table (1) for the abbreviations.

Table 3.9(3). Synthesis relations for **andesite** (ANDS) glass samples containing a trace amount of Cu and their spectroscopic data for Cu^{2+} ions in the resulting silicate glasses.

Sample No.	Atmosphere	T_{eq} (°C)	Duration (hrs)	Thickness of sample (mm)	fo_2 bar	Absorption (A)	Band position cm^{-1}	concntration of Cu species in glass			log fo_2	log (Cu^{2+}/Cu^{1+})	Colour	remarks
								Cu2+(mol/l)	Cu+(mol/l)	Cu2+/Cu+				
STD10	pure O_2	1250	4.00	2.145	3.00E+01	0.725	13141	0.291	0.000		1.477		blue-green	ok
ANDSA1	air with $0.21O_2$	1400	4.00	1.469	2.10E-01	0.316	12783	0.185	0.106	1.757	-0.678	0.245	clear green	ok
ANDSA2	air with $0.21O_2$	1350	4.00	1.407	2.10E-01	0.414	12867	0.254	0.037	6.793	-0.678	0.832	intense green	ok
ANDSA3	air with $0.21O_2$	1300	4.00	1.387	2.10E-01	0.451	12833	0.280	0.011	26.227	-0.678	1.419	cloudy green	ok
ANDSA4	air with $0.21O_2$	1250		ms	2.10E-01	ms					-0.678			ms
ANDS1	pure CO_2	1400	22.00	1.512	1.91E-03	0.072	11284	0.041	0.250	0.164	-2.719	-0.785	colourless	ok
ANDS2	pure CO_2	1350	22.00	1.755	1.66E-03	0.316	12994	0.155	0.136	1.143	-2.780	0.058	colourless	ok
ANDS3	pure CO_2	1300	23.75	1.572	1.31E-03	0.264	13028	0.145	0.146	0.990	-2.883	-0.004	pale green	ok
ANDS4	pure CO_2	1250	20.50	1.21	1.19E-03	0.356	12823	0.254	0.037	6.788	-2.924	0.832	green	ok
ANDS2000	CO_2/H_2 = 400/2	1400		ms	1.47E-04	ms					-3.833			ms
ANDS2001	CO_2/H_2 = 400/2	1350	14.00	1.788	5.00E-05	0.143	13084	0.069	0.222	0.310	-4.301	-0.508	pale blue	ok
ANDS2002	CO_2/H_2 = 400/2	1300	13.50	1.663	8.69E-06	0.182	13084	0.094	0.197	0.480	-5.061	-0.319	pale green	ok
ANDS2003	CO_2/H_2 = 400/2	1250	20.50	1.729	2.53E-06	0.247	13084	0.123	0.168	0.734	-5.597	-0.134	pale green	ok
ANDS1001	CO_2/H_2 = 200/2	1400	10.00	1.539	1.88E-05	0.069	13108	0.039	0.252	0.153	-4.726	-0.815	colourless	ok
ANDS1002	CO_2/H_2 = 200/2	1350	11.50	1.549	8.43E-06	0.146	13014	0.081	0.210	0.387	-5.074	-0.412	pale green	ok
ANDS1003	CO_2/H_2 = 200/2	1300	11.50	1.675	3.01E-06	0.237	13084	0.122	0.169	0.722	-5.521	-0.142	pale green	ok
ANDS1004	CO_2/H_2 = 200/2	1250	19.00	2.332	7.44E-07	0.404	13108	0.149	0.142	1.054	-6.128	0.023	green	ok
ANDS331	CO_2/H_2 = 200/6	1400	13.00	2.068	2.96E-06	**nm**					-5.529			**nm**
ANDS332	CO_2/H_2 = 200/6	1350	18.00	1.709	8.94E-07	**nm**					-6.049			**nm**
ANDS333	CO_2/H_2 = 200/6	1300	14.00	1.433	1.59E-07	0.083		0.050	0.241	0.207	-6.799	-0.684		ok
ANDS334	CO_2/H_2 = 200/6	1250		ms	2.11E-08	ms					-7.676			ms
ANDS101	CO_2/H_2 = 200/20	1400		ms	4.21E-08	ms					-7.376			ms
ANDS102	CO_2/H_2 = 200/20	1350	13.00	1.926	1.44E-08	0.064	12284	0.029	0.262	0.109	-7.842	-0.962	colourless	ok
ANDS103	CO_2/H_2 = 200/20	1300	12.00	1.690	4.24E-09	0.103	13179	0.053	0.238	0.220	-8.373	-0.657	pale green	ok
ANDS104	CO_2/H_2 = 200/20	1250	12.00	1.729	1.09E-09	0.100	10636	0.050	0.241	0.207	-8.963	-0.685	pale green	ok

Table 3.9(4). Synthesis relations for haplogranite, **molar ratio (Na+K)/Al = 0.93,** (HPG15) glass samples containing a trace amount of Cu and their spectroscopic data for Cu^{2+} ions in the resulting silicate glasses.

Sample No.	Atmosphere	T_{eq} (°C)	Duration (hrs)	Thickness of sample (mm)	fo_2 bar	A	Band position cm^{-1}	concntration of Cu species in glass			log fo_2	log (Cu^{2+}/Cu^{1+})	Colour	remarks
								Cu2+(mol/l)	Cu+(mol/l)	Cu2+/Cu+				
STD9	pure O_2	1250	4.00	1.607	3.00E+01	0.520	12524	0.097	0.000		1.477		blue	ok
HG15A1	air with $0.21O_2$	1400	4.00	1.485	2.10E-01	0.409	12524	0.083	0.0145	5.718	-0.678	0.757	pale blue	ok
HG15A2	air with $0.21O_2$	1350	4.00	1.563	2.10E-01	0.418	12387	0.081	0.0169	4.763	-0.678	0.678	blue	ok
HG15A3	air with $0.21O_2$	1300	4.00	1.428	2.10E-01	0.413	12618	0.087	0.0104	8.415	-0.678	0.925	blue	ok
HG15A4	air with $0.21O_2$	1250	4.00	1.702	2.10E-01	0.546	12524	0.097	0.0008	115.177	-0.678		blue	ok
HG151	pure CO_2	1400	22.00	1.526	1.91E-03	0.203	11839	0.040	0.0574	0.698	-2.719	-0.156	light blue	ok
HG152	pure CO_2	1350	23.00	0.88	1.66E-03	0.216	12284	0.074	0.0235	3.142	-2.780	0.497	pale blue	ok
HG153	pure CO_2	1300	23.00	1.347	1.31E-03	0.384	12425	0.086	0.0116	7.403	-2.883	0.869	blue	ok
HG154	pure CO_2	1250	20.00	1.684	1.19E-03	0.492	12425	0.088	0.0095	9.298	-2.924	0.968	clear blue	ok
HG152001	CO_2/H_2 = 400/2	1400	15.00	2.052	1.47E-04	0.275	12133	0.040	0.0571	0.707	-3.833	-0.151	pale blue	ok
HG152002	CO_2/H_2 = 400/2	1350	14.00	1.745	5.00E-05	0.273	12262	0.047	0.0503	0.936	-4.301	-0.029	pale blue	ok
HG152003	CO_2/H_2 = 400/2	1300	14.50	1.593	8.69E-06	0.286	12107	0.054	0.0434	1.246	-5.061	0.096	light blue	ok
HG152004	CO_2/H_2 = 400/2	1250	14.00	1.642	2.53E-06	0.416	12262	0.076	0.0212	3.607	-5.597	0.557	light blue	ok
HG151001	CO_2/H_2 = 200/2	1400	10.00	1.36	1.88E-05	0.155	12725	0.034	0.0631	0.544	-4.726	-0.265	pale blue	ok
HG151002	CO_2/H_2 = 200/2	1350	11.50	1.636	8.43E-06	0.244	12391	0.045	0.0525	0.855	-5.074	-0.068	light blue	ok
HG151003	CO_2/H_2 = 200/2	1300	24.00	2.3	3.01E-06	0.354	12674	0.046	0.0511	0.907	-5.521	-0.042	light blue	ok
HG151004	CO_2/H_2 = 200/2	1250	13.00	1.357	7.44E-07	0.332	12571	0.074	0.0238	3.100	-6.128	0.491	light blue	ok
HG15331	CO_2/H_2 = 200/6	1400	18.00	1.805	2.96E-06	0.079	10636	0.013	0.0843	0.156	-5.529	-0.806	colourless	ok
HG15332	CO_2/H_2 = 200/6	1350	14.00	1.845	8.94E-07	0.097	12056	0.016	0.0816	0.194	-6.049	-0.712	colourless	ok
HG15333	CO_2/H_2 = 200/6	1300	14.00	1.579	1.59E-07	0.140	12133	0.027	0.0708	0.377	-6.799	-0.423	pale blue	ok
HG15334	CO_2/H_2 = 200/6	1250	26.00	1.742	2.11E-08	0.293	12159	0.051	0.0468	1.082	-7.676	0.034	light blue	ok
HG15101	CO_2/H_2 = 200/20	1400	12.00	2.057	4.21E-08	0.064	12107	0.009	0.0881	0.106	-7.376	-0.973	colourless	ok
HG15102	CO_2/H_2 = 200/20	1350	12.00	1.797	1.44E-08	0.059	12210	0.010	0.0876	0.113	-7.842	-0.947	colourless	ok
HG15103	CO_2/H_2 = 200/20	1300	24.00	1.544	4.24E-09	0.069	12284	0.013	0.0840	0.160	-8.373	-0.795	colourless	ok
HG15104	CO_2/H_2 = 200/20	1250	20.00	1.612	1.09E-09	0.240	12210	0.045	0.0526	0.852	-8.963	-0.069	light blue	ok

Table 3.9(5). Synthesis relations for haplogranite, **molar ratio (Na+K)/Al = 1.42 ,** (HPG2) glass samples containing a trace amount of Cu and their spectroscopic data for Cu^{2+} ions in the resulting silicate glasses.

Sample No.	Atmosphere	T_{eq} (°C)	Duration (hrs)	Thickness of sample (mm)	fo_2 bar	Absorption (A)	Band position cm^{-1}	concntration of Cu species in glass			log fo_2	log (Cu^{2+}/Cu^{1+})	Colour	remarks
								Cu2+(mol/l)	Cu+(mol/l)	Cu2+/Cu+				
STD7	pure O_2	1250	4.00	2.158	3.00E+01	0.834	12250	0.248	0.000		1.477		intense blue	ok
HG2A1	air with $0.21O_2$	1400	4.00	1.381	2.10E-01	0.304	12216	0.141	0.1066	1.323	-0.678	0.122	light blue/green	nu
HG2A2	air with $0.21O_2$	1350	4.00	1.460	2.10E-01	0.448	12387	0.197	0.0510	3.854	-0.678	0.586	water blue	nu
HG2A3	air with $0.21O_2$	1300	4.00	1.529	2.10E-01	0.600	12010	0.252	-0.0038	-66.014	-0.678		water blue	nu
HG2A4	air with $0.21O_2$	1250	4.00	1.610	2.10E-01	0.900	12376	0.358	-0.1106	-3.240	-0.678		water blue	nu
HG21	pure CO_2	1400	22.00	1.449	1.91E-03	0.218	12044	0.096	0.1513	0.637	-2.719	-0.196	light blue	ok
HG22	pure CO_2	1350	24.00	1.437	1.66E-03	0.321	12070	0.143	0.1045	1.370	-2.780	0.137	light blue	ok
HG23	pure CO_2	1300	23.00	1.369	1.31E-03	0.409	12207	0.192	0.0562	3.406	-2.883	0.532	light blue/green	ok
HG24	pure CO_2	1250	20.00	1.918	1.19E-03	0.650	12353	0.217	0.0305	7.123	-2.924	0.853	water blue	nu
HG22001	CO_2/H_2 = 400/2	1400	15.00	1.919	1.47E-04	0.270	12331	0.090	0.1575	0.572	-3.833	-0.242	pale blue	ok
HG22002	CO_2/H_2 = 400/2	1350	14.00	1.707	5.00E-05	0.350	12449	0.131	0.1163	1.130	-4.301	0.053	pale blue	ok
HG22003	CO_2/H_2 = 400/2	1300	14.50	1.571	8.69E-06	0.410	12331	0.167	0.0804	2.080	-5.061	0.318	light blue	ok
HG22004	CO_2/H_2 = 400/2	1250	14.00	1.616	2.53E-06	0.557	12331	0.221	0.0268	8.248	-5.597	0.916	intense blue	ok
HG21001	CO_2/H_2 = 200/2	1400	10.00	1.520	1.88E-05	0.207	12402	0.087	0.1604	0.544	-4.726	-0.264	pale blue	ok
HG21002	CO_2/H_2 = 200/2	1350	23.50	1.594	8.43E-06	0.286	12402	0.115	0.1327	0.867	-5.074	-0.062	light blue	ok
HG21003	CO_2/H_2 = 200/2	1300	24.00	1.303	3.01E-06	0.240	12402	0.118	0.1297	0.911	-5.521	-0.041	light blue	ok
HG21004	CO_2/H_2 = 200/2	1250	13.00	1.286	7.44E-07	0.430	12402	0.214	0.0334	6.418	-6.128	0.807	light blue	ok
HG2331	CO_2/H_2 = 200/6	1400	18.00	1.848	2.96E-06	0.090	12331	0.031	0.2165	0.144	-5.529	-0.841	colourless	ok
HG2332	CO_2/H_2 = 200/6	1350	14.00	1.606	8.94E-07	0.155	12331	0.062	0.1859	0.333	-6.049	-0.478	colourless	ok
HG2333	CO_2/H_2 = 200/6	1300	14.00	1.772	1.59E-07	0.243	12331	0.088	0.1598	0.550	-6.799	-0.260	pale blue	ok
HG2334	CO_2/H_2 = 200/6	1250	26.00	1.791	2.11E-08	0.445	12331	0.159	0.0885	1.800	-7.676	0.255	light blue	ok
HG2101	CO_2/H_2 = 200/20	1400	12.00	1.977	4.21E-08	0.041	12331	0.013	0.2344	0.057	-7.376	-1.246	colourless	ok
HG2102	CO_2/H_2 = 200/20	1350	12.00	1.783	1.44E-08	0.087	12331	0.031	0.2165	0.145	-7.842	-0.840	colourless	ok
HG2103	CO_2/H_2 = 200/20	1300	12.00	1.481	4.24E-09	0.077	12331	0.033	0.2144	0.155	-8.373	-0.808	colourless	ok
HG2104	CO_2/H_2 = 200/20	1250	12.00	1.523	1.09E-09	0.340	12331	0.143	0.1046	1.368	-8.963	0.136	light blue	ok

Table 3.9(6). Synthesis relations for haplogranite, **molar ratio (Na+K)/Al = 1.75,** (HPG25) glass samples containing a trace amount of Cu and their spectroscopic data for Cu^{2+} ions in the resulting silicate glasses.

Sample No.	Atmosphere	T_{eq} (°C)	Duration (hrs)	Thickness of sample (mm)	fo_2 bar	Absorption (A)	Band position cm^{-1}	concntration of Cu species in glass			log fo_2	log (Cu^{2+}/Cu^{1+})	Colour	remarks
								Cu2+(mol/l)	Cu+(mol/l)	Cu2+/Cu+				
STD1	pure O_2	1250	4.00	1.900	3.00E+01	0.793	12241	0.271	0.000		1.477		blue	ok
HG25A1	air with 0.21O_2	1400	4.00	1.304	2.10E-01	0.374	12319	0.186	0.0848	2.197	-0.678	0.342	blue	ok
HG25A2	air with 0.21O_2	1350	4.00	1.382	2.10E-01	0.462	12044	0.217	0.0539	4.024	-0.678	0.605	blue	ok
HG25A3	air with 0.21O_2	1300	4.00	1.447	2.10E-01	0.435	12319	0.195	0.0758	2.575	-0.678	0.411	blue	nu
HG25A4	air with 0.21O_2	1250	4.00	1.511	2.10E-01	0.386	12181	0.166	0.1051	1.578	-0.678	0.198	blue	nu
HG251	pure CO_2	1400	22.00	1.373	1.91E-03	0.220	12250	0.104	0.1670	0.623	-2.719	-0.205	light blue	ok
HG252	pure CO_2	1350	24.50	0.782	1.66E-03	0.177	11968	0.147	0.1240	1.185	-2.780	0.074	pale blue	ok
HG253	pure CO_2	1300	22.50	0.935	1.31E-03	0.329	12353	0.228	0.0425	5.372	-2.883	0.730	blue	ok
HG254	pure CO_2	1250	20.50	1.872	1.19E-03	0.705	12319	0.245	0.0265	9.238	-2.924	0.966	intense blue	nu
HG252001	CO_2/H_2 = 400/2	1400	15.00	1.875	1.47E-04	0.240	10801	0.083	0.1879	0.442	-3.833	-0.354	colourless	ok
HG252002	CO_2/H_2 = 400/2	1350	14.00	1.718	5.00E-05	0.350	12284	0.132	0.1387	0.954	-4.301	-0.021	pale blue	ok
HG252003	CO_2/H_2 = 400/2	1300	14.50	1.569	8.69E-06	0.437	12284	0.181	0.0902	2.006	-5.061	0.302	blue	ok
HG252004	CO_2/H_2 = 400/2	1250	14.00	1.566	2.53E-06	0.548	12331	0.227	0.0438	5.189	-5.597	0.715	intense blue	ok
HG251001	CO_2/H_2 = 200/2	1400	10.00	1.391	1.88E-05	0.100	12402	0.047	0.2243	0.208	-4.726	-0.682	colourless	ok
HG251002	CO_2/H_2 = 200/2	1350	11.50	2.288	8.43E-06	0.252	12402	0.072	0.1995	0.358	-5.074	-0.446	light blue	ok
HG251003	CO_2/H_2 = 200/2	1300	11.00	1.342	3.01E-06	0.351	12402	0.170	0.1012	1.679	-5.521	0.225	blue	ok
HG251004	CO_2/H_2 = 200/2	1250	23.75	2.322	7.44E-07	0.801	12402	0.224	0.0470	4.764	-6.128	0.678	blue	ok
HG25331	CO_2/H_2 = 200/6	1400	13.00	1.768	2.96E-06	0.061	12402	0.022	0.2486	0.090	-5.529	-1.045	colourless	ok
HG25332	CO_2/H_2 = 200/6	1350	14.00	1.629	8.94E-07	0.079	12402	0.031	0.2395	0.131	-6.049	-0.881	colourless	ok
HG25333	CO_2/H_2 = 200/6	1300	14.00	1.697	1.59E-07	0.331	12402	0.127	0.1444	0.877	-6.799	-0.057	pale blue	ok
HG25334	CO_2/H_2 = 200/6	1250	18.00	1.711	2.11E-08	0.419	12402	0.159	0.1120	1.420	-7.676	0.152	light blue	ok
HG25101	CO_2/H_2 = 200/20	1400	12.00	1.834	4.21E-08	0.047	12001	0.017	0.2544	0.065	-7.376	-1.184	colourless	ok
HG25102	CO_2/H_2 = 200/20	1350	12.00	1.760	1.44E-08	0.050	11366	0.018	0.2526	0.073	-7.842	-1.136	colourless	ok
HG25103	CO_2/H_2 = 200/20	1300	12.00	1.507	4.24E-09	0.116	11907	0.050	0.2210	0.226	-8.373	-0.646	pale blue	ok
HG25104	CO_2/H_2 = 200/20	1250	20.00	1.452	1.09E-09	0.283	12284	0.127	0.1445	0.876	-8.963	-0.057	pale blue	ok

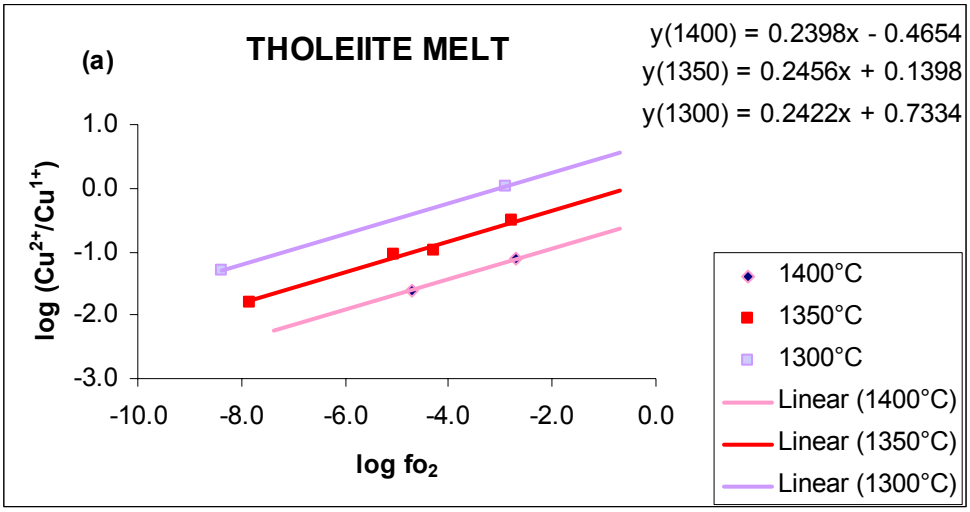
(a)
THOLEIITE MELT
y(1400) = 0.2398x - 0.4654
y(1350) = 0.2456x + 0.1398
y(1300) = 0.2422x + 0.7334
log (Cu2+/Cu1+)
log fo2
1400°C
1350°C
1300°C
Linear (1400°C)
Linear (1350°C)
Linear (1300°C)

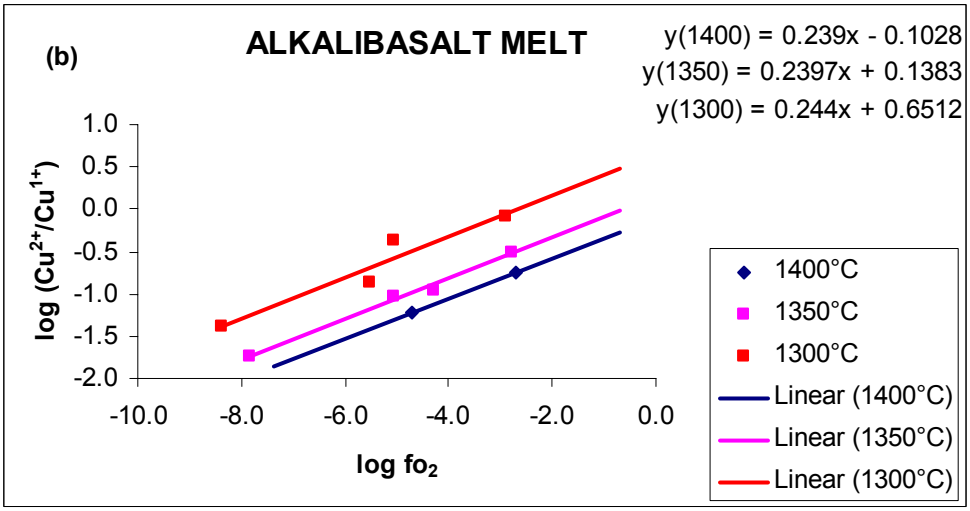
(b)
ALKALIBASALT MELT
y(1400) = 0.239x - 0.1028
y(1350) = 0.2397x + 0.1383
y(1300) = 0.244x + 0.6512
log (Cu2+/Cu1+)
log fo2
1400°C
1350°C
1300°C
Linear (1400°C)
Linear (1350°C)
Linear (1300°C)

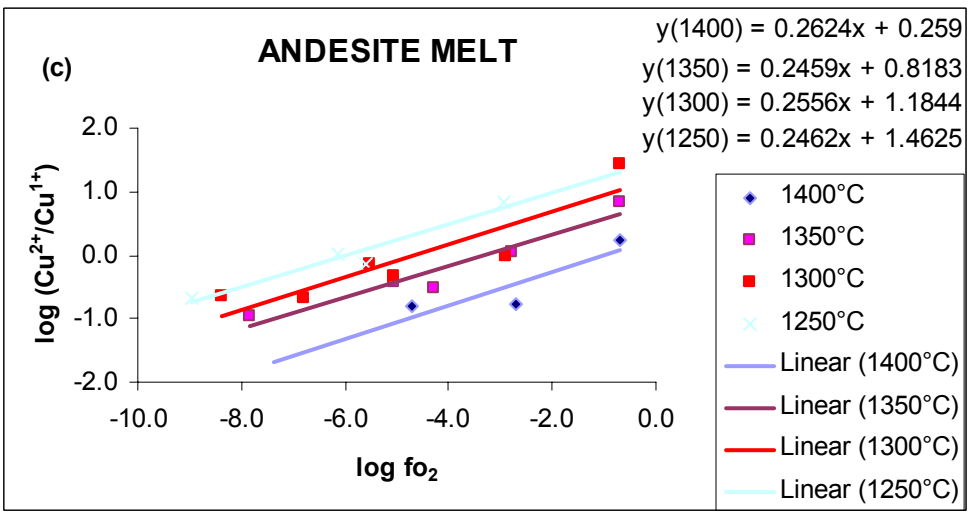
(c)
ANDESITE MELT
y(1400) = 0.2624x + 0.259
y(1350) = 0.2459x + 0.8183
y(1300) = 0.2556x + 1.1844
y(1250) = 0.2462x + 1.4625
log (Cu2+/Cu1+)
log fo2
1400°C
1350°C
1300°C
1250°C
Linear (1400°C)
Linear (1350°C)
Linear (1300°C)
Linear (1250°C)

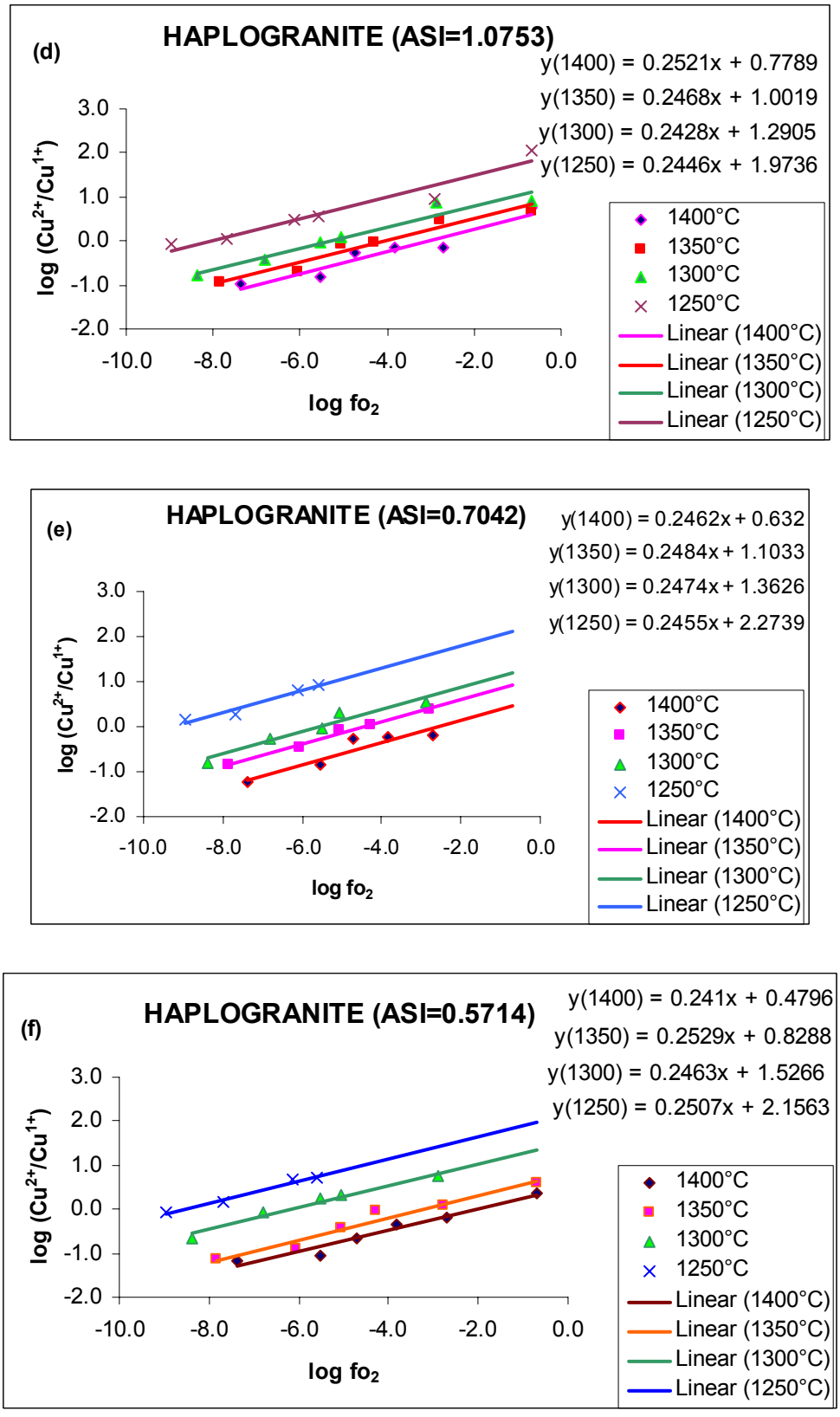

Fig. 3.11(a) – (f). Speciation of copper as a function of oxygen fugacity and temperature for glass compositions: tholeiite (**a**), alkalibasalt (**b**), andesite (**c**), haplogranite with ASI = 1/0.93 (**d**), ASI = 1/1.42 (**e**), ASI = 1/1.75 (**f**). The curves in all cases exhibit a linear relationship between the variables log (Cu^{2+}/Cu^{1+}) against log fo_2. The curves trend almost parallel to each other with their slopes in the ranging from 0.239 to 0.256. Note that for every composition, the lowest and highest temperature curves lie uppermost and lowermost, respectively.

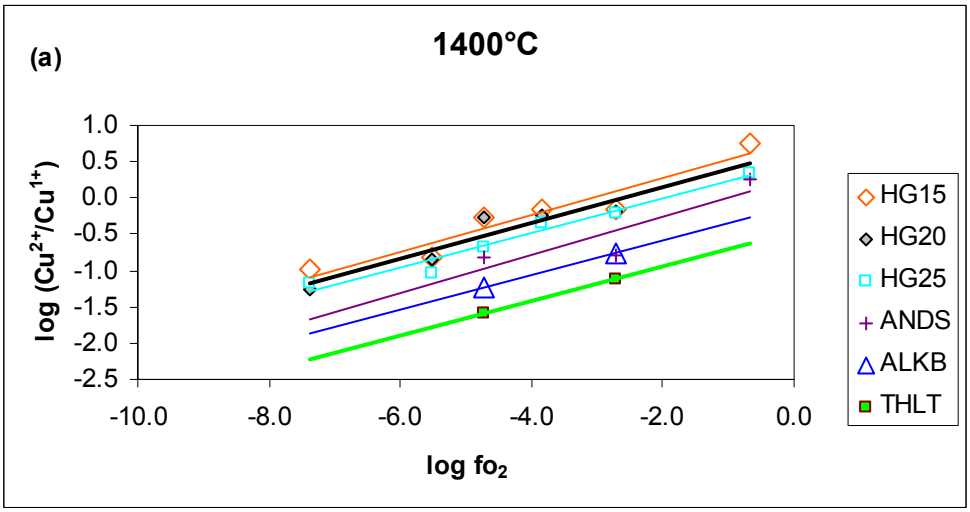
(a)
1400°C
log (Cu2+/Cu1+)
1.0
0.5
0.0
-0.5
-1.0
-1.5
-2.0
-2.5
-10.0
-8.0
-6.0
-4.0
-2.0
0.0
log fo2
HG15
HG20
HG25
ANDS
ALKB
THLT

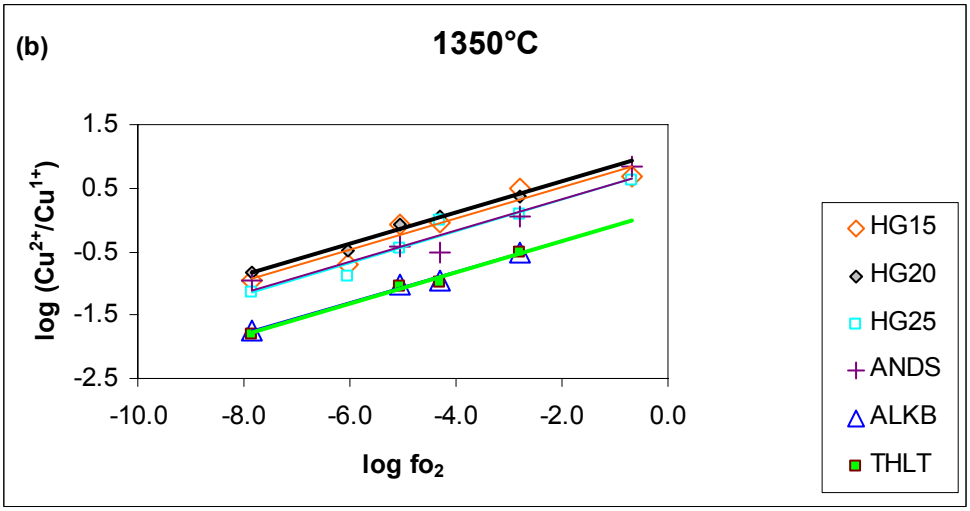
(b)
1350°C
log (Cu2+/Cu1+)
1.5
0.5
-0.5
-1.5
-2.5
-10.0
-8.0
-6.0
-4.0
-2.0
0.0
log fo2
HG15
HG20
HG25
ANDS
ALKB
THLT

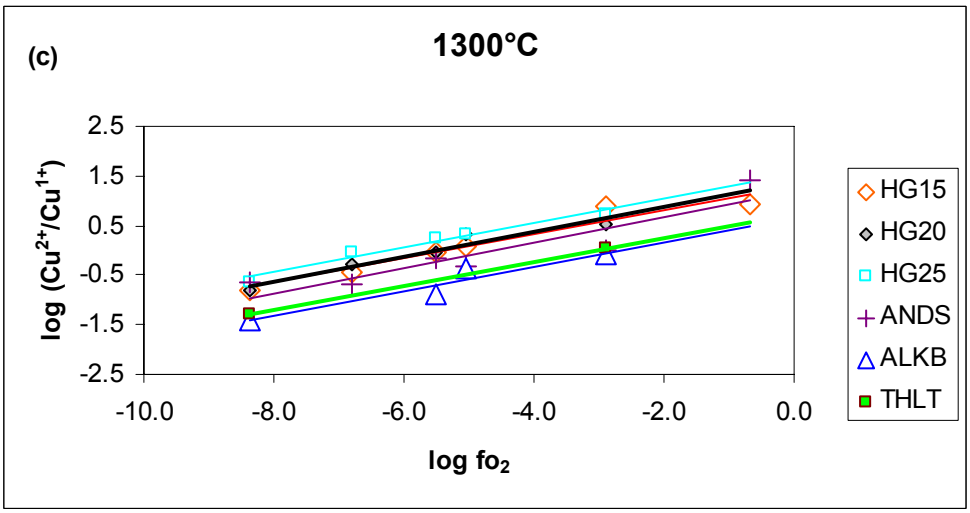
(c)
1300°C
log (Cu2+/Cu1+)
2.5
1.5
0.5
-0.5
-1.5
-2.5
-10.0
-8.0
-6.0
-4.0
-2.0
0.0
log fo2
HG15
HG20
HG25
ANDS
ALKB
THLT

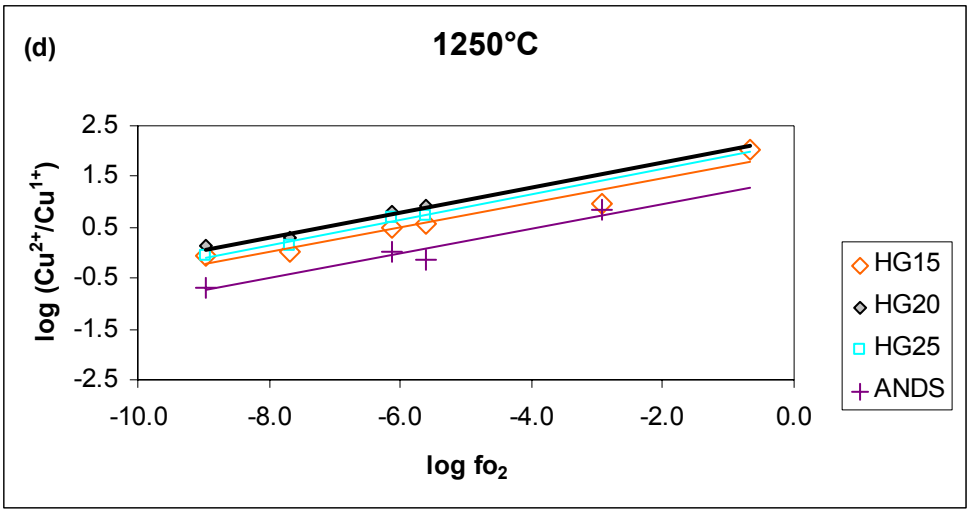

Fig. 3.12(a) - (d). Speciation of copper as a function of oxygen fugacity and composition at fixed temperatures. Generally the redox ratio Cu^{2+}/Cu^{1+} at any fixed conditions of temperature and oxygen fugacity is highest for the haplogranites and lowest for the tholeiites.

3.4. Thermodynamic data analysis

Results of experimental investigations of copper speciation in silicate melts at high temperatures employed in this study can be used to estimate the enthalpy of reactions (ΔH) for the oxidation of Cu^{1+} to Cu^{2+}. Thermodynamic functions are readily drawn from equations (3.5)-(3.8), section 3.3.

The equilibrium constant, K^*, is related to Gibbs free energy of reaction (ΔG) by the equation:

$$- RT \ln K^* = \Delta G = \Delta H - T\Delta S \qquad (3.12)$$

Therefore, $$\ln K = \frac{\Delta H}{-RT} + \frac{\Delta S}{R} \qquad (3.13)$$

where ΔH and ΔS are respectively the enthalpy and entropy of reaction at the equilibrium temperature T. R is the gas constant.

A plot of **ln K*** against $\frac{1}{T}$ yields a straight line with gradient $\frac{-\Delta H}{R}$ (see **Figure 3.13**). Experimental data of the ratio Cu^{2+}/Cu^{+} in the experimental silicate melts, including $f(O_2)$ and $f(O_2)^{\frac{1}{4}}$ at various run temperatures (**T**) have been calculated for every composition. The general equation for the resulting curves of fit is:

$$y = A_1 + B_1 x \qquad (3.14)$$

where y = **ln K***, x = $\frac{1}{T}$, A_1 = ln K* at the point where the graph intercepts the y –axis, and B1 = the gradient of the curve.

Table 3.10 is a summary list of the results of fit and enthalpies of reaction for the experimental silicate melts.

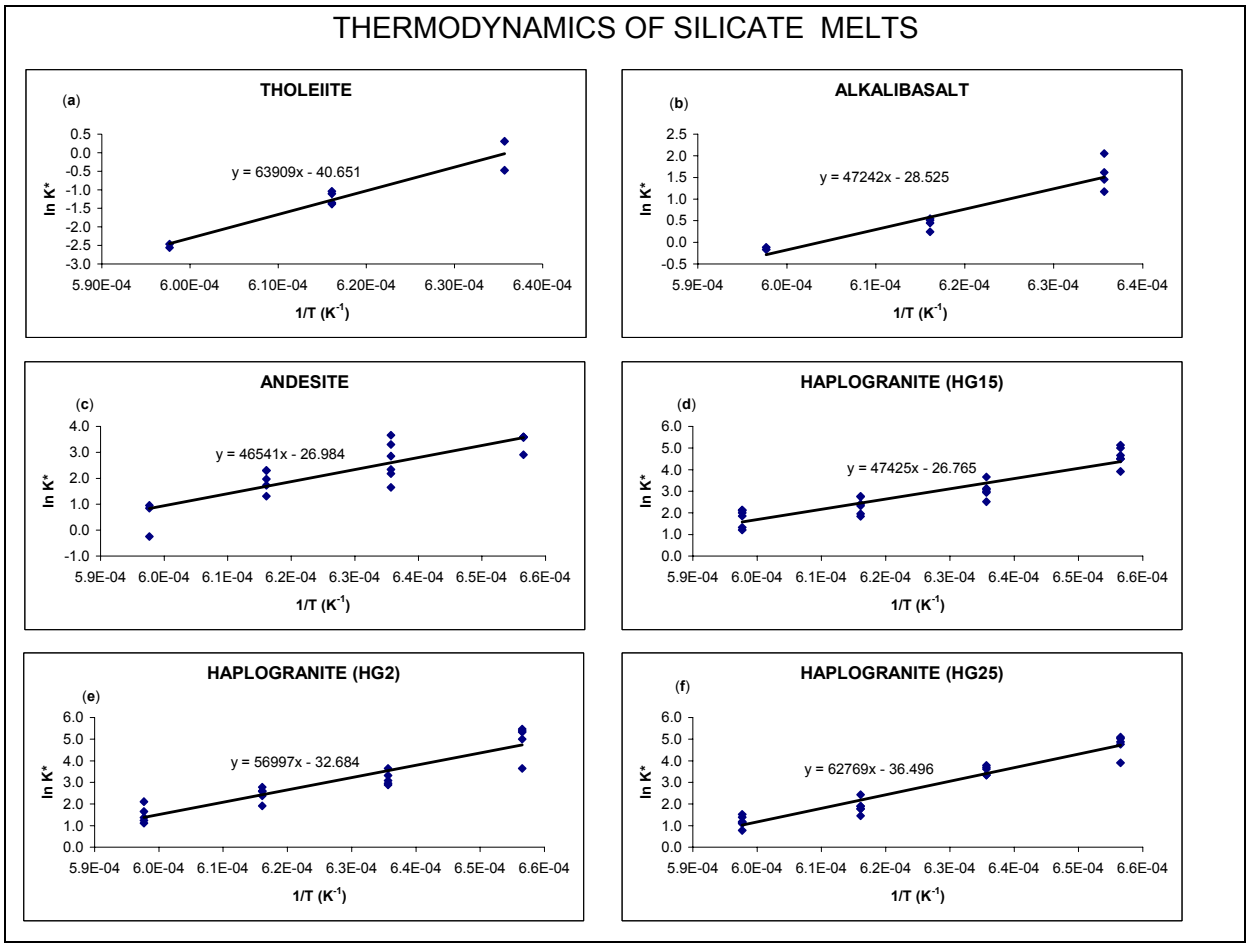

Figure 3.13. Variation of experimental equilibrium constant (**K***) with temperature (**T**). The graphs show linear relationships obtained by plotting **ln K*** against **1/T** for (a) tholeiite melt, (b) alkalibasalt, (c) andesite, (d) haplogranite (HPG15), (e) HPG2, and (f) HPG25 melts. See **Table 3.4**. for the corresponding results of fit and estimated enthalpies of reaction.

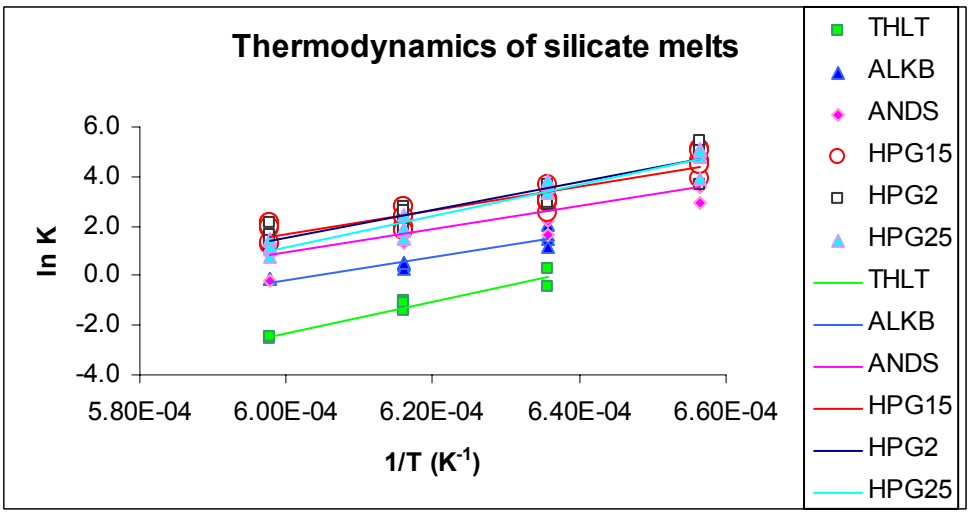

Figure 3.14. Comparison of trend curves (in **Figure 3.13**) for the experimental silicate melts. Note that the granites and basalt curves generally trend uppermost and lowermost, respectively, with the andesite plotting in between.

Table 3.10. Results of fit and estimated enthalpies of reaction derived from the graphs in Figure 3.13 for various experimental silicate melts.

Composition	A_1 (**ln K***)	B_1 (**K**)	ΔH (**kJ/mol**)
Tholeiite (THLT)	-40.651	63909	-531.3
Alkalibasalt (ALKB)	-28.525	47242	-392.8
Andesite (ANDS)	-29.984	46541	-386.9
Haplogranite (HPG15)	-26.765	47425	-394.3
Haplogranite (HPG2)	-32.684	56997	-473.9
Haplogranite (HPG25)	-36.496	62769	-521.9

Note: andesite melt shows intermediate thermodynamic character between basaltic and granitic melts.

3.5 Geological implications

The redox ratio Cu^{2+}/Cu^{+} bears some geological relevance to formation of economic porphyry copper deposits in granitic, dioritic, basaltic and other magmatic environments.
Calculation of the ratio Cu^{2+}/Cu^{+} follows from equation (3.7) rearranged to yield equation (3.8):

$$Cu^{2+}/Cu^{+} = K^{*} \times f_{O_2}^{0.25}$$

K^{*}, the equilibrium constant of a given silicate melt, can be calculated from the experimental curves in **Figure 3.4** by extrapolating the curves of fit to natural magmatic conditions of temperature (T) and oxygen fugacity $\left(f_{o_2}\right)$, inside a crystallising pluton. f_{O_2}, for natural magmatic systems, can be calculated from the following equation:

$$\text{Log } fO_2 = A + \frac{B}{T} + C\left(\frac{P-1}{T}\right) \qquad (3.15)$$

where T and P (the system's temperature and pressure) are given in units of Kelvin and bar, respectively. A, B, and C are constants related to the oxygen fugacity conditions of the melt and varies with the buffer type as follows:

Buffer:	QFM	Ni-NiO	H-M
constant			
A	8.95	9.36	13.966
B	-25287	-24930	-24630
C	0.094	0.046	0.019

Oxygen fugacity is an important intensive parameter which controls the stability of minerals and mineral-assemblages and governs the evolution of magma and ore-forming hydrothermal solutions.

Generally the Cu^{2+}/Cu^{+} ratio in silicate melts varies with magmatic environment and oxygen atmospheres as demonstrated in the next two subsections.

3.5.1. Cu^{2+}/Cu^{+} ratio in granite and diorite melts

Porphyry copper-related plutons of granitic and dioritic magmatic systems often crystallise at temperatures in the range of 700 – 800°C, under oxygen fugacities between those of QFM (quartz-fayalite-magnetite), Ni-NiO, and H-M (hematite-magnetite), Hewitt (1978); Haas and Robie (1973) and Huebner and Sato (1970).
In this study experimental thermodynamic parameters, derived from the graphs in **Figures 3.13**e, d, f (for granitic systems) and **3.13**c (for dioritic systems) in combination with equation (3.15) have been used to calculate the Cu^{2+}/Cu^{+} ratio in silicate melts from granitic and dioritic magmatic environments for each buffer system. Results of this calculation are listed in **Table 3.11** and presented graphically in **Figures 3.15** a, b, and c (top-middle left).
The results show a predominance of Cu^{2+} in granitic and dioritic plutons, i.e. the ratio Cu^{2+}/Cu^{+} is always greater than one. This is, however, not the case with

peraluminous granite systems (experimentally represented by sample HPG1), in which apparently only the reduced form of copper species (i.e. Cu^{+}) exists.

Table 3.11. Cu^{2+}/Cu^{+} ratios for granite and diorite melts (HPG25, HPG2, HPG15, and ANDS) inside a crystallising pluton at 700-800°C under oxygen atmospheres buffered by QFM, Ni-NiO, and H-M

Buffer type		**QFM**		**Ni-NiO**		**H-M**	
composition	T/°C	fo_2	Cu^{2+}/Cu^{+}	fo_2	Cu^{2+}/Cu^{+}	fo_2	Cu^{2+}/Cu^{+}
HPG25	700	1.44E-17	8.95E+07	6.87E-17	1.32E+08	4.96E-12	2.17E+09
	750	2.62E-16	7.91E+06	1.21E-15	1.16E+07	8.52E-11	1.89E+08
	800	3.65E-15	8.76E+05	1.64E-14	1.28E+06	1.12E-09	2.06E+07
HPG2	700	1.44E-17	1.08E+07	6.87E-17	1.59E+07	4.96E-12	2.61E+08
	750	2.62E-16	1.27E+06	1.21E-15	1.86E+06	8.52E-11	3.03E+07
	800	3.65E-15	1.83E+05	1.64E-14	2.66E+05	1.12E-09	4.31E+06
HPG15	700	1.44E-17	2.14E+05	6.87E-17	3.16E+05	4.96E-12	5.18E+06
	750	2.62E-16	4.09E+04	1.21E-15	5.99E+04	8.52E-11	9.75E+05
	800	3.65E-15	9.10E+03	1.64E-14	1.33E+04	1.12E-09	2.14E+05
ANDS	700	1.44E-17	6.93E+04	6.87E-17	1.02E+05	4.96E-12	1.68E+06
	750	2.62E-16	1.38E+04	1.21E-15	2.03E+04	8.52E-11	3.30E+05
	800	3.65E-15	3.21E+03	1.64E-14	4.67E+03	1.12E-09	7.56E+04

3.5.2. Cu^{2+}/Cu^{+} ratio in basaltic (tholeiite and alkalibasalt) melts

Basaltic melts (evident from the experiments on samples ALKB and THLT) seem to behave quite differently from granitic and dioritic melts in terms of their crystallising temperature range (1100 – 1200°C) and choice of suitable buffer systems (QFM and Ni-NiO), and have a different range of Cu^{2+}/Cu^{+} ratio as a consequence. Following a similar procedure as in the preceding section the Cu^{2+}/Cu^{+} ratio in basaltic melts has been calculated using thermodynamic parameters derived from the graphs in **Figures 3.13**a (for tholeiite melts) and **3.13**b (for alkalibasalt melts) in magmatic environments whose oxygen fugacities are close to the QFM and Ni-NiO buffers. The results are listed in **Table 3.12** and graphically represented in **Figures 3.15**a and b (bottom right). Contrary to the results for granites and diorites, basaltic melts show a predominance of Cu^{+} over Cu^{2+} ions, and consequently have very low ratios of Cu^{2+}/Cu^{+} (i.e. usually less than one).

Table 3.12. The Cu^{2+}/Cu^{+} ratios for basaltic melts (ALKB and THLT) at temperatures (1100-1200°C) under QFM and Ni-NiO buffers.

Buffer type		**QFM**		**Ni-NiO**	
composition	T/°C	fo_2	Cu^{2+}/Cu^{+}	fo_2	Cu^{2+}/Cu^{+}
ALKB	1100	4.69E-10	1.66E+00	1.87E-09	2.35E+00
	1150	2.06E-09	7.19E-01	8.07E-09	1.01E+00
	1200	8.17E-09	3.29E-01	3.16E-08	4.61E-01
THLT	1100	4.69E-10	1.68E+00	1.87E-09	2.38E+00
	1150	2.06E-09	4.75E-01	8.07E-09	6.68E-01
	1200	8.17E-09	1.46E-01	3.16E-08	2.05E-01

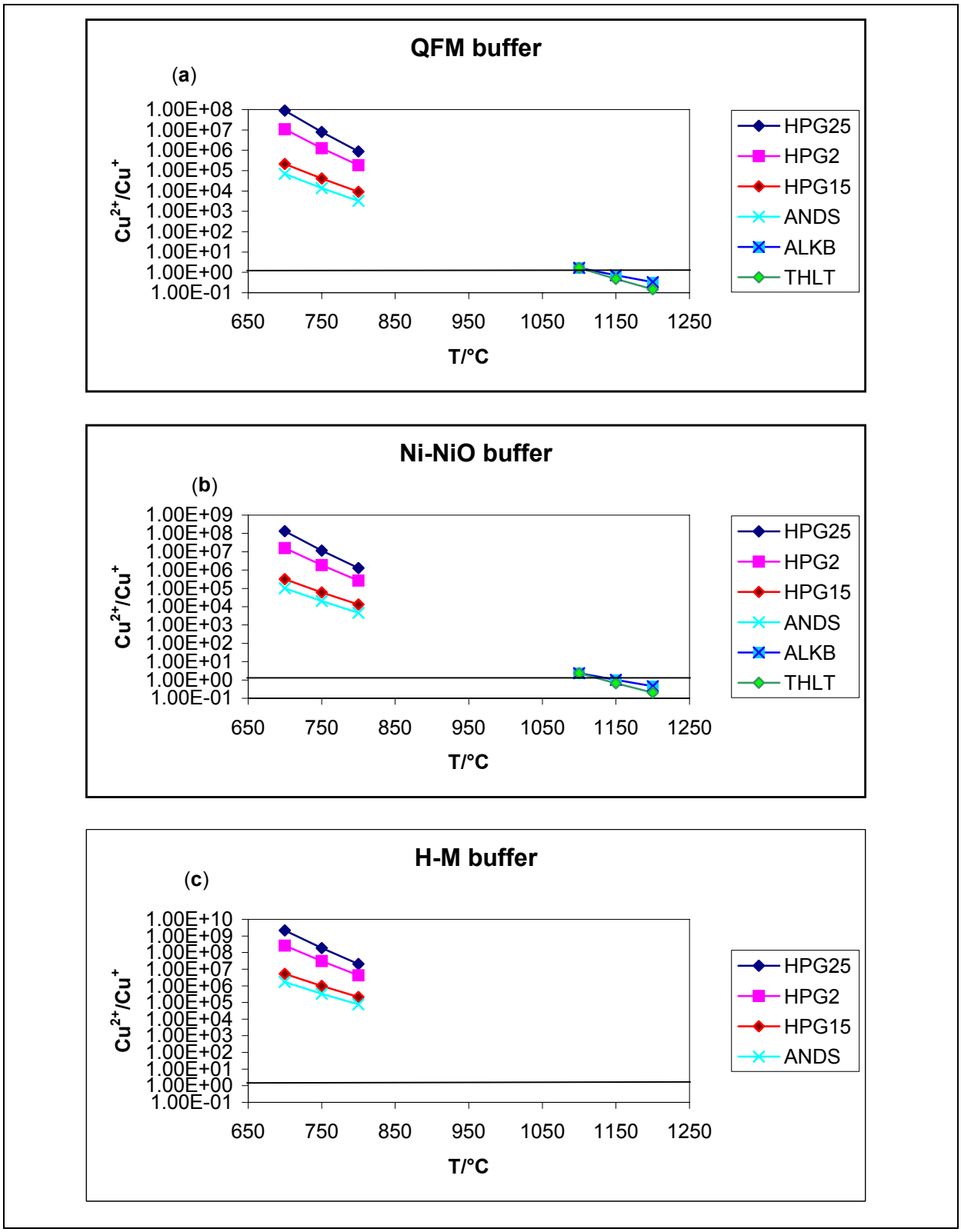

Figure 3.15. Cu^{2+}/Cu^{+} ratio of silicate melts plotted against temperature for (1) granites (HPG25, HPG2, HPG15) and diorite (ANDS) melts inside a crystallising pluton at 700-800°C and (2) basaltic melts (ALKB and THLT) at 1100-1200°C, under (**a**) QFM (quartz-fayalite-magnetite), (**b**) Ni-NiO, and (**c**) H-M (hematite-magnetite) buffer conditions. Note: Cu^{2+} ions predominate over Cu^{+} above the horizontal line across the graphs (i.e. the ratio $Cu^{2+}/Cu^{+} > 1$). The converse is true for the field below the line (i.e. $Cu^{+} > Cu^{2+}$). See text for further explanation.

3.5.3. Implication of Cu^{2+}/Cu^{1+} ratio for mineral-melt Cu partitioning

The ratio Cu^{2+}/Cu^{+} has implications for understanding the partitioning behaviour of copper in granitic, dioritic and basaltic melts, and consequently the genesis of ore-deposits in different magmatic-hydrothermal environments.

In basaltic melts, for example, the reduced form of copper (Cu^{1+}) predominates over the oxidised form (Cu^{2+}). Therefore, the partition coefficient of copper in the crystallising mineral phases will be significantly influenced by the Cu^{1+} species in the melt, substituting for the major elements in the appropriate lattice sites of the mineral crystals. By reference to the treatment of the Brice model in chapter 2 of this thesis, equations (2.7) and (2.9) have been used to predict the partitioning behaviour of copper between the crystallising relevant major rock-forming minerals and their equilibrium melts in basaltic systems. **Table 3.13** shows the calculated partition coefficients of copper, including the elastic strain model input lattice site parameters and their sources. The calculation considers the ionic radius of Cu^{1+} to be 0.77 Å (adopted from Shannon, 1976), and assumes negligible crystal field effects.

Table 3.13. Partition coefficients of copper between minerals and melts in a crystallising basaltic system under oxygen fugacity controlled by Ni-NiO buffer at 1150°C

Mineral	Major-Element (a)	Lattice-site (s)	D_a or D_o	E_s^{1+} (GPa)	r_o (Å)	r_a (Å)	D_{Cu}	Sources (references)
Clino-pyroxene	Na	M2	0.0728	89.58	1.02	1.02	1.58×10^{-2}	Blundy et al.(1994) Blundy et al.(1995) Blundy et al.(2003)
Plagioclase	Na	M	0.6325	64	1.2424	1.02	2.83×10^{-2}	Blundy et al.(1994) Bindeman et al.(1998) Blundy et al.(2003)
Amphibole	Li	M4	4.604	390	1.03		0.34×10^{-2}	La Tourrette et al.(1995) Blundy et al.(2003)
Biotite1	K	**X**	3.568	46.5	1.428		0.61×10^{-2}	Blundy et al.(2003) This study (Table 2.15)
Biotite2	Rb	**X**	1.4	50	1.72	1.52	0.60×10^{-6}	Blundy et al.(1994) Schmidt et al (1999)

Following similar arguments as in the last section of chapter 2, it can be concluded that late stage crystallisation and fractionation of major rock-forming minerals in a basaltic system, originally with trace amounts of copper, will enrich the residual melts in Cu^{1+} ions. This is because of the incompatibility nature of copper in the crystallising rock-forming minerals. Fluid saturation is hardly attainable in basaltic systems as the initial amount of volatiles in the melt is very minimal. Instead there will be a progressive increase in the amount of sulphide dissolved in the residual melt during fractional crystallisation of the system. As solidification proceeds and magma temperature falls, sulphide saturation can be achieved with formation of small immiscible sulphide globules that accumulate to form a single cohesive layer of melt. Cu is likely to partition strongly in the sulphide phase rather than remain in the silicate residual melt, i.e. economic Cu-ore deposits in basaltic systems possibly results from the concentration of Cu in the precipitating sulphide phases, if sulphide saturation in the magma is reached.

4. SOLUBILITY OF COPPER IN ROCK-FORMING MINERALS

4.1. Aims

The majority of copper deposits are related to hydrothermal fluids which (as a response to thermal or pressure gradients in the earth's crust) travel long distances interacting with large volumes of country rocks before depositing their metal contents. While in movement, hydrothermal fluids may either scavenge copper from the country rocks and deposit it in some appropriate localities at the right conditions of temperature and pressure or be stripped of all their copper content by the rock-forming minerals in the surrounding rocks through which they travel, consequently being rendered unable to yield economically viable copper ore deposits.
Similarly at saturation a copper-rich magmatic fluid exsolving from a crystallizing granitic magma may loose all its copper content while in transit through the surrounding country rocks.

Whether the circulating fluids gain or loose copper will largely depend on the way copper partitions itself between the fluids and the rock-forming minerals, at some defined equilibrium conditions of temperature and pressure. Thus both processes can be quantitatively investigated if the partition coefficient of copper (D_{Cu}) between a particular fluid and a mineral is known.

$$D_{Cu}(\text{fluid}/\text{mineral}) = \frac{(\text{concentration of Cu in fluid})}{(\text{concentration of Cu in mineral})} \qquad (4.1)$$

In principle, one may obtain the D_{Cu} values for a variety of minerals and fluids at different equilibrium conditions of temperature and pressure by experimentally investigating their copper concentrations and applying this information to the standard formula stated above. Such experiments however, take an enormous amount of time to achieve equilibrium conditions because the diffusion of Cu through the minerals' crystal-lattices is a very slow process mineral.

This study circumvents the problem (i.e. the slow diffusion rates of Cu in the mineral crystal lattices) by investigating a range of synthetic systems at 2 kbar and 600-700°C to determine the solubility of copper in some common rock-forming minerals crystallizing in equilibrium with metallic copper and copper oxide. The oxygen fugacity in these systems is buffered by Cu-Cu_2O. This buffer system ensures the presence of excess Cu and Cu_2O required for saturating the crystallizing minerals with copper as well as fixing both the copper activity and the oxygen fugacity of the system. This also means that the solubility of Cu in the crystallizing minerals will only depend on pressure and temperature conditions of the system.

By consulting thermodynamic data bases the solubility of copper in a fluid of known composition (at specified conditions of pressure and temperature) and in equilibrium with metallic Cu and Cu_2O can be calculated, giving results that are reasonably correct at relatively low temperatures.

The results of this study can be used to calculate the partition coefficients of copper (D_{Cu}(fluid/mineral)) from the acquired solubility or concentration values of copper in fluids and minerals under the same equilibrium conditions.
This study is the first of its kind to investigate the solubility of Cu in rock-forming minerals as previous works have only been able to establish the solubility of copper in fluids exsolving from crystallising magmatic melts at saturation. Feldspars (orthoclase and albite) and micas (muscovite and phlogopite) were chosen since they tend to be the most frequent and abundant minerals in intrusive granites and their surrounding country rocks.

4.2. Sample synthesis

4.2.1. Starting materials and sample preparation

A range of synthetic systems was experimentally investigated at isobaric and isothermal conditions (2 kbar and 600-700°C) to determine the solubility of copper in some common rock-forming minerals which crystallize from hydrothermal solutions in equilibrium with excess metallic Cu and Cu_2O.

The rock-forming minerals (referred to as target minerals in the text) investigated in this experimental study included muscovite ($KAl_2[AlSi_3O_{10}][OH]_2$), phlogopite ($KMg_3[AlSi_3O_{10}][OH]_2$), orthoclase ($KAlSi_3O_8$) and albite ($NaAlSi_3O_8$). Experiments were performed in two options, with each option having different sample mixtures.

Target minerals in option 2 experiments were each doped with own corresponding hypothetical mineral (i.e. $Cu^{1+}Al_2(AlSi_3O_{10})(OH)_2$, $Cu^{1+}Mg_3(AlSi_3O_{10})(OH)_2$, & $Cu^{1+}AlSi_3O_8$) in the ratio of 9:1.

The synthetic minerals and their hypothetical counterparts were prepared separately and later mixed in the ratios of 9:1, i.e. mixtures of reagent grade chemicals corresponding to 90 wt% target mineral and 10 wt% hypothetical mineral were prepared. Therefore the following pairs of minerals were mixed to yield samples for experiments in option 2:

1) $KMg_3[AlSi_3O_{10}][OH]_2$ + $Cu^{1+}Mg_3(AlSi_3O_{10})(OH)_2$, sample **A**
2) $KAl_2[AlSi_3O_{10}][OH]_2$ + $Cu^{1+}Al_2(AlSi_3O_{10})(OH)_2$, sample **B**
3) $NaAlSi_3O_8$ + $Cu^{1+}AlSi_3O_8$, sample **C** and
4) $KAlSi_3O_8$ + $Cu^{1+}AlSi_3O_8$, sample **D**.

Similarly for experiments in option 1, samples were prepared by mixing reagent grade chemicals corresponding to ~65 wt % target mineral and ~ 35 wt % Cu_2O. Therefore samples for option 1 experiments included:

1) $KMg_3[AlSi_3O_{10}][OH]_2$ + Cu_2O, sample **Phl.Cu**
2) $KAl_2[AlSi_3O_{10}][OH]_2$ + Cu_2O, sample **Mu.Cu**
3) $NaAlSi_3O_8$ + Cu_2O, sample **Ab.Cu**
4) $KAlSi_3O_8$ + Cu_2O, sample **Or.Cu**.

Unlike the starting materials for the experiments in chapters 2 and 3, for which reagent grade oxides and carbonates were first converted into synthetic silicate glasses, the sample mixtures of reagent-grade oxides and carbonates employed in this study were used while still in raw powder form. The mixtures, however, were thoroughly blended and homogenised under ethanol, and later dried and ground to powder, in the same way as described sections 2.2 and 3.2 of chapters 2 and 3, respectively.

Compositions of the starting materials in this study are, therefore, only presented in nominal form, calculated from appropriate stoichiometric formulas (see **Tables 4.1**a-d) of the sample components in each mixture.

Table 4.1.(a). Composition of starting materials. The volatile-free bulk composition of sample **A** corresponds to a mixture of phlogopite (90 wt%) and its hypothetical copper counterpart mineral Cu-Phl (10 wt%). Similarly the volatile-free bulk composition of sample **Phl.Cu** corresponds to a mixture of phlogopite (65 wt%) and cuprite (35 wt%).

Sample	Phl	Cu-Phl	(Phl, 90wt%)	(Cu-Phl, 10wt%)	**A**	Cu_2O	(Phl, 65wt%)	(Cu_2O, 35wt%)	**Phl.Cu**
Reagent									
SiO_2	34.64	34.48	31.18	3.45	**34.63**	0	22.52	0.00	**22.52**
$Al(OH)_3$	14.99	14.92	13.49	1.49	**14.98**	0	9.74	0.00	**9.74**
$Mg(OH)_2$	33.62	33.47	30.26	3.35	**33.61**	0	21.86	0.00	**21.86**
$K_2(CO_3)$	13.28	0.00	11.95	0.00	**11.95**	0	8.63	0.00	**8.63**
$Na_2(CO_3)$	0.00	0.00	0.00	0.00	**0.00**	0	0.00	0.00	**0.00**
Cu_2O	0.00	13.69	0.00	1.37	**1.37**	100	0.00	35.00	**35.00**
H_2O	3.46	3.45	3.12	0.34	**3.46**	0	2.25	0.00	**2.25**
Total	100.00	100.00	90.00	10.00	100.00	100	65.00	35.00	100.00

Table 4.1.(b). The volatile-free bulk composition of sample **B** corresponds to a mixture of muscovite (90 wt%) and its hypothetical copper counterpart mineral Cu-Mu (10 wt%). The volatile-free bulk composition of sample **Mu.Cu** corresponds to a mixture of muscovite (65 wt%) and cuprite (35 wt%).

Sample	Mu	Cu-Mu	(Mu, 90wt%)	(Cu-Mu, 10wt%)	**B**	Cu_2O	(Mu, 65wt%)	(Cu_2O, 35wt%)	**Mu.Cu**
Reagent									
SiO_2	35.95	35.78	32.35	3.58	**35.93**	0	23.37	0.00	**23.37**
$Al(OH)_3$	46.68	46.45	42.01	4.64	**46.65**	0	30.34	0.00	**30.34**
$Mg(OH)_2$	0.00	0.00	0.00	0.00	**0.00**	0	0.00	0.00	**0.00**
$K_2(CO_3)$	13.78	0.00	12.41	0.00	**12.41**	0	8.96	0.00	**8.96**
$Na_2(CO_3)$	0.00	0.00	0.00	0.00	**0.00**	0	0.00	0.00	**0.00**
Cu_2O	0.00	14.20	0.00	1.42	**1.42**	100	0.00	35.00	**35.00**
H_2O	3.59	3.57	3.23	0.36	**3.59**	0	2.33	0.00	**2.33**
Total	100.00	100.00	90.00	10.00	100.00	100	65.00	35.00	100.00

Table 4.1.(c). The volatile-free bulk composition of sample **C** corresponds to a mixture of albite (90 wt%) and its hypothetical copper counterpart mineral Cu-Ab (10 wt%). The volatile-free bulk composition of sample **Ab.Cu** corresponds to a mixture of albite (65 wt%) and cuprite (35 wt%).

Sample	Ab	Cu-Ab	(Ab, 90wt%)	(Cu-Ab, 10wt%)	**C**	Cu_2O	(Ab, 65wt%)	(Cu_2O, 35wt%)	**Ab.Cu**
Reagent									
SiO_2	57.91	54.65	52.12	5.47	**57.59**	0	37.64	0.00	**37.64**
$Al(OH)_3$	25.06	23.65	22.56	2.37	**24.92**	0	16.29	0.00	**16.29**
$Mg(OH)_2$	0.00	0.00	0.00	0.00	**0.00**	0	0.00	0.00	**0.00**
$K_2(CO_3)$	0.00	0.00	0.00	0.00	**0.00**	0	0.00	0.00	**0.00**
$Na_2(CO_3)$	17.03	0.00	15.32	0.00	**15.32**	0	11.07	0.00	**11.07**
Cu_2O	0.00	21.69	0.00	2.17	**2.17**	100	0.00	35.00	**35.00**
Total	100.00	100.00	90.00	10.00	100.00	100	65.00	35.00	100.00

Table 4.1.(d). The volatile-free bulk composition of sample **D** corresponds to a mixture of orthoclase (90 wt%) and its hypothetical copper counterpart mineral Cu-Or (10 wt%). The volatile-free bulk composition of sample **Or.Cu** corresponds to a mixture of orthoclase (65 wt%) and cuprite (35 wt%).

Sample	Or	Cu-Or	(Or, 90wt%)	(Cu-Or, 10wt%)	**D**	Cu_2O	(Or, 65wt%)	(Cu_2O, 35wt%)	**Or.Cu**
Reagent									
SiO_2	55.06	54.65	49.55	5.47	**55.02**	0	35.79	0.00	**35.79**
$Al(OH)_3$	23.83	23.65	21.45	2.37	**23.81**	0	15.49	0.00	**15.49**
$Mg(OH)_2$	0.00	0.00	0.00	0.00	**0.00**	0	0.00	0.00	**0.00**
$K_2(CO_3)$	21.11	0.00	19.00	0.00	**19.00**	0	13.72	0.00	**13.72**
$Na_2(CO_3)$	0.00	0.00	0.00	0.00	**0.00**	0	0.00	0.00	**0.00**
Cu_2O	0.00	21.69	0.00	2.17	**2.17**	100	0.00	35.00	**35.00**
Total	100.00	100.00	90.00	10.00	100.00	100	65.00	35.00	100.00

4.2.2. Charge preparation

One-meter long copper tubes (OD ~ 5 mm and ID ~ 4 mm) were sawn into pieces, of about 45 mm long. Their rough ends were polished smooth before being immersed in acetone and cleaned in an ultrasonic bath for about 5 minutes. The Cu-tubes, now measuring approximately 40 mm length after trimming, had one of their open ends closed using a jaw chuck (Drei-Backenfutter), which gave it a triangular or star-like shape. By this stage the copper tube had been converted into an open capsule. The closed/crimped ends of the capsules were completely sealed by welding under protective gas (argon). Following the same procedure as in chapter 2, section 2, a label or a symbol was engraved on the body of each capsule, for future identification, after the experiment. The half open capsule was then weighed.

Cold doubly-distilled water (about 15-17µl) was loaded into the clean empty capsule using a micro syringe. This was followed by the sample powder (about 200 mg), carefully pressed into the capsule, leaving enough empty space above the sample, to prevent the final welding from interfering with its contents.
The loaded capsule was quickly sealed using a jaw chuck, which also imparted a streamlined form to the capsule. The sealed end of the capsule was further secured using a pair of pliers. Finally the capsule was welded while suspended in an ice-bath or liquid N_2, which helped to prevent excessive water loss from the enclosed sample. The capsules were weighed at every stage of the charge preparation. Finally the sealed capsules were tested for possible leaks by checking for weight losses after being dried overnight in an oven at a temperature of 150°C. Note: the star-like form of the capsule ends was intended for easy recovery at the end of the experiment.

4.2.3. Experimental technique

The equipment and technique employed in these experiments was very similar to that employed for the experiments in section 2, chapter 2 of this thesis, except for a few modifications in conditions and duration.

In this study, run temperatures were relatively low, in the range 600-750°C, and the duration shorter (15-20 days) than for the experiments in chapter 2, as a longer duration would have lead to the dissolution of the capsule body and consequently contaminated the contents therein. It should also be noted that the temperatures were measured using external thermocouples as the Cu-capsules tend to be larger and longer than the Au-capsules used in chapter 2 experiments. These capsules do not leave enough space for the thermocouple to be installed internally (see **Figure 2.3**, cross-section of an autoclave, for the position of the external thermocouple). The type of buffers (Cu-Cu_2O) employed was also different, with Cu obtained from the inner walls of the capsule and Cu_2O obtained from the excess Cu_2O powder of the sample itself. Pressure was kept constant at 2 kbar, as before.

At the end of the experiment the capsules were washed clean, weighed and carefully sawed open to extract the loose matrix and crystalline run-products, which were subsequently prepared for chemical analysis using electron microprobe techniques.

4.2.4. Investigation of run products

The experimental run-products under this study were loose, unlike the run-products in study 2 and 3, and received a special mounting procedure in the technical laboratory at the University of Bayreuth. The polishing procedure and the subsequent investigations were, however, done in a similar manner to that already described in section 2.2.3, chapter 2.

4.3. Results and discussion

All runs produced large homogeneous crystal phases of the target rock-forming minerals (i.e. orthoclase, albite, muscovite, and phlogopite). Quartz (Qtz) and some unknown phases R, T, U, and X were also observed, as subsidiary products, especially in the run products of experimental option 2. The target mineral grains in run products were, in most cases, observed to be euhedral to subhedral, yielding consistent analytical results. This could possibly serve to indicate that chemical equilibrium was achieved during the experimental runs. A summary of the EMP analytical results of the experimental run-products are presented in **Table 4.2**. The results show that different starting mixtures prepared for the production of a given target mineral (e.g. sample mixtures Ab.Cu, in experimental option 1 and mixtures C, in option 2, both prepared for the same purpose of investigating the solubility of copper in the common rock-forming mineral, albite) gave rise to different phase assemblages in their run products (i.e. phases Ab1 and R1, for sample mixtures Ab.Cu, and phases Ab2, Qtz2, R2 and X2, for sample mixtures C), hence the difference in copper solubility observed in the same mineral (Ab1 and Ab2). Copper solubility is thus determined by the equilibrium between the phases present in the run products. If the phase assemblages are different the solubilities will also be different for the same mineral existing in different mixtures. In the rest of the text to follow, mineral products resulting from option 1 and 2 experiments will also be designated 1 and 2, respectively, attached on their symbol names.

4.3.1. Copper solubility in orthoclase

The solubility of copper in orthoclase was investigated using sample mixtures Or.Cu, for experimental option 1 (with reagent grade mixtures corresponding to 61 wt% orthoclase, 31 wt% Cu_2O and 8 wt% H_2O, as starting materials) and sample mixtures D, for experimental option 2 (with reagent grade mixtures corresponding to 82.8 wt% orthoclase, 9.2 wt% hypothetical mineral ($Cu^{1+}AlSi_3O_8$) and 8 wt% H_2O, as starting materials). In the run **Tables 4.2**, the starting mixtures for samples Or.Cu and D are designated as Or/Cu_2O/H_2O and Or/Cu-Or/H_2O, respectively. Orthoclase (Or1) was the only phase observed in the run products of samples Or.Cu, at all experimental run temperatures. In the run products for sample mixtures D, however, the observed phase assemblage comprised of orthoclase (Or2), quartz (Qtz2), muscovite (Mu2), and, in addition, some unknown phases R2 (with EMPA oxide composition: 56.03 wt% SiO_2, 27.36 wt% Al_2O_3, 13.95 wt% K_2O, and 0,027 wt% CuO) and T2 (2.04 wt% SiO_2, 42.77 wt% Al_2O_3, 0.07 wt% K_2O, and 0,345 wt% CuO).

The solubility of Cu is markedly higher in Or1 than Or2 (see **Figure 4.1**) and increases slightly with decreasing temperatures (700-600°C). It ranges from 0.670 to 0.863 and 0.049 to 0.089 in Or1 and Or2, respectively. The run products from both experimental options avail large subhedral grains (> 10 μm) of orthoclase (see **Figures 4.2a** and **b**). **Table 4.3** shows the analytical chemical compositions of orthoclase observed in the run products from both experimental options.

Table 4.2. Run tables listing the experimental run-conditions and products, including results of EMPA of the solubility of Cu in wt% CuO_{total} and Cu_2O for the target phases. See section 4.2 for definitions of the abbreviations and sample names used in this table.

Run No.	Sample name	pressure (bar)	Temperature (°C)	duration (days)	starting-materials	Run-products (phases)	wt% Cu in target phase as phase	CuO_{total}	Cu_2O
BT 86c	(Or.Cu)1	2kbar	600	21	31wt%**Cu_2O**	Or	Or (0.96)	**0.960** ± 0.169	**0.863** ± 0.152
TUE 86c	(Or.Cu)2	2kbar	600	21	8wt%H_2O	Or	Or (0.96)	**0.959** ± 0.211	**0.862** ± 0.190
TUE 106a	(Or.Cu)3	2kbar	650	21	61wt%**Or**	Or	Or (1.05)	**0.847** ± 0.314	**0.762** ± 0.282
BT 86b	(**Or.Cu**)4	2kbar	**700**	21		**Or**	Or (0.75)	**0.745** ± 0.154	**0.670** ± 0.139
BT 90	(Phl.Cu)1	2kbar	600	20	31wt%Cu_2O	Phl	Phl (1.27)	**1.270** ± 0.261	**1.142** ± 0.235
BT 87	(Phl.Cu)2	2kbar	650	20	8wt%H_2O	Phl	Phl (0.87)	**0.868** ± 0.205	**0.781** ± 0.185
BT 107	(Phl.Cu)3	2kbar	700	21	61wt%Phl	Phl	Phl (0.62)	**0.617** ± 0.132	**0.555** ± 0.119
BT 86	(Mu.Cu)1	2kbar	600	25	29wt%**Cu_2O**	Mu and Qtz(1.31)	Mu (1.07)	**1.073** ± 0.262	**0.965** ± 0.236
BT 86a	(**Mu.Cu**)2	2kbar	**600**	25	12wt%H_2O 61wt%**Mu**	**Mu**, **Or**(1.11), **Qtz**(1.51), and **X**(1.344).	Mu (0.91)	**0.908** ± 0.119	**0.817** ± 0.107
BT 89	(Mu.Cu)3	2kbar	600	20		Mu	Mu (0.93)	**0.925** ± 0.262	**0.832** ± 0.236
BT 105	(Mu.Cu)4	2kbar	600	21		Mu	Mu (0.92)	**0.917** ± 0.131	**0.825** ± 0.117
BT 106b	(Mu.Cu)5	2kbar	650	21		Mu, Or(1.32), and V(1.236)	Mu (0.87)	**0.870** ± 0.181	**0.783** ± 0.163
BT 88	(Mu.Cu)6	2kbar	700	20		Mu, Qtz(1.49), and U(0.719)	Mu (0.71)	**0.705** ± 0.153	**0.634** ± 0.138
TUE 103a	(**Ab.Cu**)1	2kbar	**600**	21	8wt%H_2O	**Ab** and **R**(1.13)	Ab (1.31)	**1.307** ± 0.185	**1.175** ± 0.166
BT 104	(Ab.Cu)2	2kbar	650	21	31wt%**Cu_2O**	Ab and R(0.88)	Ab (0.86)	**0.864** ± 0.154	**0.777** ± 0.139
BT 103b	(Ab.Cu)3	2kbar	700	21	61wt%**Ab**	Ab and R(0.77)	Ab (0.70)	**0.700** ± 0.149	**0.630** ± 0.134
BT 132	(**C**)1	2kbar	**600**	40	82.8wt%**Ab** 9.2wt%**Cu-Ab** 8wt%H_2O	**Ab**, **Qtz**(0.060), **R**(0.096), and **X**(0.036).	Ab (0.045)	**0.045** ± 0.028	**0.041** ± 0.025
BT 134	(D)1	2kbar	600	40	82.8wt%**Or**	Or, Qtz(0.056), and R(0.068)	Or (0.099)	**0.099** ± 0.035	**0.089** ± 0.031
BT 137	(D)2	2kbar	650	40	9.2wt%**Cu-Or**	Or and Qtz(0.055)	Or (0.055)	**0.055** ± 0.023	**0.049** ± 0.021
BT 136	(**D**)3	2kbar	**700**	40	8wt%H_2O	**Or**, **Mu**(0.000), **R**(0.027), and **T**(0.345)	Or (0.054)	**0.054** ± 0.024	**0.049** ± 0.022
BT 133	(**B**)1	2kbar	**600**	40	9.2wt%**Cu-Mu** 82.8wt%**Mu** 8wt%H_2O	**Mu**, **Qtz**(0.068), **Or**(0.030), **R**(0.041), **X**(0.040), **T**(0.039), and **U**(0.062).	Mu (0.089)	**0.089** ± 0.062	**0.080** ± 0.056

Ab = albite; Mu = muscovite; Or = orthoclase; Phl = phlogopite; Qtz = quartz; R, T, U, and **X** are unknown phases, see text for their chemical compositions.

Table 4.3. Average composition of **orthoclase** in experimental run-products, including the solubility of Cu both as wt% CuO and Cu_2O in orthoclase.

Run No.	SiO_2	Al_2O_3	K_2O	CuO	Total	Cu_2O
BT 86b/700	64.638	16.558	17.133	**0.745**	99.075	**0.670** (24)
TUE 106a/650	64.599	18.181	16.265	**0.847**	99.891	**0.762** (124)
TUE 86c/600	65.109	17.025	15.515	**0.959**	98.608	**0.862** (22)
BT 86c/600	64.654	16.285	16.804	**0.960**	98.702	**0.863** (20)
BT 136/700	60.657	21.620	15.796	**0.054**	98.127	**0.049** (10)
BT 137/650	64.370	17.152	15.163	**0.055**	96.740	**0.049** (12)
BT 134/600	63.632	17.811	15.318	**0.099**	96.860	**0.089** (12)

Note: Samples in the upper part of the table belong to sample mixtures **Or.Cu**, for option 1 experiments, whereas those in the lower part of the table belong to sample mixtures **D**, for experiments in option2 (see section 4.2 for definitions of these groups). Numbers given in parenthesis indicate the number of analyses on which the averages in the corresponding row of data is based. Experimental run temperatures are indicated in the column for run No., e.g. BT 86b/700, means sample BT 86b was run at 700°C.

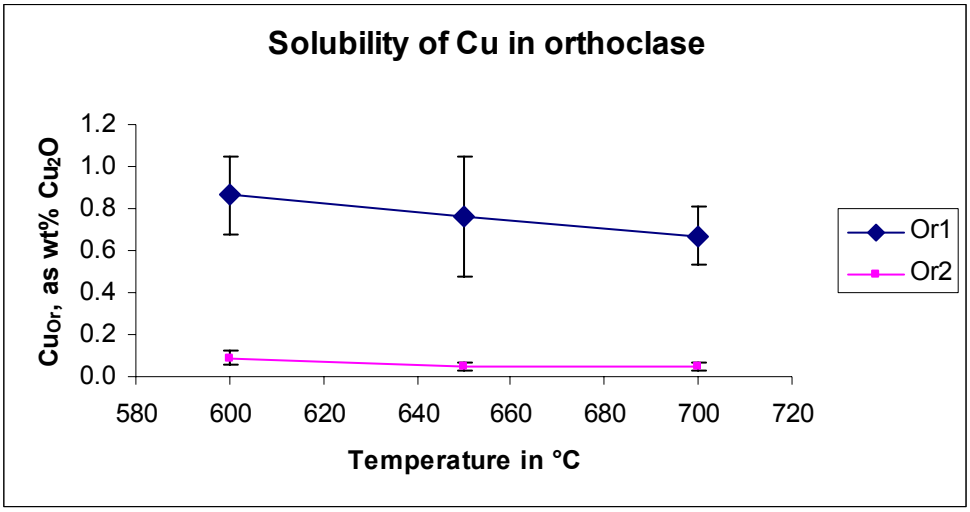

Fig. 4.1. Variation of measured Cu solubilities (Cu_{Or}) in orthoclase with temperature. The upper curve (Or1) shows the evolution of copper solubility, Cu_{Or}, with temperature for orthoclase observed in run products of sample mixtures Or.Cu, in option 1 experiments. The lower curve (Or2) shows the evolution of Cu_{Or} with temperature in orthoclase Or2 produced in the run products of option 2 experiments.

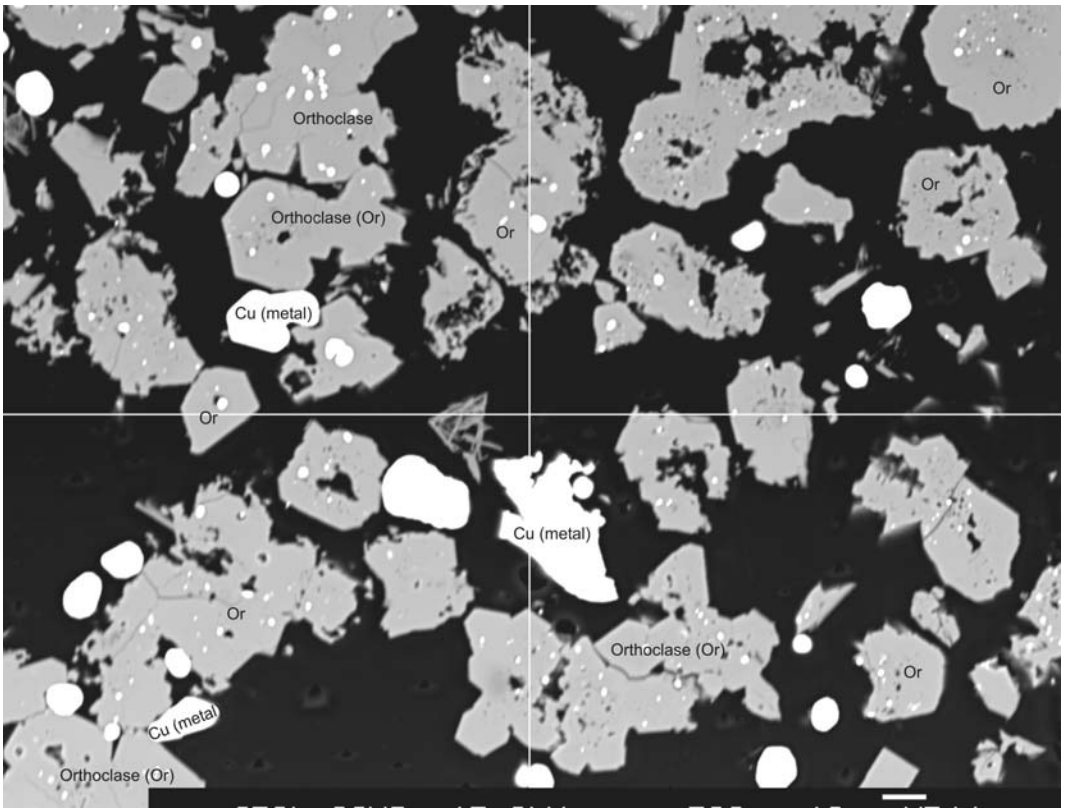

(a)

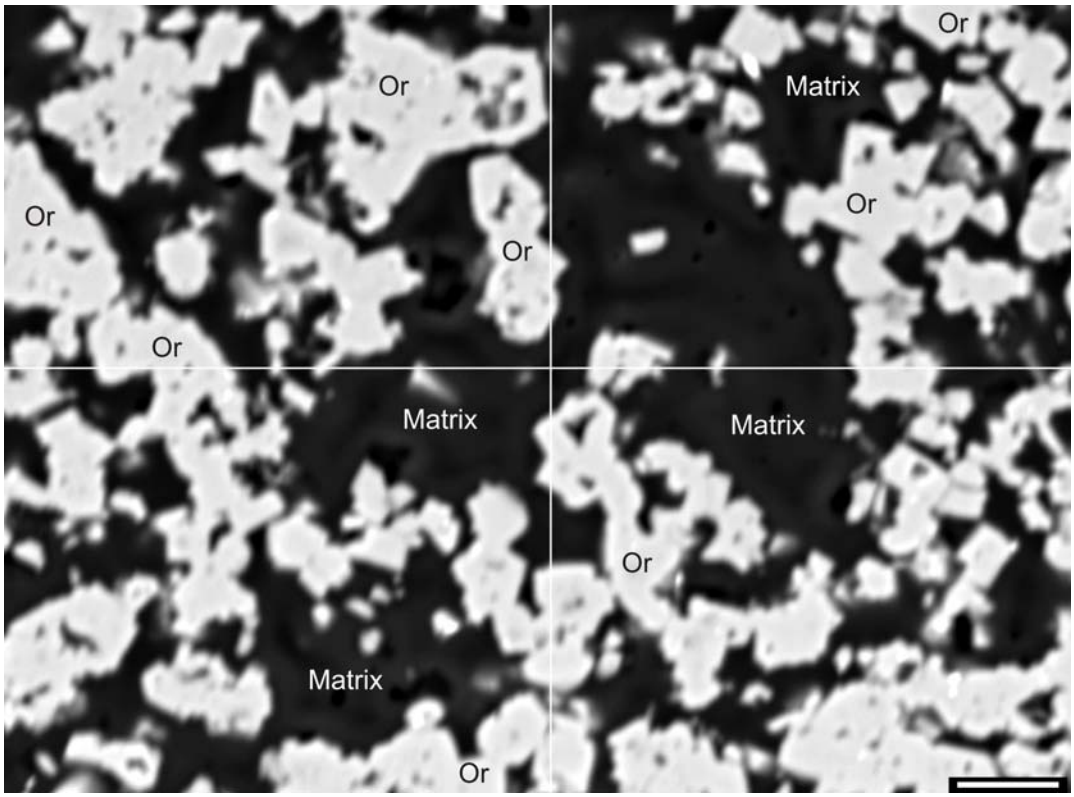

(b)

Fig.4.2(a-b). Back-scattered electron images, (a) of run-products from option 1 experiments, sample BT 86b (**Or.Cu**)4 and (b) from option 2 experiments, sample BT 137 **D**, showing grains of orthoclase (Or, in shades of light gray) that crystallise from hydrothermal solutions during the run. The experiments were conducted at 700°C and 2 kbar, under H_2O-saturated conditions buffered by the system Cu-Cu_2O.

4.3.2. Solubility of copper in albite

The solubility of copper in albite was investigated in two options. Option 1 experiments used sample mixtures Ab.Cu (with reagent grade mixtures corresponding to 61 wt% albite, 31 wt% Cu_2O and 8 wt% H_2O, as starting materials) and option 2 experiments used sample mixtures C (with reagent grade mixtures corresponding to 82.8 wt% orthoclase, 9.2 wt% hypothetical mineral $Cu^{1+}AlSi_3O_8$, and 8 wt% H_2O, as starting materials).
In run tables 4.2, the starting mixtures for samples Ab.Cu are designated as $Ab/Cu_2O/H_2O$, and those of sample C, with the hypothetical mineral, as Ab/Cu-Ab/H_2O. The phase assemblage observed in the run products for samples Ab.Cu comprises albite (Ab1) and an unknown phase R1 (50.8 wt% SiO_2, 30.5 Al_2O_3, 15.3 Na_2O, and 1.13 CuO). In the run products for samples C, however, the phase assemblage was quite different, comprising of albite (Ab2), quartz (Qtz2), and two unknowns, R2 and X2, whose analytical compositions at 600°C (in wt%) are as follows:
R2 (59.2 SiO_2, 27.6 Al_2O_3, 9.8 Na_2O, and 0.096 CuO), and X2 (79.04 SiO_2, 12.53 Al_2O_3, 6.8 Na_2O, and 0.036 CuO).

The solubility of copper, Cu_{Ab}, is markedly higher in Ab1 than Ab2 (see **Figure 4.3**) and increases slightly with decreasing temperatures (700-600°C). Cu_{Ab} ranges from 0.630 to 1.175 in Ab1. Its evolution in Ab2, however, could not be shown in the Figure 4.3 as experimental data for two run temperatures (650 and 700°C) was missing. Nevertheless it could be seen from the value of the single plot at 600°C (i.e. 0.041) that curve Ab1 trends higher than Ab2, possibly at all run temperatures. **Table 4.4** shows EMP analytical composition of albite observed in the run products from both experimental options.
Large subhedral phenocrysts (more than 20μm in diameter) of albite could be observed in run-products of charge BT 103b/700 (Ab.Cu)3, a sample from option 1 experiments (see back-scattered electron image, **Figure 4.4**).

Table 4.4. Average composition of **albite** in experimental run-products, including the solubility of Cu as both CuO and Cu_2O in this phase.

Run No.	SiO_2	Na_2O	Al_2O_3	CuO	Total	Cu_2O
BT 103b/700	67.995	10.168	18.712	**0.700**	97.575	**0.630** (10)
BT 104/650	68.490	9.984	19.273	**0.864**	98.610	**0.777** (24)
TUE 103a/600	67.484	11.254	19.310	**1.307**	99.354	**1.175** (14)
BT 132/600	68.035	10.795	19.434	**0.045**	98.309	**0.041** (10)

Note: Samples in the upper part of the table belong to sample mixtures Ab.Cu, for option 1 experiments, whereas those in the lower part of the table belong to sample mixtures C, for experiments in option2 (see section 4.2 for definitions of these groups). Numbers given in parenthesis indicate the number of analyses on which the averages in the corresponding row of data is based.

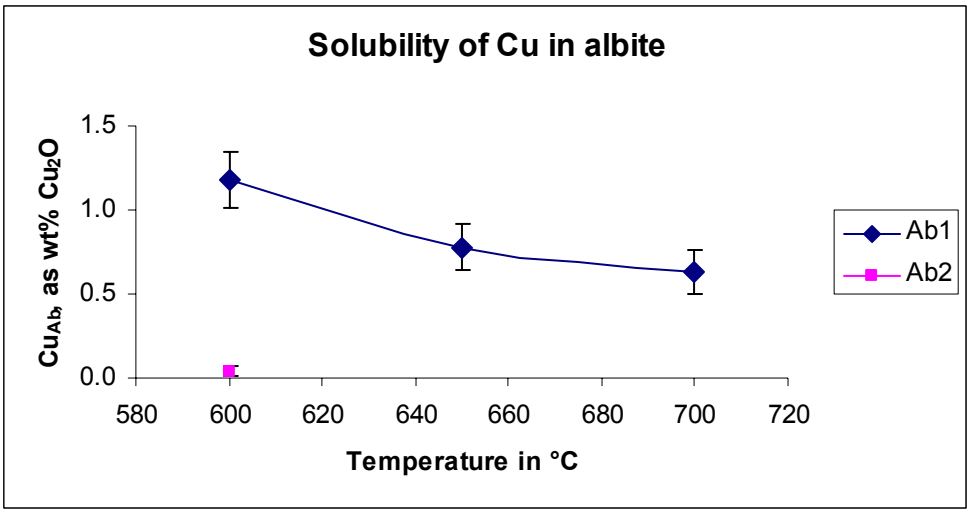

Fig. 4.3. Variation of measured Cu solubilities in albite (Cu_{Ab}) with temperature. The upper curve (Ab1) shows the evolution of copper solubility, Cu_{Ab}, with temperature for albite observed in run products of sample mixtures Ab.Cu, option 1 experiments. The single plot below the curve shows Cu_{Ab} at 600°C for albite (Ab2) produced in the run products of option 2 experiments.

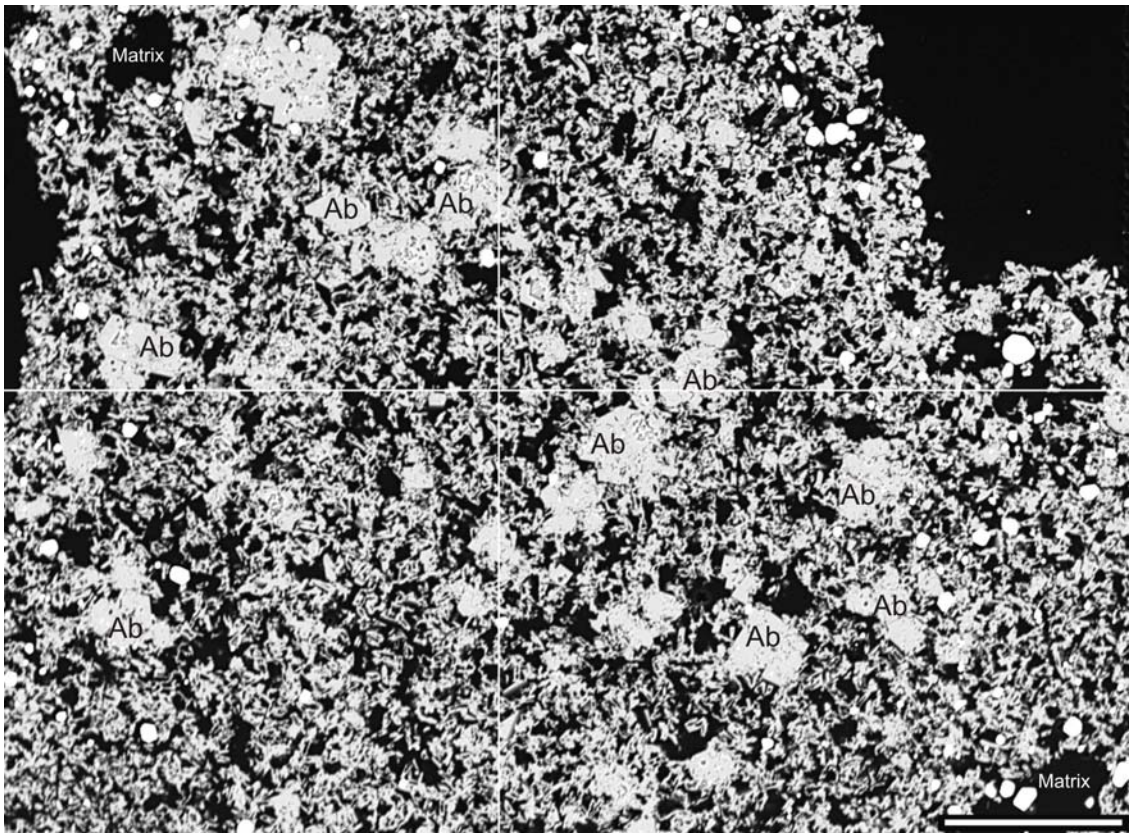

Fig.4.4. Back-scattered electron image for run-products in option 1 experiment, sample BT 103b (Ab.Cu)3, showing grains of albite (Ab, in shades of light gray) that crystallised from hydrothermal solutions during the run. The experiment was conducted at 700°C and 2 kbar, under H_2O-saturated conditions buffered by the system Cu-Cu_2O. The scale bar, bottom right, is 100 μm.

4.3.3. Solubility of Cu in muscovite

The solubility of copper in muscovite was investigated using sample mixtures Mu.Cu (with reagent grade mixtures corresponding to 61 wt% muscovite, 29 wt% Cu_2O and 12 wt% H_2O, as starting materials) in option 1 experiments and sample mixtures B (with reagent grade mixtures corresponding to 82.8 wt% muscovite, 9.2 wt% hypothetical mineral $Cu^{1+}Al_2(AlSi_3O_{10})(OH)_2$, and 8 wt% H_2O, as starting materials) in option 2 experiments. In run tables 4.2, the starting mixtures for samples Mu.Cu are designated as Mu/Cu_2O/H_2O, and those of sample B, with the hypothetical mineral, as Mu/Cu-Mu/H_2O.
The phase assemblage observed in the run products of samples Mu.Cu in the experimental temperature range between 700 and 600°C consists of muscovite (Mu1), orthoclase (Or1), quartz (Qtz1), and three unknown phases (U1, V1, and X1), with the following analytical compositions: U1 (29.4 SiO_2, 22.9 Al_2O_3, 7.3 K_2O, and 0.72 CuO); V1 (25.2 SiO_2, 72.4 Al_2O_3, 0.1 K_2O, and 1.27 CuO); and X1 (83.5 SiO_2, 12.4 Al_2O_3, 0.9 K_2O, and 1.34 CuO). Whereas the phase assemblage in the run products of sample B is slightly different, mainly composed of muscovite (Mu2), quartz (Qtz2), orthoclase (Or2), and four unknown phases (R2, T2, U2, and X2), with compositions: R2 (57.3 SiO_2, 25.6 Al_2O_3, 15.0 K_2O, and 0.041 CuO); T2 (2.1 SiO_2, 56.1 Al_2O_3, 0.1 K_2O, and 0.039 CuO); U2 (22.0 SiO_2, 31.6 Al_2O_3, 5.4 K_2O, and 0.062 CuO); and X2 (90.1 SiO_2, 7.7 Al_2O_3, 0.1 K_2O, and 0.040 CuO).

The solubility of Cu, in muscovite (Mu1) observed in the run products of samples Mu.Cu, ranges from 0.965 – 0.634 at the experimental temperatures between 600 and 700°C, and 0.080 in muscovite (Mu2) from the run products of sample B (see **Table 4.5** and **Figure 4.5**).
BSE image for sample BT 106b/650 shows large euhedral plates of muscovite crystals whilst thin fibre-like platelets could be observed in the image for the run products of sample BT 86a/600 (**Figures 4.6**a-b).
Table 4.5 shows the average EMP analytical compositions (in wt% component oxides) of muscovite observed in run products of samples from both experimental options.

Table 4.5. Average EMPA composition of **muscovite** in run-products of samples Mu.Cu and B.

Run No.	SiO_2	Al_2O_3	K_2O	CuO	Total	Cu_2O
BT 88/700	39.254	32.042	10.228	**0.705**	82.228	**0.634** (20)
BT 106b/650	34.887	30.617	9.520	**0.870**	75.894	**0.783** (20)
BT 105/600	40.094	35.086	11.248	**0.917**	87.345	**0.825** (27)
BT 86a/600	40.210	33.360	10.595	**0.908**	85.073	**0.817** (24)
BT 86/600	38.006	31.904	10.032	**1.073**	81.015	**0.965** (21)
BT 133/600	42.953	30.530	10.887	**0.089**	84.459	**0.080** (3)

Note: Samples in the upper part of the table belong to samples mixtures Mu.Cu, for option 1 experiments, whereas those in the lower part belong to mixtures B, option 2 experiments (see section 4.2 for the definitions of these sample groups). The numbers given in parenthesis indicate the number of analyses for which the average values in the corresponding row of data was based.

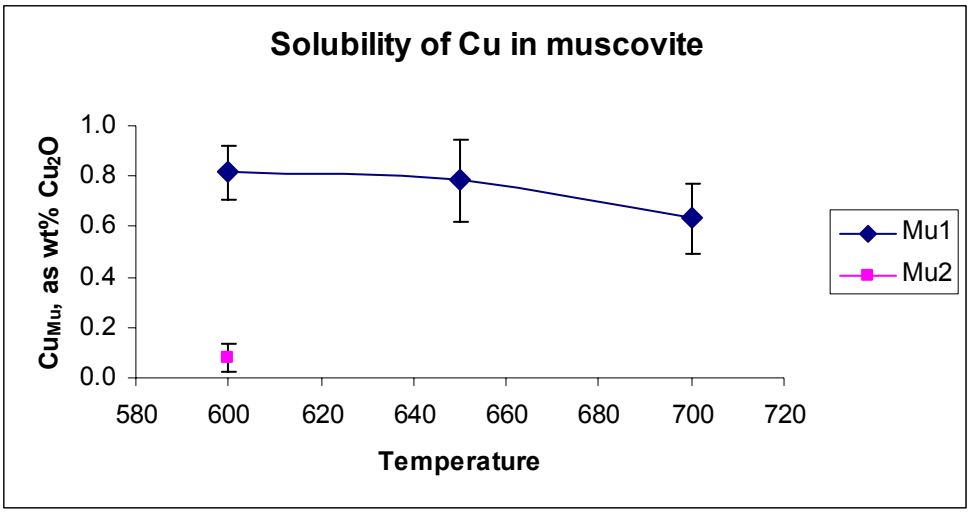

Fig. 4.5. Variation of measured Cu solubilities in muscovite (Cu_{Mu}) with temperature. The upper curve (Mu1) shows the evolution of copper solubility, Cu_{Mu}, with temperature for muscovite observed in run products of sample mixtures Mu.Cu, option 1 experiments. The single plot below the curve shows Cu_{Mu} at 600°C for muscovite (Mu2) produced in the run products of option 2 experiments.

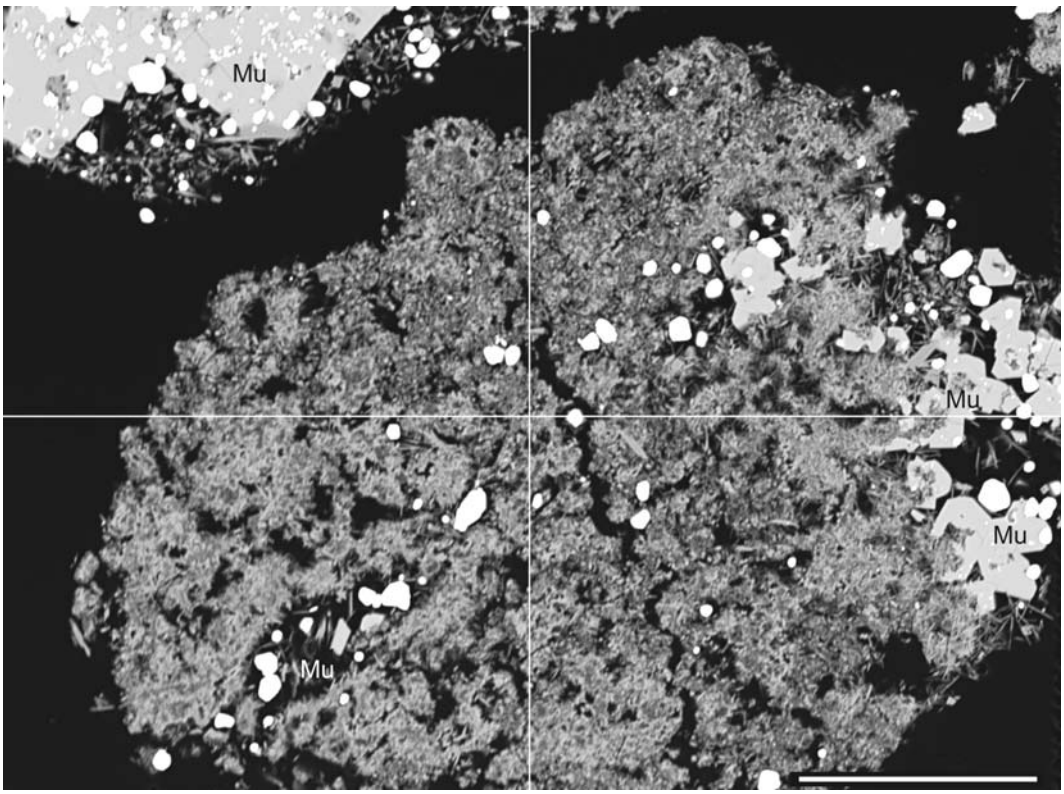

(a)

(b)

Fig. 4.6(a-b). Back-scattered electron images of run-products (**Mu.Cu**)5 (a) and (**Mu.Cu**)2 (b) for charges BT 106b/650 and BT 86a/600, respectively. The experiments were conducted isobarically at 2 kbar, under H_2O-saturated conditions, with Cu-Cu_2O buffers. The white thin strings in image (b) are muscovite fibres. In image (a) muscovite crystals (Mu) are large and euhedral. The scale bar in (a) is 100 μm and 10 μm in (b). The white spots in both images are those of excess Cu (metal) grains.

4.3.4. Solubility of Cu in phlogopite

The solubility of copper in phlogopite was investigated using samples Phl.Cu (with reagent grade mixtures corresponding to 61 wt% phlogopite, 31 wt% Cu_2O and 8 wt% H_2O, as starting materials) option 1 experiments. Option 2 experiments with sample mixtures A (with reagent grade mixtures corresponding to 82.8 wt% phlogopite, 9.2 wt% hypothetical mineral $Cu^{1+}Mg_3(AlSi_3O_{10})(OH)_2$, and 8 wt% H_2O, as starting materials) failed. In run tables 4.2, the starting mixtures for samples Phl.Cu are designated as Phl/Cu_2O/H_2O. Phlogopite (Phl1) was the only phase observed in the run-products with Cu solubility ranging from 0.555 – 1.142 at 600 – 700°C (see **Table 4.6** and **Figure 4.7**). Results of copper solubility in phlogopite (Phl2) in run products of sample mixtures A are missing, but would be guessed to be ten-fold smaller than it is for Phl1.

Table 4.6. Average EMPA composition of **phlogopite** in experimental run-products, including the solubility of Cu as both CuO and Cu_2O.

No.	SiO_2	K_2O	CuO	Al_2O_3	MgO	Total	Cu_2O
BT 107/700	33.099	7.483	**0.617**	10.000	21.424	72.623	**0.555** (36)
BT 87/650	31.313	6.891	**0.868**	9.304	20.259	68.636	**0.781** (37)
BT 90/600	35.494	8.005	**1.270**	10.614	23.425	78.808	**1.142** (10)

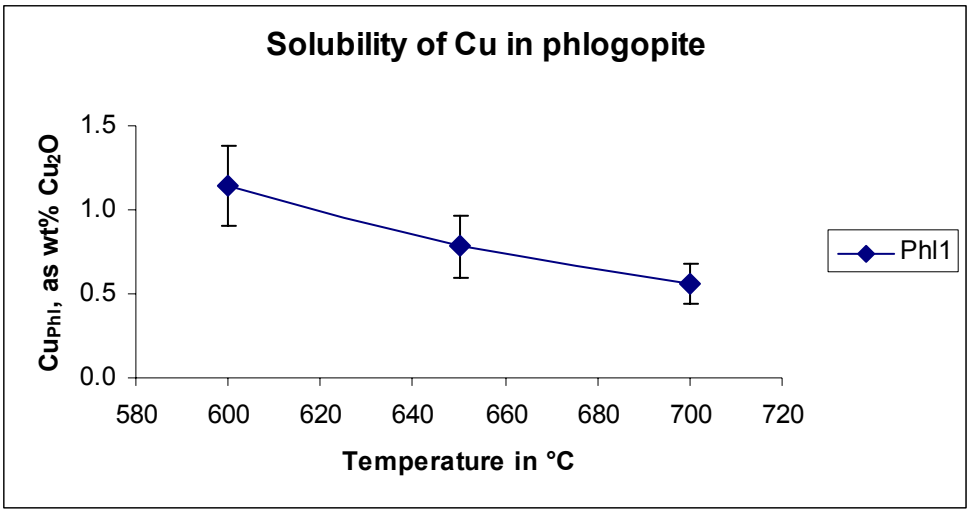

Fig. 4.7. Variation of measured Cu solubilities in phlogopite (Cu_{Phl}) with temperature. The curve (Phl1) shows the evolution of copper solubility, Cu_{Phl}, with temperature for phlogopite observed in run products of sample mixtures Phl.Cu, option 1 experiments.

4.3.5. Solubility of Cu in silica

Quartz crystals were found as by-products in run-products of samples Mu.Cu in option 1 experiments (Qtz1) and in all run products of sample mixtures in option 2 experiments (Qtz2) see run Tables 4.2.
The solubility of copper in quartz (Cu_{Qtz}) was observed to be almost constant at all run temperatures and markedly higher in Qtz1 than Qtz2 (see **Table 4.7** and **Figure 4.8**). Its average (in wt% Cu_2O) is 1.287 in Qtz1 and 0.050 in Qtz2.

Table 4.7. Average compositions of quartz in experimental run-products, including its solubility of Cu as both CuO and Cu_2O.

Run No.	SiO_2	CuO	Total	Cu_2O
BT 86/600	93.103	**1.305**	94.408	**1.173**
BT 86a/600	95.412	**1.503**	96.915	**1.352**
BT 88/700	94.895	**1.486**	96.381	**1.336**
BT 132/600	98.043	**0.060**	98.103	**0.054**
BT 134/600	97.628	**0.056**	97.684	**0.051**
BT 133/600	93.200	**0.051**	93.251	**0.046**
BT 137/650	98.007	**0.055**	98.062	**0.049**

Generally, when all rock-forming minerals in option 1 experiments are considered together, the solubility of copper in quartz plots higher, at all run temperatures, than other minerals. This is clearly illustrated in **Figure 4.9**.

In the run products of sample mixtures for option 2 experiments, however, quartz is observed to plot intermediate between the solubility range for other rock-forming minerals (i.e. 0.041 – 0.089) at lower temperatures, and merging at higher temperatures to about 0.050 for all minerals (see **Figure 4.10**).

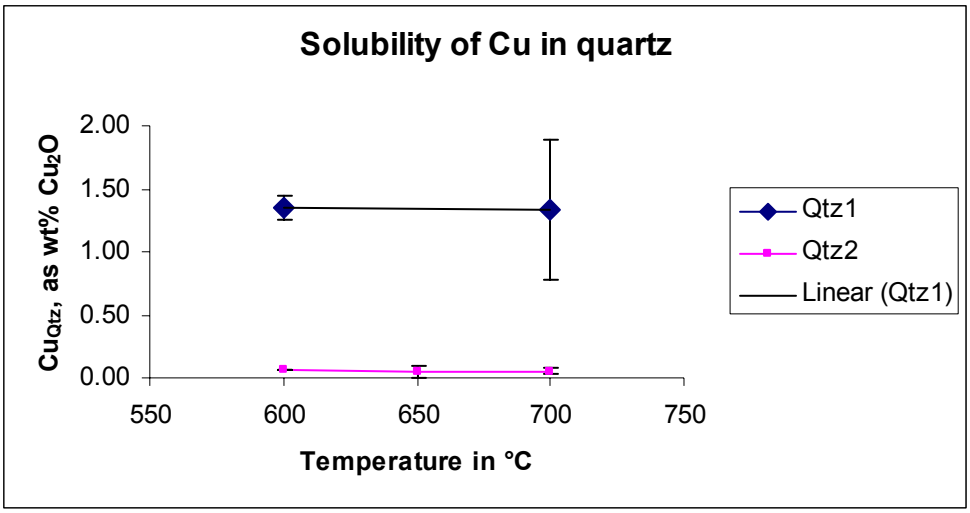

Fig. 4.8. Variation of measured Cu solubilities (Cu_{Qtz}) in quartz with temperature. The upper curve (Qtz1) shows the evolution of copper solubility, Cu_{Qtz}, with temperature for quartz observed in run products of sample mixtures Mu.Cu, in option 1 experiments. The lower curve (Qtz2) shows the evolution of Cu_{Qtz} with temperature in the same mineral quartz produced in the run products of sample mixtures B, C, and D, option 2 experiments.

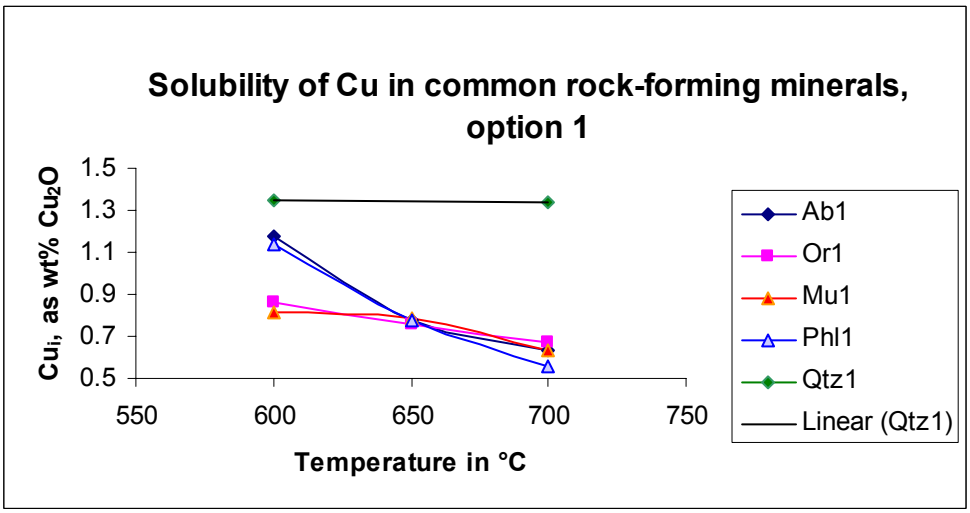

Fig. 4.9. Solubility of copper in rock-forming minerals (option 1) against temperature. The graph shows that copper solubility in quartz (Qtz1) is highest and constant at all run temperatures. At the lowest run temperature (600°C), the solubilities are approximately 1.35 (for Qtz1), ~1.16 (for Ab1 and Phl1) and ~0.866 (for Mu1 and Or1). At the intermediate temperature, 650°C, the solubility is the same (~ 0.775) for all minerals, except quartz whose solubility remains high and constant at ~1.35. At 700°C, Phl1 reads lowest (~0.555); the three minerals (Ab1, Mu1 and Or1) merge to an average value of ~ 0.645 and Qtz1 has ~1.34 wt% Cu_2O.

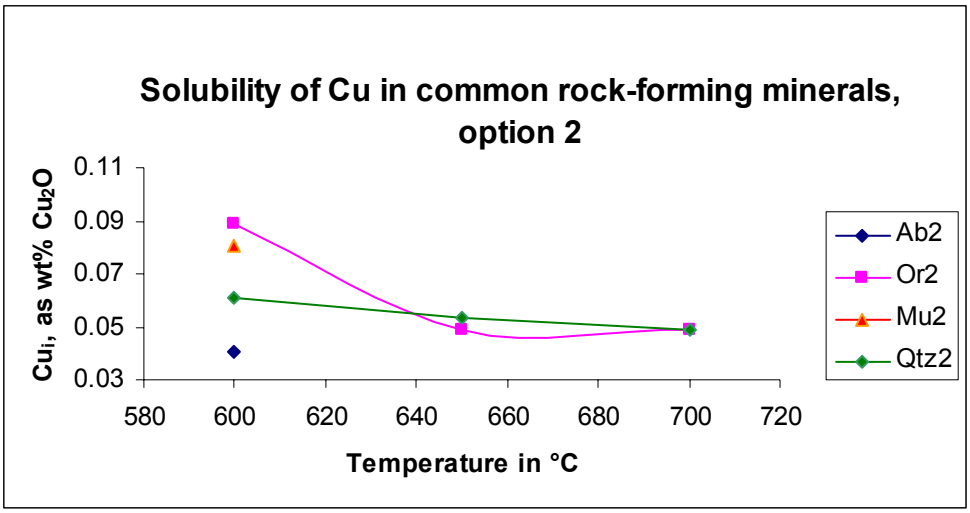

Fig. 4.10. Solubility of copper in experimental rock-forming minerals (option 2) against temperature. The graph shows that copper solubility in quartz (Qtz2) plots intermediate between other minerals (Ab2, Or2 and Mu2) at the lowest run temperature (600°C), with solubilities ranging from 0.041 (for Ab2) to 0.089 (for Or2). At the intermediate and highest temperatures, the solubility of copper in all experimental minerals, including quartz, seems to merge to an average value of ~ 0.050.

4.4. Outlook

I explored a new experimental approach to measure the solubility of copper in some common rock-forming minerals under controlled oxygen fugacity and copper activity. The method works and yields reproducible and consistent results.

I observed different solubilities for the same mineral depending on the starting mixture used (options 1 and 2). Samples for option 1 experiments consisted of reagent grade mixtures corresponding to about 60 wt% mineral (e.g. $KAlSi_3O_8$); 30 wt% Cu_2O and 10 wt% H_2O. Samples for option 2 experiments consisted of reagent grade mixtures corresponding to about 80 wt% mineral (e.g. $KAlSi_3O_8$); 10 wt% hypothetical mineral (e.g. $Cu^{1+}AlSi_3O_8$); and 10 wt% H_2O.
The difference in solubilities for the same mineral is probably due to the fact that different mixtures stabilised different mineral assemblages. Some phases produced remain to be identified whilst others simply exist in very low proportions to be identified. So there is seemingly still more work left to be done.

In principle, when the sample mixtures are fully characterised, it should be possible to calculate the partitioning of copper between fluids and minerals from these data.

REFERENCES

Albarede, F. and Michard, A. (1989) Hydrothermal alteration of the oceanic crust. In: Hart, S.R. and Gulen, L. (eds) Crust/Mantle Recycling at convergence Zones. NATO ASI Series C: Mathematical and Physical Sciences, 258. Dordrecht: Kluwer Academic, pp. 29-36.

Allwardt, J.R., Lee, S.K., and Stebbins, J.F. (2003) Bonding preferences of non-bridging O atoms: evidence from ^{17}O MAS and 3QMAS NMR on calcium aluminate and low-silica Ca-aluminosilicate glasses. American Mineralogist, 88, 949-954.

Arribas, A., Hedenquist, J.W., Itaya, T., Okada, T., Concecion, R.A. and Garcia, J.S. (1995) Contemporaneous formation of adjacent porphyry and epithermal Cu-Au deposits over 300 ka in northern Luzon, Philippines. Geology, 23, 337-340.

Atkinson, D. and Baker, D.J. (1986) Geology of the MacTung tungsten skarn deposit. In: J.G. Abbott and R.J.W. Turner (eds), Mineral deposits of the Northern Canadian Cordillera, Yulkon-North Eastern British Columbia. Geological Survey of Canada Open File 2169, 279 pp.

Audetat, A. and Pettke, T. (2003) The magmatic-hydrothermal evolution of two barren granites: A melt fluid inclusion study of the Rito del Medio and Canada Pinbete plutons in northern New Mexico (USA). Geochimica et Cosmochimica Acta, 67, 1, 97-121.

Audetat, A. and Pettke, T. (2005) Evolution of sulfur and copper in the magmas related to porphyry-Cu mineralization at Santa Rita, New Mexico (U.S.A.), “submitted”.

Beattie, P. (1994) Systematics and energetics of trace element partitioning between olivine and silicate melts: implications for the nature of mineral/melt partitioning. Chemical Geology, 117, 57-71.

Bell, R.J., Dean, P. (1972) Localization of phonons in vitreous silica and related glasses. Inter. Conf. Phys. Non-Cryst. Solids, 3rd, Univ. Sheffield, ed. R.W. Douglas, B. Ellis, pp. 443-52. London: Wiley-Interscience.

Belvin, P.L. and Chappell, B.W. (1992) The role of magma sources, oxidation states and fractionation in determining the granite metallogeny of eastern Australia. Transactions of the Royal Society Edinburgh: Earth sciences, 87, 305-316.

Bindeman, I.N., Davis, A.M., Drake, M.J. (1998) An ion microprobe study of plagioclase-basalt partition experiments at natural concentration levels of trace elements. Geochimica et Cosmochimica Acta, 62, 1175-1192.

Blundy, J.D. and Wood, B.J. (1994) Prediction of crystal-melt partition coefficients from elastic moduli. Nature 372, 452-454.

Blundy, J.D. and Wood, B.J. (2001) The effect of cation charge on crystal-melt partitioning of trace elements. Earth and Planetary Science Letters, 188, 59-71.

Blundy, J.D. and Wood, B.J. (2003) Partitioning of trace elements between crystals and melts. Earth and Planetary Science Letters, 210, 383-397.

Blundy, J.D. and Wood, B.J. (2003) Trace element partitioning under crustal and uppermost mantle conditions: the influence of ionic radius, cation charge, pressure, and temperature. In: R. W. Carlson (ed.), Treatise on Geochemistry, Vol. 2, The Mantle and Core. Elsevier, pp. 395-424.

Bottinga, Y., Weill, D.F., Richet, P. (1982) Density calculations for silicate liquids. I. Revised method for aluminosilicate compositions. Geochimica et Cosmochimica Acta, 46, 909-19.

Brenan, J.M., Shaw, H.F., Ryerson, F.J., and Phinney, D.L. (1995) Experimental determination of trace-element partitioning between pargasite and a synthetic hydrous andesitic melt. Earth and Planetary Science Letters, 135, 1-11.

Brice, J.C. (1975) Some thermodynamic aspects of the growth of strained crystals. Journal of crystal growth 28, 249-253.

Burnham, C.W. (1967) Hydrothermal fluids in the magmatic stage. In: H.L. Barnes (ed.), Geochemistry of hydrothermal ore deposits. Holt, Rinehart and Winston, pp. 34-76.

Burnham, C.W., (1979) Magmas and hydrothermal fluids. In: H.L.Barnes (ed.), Geochemistry of hydrothermal ore deposits, 2rd edition, John Wiley & Sons, pp. 71-136.

Burnham, C.W., (1997) Magmas and hydrothermal fluids. In: H.L.Barnes(ed.), Geochemistry of hydrothermal ore deposits, 3rd edition, John Wiley & Sons, pp. 63-123.

Burnham, C.W., and Ohmoto, H. (1980) Late-stage processes in felsic magmatism, Mining geology, 8, 1-11.

Candela, P.A. (1991) Physics of aqueous phase evolution in plutonic environments. American Mineralogist, 76, 1081-1091.

Candela, P.A. (1992) Controls on ore-metal ratios in granite related ore-systems: an experimental and computational approach. Transactions of the Royal Society Edinburgh: Earth Sciences, 83, 317-26.

Candela, P.A. and Holland, H.D. (1984) The partitioning of copper and molybdenum between silicate melts and aqueous fluids. Geochimica et Cosmochimica Acta, 48, 373-380.

Candela, P.A. and Holland, H.D. (1986) A mass transfer model for copper and molybdenum in magmatic hydrothermal systems: the origin of porphyry-type copper deposits. Economic Geology, 81, 1-18.

Candela, P.A. and Piccoli, P.M. (1995) Model ore-metal partitioning from melts into vapor and vapor/brine mixtures, Mineralogical Association of Canada Short Course Series 23, 101-127.

Candela, P.A. (1989a) Felsic magma, volatiles and metallogenesis. Reviews in Economic Geology, 4, 223-33.

Candela, P.A. (1989b) Magmatic ore-forming fluids: Thermodynamic and mass transfer calculations of metal concentrations. In: Ore deposition associated with magmas, Vol. 4 (eds. J.A. Whitney and A.J. Naldrett), Society of economic geologists, Littleton CO. pp. 203-221

Canil, D (2004) Mildly incompatible elements in peridotites and the origins of mantle lithosphere. Lithos. 77, 375-393.

Cathles, L. M. (1981) Fluid flow and genesis of hydrothermal ore deposits: Economic Geology, 75, 424-457.

Cerny, P. (1991) Fertile granites of Precambrian rare-element pegmatite fields: is geochemistry controlled by tectonic setting or source lithologies? Precambrian Research, 429-468.

Chou, I-M. (1987) Oxygen buffer and hydrogen sensor techniques at elevated pressures and temperatures. In: G.C. Ulmer and H.L. Barnes (eds.), Hydrothermal Experimental Techniques, John Wiley & Sons, pp. 61-99.

Cline, J.S. and Bodnar, R.J. (1991) Can economic porphyry copper mineralization be generated by a typical calc-alkaline melt?, Journal of Geophysical Research, 96, 8113-8126.

Cline, J.S. and Bodnar, R.J.J., (1991) Geophys. Res. 96, 8113-8126.

Cooke, D.R. and Simmons, S.F. (2000) Characteristics and genesis of epithermal gold deposits. Reviews in Economic Geology, 13, 221-244.

Corbett, G.J. and Leach, T.M. (1998) Southwest pacific rim gold-copper systems: structure, alteration and mineralization. Society of Economic Geologists, Special publication, 6, 237pp.

Dietrich, R.V. and Skinner, B.J. (1979) Rocks and Rock minerals, John Wiley & Sons, 319 pp.

Dingwell, D.B., Holtz, F. and Behrens, H. (1997) The solubility of H_2O in peralkaline and peraluminous granitic melts. American Mineralogist, 82, 3-4.

Einaudi, M., Meinert, L.D. and Newberry, R.J. (1981) Skarn deposits. Economic Geology, 75, 317-391.

Einaudi, M. (1982) Description of skarns associated with porphyry copper plutons: southwestern North America. In S.R. Titley (ed.), Advances in Geology of the

Porphyry Copper Deposits: Southwestern North America. University of Arizona Press, pp.139-83.

Evans, A.M. (1993) Ore geology and Industrial Minerals, an Introduction. Blackwell Science, 389 pp.

Guilbert, J.M. and Park, J.R. C.F. (1986) The Geology of Ore Deposits, 4th edition, Freeman and Co., 985 pp.

Guo, J. and Green, T.H. (1990) Experimental study of barium partitioning between phlogopite and silicate liquid at upper-mantle pressure and temperature. Lithos, 24, 83-95.

Haas, J.L., Jr. and Robie, R.A. (1973) Thermodynamic data for wüstite, $Fe_{0.947}O$, magnetite, Fe_3O_4, and hematite, Fe_2O_3. Transactions of American Geophysical Union, 54, 483.

Hedenquist, J.W., Arribas, R.A., and Gonzalez, U.E. (2000) Exploration for epithermal gold deposits. In S. Hagemann and P.E. Brown (Eds), Gold in 2000. Society of Economic geologists, Reviews in Economic Geology, 13, 245-77.

Hedenquist, J.W. & Lowenstern, J.B. (1994) The role of magmas in the formation of hydrothermal ore deposits. Nature, 370, 519-527.

Heinrich, C.A., Gunther, D., Audetat, A., Ulrich, T. and Frischknecht, R. (1999) Metal fractionation between magmatic brine and vapour, dertermined by micro-analysis of fluid inclusions. Geology, 27, 755-8.

Hemley, J.J. (1992) Hydrothermal ore-forming processes in the light of studies in rock-buffered systems, Economic Geology, 87, 1-22.

Hemley, J.J. and Hunt, J.P. (1992) Hydrothermal ore-forming processes in the light of studies in rock-buffered systems: II. Some general geologic applications. Economic Geology, 87, 23-43.

Hess, P.C. (1989) Origins of Igneous Rocks, Harvard University Press, 336 pp.

Henley, R.W. and Ellis, A.J. (1983) Geothermal systems, ancient and modern. Earth Science Reviews, 19, 1-50.

Hewitt, D.A. (1978) A redetermination of the fayalit-magnetite-quartz equilibrium between 650°C and 850°C. American Journal of Science, 278, 715-724.

Hoefs, J. (1997) Stable Isotope Geochemistry, 4th edition, Springer-Verlag, 201 pp.

Holland, H.D. (1972) Granites, solutions, and base metal deposits. Economic Geology, 67, 281-301.

Hollings, P. and Wyman, D. (2005) The geochemistry of trace elements in igneous systems: principles and examples from basaltic systems. In: R.L. Linnen and I.M.

Samson (eds.), Rare-Element Geochemistry and Mineral Deposits: Geological Association of Canada, GAC Short Course Notes, 17, pp. 1-16.

Holloway J.R. and Wood B.J. (1988) Simulating the Earth: Experimental Geochemistry. Unwin/Hyman, Boston, 196 pp.

Huebner, J.S. and Sato, M. (1970) The oxygen fugacity-temperature relationships of manganese and nickel oxide buffers. American Mineralogist, 55, 934-952.

Icenhower, J. and London, D. (1995) An experimental study of element partitioning among biotite, muscovite, and coexisting peraluminous silicate melt at 200 MPa (H_2O). American Mineralogist, 80, 1229-1251.

Ishihara, S. (1981) The granitoid series and mineralization. Economic Geology, 75, 458-484.

Ishihara, S. (1977) The magnetite-series and ilmenite-series granite rocks. Mining Geology, 26, 293-305.

Jahns, R.H. and Burnham, C.W. (1969) Experimental studies of pegmatite genesis: I. A model for the derivation and crystallisation of granitic pegmatites. Economic Geology, 64, 843-64.

Johannes, W. and Holtz, F. (1996) Petrogenesis and Experimental Petrology of Granitic Rocks. Springer-Verlag, 335 pp.

Jugo, P.J., Candela, P.A. and Piccoli, P.M. (1999) Magmatic sulfides and Au:Cu ratios in porphyry deposits: an experimental study of copper and gold partitioning at 850°C, 100 MPa in a haplogranitic melt-pyrrhotite-intermediate solid solution-gold metal assemblage, at gas saturation. Lithos, 46, 573-589.

Kerrick, D.M. (1987) Cold-seal systems. In: G.C. Ulmer and H.L. Barnes (ed.), Hydothermal Experimental Techniques. John Wiley, New York, pp. 293-323.

Keppler, H. and Wyllie, P.J. (1991) Partitioning of Cu, Sn, Mo, W, U and Th between melt and aqueous fluid in the systems haplogranite-H_2O-HCl and haplogranite-H_2O-HF. Contributions to Mineralogy and Petrology, 109, 139-150.

Keppler, H. (1992) Crystal field spectra and geochemistry of transition metal ions in silicate melts and glasses. American mineralogist, 77, 62-75.

Keppler, H. (1999) Experimental evidence for the source of excess sulphur in explosive volcanic eruptions, Science, 284, 1652-1654.

Kesler, S.E. (2005) Ore-Forming Fluids. Elements,1,13-18.

Kilinc, I.A. and Burnham, C.W. (1972) Partitioning of chloride between a silicate melt and coexisting aqueous phase from 2 to 8 kilobars, Economic geology, Vol. 67, pp. 231-235.

King, P.L., and White, A.J.R. (2004) Granites, volatile solubility and tracking the formation of magmatic fluids. In the Ishihara symposium: Granites and Associated metallogenesis, Geoscience Australia, pp. 85-88.

La Tourrette, T., Herving, R.L. and Holloway, J.R. (1995) Trace element partitioning between amphibole, phlogopite, and basanite melt. Earth and Planetary Science Letters, 135, 13-30.

LeMaitre, (1976) The chemical variability of some common igneous rocks. Journal of Petrology, 17.

Lindgren, W. (1933) Mineral Deposits. McGraw-Hill, 930 pp.

London, D. (1990) Internal differentiation of rare element pegmatites: a synthesis of recent research. Geological Society of America, Special paper, 246, 35-50.

London, D. (1992) The application of experimental petrology to the genesis and crystallisation of granitic pegmatites. Canadian Mineralogist, 30, 499-540.

London, D. (1995) Geochemical features of peraluminous granites, pegmatites, and rhyolites as sources of lithophile metal deposits. In: Thompson J.F.H (ed), Magmas, Fluids, and Ore Deposits, Mineralogical Association of Canada-short course series, Mineral Deposit Research Unit; Vitoria, British Columbia, Vol.23. pp.175-202.

London, D. (1996) Granitic pegmatites. Transactions of the Royal Society Edinburgh: Earth Sciences, 87, 305-19.

Lorand, J.P., (1990) Are spinel lherzolite xenoliths representative of the abundance of sulphur in the upper mantle? Geochimica Cosmochimica Acta, 54, 1487-1492.

Lowell, J.D. and Guilbert, J.M. (1970) Lateral and vertical alteration-mineralization zoning in porphyry ore deposits. Economic Geology, 65, 373-408.

Lowenstern, J.B., Mahood, G.A., Rivers, M.L. and Sutton, S.R. (1991) Evidence for extreme partitioning of copper into a magmatic vapour phase. Science, 252, 1405-1409.

Lowenstern, J.B. (1993) Evidence for a copper-bearing fluid in magma erupted at the Valley of Ten-Thousand-Smokes, Alaska. Contributions to Mineralogy and Petrology, 114, 409-421.

Lowenstern, J.B. (2001) Carbon dioxide in magmas and implications for hydrothermal systems. Mineralium Deposita, 36, 490-502.

Manning, D.A.C. and Henderson, P. (1984) The behaviour of tungsten in granitic melt-vapor systems. Contributions to Mineralogy and Petrology, 76, 257-262.

McLean, W.H. (1969) Liquidus phase relationships in the FeS-FeO-Fe_3O_4-SiO_2 system, and their application in geology. Economic Geology, 64, 865-884.

Meinert, L.D. (1992) Skarns and skarn deposits. Geoscience Canada, 19, 145-162.

Misra, K.C. (2000) Understanding Mineral Deposits. Kluwer Academic Publishers, 845 pp.

Morgan GB VI and London D. (1996) Optimizing the electron microprobe analysis of hydrous alkali aluminosilicate glasses. American Mineralogist 81, 1176-1185.

Muan, A. and Osborn, E.F. (1965) Phase Equilibria among Oxides in Steelmaking. Addison-Wesley Publishers.

Mysen, B.O. (1983) The structure of silicate melts. Ann. Rev. Earth Planet. Sci. 11, 75-97.

Nelson, C. and White, W.B. (1980) Transition metal ions in silicate melts-I. Manganese in sodium silicate melts. Geochimica et Cosmochimica Acta, 44, 887-893.

Norton, I. and Cathles, L.M. (1973) Breccia pipe products of exsolved vapour from magmas. Economic Geology, 68, 540-546.

Norton, I. and Cathles, L.M. (1979) Thermal aspects of ore deposition. In: H.L.Barnes (ed.), Geochemistry of hydrothermal ore deposits. 2rd edition, John Wiley & Sons, pp. 611-631.

Norton, D., (1982) Fluid and heat transport phenomena typical of copper-bearing pluton environment. In Advances in geology of the porphyry copper deposits of southwestern North America (ed. Titly, S. R.) Tuscon, Univ. Arizona Press, 59-72.

Onuma N., Higuchi H., Wakita H., and Nagasawa H. (1968) Trace element partitioning between two pyroxenes and the host lava. Earth and Planetary. Science Letters 5, 47-51.

Reed S.J.B. (1996) Electron Microprobe Analysis and Scanning Electron Microscopy in Geology. Cambrigde, 201 pp.

Robb, L. (2005) Introduction to Ore-Forming Processes, Blackwell publishers, 373 pp.

Roedder, E. (1984) Fluid inclusions. Reviews in mineralogy, 12, Mineralogical Society of America, pp. 644.

Rollinson H. (1993) Using Geochemical Data: Evaluation, Presentation, Interpretation. Longman, 352 pp.

Rowins, S.M. (1999) Reduced porphyry Cu-Au deposits: a newly recognized style of gold mineralization, Geological Society of America Abstracts with Program, 31, No. 7, A92.

Rye, R.O. (1993) The evolution of magmatic fluids in the epithermal environment: The stable isotope perspective: Economic geology, 88, 733-752.

Sawkins, F.J. (1990) Metal Deposits in Relation to Plate Tectonics, 2nd edition, Springer-Verlag, 461 pp.

Schmidt, K.H., Bottazz, P., Vannucci, R., Mengel, K. (1999) Trace element partitioning between phlogopite, clinopyroxene and leucite lamproite melt. Earth and Planetary Science Letters, 168, 287-300.

Shannon R.D. and Prewitt C.T (1969) Effective ionic radii in oxides and fluorides. Acta Cryst. 25, 925-946.

Shannon R.D. (1976) Revised effective ionic radii and systematic studies of interatomic distances in halides and chalcogenides. Acta Cryst. 32, 751-767.

Shaw D.M. (1970) Trace element fractionation during anatexis. Geochimca et Cosmochimica Acta 34, 237-243.

Shen, A. and Keppler, H. (1995) Infrared spectroscopy of hydrous silicate melts to 1000°C and 10 kbar: direct observation of H2O speciation in a diamond-anvil cell. American Mineralogist, 80, 1335-1338.

Shinohara, H., Iiyama, J.T. and Matso, S. (1989) Partition of chlorine compounds between silicate melt and hydrothermal solutions: I. Partitioning of NaCl-KCl. Geochimica et Cosmochimica Acta, 53, 2517-2563.

Sillitoe, R.H. (1973) The tops and bottoms of porphyry copper deposits, Economic Geology, 68, 799-815.

Sillitoe, R.H. (1989) Gold deposits in western Pacific island arcs: the magmatic connection. Economic Geology Monograph 6, 274-291.

Soules, T.F. (1979) A molecular dynamics calculation of the structure of sodium silicate glasses. J. Chem. Phys. 71, 4570-78.

Stevels, J.M. (1957) Handbook of Physics, 20, 350pp.

Stolper, E. (1982) The speciation of water in silicate melts. Geochimica et Cosmochimica Acta, 46, 2609-2620.

Strong, D.F. (1988) A review and model for granite-related mineral deposits. In Taylor, R.P. and Strong, D.F. (eds), Recent Advances in the Geology of Granite-related Mineral Deposits. Canadian Institute of Mining, Metallurgy, Special vol. 39, pp. 424-445.

Taura, H., Yurimoto, H., Kurita, K., and Sueno, S. (1998) Pressure dependence on partition coefficients for trace elements between olivine and the coexisting melts. Physics and Chemistry of Minerals, 25, 469-484.

Thomas, R., Webster, J.D. and Heinrich, W. (2000) Melt inclusions in pegmatitic quartz: Complete miscibility between silicate melts and hydrous fluids at low pressure. Contribution to Mineralogy and Petrology, 139, 394-401.

Titley, S.R. & Beane, R.E., (1981) Porphyry copper deposits, part I. Geological settings, petrology, and tectogenesis. Economic Geology, 75, 214-235.

Tuttle O.F. and Bowen N.L (1958) Origin of Granite in the Light of Experimental Studies in the System $NaAlSi_3O_8$-$KAlSi_3O_8$-SiO_2-H_2O. Geological Society of America Memoirs 74, 153 pp.

Ulrich, T., Gunther, D. and Heinrich, C. (2001) The evolution of a porphyry Cu-Au deposit based on LA-ICP-MS analysis of fluid inclusions: Bajo de Alumbrera, Argentina. Economic Geology, 96, 1743-1774.

Wallace, P.J., Carn, S.A., Rose, W.I., Bluth, G.J.S., and Gerlach, T. (2003) Integrating petrologic and Remote sensing perspectives on magmatic volatiles and volcanic degassing. Eos, 84, 441-456.

Whitney, A. (1989) Origin and evolution of silicic magmas, Reviews in Economic Geology, 4, 183-201.

Williams-Jones, A.E., and Gammons, C.H. (1997) Chemical mobility of gold in the porphyry-epithermal environment, Economic Geology, 92, 45-59.

Wood B.J. and Blundy J.D. (1997) A predictive model for rare earth element partitioning between clinopyroxene and anhydrous silicate melt. Contributions to Mineralogy and Petrology 129, 166-181.

Appendix 1

Silicate structure in glass

Glass is a solid material that has hardened and become rigid without crystallising. In silicate glass, SiO_4 tetrahedral units provide short range order, with each tetrahedron connected to another through jointly shared apex oxygen, thus producing the 3D framework of strong Si-O-Si. The oxygen polyhedra share corners only, not edges or faces. Three or more corners of each polyhedral coordination unit must be shared to ensure polymerisation of a 3D network.
RO_2 and R_2O_3 oxides are the most likely candidates for glass formation. These are known as network formers or glass formers.

Two types of oxygens can exist in silicate structures: 1) bridging oxygen, which is bonded by two Si atoms, and 2) nonbridging oxygen (NBO), in which one oxygen is bonded to one Si atom.

NBOs are formed by the addition of, for the most part, either alkali or alkaline-earth metal oxides to the silica melt. The number of NBOs is proportional to the number of moles of oxides added. Addition of alkali or alkaline-earth metal oxides to silica increases the overall O/Si ratio of the silicate. Increasing the number of NBOs results in the progressive breakdown of the silicate structure into smaller units.

Calculation of NBO

A critical parameter that determines the structure a silicate is the number of NBOs per tetrahedron (NBO/T), which in turn is determined by the O/Si ratio. The ratio O/Si, also called R, is 2 for SiO_2.
For glass containing 12 mol% Na_2O, 10 mol% CaO, and 78 mol% SiO_2

$$R = \frac{12 + 10 + 156}{78} = 2.28$$

$$\frac{NBO}{T} = 2R - 4 \qquad \text{(Stevels, 1957)}$$

For silicate glasses containing more alkali and alkaline earth oxides than Al_2O_3, the Al^{3+} is believed to occupy the centres of AlO_4 tetrahedra. Hence the addition of Al_2O_3 in such cases introduces only 1.5 oxygens per network-forming cation, and NBOs of the structure are used up and converted to bridging oxygens.

Table 3.2. Averages from the EMPA of starting silicate glasses. These are the bulk compositions (molar) for starting materials (glasses) for copper speciation experiments.

Sample	THLT	ALKB	ANDS	HPG1	HPG15	HPG2	HPG25
mol.%							
SiO_2	50.02	49.91	62.74	87.48	86.51	85.74	85.98
Na_2O	2.43	3.26	3.66	2.18	3.40	4.62	4.99
K_2O	0.21	0.63	0.91	2.37	2.96	3.35	3.51
Al_2O_3	8.33	12.31	12.30	7.71	6.84	5.63	4.85
MgO	27.27	22.23	11.73	0.00	0.00	0.00	0.00
CaO	11.23	11.13	7.93	0.00	0.00	0.00	0.00
CuO	0.506	0.536	0.740	0.259	0.279	0.660	0.676
Total	100.00	100.00	100.00	100.00	100.00	100.00	100.00
NBO/T	1.28	1.02	0.50	0.020	0.07	0.13	0.15
R	2.64	2.51	2.25	2.01	2.03	2.06	2.07
X	1.28	1.02	0.50	0.02	0.06	0.12	0.14
Y	2.72	2.98	3.50	3.98	3.94	3.88	3.86

Table 3.3. Molar ratios (Na+K)/Al) and NBO/T in starting silicate glasses

Glass compostion	THLT	ALKB	ANDS	HPG1	HPG15	HPG2	HPG25
(Na+K)/Al (Molar)	**0.32**	**0.32**	**0.37**	**0.60**	**0.93**	**1.42**	**1.75**
NBO/T	**1.28**	**1.02**	**0.50**	**0.020**	**0.07**	**0.13**	**0.15**

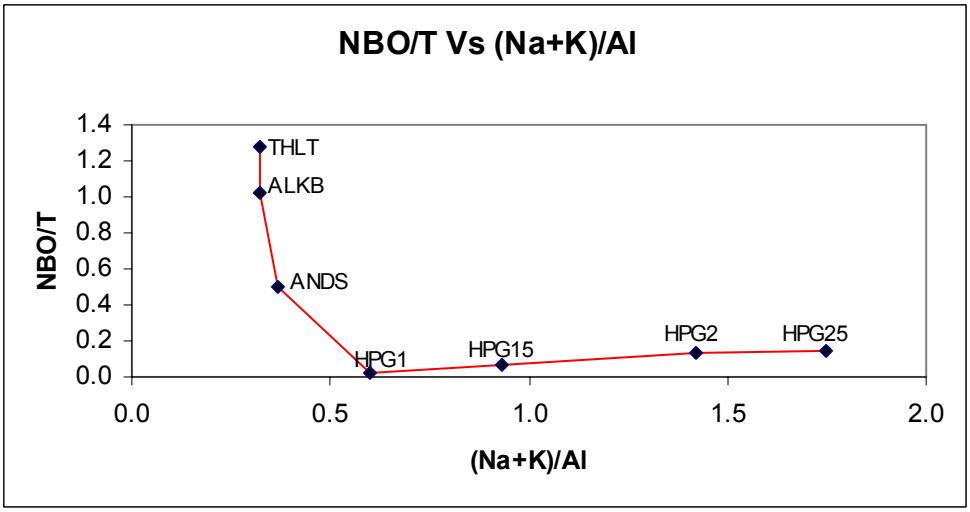

Fig. 3.7. Variation of the ratio of non-bridging oxygen atoms per tetrahedral atom (NBO/T) with the reciprocal ASI. Note: NBO/T ratio has influence over many physical-chemical and optical properties of silicate melts, e.g. optical absorption and density of the experimental glasses apparently increase with increasing NBO/T ratio

Appendix 2

Pressure generated in the capsule for standard glass

PtO_2 enclosed in the capsule with the glass material decomposes to yield solid Pt and gaseous O_2, according to the equation (2.1)

$$PtO_2 \rightarrow Pt_{(s)} + O_{2(g)}$$

Thus, 1 mole PtO_2 decomposes to yield 1 mole of oxygen, in gaseous form.

Therefore 2.45 mg PtO2 used in the experiment will decompose to yield

$$\frac{2.45\times10^{-3}}{227.0788} = 1.08\times10^{-5}\ moles\ oxygen,$$

where 227.0788 is the molar mass (in gram) of PtO2.

This amount of oxygen spreads to occupy the empty space of volume V in the capsule. The inner radius (r) of the capsule is ~ 2.0 mm and the length or height (h) of this space is ~ 3.5 mm. Therefore, V, the volume of this space is given by

$$V = \pi r^2 h$$

$$V = 3.14\times2.0^2\times3.5\times10^{-9}\ \ m^3$$
$$= 4.40\times10^{-8}\ \ m^3$$

If the equilibrium temperature (T) in the capsule was 1523 K, the pressure, P, generated during standard glass preparation is given by the equation of state, thus,

$P = \frac{nRT}{V}$ (Nm^{-2}) where R, the gas constant, equal 8.314 J $K^{-1}mol^{-1}$.

$$P = \frac{1.08\times10^{-5}\times8.314\times1523}{4.40\times10^{-8}\times10^{5}}\ \text{(bar)}$$

$$= 31.1\ \ bar$$

~ 30 bar

Appendix 3

EMPA tables for biotite and residual melt at 800°C and 2 kbar.

COMPOSITION OF BIOTITE AT 800°C and 2 kbar
(Analytical values values, EMPA)

Sample	M10	M20	M31	M32	MAO	MBO	MCO	MDO	mca
Comp. wt%	5 (pts)	4 (pts)	14 (pts)	3 (pts)	7 (pts)	7 (pts)	6 (pts)	10 (pts)	Avrg
SiO_2	40.37	38.71	42.71	44.28	46.90	45.48	46.49	38.12	39.70
K_2O	7.14	7.53	6.92	7.98	8.47	7.40	7.49	8.38	7.52
Na_2O	0.8478	0.61	0.88	0.5872	0.7894	0.6392	0.60	0.62	0.9167
Al_2O_3	15.26	14.48	15.10	16.02	8.60	15.12	14.69	13.34	14.18
CaO	0.0178	0.02	0.04	0.2671	0.0824	0.2182	0.33	0.03	0.0678
MgO	9.17	13.72	7.96	16.36	12.58	11.02	11.27	12.56	9.14
FeO	10.83	10.83	9.43	10.99	10.79	10.22	12.32	9.62	9.17
NiO	11.61	7.82	10.58	0.0859	1.020	6.49	2.77	**8.55**	**10.30**
Gd_2O_3	**0.0077**	-	-	-	-	-	-	-	-
Sm_2O_3	**0.0116**	-	-	-	-	-	-	-	-
Ho_2O_3	-	**0.0097**	-	-	-	-	-	-	-
Ta_2O_5	-	**0.2506**	-	-	-	-	-	-	-
SrO	-	-	**0.0852**	-	-	-	-	-	-
La_2O_3	-	-	**0.0083**	-	-	-	-	-	-
Er_2O_3	-	-	-	**0.0977**	-	-	-	-	-
Pr_2O_3	-	-	-	**0.0087**	-	-	-	-	-
CoO	-	-	-	-	**5.00**	-	-	-	**2.173**
TiO_2	-	-	-	-	**3.17**	-	-	-	**1.538**
V_2O_3	-	-	-	-	-	**0.5046**	-	-	**0.3703**
CuO	-	-	-	-	-	**0.0038**	-	-	**0.0085**
Cr_2O_3	-	-	-	-	-	-	**0.3370**	-	**0.0579**
ZnO	-	-	-	-	-	-	**0.2082**	-	**0.0975**
TiO_2	-	-	-	-	-	-	-	**2.4300**	-
Total	95.25	93.99	93.70	96.67	97.39	97.09	96.48	93.65	97.39

COMPOSITION OF BIOTITE at 800°C and 2 kbar
(Analytical values values, EMPA)

Sample	M40	M51	M52	M61	M62	M70	M71	M72	M83
Comp. wt%	5 (pts)	5 (pts)	14 (pts)	4 (pts)	5 (pts)	7 (pts)	6 (pts)	10 (pts)	8 (pts)
SiO_2	43.42	44.62	42.08	41.05	47.51	41.18	49.17	41.13	43.55
K_2O	7.41	7.65	7.55	7.57	7.20	7.96	7.33	7.75	8.05
Na_2O	0.55	0.64	0.66	0.7723	0.67	0.61	0.70	0.77	0.66
Al_2O_3	14.59	14.71	13.86	14.65	14.09	14.66	14.36	14.01	14.74
CaO	0.39	0.20	0.15	0.1216	0.27	0.14	0.29	0.09	0.14
MgO	13.70	15.27	12.78	12.03	11.20	14.38	12.98	11.36	13.33
FeO	12.26	11.85	11.72	11.65	10.63	10.63	8.18	9.27	14.91
NiO	1.85	0.84	4.91	7.03	4.25	4.88	4.02	10.37	1.33
Lu_2O_3	**0.0479**	-	-	-	-	-	-	-	-
Tm_2O_3	**0.0269**	-	-	-	-	-	-	-	-
BaO	-	**0.8019**	-	-	-	-	-	-	-
Yb_2O_3	-	**0.0398**	-	-	-	-	-	-	-
Rb_2O	-	-	**1.0498**	-	-	-	-	-	-
Nd_2O_3	-	-	**0.0075**	-	-	-	-	-	-
Tb_2O_3	-	-	-	**0.0088**	-	-	-	-	-
WO_3	-	-	-	**0.1412**	-	-	-	-	-
PbO	-	-	-	-	**0.0205**	-	-	-	-
Dy_2O_3	-	-	-	-	**0.0055**	-	-	-	-
Cs_2O	-	-	-	-	-	**0.2938**	**0.0065**	-	-
CeO_2	-	-	-	-	-	**0.0164**	**-**	**0.0078**	-
Nb_2O_5	-	-	-	-	-	**0.4423**	**-**	**0.0110**	-
ZrO_2	-	-	-	-	-	**0.0022**	**0.0137**	-	-
Eu_2O_3	-	-	-	-	-	-	-	-	**0.0098**
MoO_3	-	-	-	-	-	-	-	-	**0.0104**
Total	94.23	96.64	94.76	95.03	95.84	95.21	97.06	94.77	96.73

COMPOSITION OF RESIDUAL MELT at 800°C and 2 kbar
(Analytical values values, EMPA)

Sample	M10	M20	M31	M32	MAO	MBO	MCO	MDO	mca
Comp. wt%	5 (pts)	4 (pts)	14 (pts)	8 (pts)	10 (pts)	7 (pts)	6 (pts)	21 (pts)	Avrg
SiO_2	73.23	71.38	71.63	69.34	74.25	71.34	70.86	71.58	70.70
K_2O	3.33	2.30	3.23	4.20	3.84	3.79	3.59	3.85	2.66
Na_2O	2.05	2.46	2.61	2.14	1.34	1.76	1.41	1.91	2.03
Al_2O_3	12.12	13.58	12.57	14.61	9.19	13.64	13.00	13.02	13.45
CaO	0.25	1.47	0.30	1.50	0.3427	1.58	1.43	1.75	1.86
MgO	0.20	0.22	0.21	0.25	0.3752	0.1516	0.21	0.17	0.2283
FeO	0.90	0.96	0.97	0.97	3.18	0.9515	1.25	0.90	1.10
Gd_2O_3	**0.1898**	-	-	-	-	-	-	-	-
Sm_2O_3	**0.2194**	-	-	-	-	-	-	-	-
Ho_2O_3	-	**0.1373**	-	-	-	-	-	-	-
Ta_2O_5	-	**0.1328**	-	-	-	-	-	-	-
SrO	-	-	**0.1493**	-	-	-	-	-	-
La_2O_3	-	-	**0.0137**	-	-	-	-	-	-
Er_2O_3	-	-	-	**0.1028**	-	-	-	-	-
Pr_2O_3	-	-	-	**0.0749**	-	-	-	-	-
CoO	-	-	-	-	**0.1481**	-	-	-	**0.0641**
TiO_2	-	-	-	-	**0.4871**	-	-	-	**0.1094**
V_2O_3	-	-	-	-	-	**0.0176**	-	-	**0.0161**
CuO	-	-	-	-	-	**0.0036**	-	-	**0.0100**
Cr_2O_3	-	-	-	-	-	-	**0.0211**	-	**0.0499**
ZnO	-	-	-	-	-	-	**0.0246**	-	**0.0125**
NiO	-	-	-	-	-	-	-	**0.0259**	**0.1224**
TiO_2	-	-	-	-	-	-	-	**0.1854**	
Total	92.49	92.63	91.67	93.19	93.16	93.23	91.80	93.39	92.42

COMPOSITION OF RESIDUAL MELT at 800°C and 2 kbar
(Analytical values values, EMPA)

Sample	M40	M51	M52	M61	M62	M70	M71	M72	M83
Comp. wt%	5 (pts)	5 (pts)	14 (pts)	4 (pts)	10 (pts)	7 (pts)	6 (pts)	10 (pts)	8 (pts)
SiO_2	71.17	70.65	69.03	71.86	70.59	70.29	69.95	70.61	71.95
K_2O	3.93	3.81	4.13	3.34	3.95	1.86	4.15	3.71	3.54
Na_2O	1.76	2.45	2.53	2.14	2.09	0.61	2.75	2.57	1.33
Al_2O_3	13.97	13.12	13.12	13.61	13.01	13.10	12.60	12.60	13.16
CaO	1.63	1.39	1.46	1.60	1.46	1.31	1.43	1.51	1.29
MgO	0.31	0.22	0.23	0.15	0.23	0.20	0.23	0.15	0.19
FeO	1.61	0.97	1.15	0.93	1.14	0.94	0.90	0.80	1.35
Lu_2O_3	**0.1221**	-	-	-	-	-	-	-	-
Tm_2O_3	**0.1332**	-	-	-	-	-	-	-	-
BaO	-	**0.4605**	-	-	-	-	-	-	-
Yb_2O_3	-	**0.1310**	-	-	-	-	-	-	-
Rb_2O	-	-	**0.4001**	-	-	-	-	-	-
Nd_2O_3	-	-	**0.0896**	-	-	-	-	-	-
Tb_2O_3	-	-	-	**0.1522**	-	-	-	-	-
WO_3	-	-	-	**0.0790**	-	-	-	-	-
PbO	-	-	-	-	**0.0250**	-	-	-	-
Dy_2O_3	-	-	-	-	**0.1516**	-	-	-	-
Cs_2O	-	-	-	-	-	**0.4049**	-	-	-
CeO_2	-	-	-	-	-	**0.0601**	-	-	-
Nb_2O_5	-	-	-	-	-	**0.1198**	-	-	-
ZrO_2	-	-	-	-	-	**0.0311**	-	-	-
Cs_2O	-	-	-	-	-	-	**0.0127**	-	-
ZrO_2	-	-	-	-	-	-	**0.0328**	-	-
Nb_2O_5	-	-	-	-	-	-	-	**0.0218**	-
CeO_2	-	-	-	-	-	-	-	**0.0212**	-
Eu_2O_3	-	-	-	-	-	-	-	-	**0.1436**
MoO_3	-	-	-	-	-	-	-	-	**0.0632**
Total	94.63	93.21	92.14	93.86	92.64	88.92	92.05	91.99	93.02

Erklärung

Ich erkläre hiermit, dass

- ich die Dissertation ohne andere als die in ihr erwähnte Hilfe verfasst habe,
- ich keine früheren Promotionen oder Promotionsversuche unternommen habe.

Tübingen, den 12.02.2007

Patrick Were.